The Dissertation Committee for Joseph Turner Graham
certifies that this is the approved version of the following dissertation:

A Study of the Ferroelectric Properties of Neutron Irradiatied Lead Zirconate Titanate

Committee:

Sheldon Landsberger, Supervisor

Paulo Ferreira, Co-supervisor

Jon Ihlefeld

Erich Schneider

Steven Biegalski

A Study of the Ferroelectric Properties of Neutron Irradiatied Lead Zirconate Titanate

by

Joseph Turner Graham, B.S., M.S.E.

DISSERTATION

Presented to the Faculty of the Graduate School of
The University of Texas at Austin
in Partial Fulfillment
of the Requirements
for the Degree of

DOCTOR OF PHILOSOPHY

THE UNIVERSITY OF TEXAS AT AUSTIN
August 2013

Dedicated to my brother Jeffrey Graham

Acknowledgments

I wish to thank my advisor, Sheldon Landsberger, who has not only helped point me towards a scientific career from which I will get immense satisfaction for years to come, but who has also showed me the rewards of teaching and who has become a good friend. Thanks to Paulo Ferreira, my co-advisor who has always taken the time to discuss technical challenges and brainstorm ideas for new projects. I would also like to thank the professors of the Nuclear and Radiation Engineering program at UT, Erich Schneider and Steven Biegalski and the staff at the Nuclear Engineering Teaching Lab.

I am grateful to my PIs out at Sandia: Bruce Tuttle, Geoff Brennecka and Jon Ihlefeld who showed me the ropes of ferroelectrics and who were gracious enough to bring me out to Albuquerque to work with them for three summers. Special thanks goes to Jon who gave me many opportunities in the lab and from whom I learned a great deal.

Thanks to my fellow graduate students and friends at UT who make going to class and into the lab seem more like play than work. I hope you all make interesting futures for yourselves. Finally, I thank my family, who have instilled in me a respect for learning and a love of science. Certainly my degree would not be possible without their support.

A Study of the Ferroelectric Properties of Neutron Irradiatied Lead Zirconate Titanate

Joseph Turner Graham, Ph.D.
The University of Texas at Austin, 2013

Supervisor: Sheldon Landsberger
Co-supervisor: Paulo Ferreira

Lead zirconate titantate (PZT) is an electroceramic material with many important technological applications in sensing and computer memory. Some of these applications require the PZT based devices to operate in radiation fields where they will be exposed to a high flux of energetic, heavy and light, charged and uncharged particles. The risk to any device exposed to ionizing radiation is the accumulation of displacement and ionization damage. Significant damage accumulation over time can lead to property drifts and, in some cases, failure of the device to perform properly. The goal of the undertaking recounted in this dissertation was to study changes in the ferroelectric properties of PZT exposed to the neutron field of a research nuclear reactor and to help develop an understanding for the type of radiation induced defects that play a dominant role in the degradation process. Thin film PZT capacitors were prepared using a wet chemical technique. The capacitors were then irradiated in a 1 MW TRIGA research nuclear reactor at the University of Texas

at Austin up to a maximum 1 MeV equivalent neutron flux of 5.2×10^{15} cm^{-2}. Following irradiation, electronic characterization of polarization-electric field hysteresis loops, first order reversal curves, and small-signal permittivity were performed to ascertain tendencies between irradiation dose and ferroelectric properties. The measurements indicate a drop in remanent polarization, a loss of domain wall mobility, shifts in local switching fields and the formation of dipolar defects. These effects are all attributed to the introduction of defects into the material through displacement damage cascades. Numerical models of the damage cascades were performed to determine the displacement concentration. Comparison of those values and the primary recoil spectrum with typical survival rates found in the literature suggest that both free point defects as well as defect clusters are produced in comparable if not larger concentrations. It is proposed that defect clusters play a more significant role in ferroelectric property change than previously believed.

Table of Contents

List of Tables

List of Figures

Chapter 1

Introduction

1.1 The Big Picture

Lead zirconate titanate (PZT) has established itself as a material of great utility within a number of solid state technologies. Its virtues stem from the fact that it shows a marked piezoelectric effect and some of the strongest room temperature dielectric constants of any inorganic compound. This implies that the leverage between applied force (be it mechanical, electrical, etc.) and the material response is strong and therefore ideal for transducing energy, performing a sensing operation, or storing information. A number of scientific, industrial and consumer PZT-based devices have been manufactured on a large scale for years now. Even so, new PZT-based devices are being investigated such as non-volatile memory, micro/nano-sensors, and energy harvesting devices.

An important area of research has looked at the behavior of PZT devices within extreme environments. In such environments the material is prone to degradation or property change. Several niche applications expose the material to substantial doses of ionizing radiation, be it from gamma rays, neutrons, space radiation, etc. Although much has been learned about radiation effects

in conventional electronics in the past half-century, relatively little is known about effects in ferroelectric/piezoelectric materials. Therefore, any attempt to contribute to the understanding of radiation damage in PZT is helpful both for the PZT device community and in contributing to the general knowledge of radiation effects in ferroelectrics and piezoelectrics.

1.2 The Approach

Studying radiation effects in PZT is a task wide in scope. For example one could consider different radiation fields (e.g. gamma, electron, and heavy ion), different PZT based devices, material compositions or processing conditions, etc. To reduce the objectives to something more focused and achievable, this work looks in particular at the effect of neutrons produced in a nuclear reactor on the ferroelectric properties of PZT thin film capacitors of a specific composition. Neutron damage is pertinent to space and nuclear reactor applications of PZT devices. It should be mentioned that although fast neutrons are not a dominant component of space radiation, damage cascades induced by cosmic rays and fast neutrons are very similar (as compared to those induced by gamma or electron irradiations). Thin film capacitors are relevant to non-volatile computer memory applications and are amenable to ferroelectric characterization.

Studying the radiation effects was done through a combination of experimental and modeling techniques. The experimental techniques were used to characterize the ferroelectric properties of prepared, irradiated PZT capac-

itors and help diagnose the types of irradiation induced defects present in the material. Complimentary numerical modeling was performed as a means of quantifying the amount of accumulated damage in the samples and to produce estimates of the types and concentrations of defects in order to help weigh the possible interpretations of the experimental results.

1.3 Objectives

The objectives for this work were:

1. Prepare and/or obtain PZT thin film capacitors
2. Irradiate them to different damage dose levels
3. Perform electronic characterization to determine the dose vs. effect relationships for various ferroelectric property parameters
4. To use the experimental results to draw conclusions about nature of the post-irradiation defect microstructure
5. To perform numerical simulations and employ models to investigate the damage event at the atomic scale and, if possible, make predictions about the resulting damage microstructure and its effect on measured material property changes

1.4 Main Contributions

Although many kinds of measurements and experiments will need to be performed in future to help complete our understanding, the main objectives of this work were accomplished and the information they reveal contributes to the knowledge of radiation effects in PZT. In summary, this work is the first to study (at least in the published literature) the effects of neutron damage on domain wall mobility and domain switching processes in a rigorous manner. Furthermore, it presents evidence against the oxygen-vacancy hypothesis of neutron damage espoused in some of the literature and evidence that defect clusters play an important if not dominant role in ferroelectric property change. Along a different line, this work shows that neutron irradiation (and possibly irradiation in general) can be used as a technique for introducing structural defects into ferroelectric materials in a controlled manner. The hope is that researchers within the electroceramics community adopt controlled irradiation as a new tool in the systematic study of defects and their relation to ferroelectric properties.

1.5 Outline of Subsequent Chapters

The following chapters are summarized as follows:

- Chapter 2: State of Understanding provides background on radiation environments, radiation damage theory, PZT and its properties, and a review of the published literature on radiation damage in PZT. Its main

purpose is to introduce some of the concepts and terminology found in the remaining chapters and to frame the activities performed in this work within the current understanding of neutron damage in PZT thin films

- Chapter 3: Sample Preparation overviews the techniques performed to prepare the samples used in the study, to characterize the irradiation facility, and to show how the irradiations were performed and the samples were readied for electronic characterization

- Chapter 4: Characterization presents details of the electronic measurements taken with explanations of the techniques, the procedures used, and analysis and interpretation of the results

- Chapter 5: Modeling explains how several computer codes were used to obtain useful information about the radiation damage event from the creation of the primary recoil atom (PKA) to the early stages of cascade development. A discussion of the results with order-of-magnitude estimates is presented to help formulate conclusions regarding the roles that defects play in the observed ferroelectric property changes

- Chapter 6: Conclusions and Further Work presents a summary of the work and the central conclusions drawn from it. Questions remaining about the damage event and its outcomes are outlined here and recommendations for further experimental and modeling work are suggested

Chapter 2

State of Understanding

2.1 Radiation Environments

2.1.1 Radiation in Space

Sending spacecraft and satellites into space is a costly venture. Once in space it is extremely difficult to repair these crafts if they are damaged. Therefore, as with all other parts on-board, their electronics and optoelectronic devices are designed with durability and reliability in mind. Radiations in space cause both temporary and permanent damage to such devices, leading, in many cases, to eventual operational failure. To build a device that successfully operates in space one must understand what mechanisms cause degradation, how degradation evolves over the lifetime of the device, and how to test said device on earth to assure that it will perform within acceptable parameters.[1] There are three main components to space radiation. They are: trapped radiation, cosmic rays and solar flares.

Trapped radiation constitutes charged particles over a broad range of energies trapped by Earth's magnetic field. The charged particles are concentrated in the Van Allen radiation belts - rings of high flux that lie in Earth's orbital plane. The two primary forms of trapped radiation are electrons and protons. The electrons span an energy range up to several MeV and have flux

maxima of several 10^6 cm^{-2} s^{-1} at distances of about 1.5 and 5 times the Earth radius. Protons are found with energies up to several hundred MeV and have a flux maximum of several 10^6 cm^{-2} s^{-1} at about 2 times the Earth radius.[2] Figure 2.1 shows the daily integrated trapped radiation fluence as a function of altitude along Earth's equatorial plane.

Cosmic rays consist of heavy ions. These ions may be very energetic reaching beyond the TeV range. Cosmic rays are classified as being either primary or secondary. Primary cosmic rays originate from outside the solar system; predominantly from the Milky Way galaxy and from other galaxies to a small extent. They contribute a constant low flux of charged particles. Primary cosmic rays consist of about 85% protons, 14% alpha particles and 1% heavier ions mostly spanning the range from hydrogen to nickel and energies up to about 1 GeV.[4] Secondary cosmic rays originate from interactions between primary cosmic rays and Earth's atmosphere. These interactions produce cascades consisting of a variety of neutral and charged particles such as neutrons, mesons, muons and electrons.[5]

Solar flares are intermittent bursts of radiation arising from solar storms. Such bursts can throw off high fluxes of protons and, to a lesser extent, alpha particles and electrons. Their frequency depends on the number of sun spots and the solar cycle.[6] The proton flux from a solar flare can dominate the total particle flux in space. In some cases, supra-10 MeV integrated proton fluences exceeding 10^{10} cm^{-2} have been observed.[7]

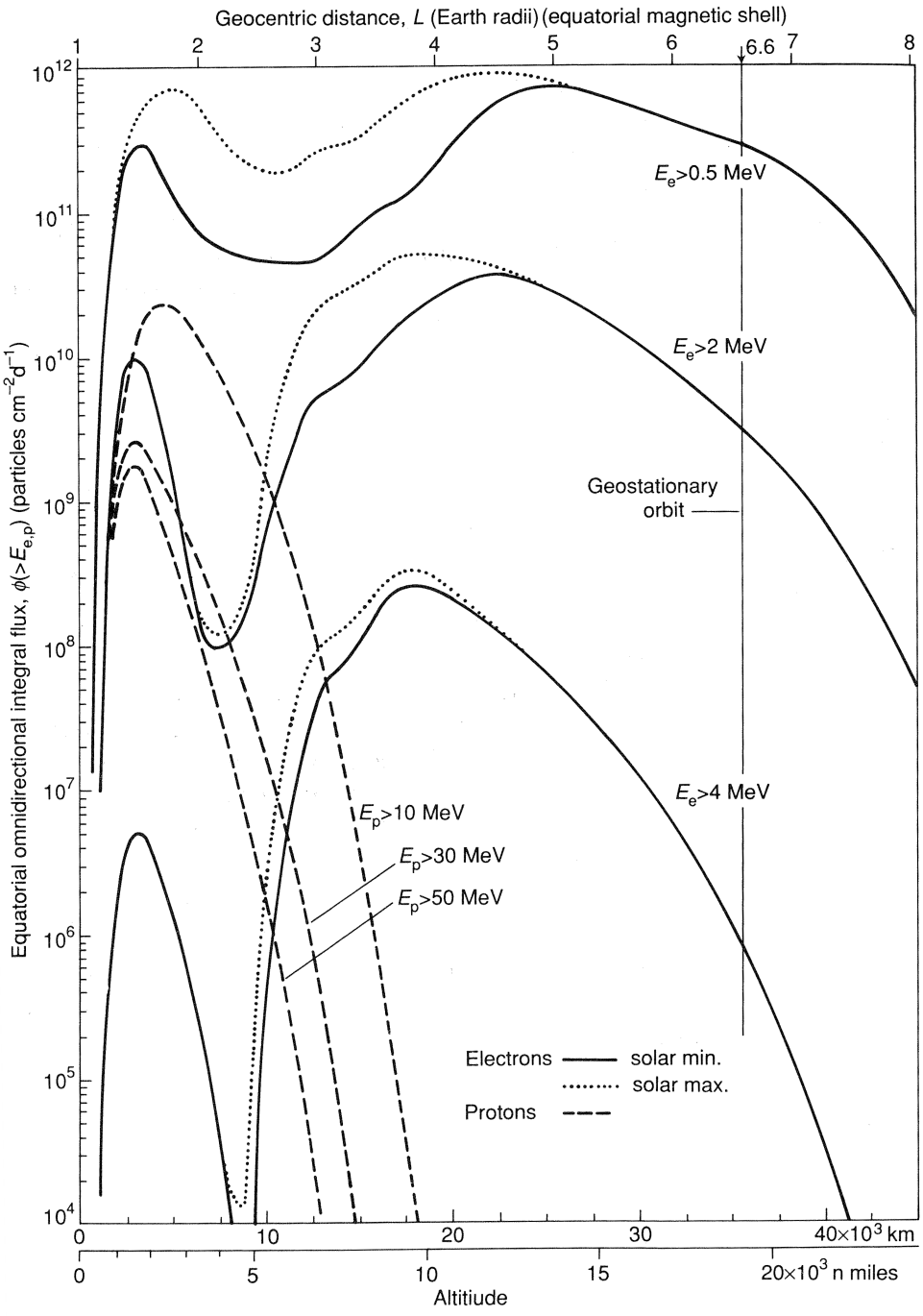

Figure 2.1: Radial profiles of trapped proton and electron radiation around the earth.[3]

2.1.2 Radiation in Nuclear Reactors

Materials in nuclear reactors are exposed to intense neutron and gamma fields. The stability of structural materials used in reactor core parts is of utmost importance in assuring the service lifetime of those parts, and maximizing the safety and lifetime of the core as a whole. Furthermore, many of the solid state sensors and electronic control systems implemented at various parts of a nuclear power plant are exposed to sizable doses of radiation. While not typically exposed to the levels seen by the fuel, cladding, and structural steels in the core, many of the materials used within sensors and electronics are highly sensitive to radiation and prone to degradation and failure over the 40+ years that they are expected to operate.

While in-core neutron fluxes on the order of 10^{14} cm^{-2} s^{-1} are typical for commercial light water reactors (LWRs), in-containment fluxes (fluxes at different locations within the containment structure) may only be as high as 10^{5} cm^{-2} s^{-1}. Furthermore, while gamma dose rates from 10 - 10^{4} Mrad h^{-1} are present in-core, in-containment rates may be no higher than 1 Mrad y^{-1} except in accident conditions.[3]

Instrumentation and monitoring equipment is also placed within the air cavity between a reactor pressure vessel (RPV) and its concrete shield-support. Fast neutron fluxes, while still considerably lower than inside the core itself can reach 10^{9} cm^{-2} s^{-1}; much higher than the in-containment levels.[8,9] At these fluxes, the accumulated damage over a period of several months to a year is enough to affect the operability of many electronics.

2.1.3 Weapons Environment

Nuclear bombs release most of their energy in the form of a blast wave and thermal radiation. About 15%, however, of their energy is released as prompt and delayed nuclear radiation, mainly in the form of gamma rays and fast neutrons.[10] The neutron spectrum for a fission bomb near the blast epicenter is essentially equivalent to the Watt fission spectrum, having an average neutron energy of about 2 MeV. D-T thermonuclear devices on the other hand have a 14 MeV neutron component in addition to the fission spectrum. The neutron and gamma doses from a 1 Mt nuclear device at 1 mile from the epicenter are approximately 1800 rads (8×10^{11} cm^{-2}) and 10,000 R, respectively.[10] For high altitude detonations, delayed gamma rays can also generate a source of Compton electrons which fly off into the atmosphere where they interact with Earth's magnetic field, generating a powerful burst of synchrotron radiation, the so-called electromagnetic pulse (EMP). These forms of neutron and photon radiation can cause both transient and permanent effects in civilian and military electronics.

2.1.4 Radiation Processing Environments

Many radiation processing environments are characterized by high gamma dose rates. Examples include food, sewage and medical irradiation, and polymer modification facilities that frequently employ many MCi ^{60}Co sources and other strong gamma sources to sterilize or process various materials. Spent fuel reprocessing and nuclear waste processing plants can contain strong mixed

gamma, alpha and beta environments. In many phases of the reprocessing stream and in hot cells, the radiation environment is far too extreme for humans, requiring the extensive use of robotics. The sensors and electronics in these robotics are prone to radiation degradation.

2.1.5 Fusion Reactors

The large flux and hard neutron spectrum of a controlled fusion reactor poses a serious challenge to sensor designers. Diagnostic instruments and sensors are required to penetrate through shielding near the inner torus of a tokomak style fusion reactor, as well as outside the confining magnets, the torus hall, and support structure. The 1 MeV equivalent neutron flux at these locations may vary from 10^{11} - 10^{16} cm^{-2} s^{-1}.[11] The use of diagnostic sensors in such environments will require limitations on exposure time, frequent replacements, careful shielding design, and the development of extremely radiation tolerant materials and technologies. Radiation hardness testing protocols will also be needed to evaluate the suitability of devices within the controlled fusion environment.

2.1.6 Particle Accelerators

Particle accelerators and spallation sources generate large fluences of high energy photons, hadrons and leptons at energy scales of GeV and above. Some of these originate from particles escaping the accelerator beam line, possibly causing nuclear interactions with structural materials on their way out

and producing secondary radiation. Other particles are produced in collisions within detector arrays. There are numerous electronics both surrounding the beam lines and as part of the detection systems. Figure 2.2 shows the radial dependence of the neutron and other hadron yearly fluences near the core of the ATLAS detector of CERN's Large Hadron Collider (LHC). Clearly, fluences as high as 10^{14} cm^{-2} may be seen from the innermost particle detectors.

2.2 Radiation Effects

Radiation effects comprise the variety of microscopic and macroscopic material property changes upon exposure to ionizing radiation. There is a wide range of radiation damage phenomena shared by many types of solids. Some phenomena, however, are unique to a particular solid and depend on its structure, composition, physical dimensions, etc.[13] As a convenience, radiation effects are frequently broken up into two categories: displacement effects and ionization effects. Displacement effects pertain to those properties tied to the arrangement of atoms within a structure, while ionization effects relate to the re-distribution of electrons within the solid. Therefore, displacement effects come about from the quasi-permanent displacement of atoms from their equilibrium positions, while ionization effects result from the separation of orbital electrons from their host atoms.

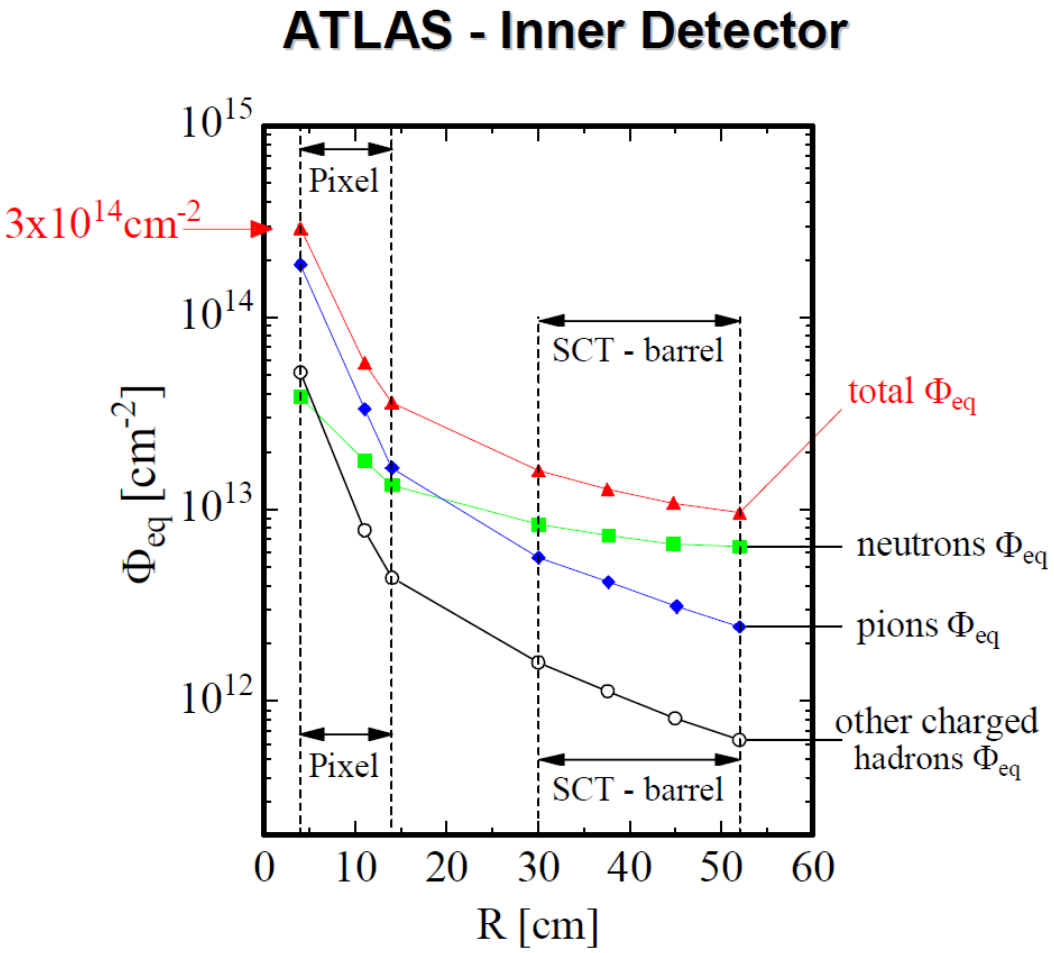

Figure 2.2: Radial fluence profiles of neutrons and other hadrons in the ATLAS detector array at the Large Hadron Collider (LHC).[12]

2.2.1 Stopping Power

The radiation damage event occurs when an incident particle dissipates its energy in the solid in the form of nuclear and electronic interactions. The stopping power describes the energy dissipated by a charged particle along its trajectory as it slows down. It consists of two main components: the nuclear stopping power and the electronic stopping power. The former accounts for energy loss in the form of kinetic energy transfer to nuclear matter while the latter accounts for energy loss due to electronic excitation and ionization. The strength of the stopping power depends on the composition of the material as well as the mass and charge of the incident radiation. For example, there is no direct electronic stopping associated with neutrons. Neutrons dissipate their energy in the form of neutron-nuclear collisions. For the energies associated with thermal nuclear reactors, these interactions are primarily elastic and inelastic scattering collisions. For high energy neutrons, non-elastic absorption reactions must be taken into consideration both because they contribute to the total dissipation of the neutron's kinetic energy, but also because they can produce highly energetic secondary radiation, and therefore, other modes of radiation damage.

High energy heavy charged particles dissipate the majority of their energy through electronic processes. For ions, the electronic stopping power dominates at energies above 1 MeV, while below a few keV, nuclear stopping dominates. This energy dependence results in a damage profile characterized by a trail of ionization damage followed by a dense region of displacement

damage located around the terminus of the ion trajectory.

2.2.2 The Displacement Cascade

At the atomic scale, nuclear stopping is a process in which the incident radiation transfers sufficient kinetic energy to an atom within the solid to displace it. Below a certain threshold energy called the displacement energy, E_d, displacements are not possible as the energy transferred is lower than the binding energy of the atom within its equilibrium site. The transfer of energy below E_d results in the excitation of phonons; collective oscillations of structure.

Above the displacement energy, the struck atom's bonds are severed and it is displaced into the surrounding matrix. The first displaced atom is called the primary knock-on atom (PKA). If once displaced, the PKA possesses additional kinetic energy in excess of the displacement energy, it may initiate the displacement of neighboring atoms resulting in the formation of secondary knock-on atoms (SKAs). Extending the reasoning, SKAs may give rise to additional knock-ons and so forth. A displacement cascade thus forms in which a volume of initially ordered material becomes saturated with displacements. The size and energy density of the volume, however, is restricted by the incident particle type and its energy.

Gamma rays, and sub-MeV electrons experience nuclear stopping through small energy transfers slightly above the displacement energy, the accumulated displacement damage mainly consists of isolated Frenkel pairs (vacancy-

interstitial pairs). In other words, cascades are unlikely to form. Since most of the PKA's energy is consumed in its formation, little energy is available for the creation of SKAs. Fast neutrons and swift ions, on the other hand, can produce high energy PKAs (and by extension, large displacement cascades). When SKAs are produced with energies in the electron stopping regime, they might travel a certain distance away from the cascade core experiencing little nuclear stopping. As soon as they dissipate enough energy through electronic processes, they will dispose of much of the remainder of their energy in the formation of terminal sub-cascades as shown in figure 2.3.

2.2.3 Stages of the Cascade

Isolated Frenkel pairs have two fates. Either the vacancy and interstitial pair will undergo immediate recombination or they will thermally diffuse away from one another. Thus steady, low energy irradiations result in a supersaturation of point defects. Displacement cascades on the other hand proceed through a complicated set of stages towards thermodynamic equilibrium. The initial PKA is formed in less than 1 fs. Subsequent growth of the cascade proceeds up to about 1 ps in the collisional phase. During this phase the total number of displacements reaches its maximum. The exact occurrence of the displacement peak depends on the maximum size of the cascade and the material in question. At this point, the energy density is heterogeneously concentrated amongst the knock-ons in the cascade core.

In the thermal spike, these knock-ons dissipate their energy to neighbor-

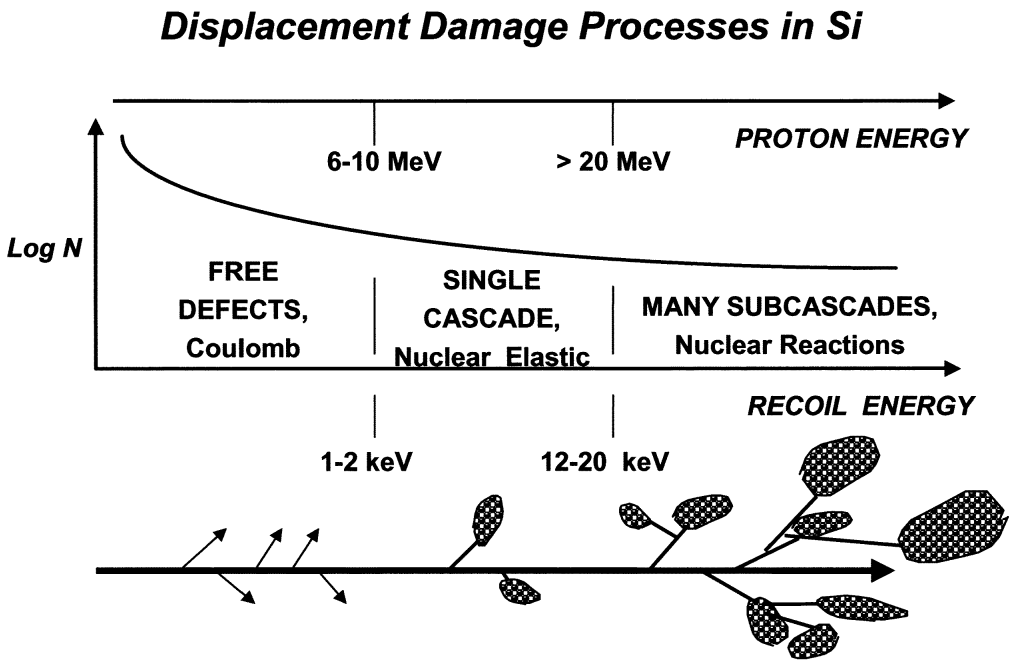

Figure 2.3: Depiction of the relationship between ion energy and cascade structure for protons incident on Si. Low energy ions produce isolated displacements through a large number of interactions (N). High energy ions produce many sub-cascades through relatively few interactions.[14]

ing atoms within the cascade core and eventually the surrounding matrix until a state of thermodynamic equilibrium is established. During the thermal spike phase, the cascade volume may be considered a quasi-molten region within the crystal. During the quench phase, this molten region solidifies and stable lattice defects form. Note that, in crystalline materials where the quench occurs more rapidly than the onset of homogeneous nucleation, the molten volume will be undercooled and form an amorphous phase. This effect is called direct impact amorphization. The quench stage takes on the order of several ps to complete. For non-amorphized materials the remaining defects include point defects and point defect clusters. Because of in-cascade recombination, the total number of surviving point defects is smaller than the peak number of displacements in the collisional phase. As a general rule, the larger the cascade volume, the greater the in-cascade recombination rate and the smaller the fraction of surviving defects. Ceramics and ionic solids have higher surviving defect fractions than other materials. This is attributed to their inability to flow plastically and relieve internal stresses.[13] Two important distinctions between radiation damage through isolated Frenkel pair production and through cascades is that isolated pairs produce a nearly spatially uniform source of point defects and zero in-cascade clustering while cascades result in both a variety of mobile and immobile defect clusters as well as concentrated plumes of point defects.

The annealing stage describes the thermal diffusion of defects away from the cascade and into the surrounding bulk. It ends when either all mo-

bile defects have left the cascade volume or another cascade occurs within it. Therefore it describes an interval of time anywhere from several ns to months.

2.2.4 Damage Evolution

To recap, the damage cascade produces the following: immobile defect clusters, mobile defect clusters, and a supersaturation of point defects. The subsequent damage evolution of the material is a consequence of the thermal diffusion of the mobile defects throughout the lattice, their interactions with one another, and their interactions with immobile imperfections distributed throughout the crystal. The main categories of point defect source and loss mechanisms include:

- in-cascade generation
- bulk thermal generation (this is usually negligibly small compared to in-cascade generation)
- recombination of complimentary point defects (i.e. annihilation of self-interstitial atoms with vacancies)
- loss to sinks including non-complimentary point defects (e.g. substitutional impurities), defect clusters, grain boundaries, dislocations, etc.
- thermal emission from defects

Coupled to the point defect evolution is the evolution of defect clusters and pre-existing sinks. Through point defect capture (sink capture) and

thermal emission, clusters and other extended defects change in size, shape and mobility. The permanent displacement damage effects are most directly related to the final, quasi-steady state, defect microstructure. For example, mechanical properties of irradiated metals and alloys are largely determined by the nucleation and growth of dislocations and voids. In electronic materials, even small defects can play a dominating role in property drift. Increase in concentrations of point defects and point defect complexes, have significant ramifications on charge carrier scattering and trapping.

2.2.5 Ionization Damage

As mentioned previously, high energy ions, whether produced from an external radiation source - such as cosmic rays or an ion beam - or internally from PKAs and SKAs, dissipate a large fraction of their energy through the electronic stopping process of ionization. In the solid state one interprets this ionization as the promotion of a valence electron to a conduction band (or to any higher unoccupied band) and the production of an electron hole. For metals where the conduction and valence bands overlap, electron hole recombination/de-excitation is a nearly spontaneous process. Any excitation energy in the conduction band is quickly dissipated in the form of heat. Thus ionization effects in metals are of zero practical significance.

In semiconductors and insulators where a finite band gap separates electron hole pairs, there is an associated recombination time. In both materials, the injection of an excess of holes and electrons via ionization trails increases

the conductivity, a condition known as radiation induced conductivity. The presence of structural defects either from initial processing or displacement damage introduce interband energy levels which act as traps for charge carriers and generation and recombination sites. Such traps are classified as deep levels or shallow levels according to their proximity to either band edge; deep levels being found near mid-band while the shallow levels are near the conduction and valence band edges.

In semiconductors, where the band gap is on the order of an eV, recombination is rapid, making ionization damage a transient condition. Deep level traps from structural defects or impurities dramatically alter the recombination and generation rates for electrons and holes. Shallow levels on the other hand, influence charge transfer time and mobility. In insulators, where the band gap is large, the recombination is a slow process. Shallow levels trap charge carriers for long periods of time contributing to quasi-permanent space charges. Although still technically a transient condition, ionization effects in insulators may persist for years or even decades. Thus both displacement and ionization effects are significant contributors to the permanent radiation effects in ceramics and other insulators.

2.3 Lead Zirconate Titanate (PZT)

Lead zirconate titanate (abbreviated as PZT) is a member of the ABO_3 family of perovskites. It can be thought of as a solid solution of lead titanate, $PbTiO_3$, and lead zirconate, $PbZrO_3$. Its chemical formula is expressed as

$PbZr_xTi_{1-x}O_3$ where x is the fraction of lead zirconate. PZT exhibits both piezoelectric and ferroelectric properties meaning that it can retain a spontaneous electric polarization and the strength of the polarization is coupled to the strain field in the crystal. In practical terms the piezoelectric effect enables the material to transduce a mechanical stress such as compression or shear into a voltage drop across the material. A converse effect also exists where an applied electric field induces crystal strain.

Figure 2.4 shows the unit cell of PZT at different temperatures. The Pb atoms occupy the unit cell vertices that is, the A sites of the perovskite structure. They have a valence state of 2+. Ti and Zr occupy the body centers, or B sites, and have a 4+ valence state. O atoms are located on the face centers and form the vertices of octahedra. The O atoms have a valence state of 2-. Above the Curie temperature (subfigure 1), the unit cell is cubic and centrosymmetric. Piezoelectricity and ferroelectricity are not possible in centrosymmetric systems due to symmetric cancellation of dipole moments. Below the Curie temperature (subfigure 2) the crystal distorts into a tetragonal, rhombohedral or orthorhombic phase, depending on the composition parameter x (figure 2.5). These three systems are non-centrosymmetric and exhibit ferroelectric (tetragonal and rhobohedra phasesl) or anti-ferroelectric (orthorhombic phase) properties. The tetragonal and rhobohedral phases are ferroelectric while the lead zirconate rich, orthorhombic phase is antiferroelectric. Ferroelectric and antiferroelectric phases both consist of an ordered array of electric dipoles. In the ferroelectric phase, however, adjacent dipoles are aligned while in the

anti-ferroelectric phase they are anti-aligned.

Owing to the spontaneous alignment of adjacent dipoles, a ferroelectric material contains regions with uniform electric polarization. Such regions are referred to as ferroelectric domains. Each ferroelectric domain may be oriented in any one of the stable directions possible for the particular phase and grain orientation. The thin transition region between two adjacent domains is called a domain wall. In the absence of an applied external electric field, the domains may be randomly oriented with respect to one another. The bulk polarization is then nearly cancelled out by the contributions of oppositely polarized domains. Under the influence of an electric field, however, domains aligned with the electric field have a lower volumetric energy density than those anti-aligned with the field. Therefore, the aligned domains grow at the expense of the anti-aligned grains (which shrink). An associated domain wall motion is observed.

Upon polling the material (application and removal of an external field), the macroscopic polarization will retain some of the polarization it had in the poled state. In other words, the act of poling the material replaces the stable random domain structure with a stable correlated one. Consequently, hysteresis is observed in the polarization as a function of applied field. Figure 2.6 shows a typical hysteresis loop formed by measuring the polarization response from an applied AC electric field. Note that the initial state has zero macroscopic polarization, corresponding to a random domain structure. The polarization increases along the initial ascending branch towards a saturation

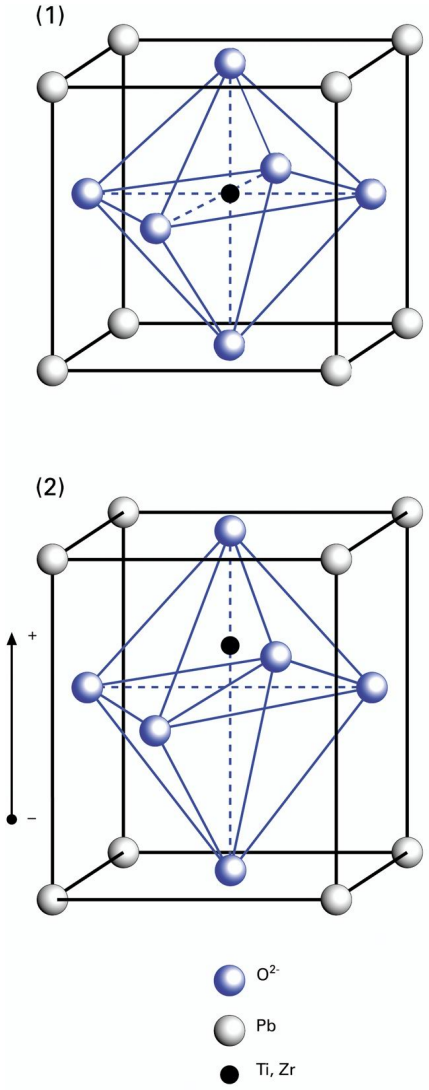

Figure 2.4: The lead zirconate titanate (PZT) unit cell. Above the Curie temperature the unit cell is cubic and centrosymmetric (1). Below, it distorts into a non-centrosymmetric phase (2). Here, an exaggerated tetragonal distortion is shown.[15]

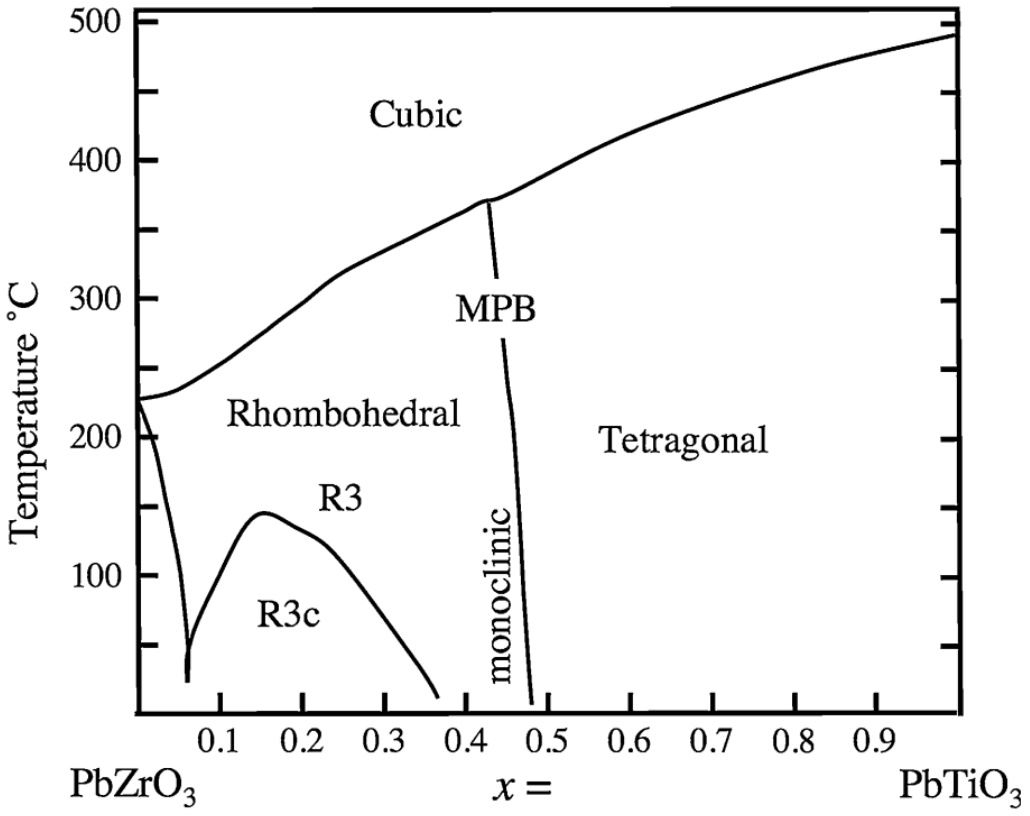

Figure 2.5: The phase diagram of PZT. The high temperature phase is cubic and non-ferroelectric. The lower temperature ferroelectric phases are tetragonal or rhobohedral. A lead zirconate rich, orthorhombic, anti-ferroelectric phase also exists.[16]

polarization at the maximum field value. Once the field is removed, the material is said to be polarized with a positive remanent polarization, P_r. Similarly, applying a negative field results in a negative saturation polarization and negative remanent polarization, $-P_r$. The intercepts on the E-field axis, E_c and $-E_c$, are the coercive field values. These values represent the electric fields needed to reverse the polarization for half of the domains. The figure is drawn symmetrically suggesting that the absolute magnitudes of the remanent polarizations and coercive fields are equal. In fact, this is not true in general. In thin films, internal bias fields and non-mirror symmetric capacitors can shift and distort the hysteresis loop.

2.3.1 Charged Defects in PZT

Charged defects influence ferroelectric behavior by acting as pinning sites that impede domain wall motion.[18] As domain walls move under the influence of an applied field, they encounter defects. The electric fields of charged defects interact with the polarization density in the vicinity of the domain wall, resulting in scattered local minima and maxima in the free energy landscape of the domain wall. This noise in the free energy basically makes up the field of pinning sites in the material. Point defect complexes that form defect dipoles (DDs) are known to be an important class of charged defects.[19–21] In PZT ceramics, mobile oxygen vacancies associate with substitutional acceptor impurities to form DDs of the $A'_B - V_O^{\bullet\bullet}$ and $A''_B - V_O^{\bullet\bullet}$ types.[19,22] These DDs are largely responsible for the domain stiffness, also termed hardness, charac-

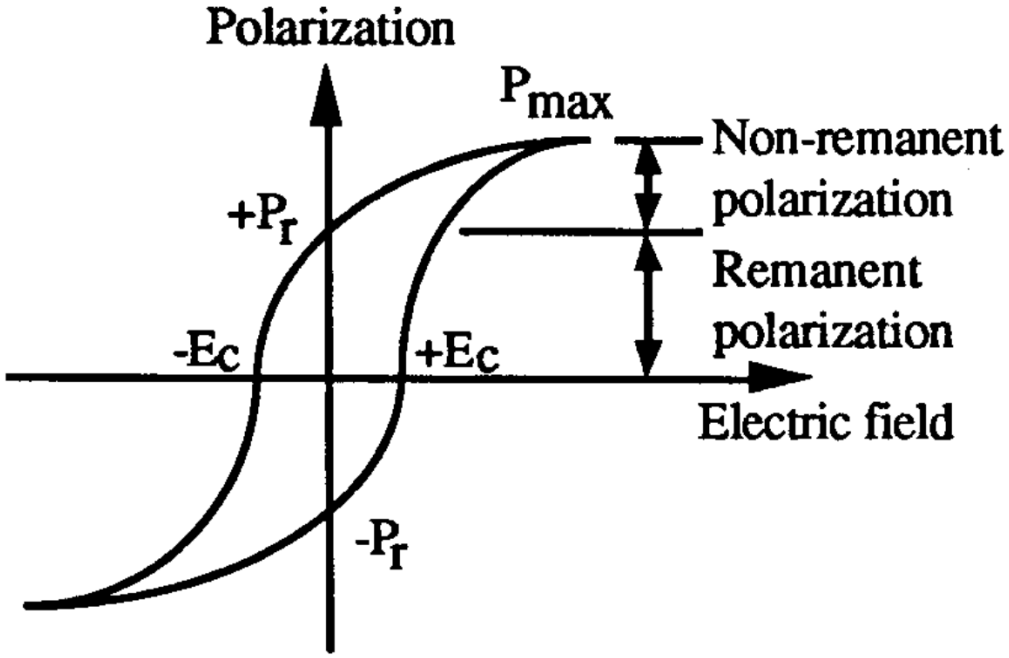

Figure 2.6: A polarization-electric field hysteresis loop indicating the saturation polarizations, the remanent polarizations, $\pm P_r$, and the coercive fields, $\pm E_c$.[17]

teristic of acceptor-doped PZT. In contrast, low mobility type DDs such as $V''_{Pb} - D^{\bullet}_{Ti}$ in soft PZT lower the oxygen vacancy concentration and increase domain wall mobility. In ambient temperature, radiation-free environments, the equilibrium population of DDs reflects chemical composition and processing conditions. Vacancy concentration is naturally dictated by a number of mechanisms such as charge compensation of impurity/dopant atoms, grain growth, crystallization temperature, unbalanced ionic volatility, and substrate interactions to name a few.

2.3.2 Applications of PZT

Perovskite oxides have a particularly wide range of applications. The ferroelectric and piezoelectric properties of PZT have been exploited in sensors, transducers and electronics components.[23] Some of these devices are commercially produced while some of the novel ones are undergoing development. The list below names a few of the applications of PZT.

- voltage tunable capacitors
- infrared detectors
- surface acoustic wave (SAW) devices
- microactuators
- non-volatile ferroelectric random-access computer memory (Fe-RAM)

Situations in which a PZT based device might be used in the future place the device in intense radiation environments such as those mentioned earlier. Proposed applications of PZT sensors in the nuclear reactor environment include ultrasonic vibration monitors placed either on top of the reactor pressure vessel or in various locations within the containment structure.[24,25] Such sensors may be sensitive to tremors caused by abnormal behavior within a pressurized system or seismic activity. Authors have also investigated the feasibility of PZT based fission product pressure sensors for monitoring the buildup of fission product gases within nuclear fuel pins.[26]

Potential satellite and spacecraft applications of PZT include: Fe-RAM in satellites,[27–29] tilt positions systems,[30] and cosmic dust impact detectors for solar panels.[31] Other high radiation applications of PZT include a high intensity and energy radiation detector[32] and a temperature sensitive element for fusion devices.[33]

2.4 Radiation Damage in PZT

The role(s) of defects on ferroelectric behavior in PZT ceramics and thin films are important because of their strong influence on extrinsic properties - properties related to the interaction of electronic or crystallographic defects and domain walls. Understanding damage accumulation is necessary to assess a device's suitability and lifetime in one of the aforementioned radiation environments. Inducing radiation damage defects in PZT is also of novel experimental value. Neutron irradiation is a means of introducing crystallo-

graphic defects in a material in a controlled manner. It can thus be looked at as a tool complimentary to controlled doping and processing parameters to vary the type and amount of defects in the material. In irradiated materials the vacancy, SIA, and cluster concentrations are process independent. They primarily depend on dose, irradiation temperature, and defect reactions.

That said, microstructure plays a critical role in damage evolution and subsequent changes in material properties. Indeed, comparison of previous studies on neutron effects in PZT indicate roughly an order of magnitude lower damage thresholds in thin film compared to bulk.[34–36] It is expected that a wider variety of DDs and other charged defects may form in irradiated PZT than occur during typical processing, providing a broader landscape of domain wall pinning sites and other possible effects on switching behavior.

While much effort has been spent studying the role temperature and mechanical stress plays on the degradation of PZT, relatively little is known about the displacement and ionization effects. What has been studied in the open literature has focused mainly on device level properties although some inferences have been made as to the microscopic degradation mechanisms important in radiation induced degradation. Furthermore, few studies have specifically examined displacement damage in thin films where the effects of clustering and defect reactions may play a heightened role. The following sections summarize the literature on radiation effects in neutron and gamma irradiated PZT.

2.4.1 Neutron Irradiation Effects

Based on elementary damage theory, defects expected to exist within neutron irradiated perovskites include A, B and O site vacancies and interstitials as well as trapped mobile charge carriers and defect clusters. Several authors have suggested oxygen vacancies play a dominant role.[35–37] These conclusions, however, are based on similarities in the behavior of irradiated PZT with PZT in which the concentration oxygen vacancies are increased through the controlled use of acceptor dopants. Since the effects of cation self-interstitials, non-oxygen vacancies, and higher order cluster defects have been all but ignored in the literature, it is prudent to at least look into these effects, if only to discount them as unimportant. Initially, radiation effects studies focused on bulk samples. Recently, more work has been done looking at the effects of neutron irradiation in PZT thin films.

2.4.1.1 Electromechanical Properties

The electromechanical coupling coefficient, k_p, is defined as the square root of the electrical or mechanical energy produced per unit total energy consumed. It is essentially a measure of the strength of the electromechanical response.[38] The mechanical quality factor, Q_M, accounts for dielectric and mechanical losses during the energy conversion process. Thus, a piezoelectric material with a high electromechanical coupling coefficient and a small mechanical quality factor is considered an efficient transducer of electrical (mechanical) energy to mechanical (electrical) energy.

Miclea *et al.* studied the effects of neutron irradiation on the electromechanical coupling coefficient and mechanical quality factor.[35] They examined the behavior of these values as a function of integrated neutron fluence and doping in 15 mm diameter by 1.5 mm thick bulk discs prepared via powder processing and sintering. One of the two materials studied was acceptor doped with Mn and donor doped with Nb in a composition of $PbZr_{0.45}Ti_{0.49}Mn_{0.17}Nb_{0.033}O_3$ while the other, a donor doped material, had a $PbZr_{0.45}Ti_{0.49}Li_{0.007}Nb_{0.02}O_3$ composition. The authors referred to these samples as hard and soft PZT, respectively.

Figures 2.7 and 2.8 show the results of the mechanical tests upon irradiation to various fluences. Evidently, there is a significant change in both properties for fluences above about 10^{14} cm^{-2}. Most notably, there is an increase of over 100% within the mechanical quality factor in both materials at the maximum fluence, indicating a significant increase in hardness and mechanical losses, presumably due to irradiation induced defects.

Toacsan *et al.* reported similar behavior in a similar study.[36] They examined PZT with $Pb_{0.98}Zr_{0.515}Ti_{0.485}Nb_{0.02}O_3$ and $Pb_{0.93}Zr_{0.6}Ti_{0.4}La_{0.07}O_3$ prepared as 10 mm diameter by 1 mm thick disks. They noted losses of k_p comparable to that of Miclea *et al.* at a fast neutron fluence of 10^{18} cm^{-2}.

2.4.1.2 Dielectric Properties

The relative permittivity, ϵ_r, of a dielectric insulator determines its polarizability. The higher the relative permittivity, the greater the polarization

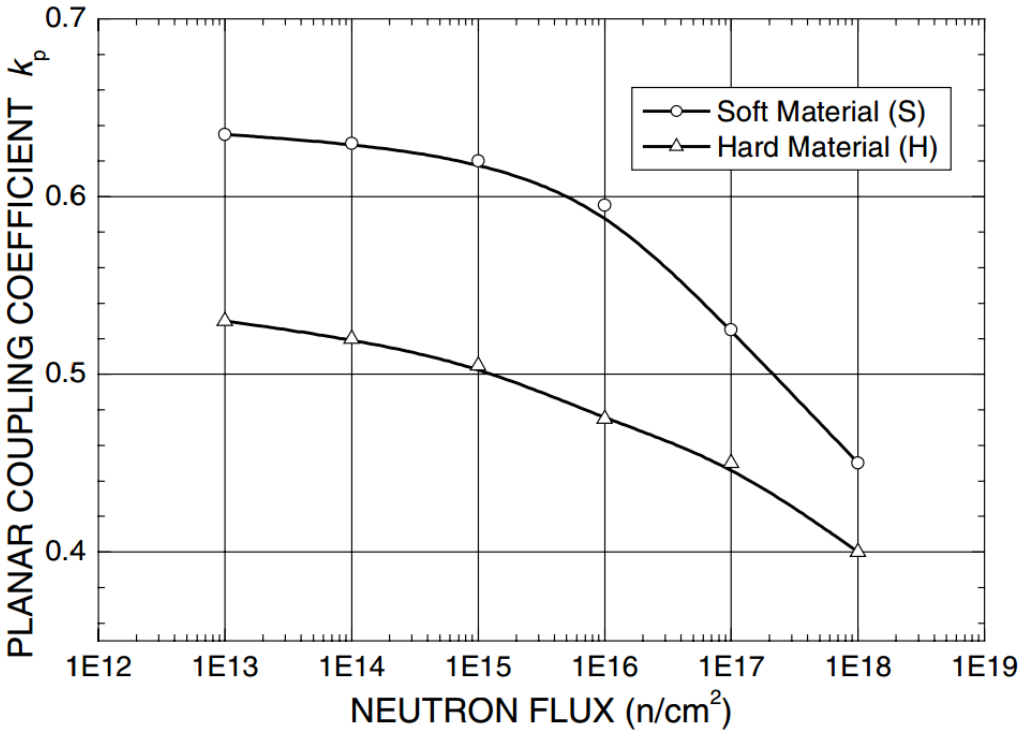

Figure 2.7: Electromechanical coupling coefficient k_p as a function of the integrated neutron fluence for acceptor doped (hard) and donor doped (soft) PZT disks.[35]

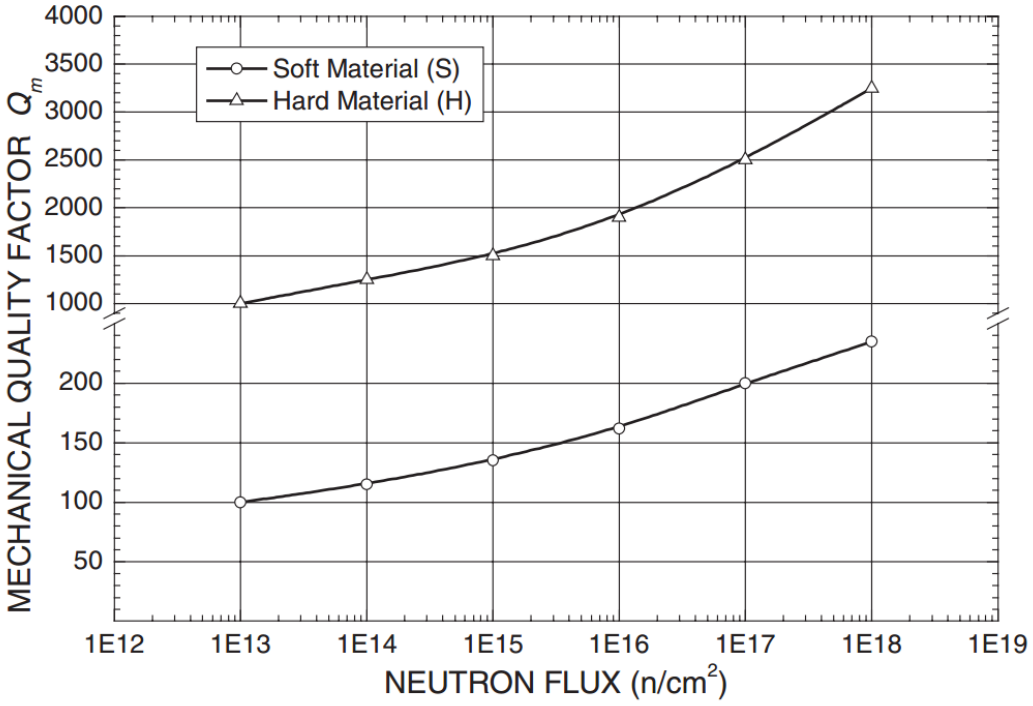

Figure 2.8: Mechanical quality factor Q_M as a function of the integrated neutron fluence.[35]

for a given electric field strength. In the context of charge storage within a capacitor, more charge can be stored using a dielectric with large ϵ_r than with a small one. In a linear dielectric, the relative permittivity is a constant value. Thus the name dielectric constant is sometimes used in this case. It is important to keep in mind, however, that in ferroelectrics such as PZT, the relationship between applied fields and polarization is non-linear. Therefore, the relative permittivity shows correspondingly non-linear behavior and its value is reported with respect to a particular applied field (typically zero or low-field). We may express the relative permittivity as

$$\epsilon(E)_r = \epsilon'_r(E) - i\epsilon''_r(E) \tag{2.1}$$

where ϵ'_r is the real component of the relative permittivity and ϵ''_r is the imaginary component.

The loss tangent is related to the relative permittivity. It is a measure of power dissipation in a dielectric from power supplied by a time varying electric field. In a capacitor it accounts for stored charge loss mechanisms. The relative permittivity and loss tangents are somewhat analogous to the electromechanical coupling coefficient and mechanical quality factors mentioned in the previous section. Together they describe the efficiency of the material to convert electrical potential energy (via and applied field) into a polarization response (or stored charge). For an applied AC field the loss tangent takes the form

$$\tan\delta = \frac{\omega\epsilon_r'' + \sigma/\epsilon_0}{\omega\epsilon_r'} \tag{2.2}$$

where ω is the AC field frequency, σ is the conductivity of the dielectric, and ϵ_0 is the permittivity of free space. Note that the field dependence has been suppressed in equation 2.2 but it is implicitly present, hence, the loss tangent is also field and frequency dependent.

In the same paper in which Miclea *et al.* reported their observations on electromechanical properties upon neutron irradiation, the authors found that the dielectric properties, too, change.[35] As figure 2.9 shows, the relative permittivity in both acceptor and donor doped bulk PZT disks decrease significantly. At 10^{18} cm^{-2}, the drop corresponds to about a 75% loss in ϵ_r. The loss tangents too, were observed to decrease (up to about half at 10^{18} cm^{-2}) as seen in figure 2.10. Together these results tell us that, somehow, radiation induced defects diminish the polarizability of the PZT while also suppressing loss mechanisms. Toacsan *et al.* also reported similar results in their dielectric measurements.[36] They observed larger changes in the loss tangents however. This may reflect any number of differences in their sample compositions, processing conditions, etc.

The authors in the Miclea *et al.* study claim that the decrease in permittivity, loss tangent, and increase in mechanical quality factor indicate oxygen vacancies are the main type of defect produced by neutron irradiation. This assertion is based on the well-known behavior of PZT ceramics doped with

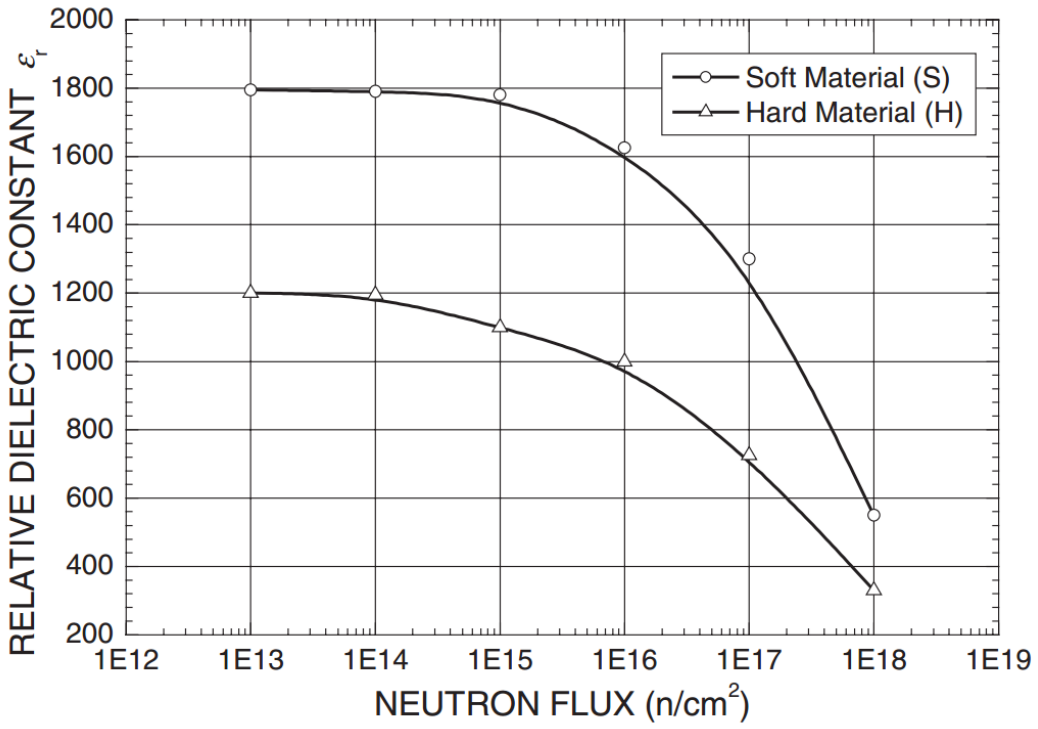

Figure 2.9: Relative permittivity as a function of neutron fluence for acceptor doped (hard) and donor doped (soft) bulk PZT disks.[35]

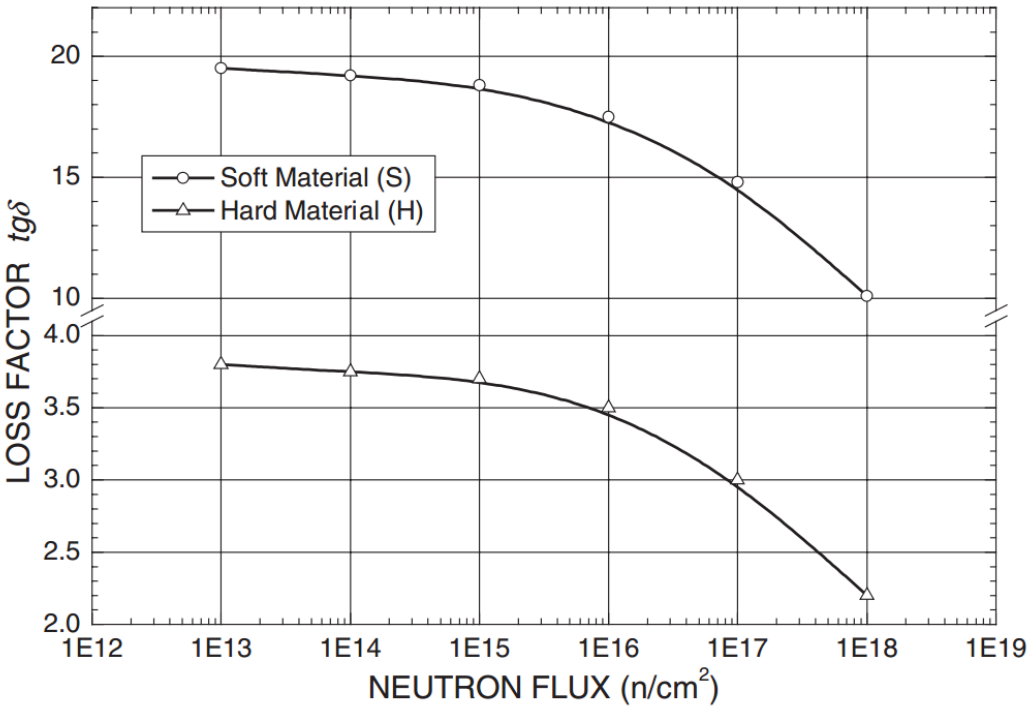

Figure 2.10: Loss tangent as a function of neutron fluence for hard and soft PZT disks.[35]

low concentrations of acceptor dopants. Adding impurities with valencies lower than those of the A or B site cations effectively increases the concentration of oxygen vacancies to maintain charge balance.[39] Thus the authors' reasoning is as follows: the observed changes are similar to those seen in PZTs with acceptor impurities, therefore oxygen vacancies are the dominant type of defect in neutron irradiated PZT. They did not, however, attempt to rule out other defects such as Pb, Zr and Ti point defects or defect clusters nor did they attempt to explain the role of O interstitials, which must necessarily exist if O vacancies are introduced from knock-on sources. Furthermore they noted that their results indicated changes over two orders of magnitude greater than those predicted from a model put forth by Kulikov *et al.* that only considers the effects of oxygen vacancies.[37] There still seems to be quite a lot of unknown details regarding the role that various types of point defects and defect clusters play in the dielectric properties.

2.4.1.3 Microstructure

The Curie temperature of PZT ranges between about 300-500°C depending on the Zr/Ti molar ratio. At the Curie temperature, upon cooling, it undergoes a first-order phase transition from a cubic to tetragonal or rhombohedral phase. The cubic, paraelectric phase occurs for all compositions above the Curie temperature while there is a morphotropic phase boundary between the tetragonal and rhobohedral ferroelectric phases at $Pb_{0.98}Zr_{0.52}Ti_{0.48}O_3$ with only slight temperature dependence. The lattice constants, too depend on the

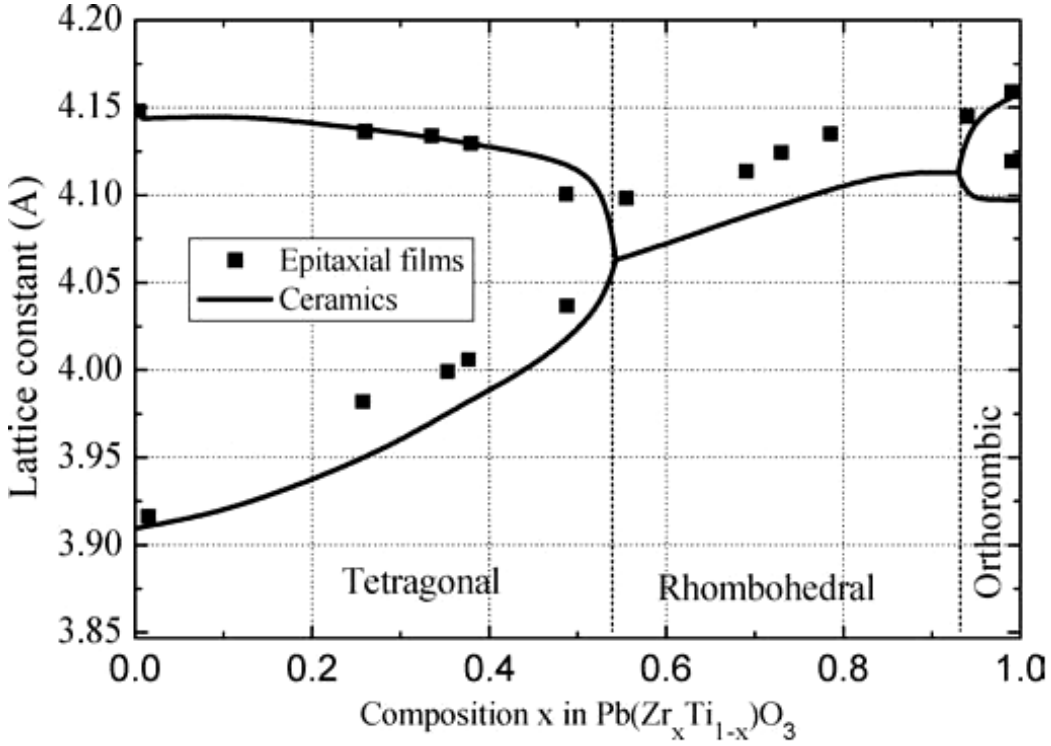

Figure 2.11: Lattice constants of bulk and epitaxial PZT as a function of composition.[23]

molar ratio as figure 2.11 shows. This figure also indicates the lattice constants for an epitaxial thin film where the lattice and thermal mismatch occur between substrate and perovskite layers resulting in strain in the unit cell in one or more directions.

Upon neutron irradiation up to 10^{16} cm^{-2} fluence little change is observed in the lattice constants of tetragonal PZT, according to XRD studies.[35,36] At higher fluences however, an increase in lattice constant a is observed while lattice constant c is more or less unaltered. Figure 2.12 shows

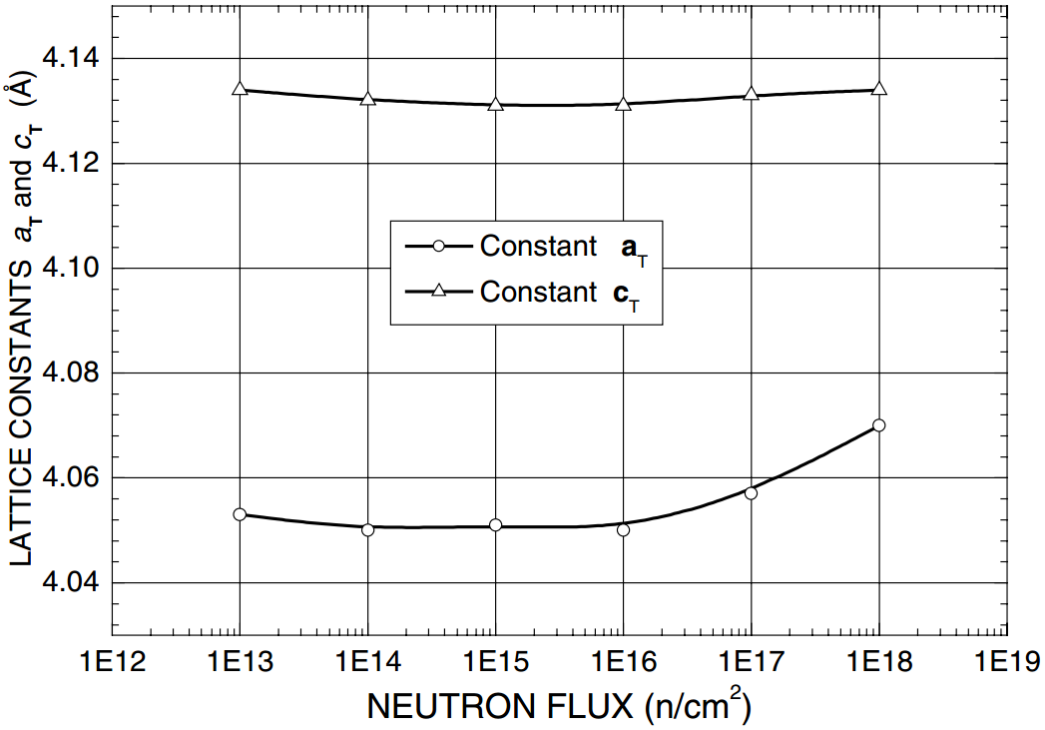

Figure 2.12: Lattice constants, a and c for bulk tetragonal PZT as a function of neutron fluence.[35]

this behavior as a function of neutron fluence.

The calculated tetragonal ratio, c/a, deceases continuously as seen in figure 2.13. Toacsan *et al.* argued that is evidence of a tetragonal to cubic phase transition. They also attributed the increase in the average unit cell volume to the presence of interstitials. This phenomenon has long been known in radiation effects as the result of a relaxation volume differential between vacancies and interstitials. If their claims are correct the combined increase in volume and essentially unchanged c lattice constant would indicate that inter-

stitials preferentially occupy positions within the basal planes of the unit cell. The observed increase in unit cell volume also offers some evidence against the arguments of Miclea *et al.* and Kulikov *et al.* that oxygen vacancies are the predominant defect specie. Although similar trends in dielectric and electromechanical properties are seen in both irradiated and acceptor doped PZT, the addition of acceptor dopants is known to result in a decrease in unit cell size.[39,40] In other words, if oxygen vacancies were the only radiation induced defect, the unit cells should shrink. Since they don't some other defects must be compensating; for example interstitials as Toacsan *et al.* suggest. The differential in relaxation volumes between interstitials and vacancies is a known cause of volume expansion in irradiated crystals.

There are two types of oxygen vacancies. They occur along the linear O-(Ti/Zr)-O chains that extend in the c and a directions. Vacancies on the c-axis O-(Ti/Zr)-O chains occupy the unit cell base centers while those on the two a-axes occupy the other face centers (sides). In figure 2.14 the particular oxygen sites are named O(1) and O(2) for the c- and a-axis chains, respectively.

Based on local density approximation density functional theory (LDADFT) methods, Park and Chadi calculated that the $V_{O(1)}$ vacancies result in a tail-to-tail dipole configuration in which the dipole moment of the unit cell above the vacancy is opposite that of the dipole below the vacancy.[41] There is a net cancelation of both dipole moments and a corresponding decrease in the macroscopic polarizability. The $V_{O(2)}$ vacancies on the other hand have two configurations; a tail-to-tail configuration and a switchable configurations that

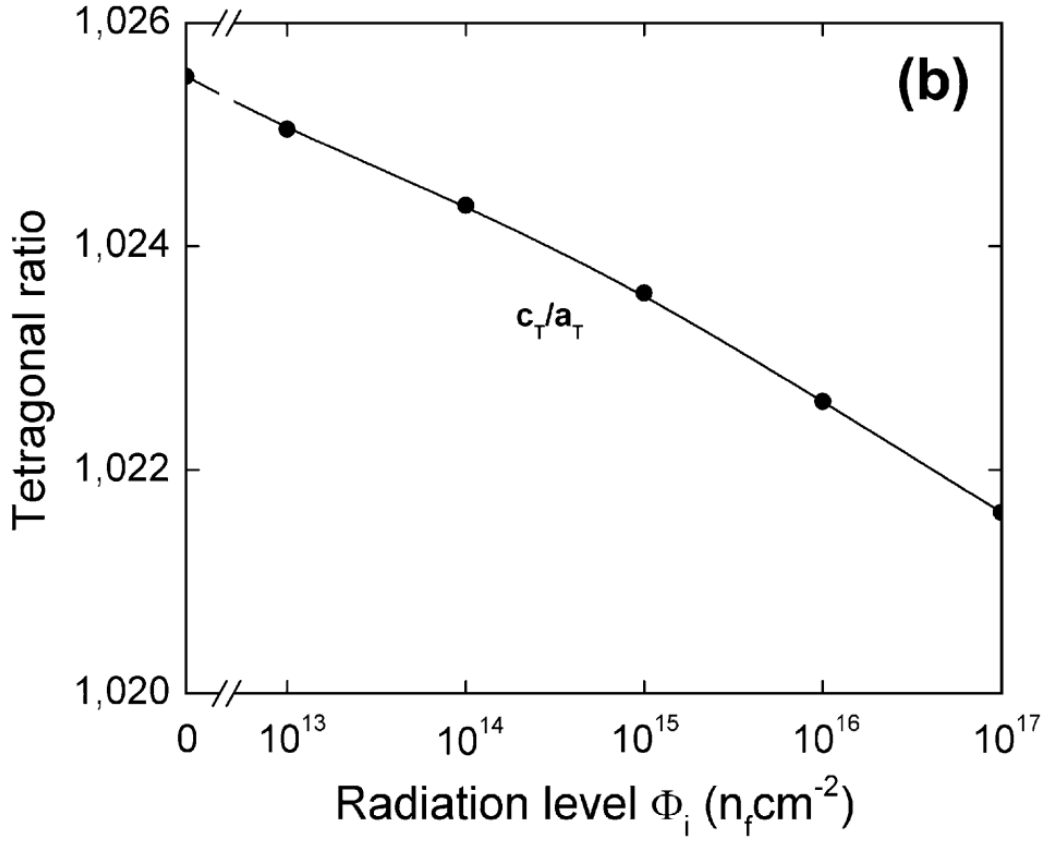

Figure 2.13: Tetragonal ratio, c/a, for bulk PZT as a function of neutron fluence.[36]

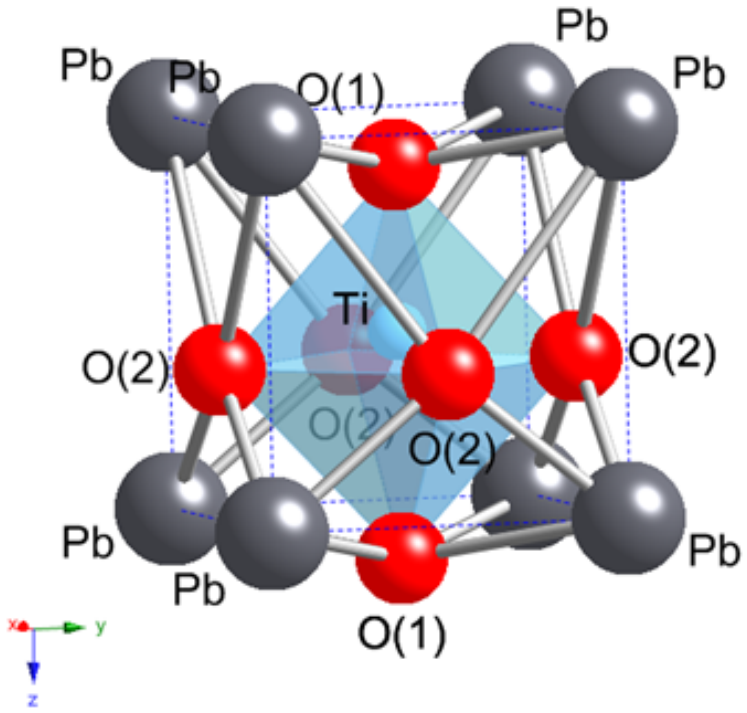

Figure 2.14: PZT unit cell with O(1) oxygen sites along the c-axis, and O(2) oxygen sites along the a-axes.

do not affect the bulk polarization. The authors also determined that the $V_{O(1)}$ vacancy is energetically more stable than the $V_{O(2)}$ vacancy because of increased tetragonal lattice strain energy at the O(2) sites. They were not able to definitely determine which polarization configuration (switchable or tail-to-tail) was more stable for the $V_{O(2)}$ vacancy but they suspected the reversible dipole would be favored.

The tail-to-tail configuration can nucleate an antiphase polarization as well as 180° domain walls. This stems from the fact that one of the tails will always be anti-aligned with the direction of the polarization projected onto the c-axis. The polarization around a switchable $V_{O(2)}$ vacancy along with the bulk polarization can be switched via an external electric field. It is therefore expected to have a smaller effect on bulk polarization than the $V_{O(1)}$ vacancy. According to Park and Chadi, however, the $V_{O(1)}$ is more stable so there is a natural driving force towards the tail-to-tail configuration. This implies that under the constraint of a constant vacancy concentration, the initially mixed switchable and tail-to-tail dipole nature will tend towards solely tail-to-tail (assuming the reversible dipole is the more stable $V_{O(2)}$) with repeated cycling or annealing.

Kulikov and Trushin estimated the relative O vacancy concentration to be on the order of 10^{-3} at a neutron fluence of 10^{18} cm^{-2}; 0.1% of the atomic number density.[42] Since the vacancies are created through knock-on reactions there is no preference as to the type of O vacancies produced. Thus they assumed a 1:2 ratio of O(1) to O(2) vacancies (there are two O(2) sites for

every O(1) site). The authors, working under the assumptions that the O(1) tail-to-tail vacancies produce the majority of the dielectric property change, reasoned that the change in dielectric properties should be of the same order of magnitude, namely 0.1%, as the concentration of oxygen vacancies. Again, based on the data of Miclea *et al.* and Toacsan *et al.*, changes of around 30-75% have been observed at such fluences; far greater than the expected 0.1%. It should be mentioned, however, that even small fractions of a percent difference in dopant concentration can bring about large changes in dielectric properties. One might question the validity of assuming that the change in dielectric constant, for example, scales linearly with the oxygen vacancy concentration. Never the less, taking the authors' conclusions at face value, this discrepancy brings into question the physical completeness of the Kulikov and Trushin model or the underlying assumption that O vacancies are the only defect of major importance.

Other factors that may account for the measured behavior could include domain wall pinning from larger or more polar defect clusters, local lattice deformation and its deleterious effects on long range polarizability, and an assortment of charged defects. Thus there is a need to examine these on equal footing and not assume that any particular defect is responsible for property changes.

2.4.1.4 Domain Morphology

When PZT is cooled below the Curie temperature, it usually deforms by lengthening in the direction of the polarization. In this lengthening process intergranular stresses are mitigated through the formation of multiple domains. As mentioned before, domains are continuous regions with a common dipole orientation. A number of different spontaneous polarization directions exist and they are determined by the symmetry of the crystal. In the cubic to tetragonal phase transition, polarization occurs along the $\langle 100 \rangle$ directions, with the direction of the polarization determining the long axis (c-axis). In the cubic to rhombohedral transition, the polarization occurs along the $\langle 111 \rangle$ directions. In this case, the direction of the polarization determines the long body diagonal. Thus tetrahedral PZT exhibits a total of 6 polarizations and both 180° and 90° domain walls, while rhombohedral PZT exhibits 8 polarizations with 180°, 109° and 71° domain walls. Figure 2.15 indicates the spontaneous polarization directions (red arrows) for rhombohedral (a) and tetragonal (b) PZT. The transition regions between adjacent domains form coherent interfaces called domain walls.

Toacsan *et al.* used scanning electron microscopy (SEM) to analyze the domain structure of their irradiated PZT.[36] The authors claim that the SEM images (figure 2.16) revealed depolarized and deformed grains as well as reduced domain sizes and randomly oriented domains. Since the unirradiated sample was left unpoled, it represents a random domain structure. The change in average domain size and correlation length is an indication that neutron

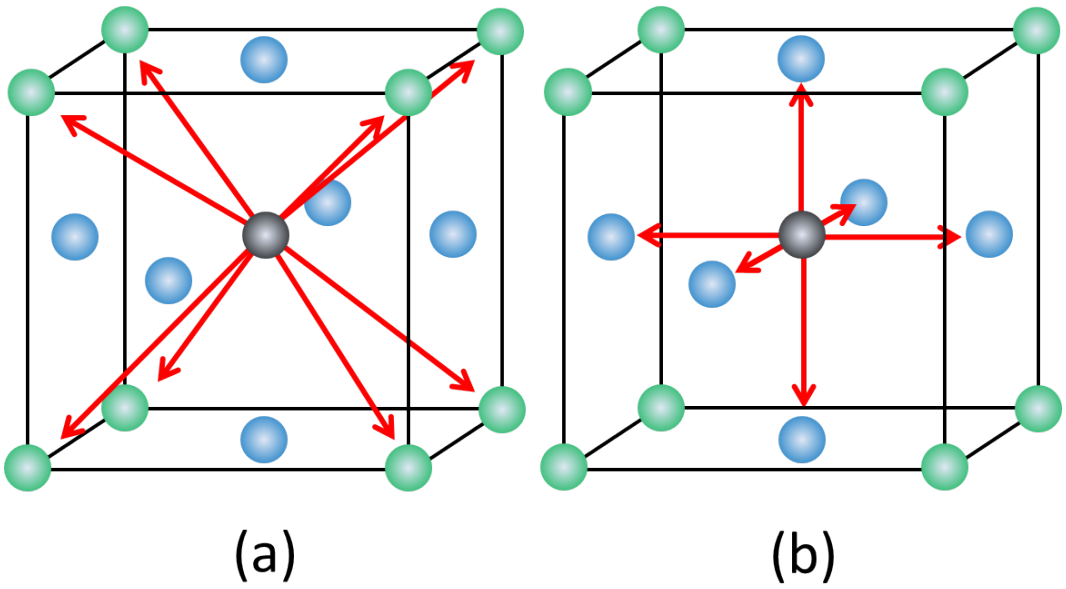

Figure 2.15: Spontaneous polarizations in the rhombohedral (a) and tetragonal (b) PZT unit cell. The red arrows indicate the directions of polarizations.

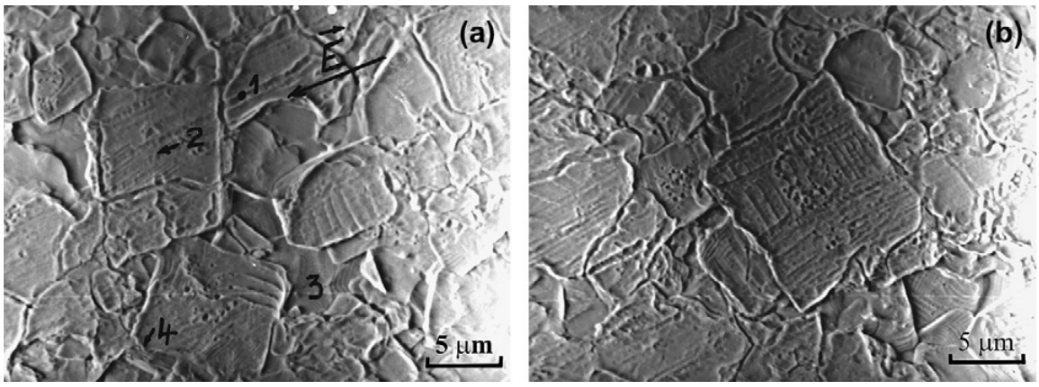

Figure 2.16: Etched, unpoled, bulk PZT before irradiation (a) and upon exposure to a neutron fluence of 10^{18} cm^{-2} (b).[36]

induced defects restructure the domains to increase the domain wall density.

According to the authors, the decrease in domain alignment was dominated by 90° domain wall motion rather than 180° domain reversal. 90° domain walls are less mobile. It follows that during poling, the growth of domains oriented parallel to the external electric field are impeded by the presence of perpendicularly oriented domains, reluctant to shrink via 90° domain wall motion. It is important to note however, that depolarization also involves dynamic processes not observable in these SEM images. These processes include inhibition of domain nucleation sites and domain wall pinning. Inhibition of domain nucleation sites seems unlikely for irradiated PZT as nucleation occurs at defects, which will be present in greater numbers in the irradiated material. Furthermore, the increased domain density observed in the Toacsan *et al.* study seems to indicate domain nucleation might be enhanced. Domain wall pinning, however, is certainly expected to be an important process since

it typically occurs at structural and charged defects within a ferroelectric and domain wall motion contributes substantially to the piezoelectric and ferroelectric properties of the material.

2.4.1.5 Polarization and Fatigue

The previous discussion pertained to neutron irradiated bulk PZT specimens. A paper from Moore *et al.* was the first to look at neutron effects in PZT thin film capacitors; the first paper which had direct applicability to FRAM for space and neutron environments.[34] They examined changes in polarization using hysteresis loops and a pulsing technique. Their samples comprised three thin films between 240-400 nm thick, of different composition, and from different manufactures. Each was exposed in decade increments to neutron fluences from 10^{13} cm^{-2} to 10^{15} cm^{-2}. The measurements showed that the remanent polarization was more or less stable up to the maximum fluence apart from one sample which exhibited about 18% loss (see figure 2.17).

Related to the remanent polarization, which pertains to continuous AC field cycling, is the retained polarization (or retained charge). This is the polarization remaining from the application of a short voltage pulse. This is an important device parameter for FRAM applications as it most directly correlates to the fidelity of the bit writing and reading process. The authors observed a 40% loss in the retained polarization after a 1 s delay following a 0.2 V, 10 ms square pulse write at only 10^{13} cm^{-2} fluence. This is shown in figure 2.18. For two of the samples, however, beyond 10^{13} cm^{-2} the re-

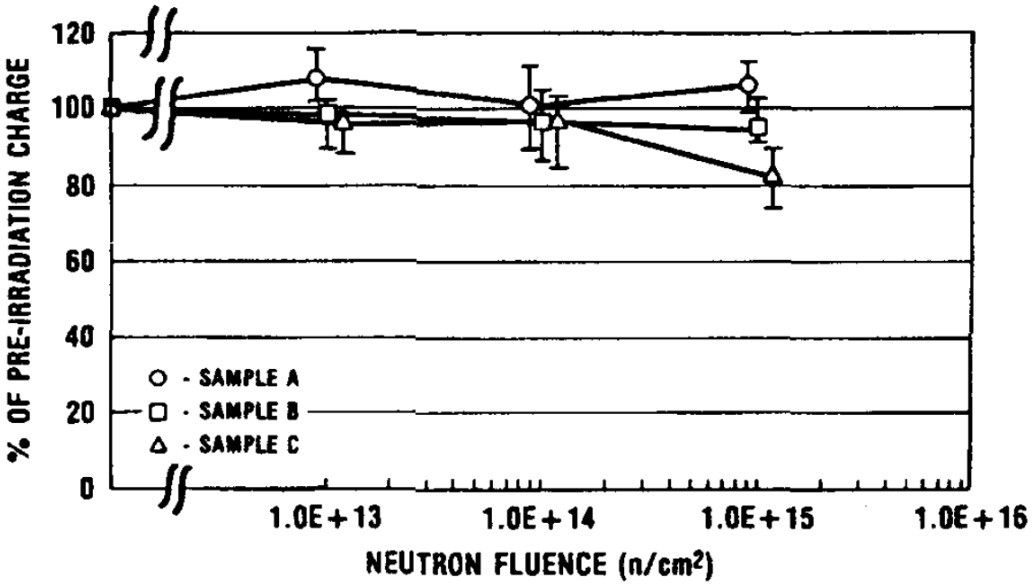

Figure 2.17: The switchable capacitor charge (proportional to remanent polarization) as a function of neutron fluence from the thin film capacitors studied by Moore *et al.*[34]

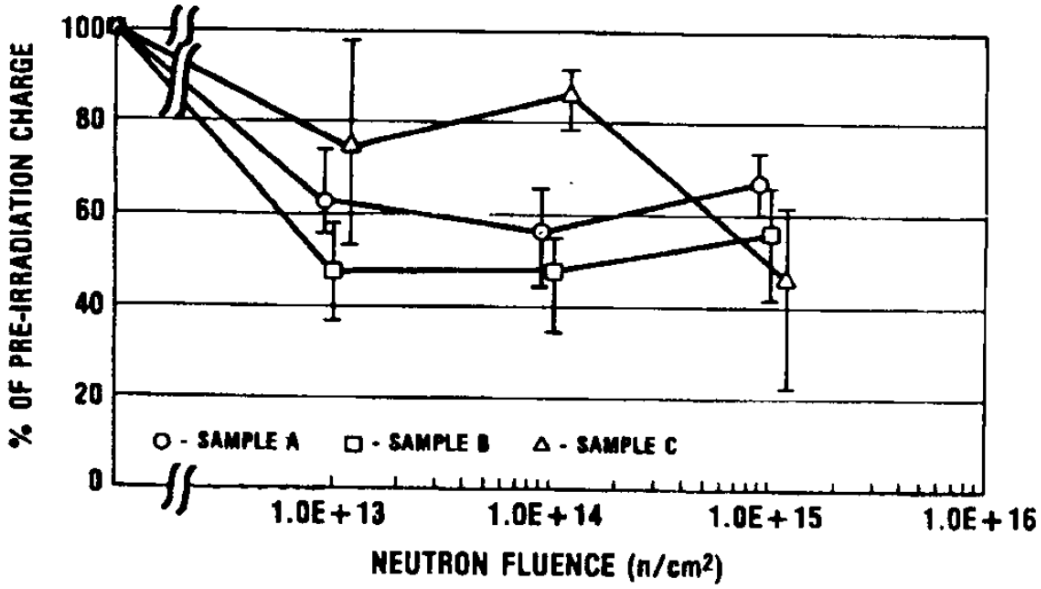

Figure 2.18: The normalized retained charge on a thin film capacitor as a function of neutron fluence. The retained charge is measured after 1 s delay following a 0.2 V, 10 ms square pulse.[34]

tained polarization did not decrease further. The authors remarked that the precipitous decrease in retained polarization and it subsequent saturation was unexpected and they offered three possible, but empirically unproven, explanations: 1) Defect clusters act as domain wall pinning sites 2) Defect clusters nucleate reverse domains and 3) neutron induced space charges polarize during the pulse and then relax during the decay removing a part of the space charge component of the retained polarization. They partially discounted the last mechanism because the concentration of space charge should increase proportionally with neutron fluence and not exhibit saturation behavior, as the measurements indicate.

The following explanation shows how cluster mechanisms could be consistent with the saturation behavior. If the clusters are amongst the strongest pinning sites in the grain, the decay in retained polarization will be largely determined by the relaxation of domain walls in the reverse direction after they have been pinned at the clusters during poling. The domain wall travel, however, is progressively limited by an increasing density of strong pinning sites nearby. Thus the amount of relaxation is reduced, compensating for the increased pinning. In a sense, such pinning sites make the domain structure more rigid.

The nucleation mechanism is also compatible with saturation behavior because, although the density of nucleation sites would be expected to increase proportionally with fluence, the equilibrium size of the reverse domains would be restricted by strong pinning. Assuming, clusters are produced isotropically in the material, the mean distance between clusters goes as $\frac{1}{N^{1/3}}$ where N is the cluster density. Assuming the volumes of reverse polarization regions that form during relaxation are found around nucleation sites but bounded by nearest neighbor pinning sites, the loss in retained polarization from reverse domains should go both as the density of nucleation sites and as the inverse density of pinning sites. Presumably the ratio of nucleation clusters and pinning clusters is independent of fluence since both represent possible outcomes of a single damage cascade. Therefore, the saturation occurs because increased nucleation of reverse domains is compensated by smaller reverse domains.

Evidence that the damage in the Moore *et al.* studies is primarily

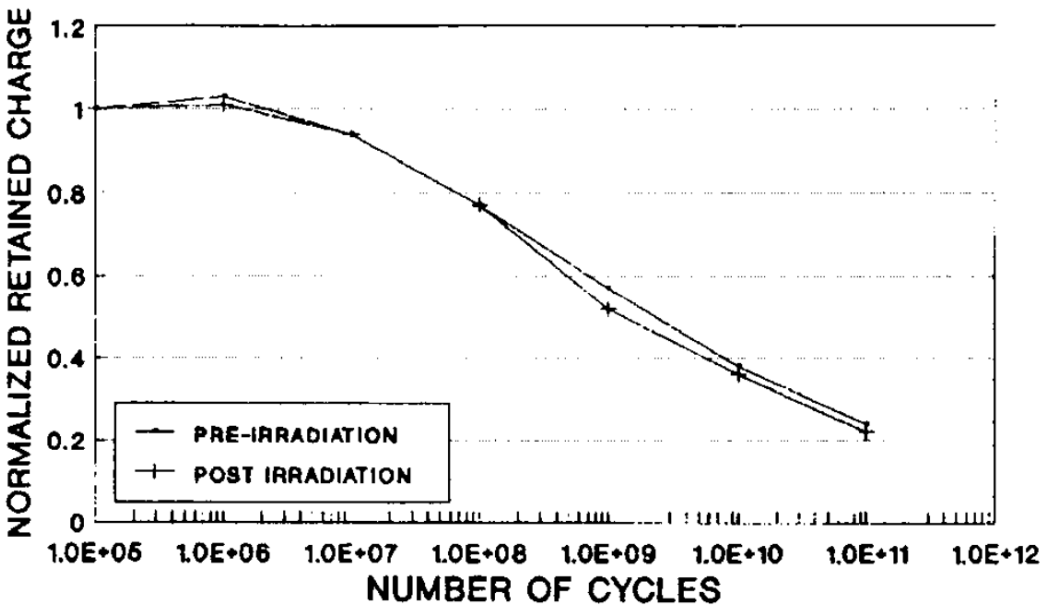

Figure 2.19: The normalized retained charge for unirradiated and irradiated capacitors with repeated cycling.[34]

structural and not due to ionization effects comes from cycling studies. As figure 2.19 shows, repeated cycling does not affect the amount of retained charge loss relative to a cycled unirradiated film. Relative improvement in the irradiated film would provide evidence for annealing of ionization damage, which, from gamma irradiation studies, is found to occur (as will be discussed in the next section). However, since the fatigue in the neutron irradiated specimens closely parallels that of the unirradiated samples, the deleterious defects are presumed to be mainly of the structural variety.

2.4.2 Gamma Ray Irradiation Effects

Several studies have investigated the total dose effects of gamma rays on PZT. In contrast to neutron damage where displacements have a large if not dominating effect of material properties, gamma irradiations bring about change primarily through ionizations and isolated Frenkel pairs. A large amount of electron-hole pairs are generated by the ionizing radiation. These mobile charges are separated by electric fields within the material. The average displacement field and local electric fields associated with the bulk of particular domains are too weak to separate charges significantly. There are, however, strong localized fields occurring near structural discontinuities such as the ferroelectric-electrode interfaces and grain boundaries. These strong fields separate charges to create space charge.

The amount of space charge accumulated should increase with the total dose (hence total number of ionizations) and the rate of accumulation is expected to depend on the total grain boundary area. Assuming, grain boundaries are responsible for trapping charge, the more grain boundaries, the more trapping. The trapped charges at grain boundaries form dipole-like local electric fields. Thus they contribute to the depolarization field which, among other things, distorts the hysteresis curve.

Figure 2.20 illustrates the cross section of a PZT thin film capacitor used in total dose irradiation experiments. Films have been prepared in different ways including pulsed laser deposition (PLD) and the sol-gel method. Authors have measured hysteresis loops and capacitance-voltage curves (C-

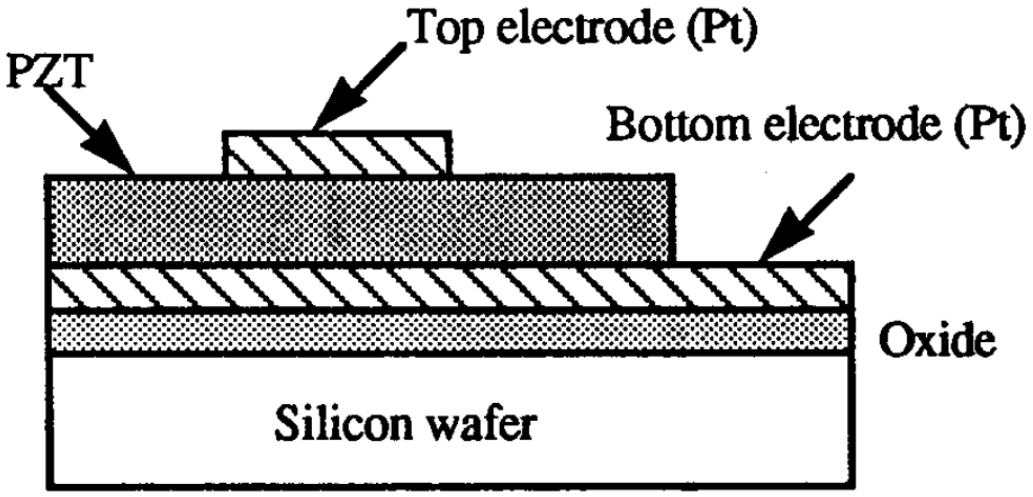

Figure 2.20: Cross section of a typical PZT/Pt/Si type capacitor.[17]

V curves) to investigate ionization effects on both pre-irradiation poled and unpoled capacitors.

In a study by Lee *et al.* the capacitors were irradiated with a ^{60}Co source up to a total dose of 0.85 Mrad.[17] The hysteresis curve upon irradiation, narrows and shifts downward, indicating a loss of remanent polarization and the presence of an internal bias field (see figure 2.21). The bias field increases the effective field necessary to switch the capacitor in one direction while reducing the effective field in the other. The authors noted that their sol-gel synthesis techniques result in films with a slight positive internal bias. Thus the irradiation induced internal bias appears in the same direction as the processing induced bias.

Lee *et al.* also discovered that by applying a negative square pulse

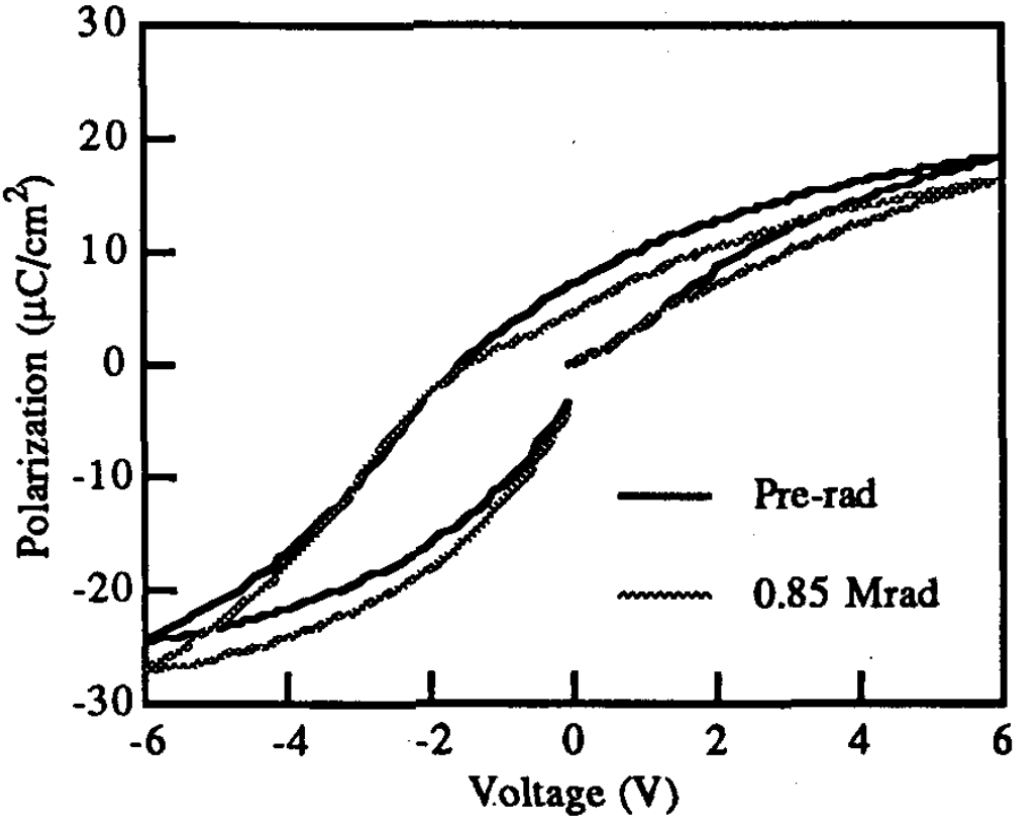

Figure 2.21: Hysteresis loops for pre-irradiated and post-gamma irradiated PZT capacitors.[17]

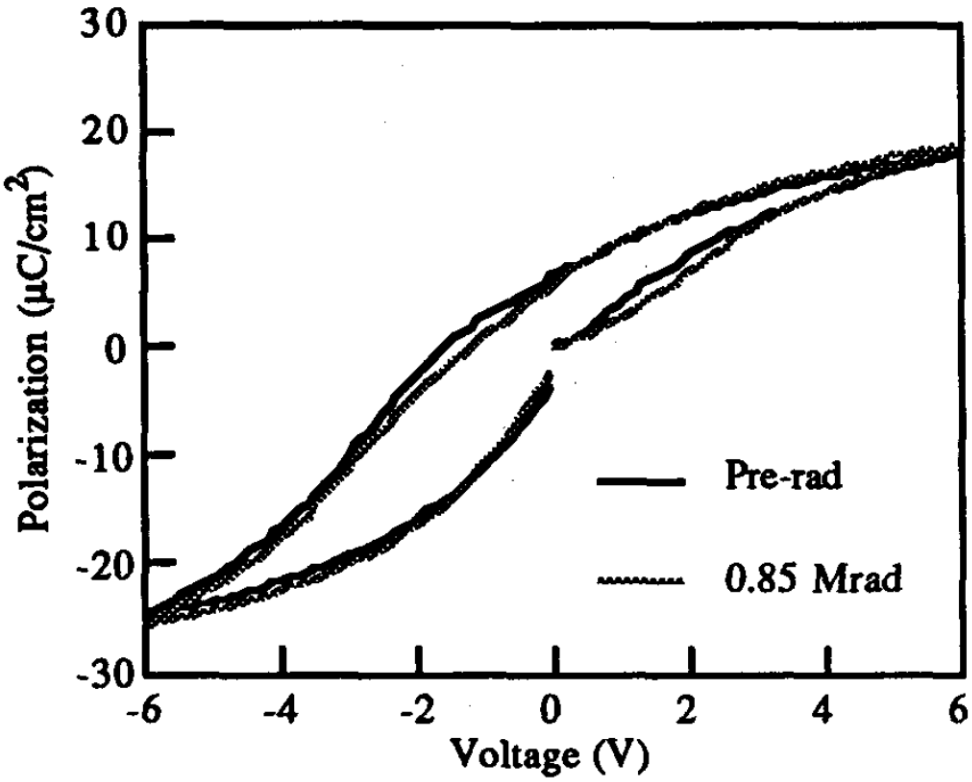

Figure 2.22: Hysteresis loop post-gamma irradiated PZT capacitor after -6 V poling for 2 ms.[17]

between irradiations restores some of the pre-irradiation shape to the curve. As figure 2.22 shows, poling the irradiated capacitor for a short time (2 ms at -6 V) between irradiations yields a hysteresis curve very similar to that of the pre-irradiated curve. This indicates that the poling counteracts some of the buildup of internal bias field. Applying a strong poling condition for 10 s, however, was found to reverse the direction of the internal bias. Subsequent irradiation then strengthened this bias field and increased the remanent polarization.

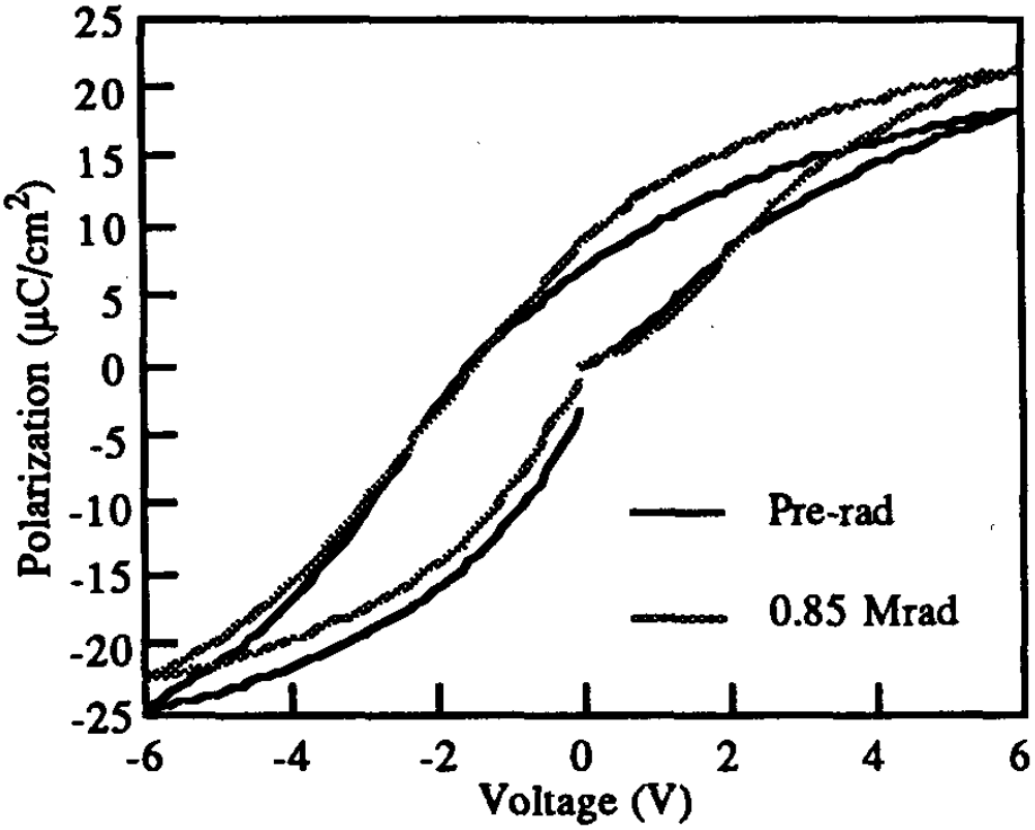

Figure 2.23: Hysteresis loop post-gamma irradiated PZT capacitor after -6 V poling for 10 s.[17]

Based on their poling studies, the Lee *et al.* authors suggest that irradiation causes a reinforcement of the internal bias. They attribute this to the formation of a sheet charge layer near the electrode interface. During irradiation, the charge carriers experience a net drift force from the internal bias field. They migrate towards the electrode interface where they become trapped, contributing to the buildup of the sheet charge. Negatively poling the capacitor for short times counteracts sheet charge buildup resulting in less accumulated bias. Poling for long times, however, results in charge drift towards the opposite electrode interface where a new sheet charge begins to form. Subsequent irradiation then contributes to the negatively biased sheet charge.

An earlier study by Benedetto *et al.* using sol-gel derived capacitors irradiated with 10 keV x-rays revealed similar distortions to those observed in the Lee *et al.* study.[43] With increased dose up to 100 Mrad, asymmetries developed in the hysteresis curves showing a buildup of internal bias and a reduction in the remanent polarization. Instead of invoking sheet charge accumulation at the electrode interfaces as the dominant effect, the authors interpreted these results as evidence of charge trapping at the grain boundaries. In a side note, they mentioned that upon irradiating a single-grain thickness sample under identical conditions to those of the sol-gel samples, no distortions in the hysteresis curve were observed. This can be taken as compelling evidence that charge trapping at grain boundaries is the dominant mechanism for distortion.

Both Lee *et al.* and Benedetto *et al.* performed post-irradiation cycling on their samples. Both groups observed reversal of the irradiation effects. The loops became more symmetric and lost some of their internal bias, reflecting more the pre-irradiation conditions. Thus in addition to short negative poling, post-irradiation cycling too appears to reverse some of the damage. This healing effect tends to improve with the number of cycles except at high cycle number where the hysteresis curves began to reflect ordinary fatigue. Unlike neutron irradiation, gamma irradiation does not appear to accelerate fatigue or degrade the retention properties. Interestingly, with increasing number of cycles the Lee *et al.* authors observed a decrease in remanent polarization while the Benedetto *et al.* authors observed an increase. It is not clear why the cycling results should differ and if it is a consequence of damage reversal or ordinary fatigue for the particular samples used in each study. It is worth mentioning, however, that increased leakage is often misinterpreted as increased remanent polarization. Such results might, therefore, indicate that the Benedetto films were more to susceptible to increased leakage upon irradiation.

Gao *et al.* irradiated capacitors prepared by the PLD method to doses as high as 20 Mrad.[44] They observed similar behavior in the internal bias field to that seen in the Lee *et al.* and Benedetto *et al.* studies (see figure 2.24). Like Benedetto *et al.*, they attributed their findings more to charge trapping at the grain boundaries, which, they noted, are highly dense in thin films. Unlike Lee *et al.* and Benedetto *et al.*, they found the remanent polarization

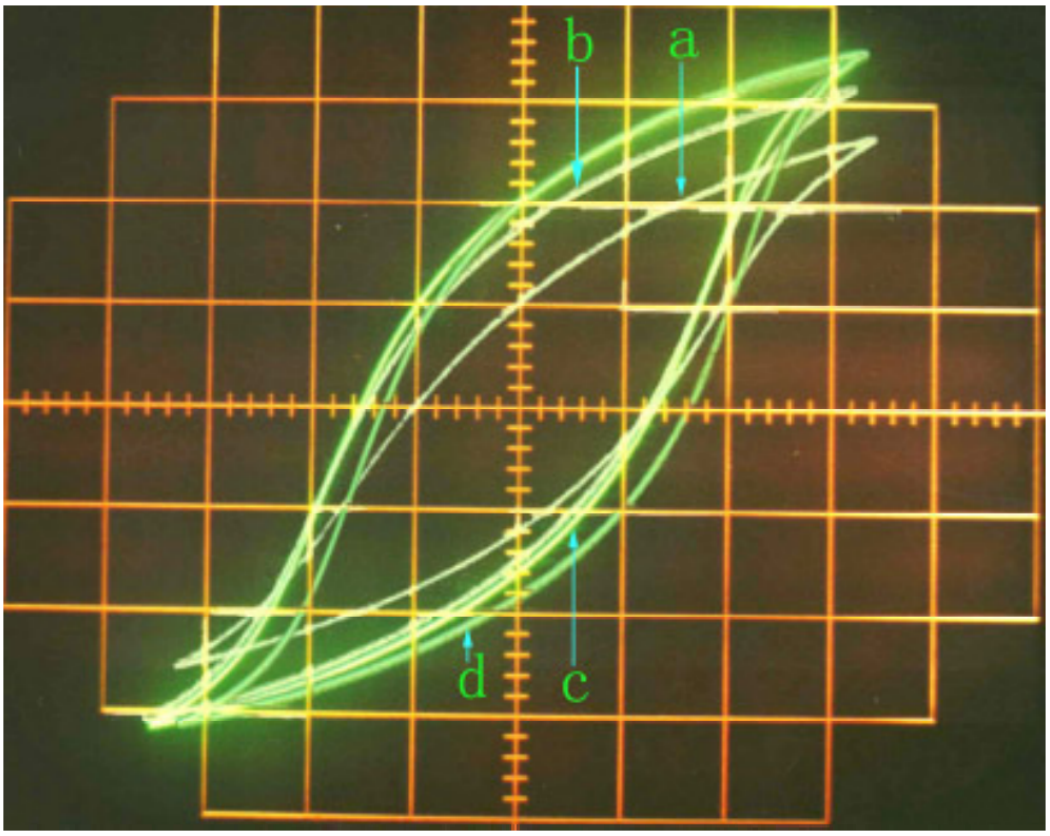

Figure 2.24: Hysteresis loops for PZT capacitors (a) before irradiation (b) 0.1 Mrad (c) 5 Mrad and (d) 20Mrad.[44]

to increase with dose. They interpreted this as a sign that the buildup of space charge around the grain boundaries magnifies the depolarization field. They also noted that the increase in remanent polarization seemed to contradict a measured drop in the permittivity with dose. Increased leakage with no increase in the underlying remanent polarization, however, would not be in contradiction with the observed permittivity behavior.

2.4.2.1 I-V Measurements

Lee *et al.* also took current-voltage (I-V) measurements post-irradiation and upon post-irradiation cycling. As figure 2.25 shows, the low-field, switching current dominated response is altered while the high-field, leakage current dominated response actually decreases. After 2.6×10^7 cycles, the authors measured very little change in the I-V curve below 5 V. Above 5 V the leakage current increased by over an order of magnitude. They attributed this to space charge buildup.

Baturin *et al.* examined switching current in greater detail for x-ray irradiated thin films.[45] They found that peaks form in the switching current I-V profile after irradiation (see figure 2.26). These were interpreted as signatures of frozen domains oriented opposite to the direction of imprint. In other words, the irradiation induced charge trapping had the effect of reinforcing the domain structure.

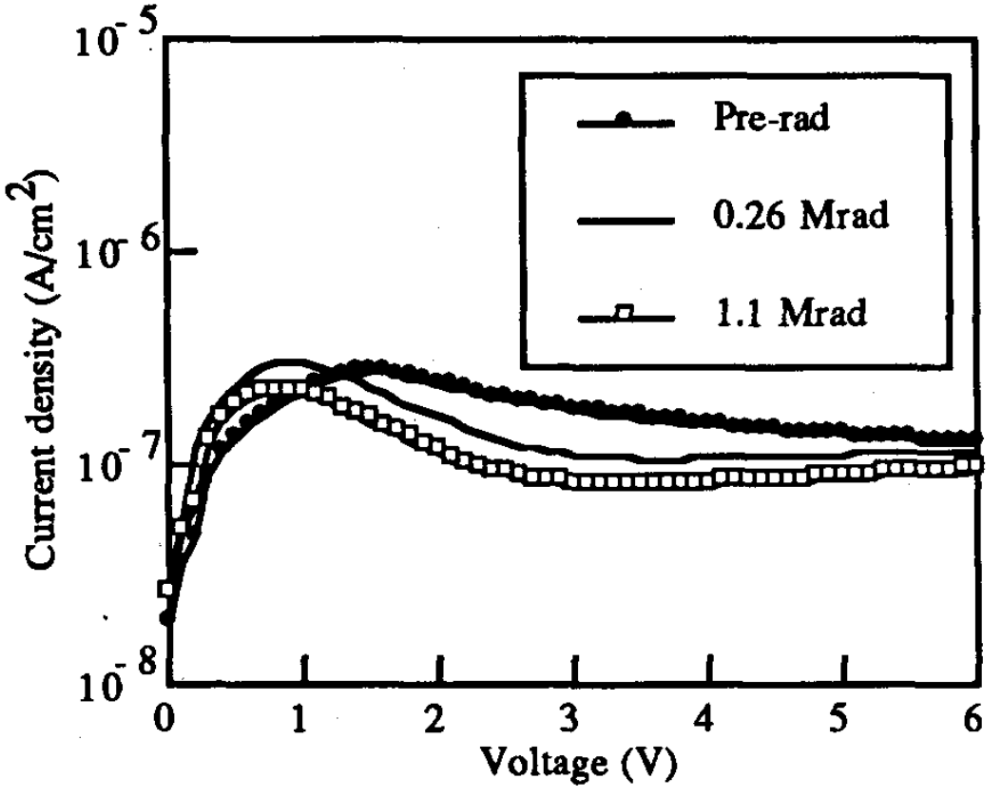

Figure 2.25: Current-voltage (I-V) curve for irradiated PZT capacitors prior to cycling.[17]

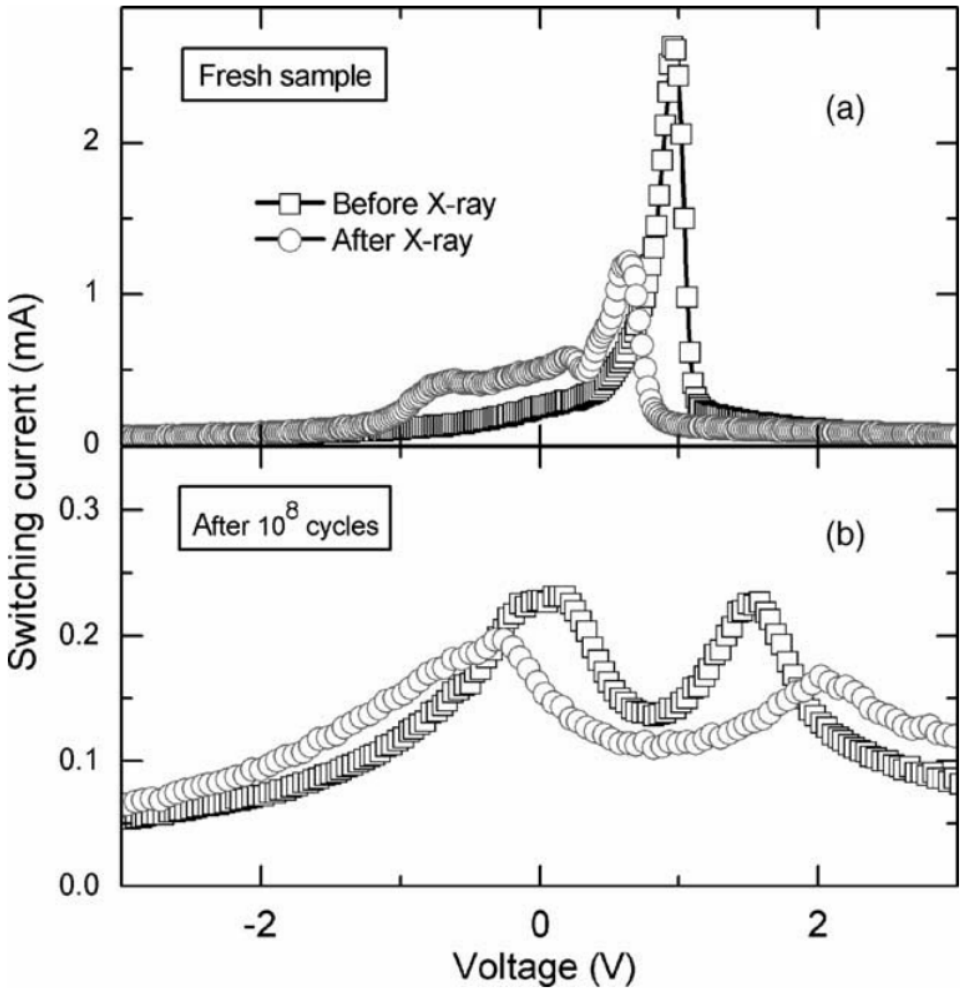

Figure 2.26: Switching current in x-ray irradiated (a) un-fatigued films and (b) extensively fatigued films.[45]

Chapter 3

Sample Preparation

3.1 Film Synthesis

The samples used in the irradiation experiments were prepared as thin film capacitors at Sandia National Laboratories. The basic structure of the PZT capacitors is shown in figure 2.20. The substrates used to prepare the samples were commercially prepared 75 mm diameter platinized silicon wafers from Silicon Quest International. From the top surface to the bottom of the substrate, the layers are 170 nm Pt, 40 nm Ti, 400 nm SiO_2, and 300 μm Si. The Pt acts as the bottom electrode for the PZT deposited over it. The Ti is included as an adhesion layer and to help buffer strain between the Pt and SiO_2 layers. Without the Ti, the Pt tends to adhere less well. The 300 μm Si acts as a support for the thin and fragile ferroelectric and electrode layers. Si is a technologically relevant substrate material as it is used extensively in microelectronics and microelectromechanical systems (MEMS).

3.1.1 Solution Preparation

The ferroelectric layers were prepared using a chemical solution deposition (CSD) method.[46,47] In this method, metal-organic precursors are blended to form an Inverse Mixing Order (IMO) solution chemistry.[48] The

organometallics used here are zirconium butoxide, $Zr(OBu)_4$, titanium isopropoxide, $Ti(OiPr)_4$, and lead acetate, $Pb(OAc)_4$ with respective purities of 80% (20% butanol), 99.999% and 95%. The solution was prepared by first blending the 0.996 g of $Zr(OBu)_4$ and 0.546 g $Ti(OiPr)_4$ in a glass vial with a magnetic stirring rod for 5 min at ambient temperature. Then 0.92 mL HOAc are added as a chelating agent along with 2.41 mL MeOH as a solvent and blended. Either 2.240 or 2.333 g of $Pb(OAc)_4$ is weighed according to the desired Pb excess. The $Pb(OAc)_4$ is dissolved in at 90°C. Finally, additional HOAc and MeOH are added to achieve the desired molarity.

The target Pb/Zr/Ti ratio was 100/52/48. These values reflect the solution stoichiometry for the Zr and Ti only. Excess lead must be added in order to compensate for lead loss to the volatilization of PbO during the firing. Two solutions containing 20% Pb excess in a 0.4 M solution and 25% in a 0.35 M solution were prepared. It was later found that the films prepared using the different solutions, differed greatly in terms of the amount of surface fluorite present. The fluorite phase is a lead deficient phase that remains on the surface when PbO volatilizes. The fluorite layer, while thin, has been associated with films with poorer dielectric properties.

3.1.2 Layer Deposition

Each solution was deposited onto the substrates using the spin coating technique. This is illustrated in figure 3.1. The substrate is secured to a chuck via a vacuum inlet. A solution is transferred via pipet onto the substrate

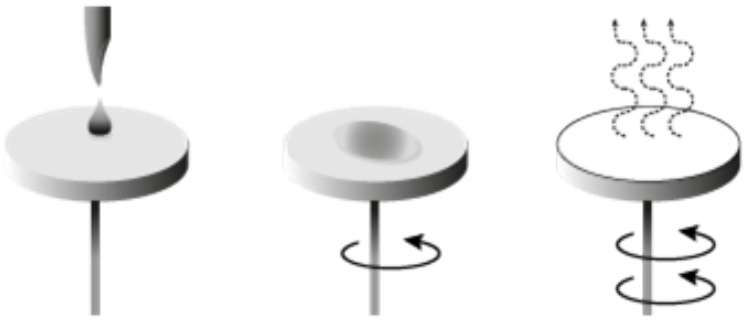

Figure 3.1: The spin coating process. A solution is injected onto the surface of a substrate mounted on a chuck. The chuck spins driving off most of the solution and leaving behind a thin film.[49]

surface to coat it. The chuck then spins, accelerating the substrate to 4000 rpm for a duration of 30 s. In the process, most of the solution is thrown off leaving behind a uniform, sub-micron thick layer of solution. After depositing a layer, the substrate is transferred to a hot plate where it bakes for 1 min. This pyrolyzes the organic groups leaving behind an amorphous gel. At this point, the wafer is removed from the hot plate and allowed to cool before additional layers are deposited. Each deposition contributes approximately 80-90 nm to the final crystallized film thickness. The thickness prior to crystallization is actually greater due to the lower density of the amorphous layer.

Each wafer received four layer depositions. This resulted in a final film thickness of 320 nm for the 0.4 M, 20% Pb excess solution and 350 nm for the 0.35 M 25% Pb excess solution. The 320 nm film was pyrolyzed at 300°C while the 350 nm film was at 350°C. After deposition of the fourth and final layer, both films were crystallized at 700°C for 10 min. This was done by

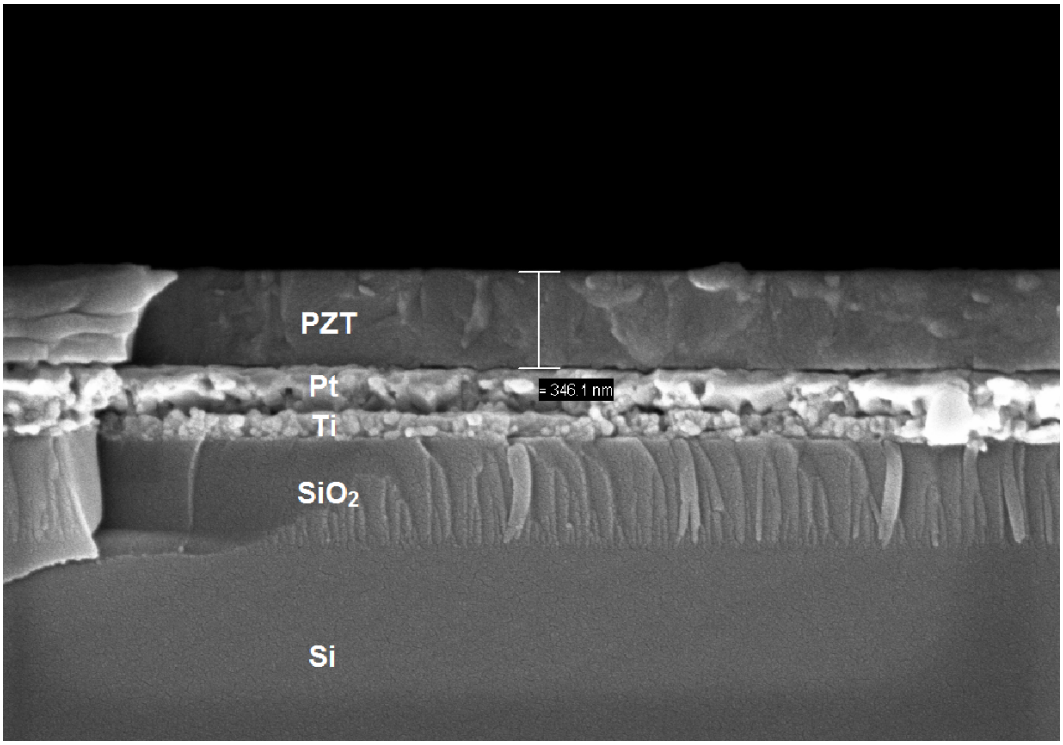

Figure 3.2: An SEM micrograph of the fractured, set B film revealing the PZT, Pt, Ti, SiO_2 and Si layers.

placing them directly into a muffle furnace immediately after the last layer was pyrolyzed. Apart from the stoichiometry and pyrolysis temperature, the processing conditions for each film were nominally equivalent. The 320 and 350 nm films will be referred to as set A and B, respectively, from here on. An SEM cross section of the freshly fractured set B film is shown in figure 3.2.

3.2 Sample Irradiation

Samples were diced prior to irradiation into 22, 1 cm^2 squares and then heat sealed in 2 polyethylene bags. The bags provide two layers of containment so that no radioactive contamination could be transferred from the irradiation vials to the samples nor any material from the samples to the vials. The films were irradiated in the TRIGA mark II research nuclear reactor at the University of Texas at Austin in an in-core Rotary Specimen Rack (RSR).

The RSR system consists of a rotating annular rack with 40 vial slots imbedded within the top of the graphite neutron reflector annulus along the periphery of the fuel assembly.[50] The RSR of a typical TRIGA reactor, pictured in figure 3.3 shows the positions of the vials around the fuel assembly.

Each RSR vial is a plastic cylinder with a screw top. The samples were placed in the vials so that the bottom surface of the substrate was laying flush with the base of the vial. Samples were equally spaced in the RSR rack slots to minimize any inhomogeneities in neutron shielding. However, this was largely overcautious as the flux perturbation due to a thin Si wafer is too small to have an appreciable effect on the flux profile at neighboring RSR slots. During the irradiation, the RSR was rotated at 2 rpm to ensure a uniform time-averaged flux. Thus all samples were exposed to a nearly identical magnitude and spectrum of neutrons. The irradiations were performed at 950kW_{th} power for durations of 15, 30, and 120 minutes (set A) and 30, 60 and 120 minutes (set B) under ambient temperature and atmospheric conditions. Control samples from each wafer were left un-irradiated for comparison. All characterization

measurements were performed post-irradiation.

The RSR was the chosen irradiation facility for reasons of consistency. Using a facility which can simultaneously irradiate a number of samples under nearly identical conditions reduces most of the uncertainty in the damage dose due to the neutron flux between samples.[50] Other facilities in the TRIGA core such as the 3L, central thimble, or fast pneumatic system offer advantages over the RSR in that they subject the specimen to harder neutron spectra and they all have Cd liners to minimize activation from thermal neutron capture. The geometric limitations of these facilities, however, would require either sample nesting and stacking or an extensive irradiation schedule where each sample must be irradiated individually. Also, with systems such as the Cd lined 3L or the Cd pneumatic terminus, where there are limitations on the maximum allowable irradiation time or reactor power, each sample would require a series of irradiations to reach the desired doses. Since activation was not a major concern for the thin film samples but consistency was, the RSR was the obvious choice.

Upon irradiation, the samples were left to decay for a period of several days. The activity of the samples was found to be dominated by the Si substrate simply because the sub-micron thick electrode and PZT layers contain very little material (and thus activate only slightly). The 157.3 min half-life of the Si activation product, ^{31}Si, determines the amount of time required for the material to be considered exempt radioactive material.

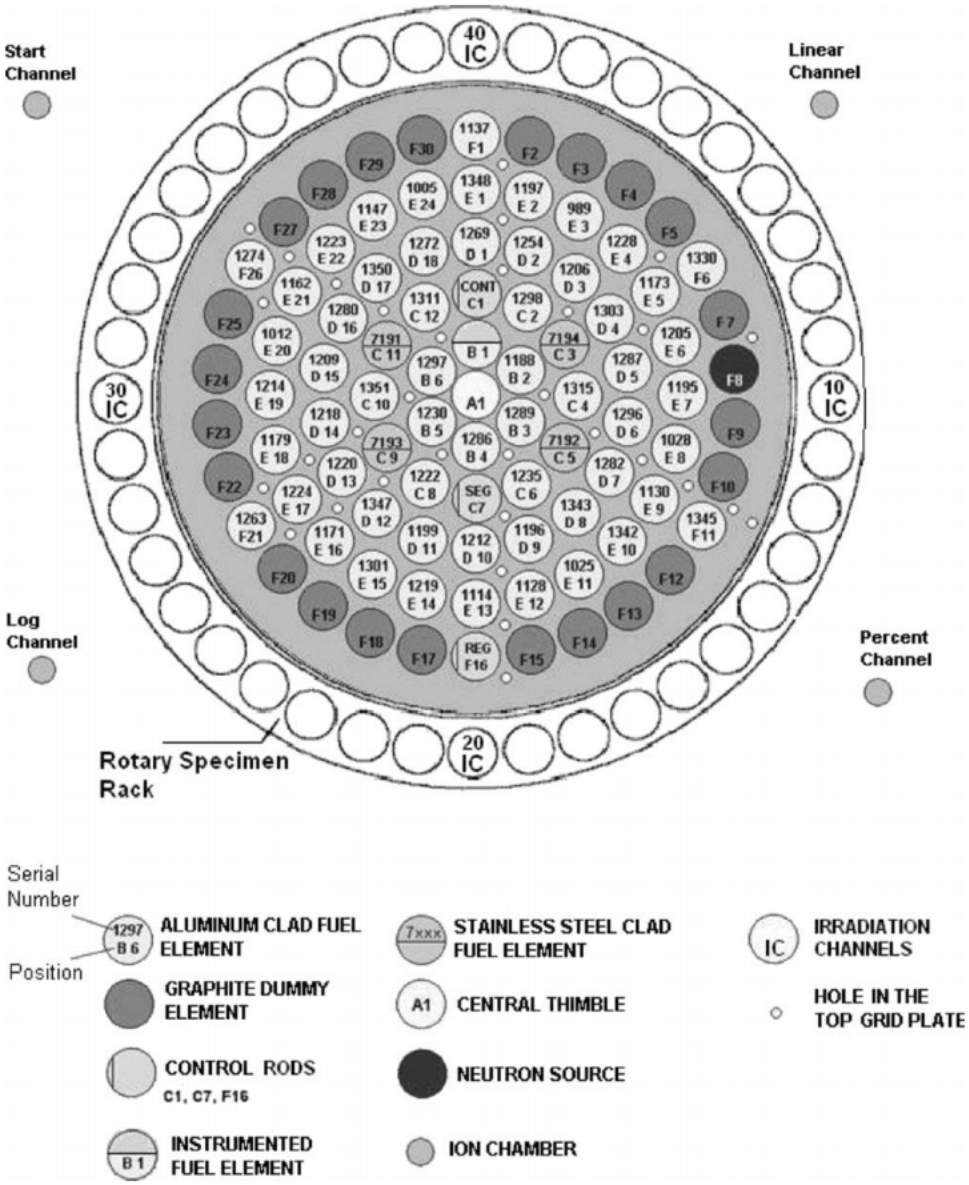

Figure 3.3: A top down view of a the IPR-R1 TRIGA core at showing the location of the rotary specimen rack (RSR).[51]

3.3 Dose Calibration

Irradiation time and total neutron fluence are not particularly useful dose units. The spectral qualities of the neutron field greatly determine the damage accumulation. For example, scattering interactions from fast neutrons will typically create the most energetic damage cascades and therefore produce the highest number of vacancies, interstitials and stable defect clusters on a per collision basis. In contrast, thermal neutrons, which make up the majority population of neutrons in many research reactors, possess insufficient energy to displace atoms (except to a small extent through capture induced recoil). Therefore, a useful dose unit must incorporate both the total fluence as well as the spectral hardness. A standard dose used for radiation testing of electronics is the 1 MeV equivalent dose for Si. This quantity weighs the energy dependent neutron flux by the displacement damage function for crystalline Si, normalized by the value of the damage function at 1 MeV. In other words, the contribution from each neutron group flux is weighed by its damage potential relative to 1 MeV neutrons in Si.

To calculate the 1 MeV equivalent flux, both the neutron flux spectrum and the Si damage function must be known. Values for the damage function are tabulated in the ASTM standard ASTM E722.[52] Figure 3.4 shows the Si damage function.

To ensure accurate numerical integration of the equivalent flux, the flux spectrum of the irradiation facility must be known with resolution comparable to the tabulated damage function. However, since the damage function has

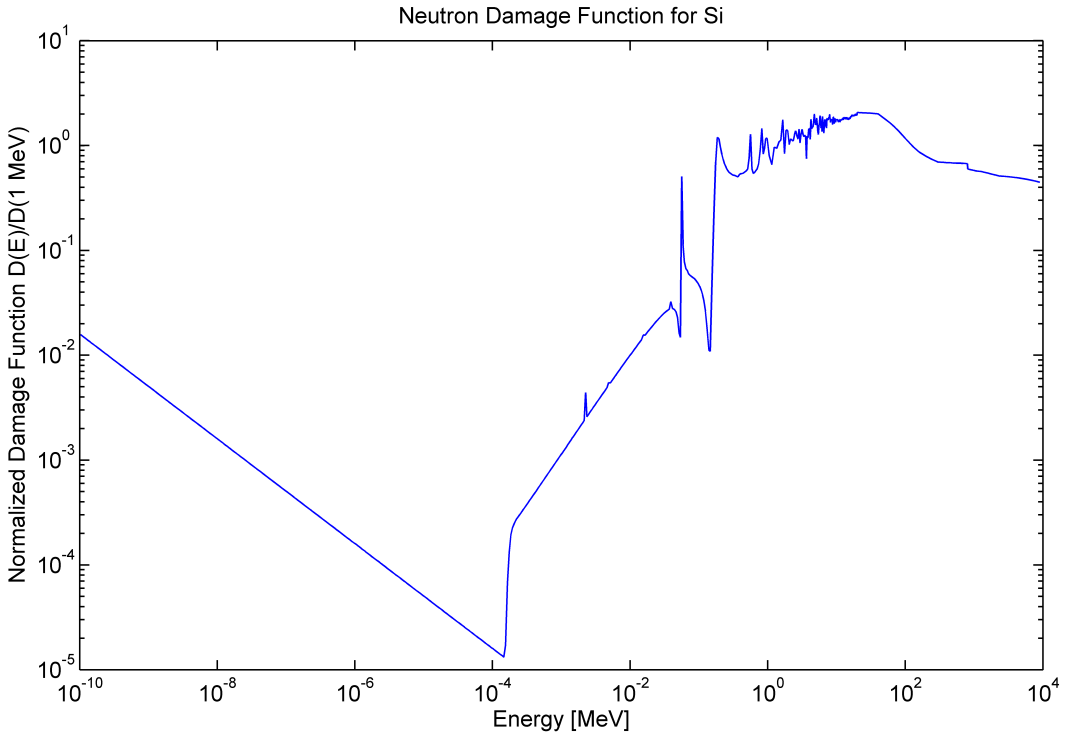

Figure 3.4: The neutron damage function for Si, normalized by the displacement rate at 1 MeV.

a much finer energy structure than reactor dosimetry methods will allow, a semi-empirical, semi-numerical approach was adopted. The flux spectrum of the RSR facility was obtained via the Monte Carlo radiation transport code MCNPX.[53] A copy of an MCNPX input deck for the TRIGA reactor, originally written by Jon Braisted was modified to include a flux tally in the RSR ring at the approximate height of the sample rotation.[50] The modified input deck can be found in the appendix. The flux tally included an energy bin card that sorts the tallies into energy bins matching the 1381 point energy structure of the Si damage function. Thus the output is prepared in a format which is amenable to numerical integration of the dose. While the spectral shape of the MCNPX generated flux is presumed to be more accurate and detailed than anything which could be determined via conventional, in-core dosimetry methods, the magnitude of the energy integrated flux is less certain. One could make a rough approximation of the flux, ϕ, at reactor power P using

$$\phi[\mathrm{cm}^{-2}\mathrm{s}^{-1}] = \phi_{\mathrm{MCNPX}}[\mathrm{cm}^{-2}\text{per history}] \times \frac{P\nu}{Q} \tag{3.1}$$

ν is the average number of neutrons created per fission (about 2.5) and Q is the average energy released per fission (180-200 MeV). The major flaw with this recipe, however, is that the power as measured by fission chambers on the periphery of the reactor core, is not made with reference to the flux integrated over the RSR so the result still differs from the true flux by an unknown conversion factor.

To circumvent this issue, the MCNPX derived spectrum was normalized and readjusted with values of the flux determined through conventional flux monitors. The flux monitors used in this case were two Al-Au activation foils. The relevant reaction in this case is $^{197}\mathrm{Au}(n,\gamma)^{198}\mathrm{Au}$. The Al is present only to dilute the Au. This reduces the activity of the sample and minimizes Au self-shielding. One foil was irradiated bare in an RSR vial while the other was encapsulated in a 0.2 mm thick Cd shell. The Cd is an effective thermal neutron absorber so the induced activity in the Cd shielded foil represents only the epithermal flux while the bare foil represents both thermal and epithermal contributions. The foils were irradiated simultaneously 180 degrees apart in the RSR ring for 5 minutes at 10 kW power. After irradiation they were left to decay in the core for a period of approximately 100 hrs to allow some of the Cd and Al activity to decay. The samples were counted on an HPGe gamma spectrometer system for 3 hrs each. The initial activity of the $^{198}\mathrm{Au}$ was extrapolated from the 411 keV photopeak. By comparing the activities for each foil it is possible to estimate the sub-0.4 eV and super-0.4 eV neutron fluxes. The 0.4 eV cutoff known as the Cd cutoff corresponds to the approximate energy above which Cd becomes transparent to neutrons. Full details of the method can be found in ASTM standard E 262.[54]

The MCNPX generated neutron group fluxes below and above 0.4 eV were summed yielding the MCNPX sub- and super-0.4 eV fluxes. These were then normalized by values obtained from the Au foil measurement. Table 3.1 shows the sub- and super-0.4 eV fluxes at 950 kW reactor power as well as

Table 3.1: The sub-0.4 eV and super-0.4 eV flux within the RSR at 950 kW reactor power.

Energy Range	Flux [cm^{-2} s^{-1}]	Ratio of measured to numerical flux [s^{-1} per history]
< 0.4 eV	$(2.55 \pm 0.12) \times 10^{12}$	$(1.88 \pm 0.09) \times 10^{10}$
> 0.4 eV	$(2.01 \pm 0.03) \times 10^{12}$	$(1.88 \pm 0.03) \times 10^{10}$

the ratio between the measured flux and numerical flux (note that the ratio has units because the MCNPX results are based on units of histories rather than seconds). There is good agreement between these two ratios indicating a certain degree of consistency between the spectral hardness of the flux derived from both numerical and dosimetric methods. The normalized flux is illustrated in figure 3.5.

The 1 MeV equivalent flux, $\phi_{1\mathrm{MeV}}$, then follows from numerical integration of the normalized group fluxes, ϕ_i, and the damage function evaluated at each energy, $D(E_i)/D(1\mathrm{MeV})$.

$$\phi_{1\mathrm{MeV}} = \sum_i \phi_i D(E_i)/D(1\mathrm{MeV}) \tag{3.2}$$

where the index, i, runs over the 1381 energy groups. The uncertainty of the equivalent flux, σ_{1MeV}, propagated from each of the uncertainties in the normalized flux, σ_i, in the sum is

$$(\sigma_{1\mathrm{MeV}})^2 = \sum_i (\sigma_i)^2 \tag{3.3}$$

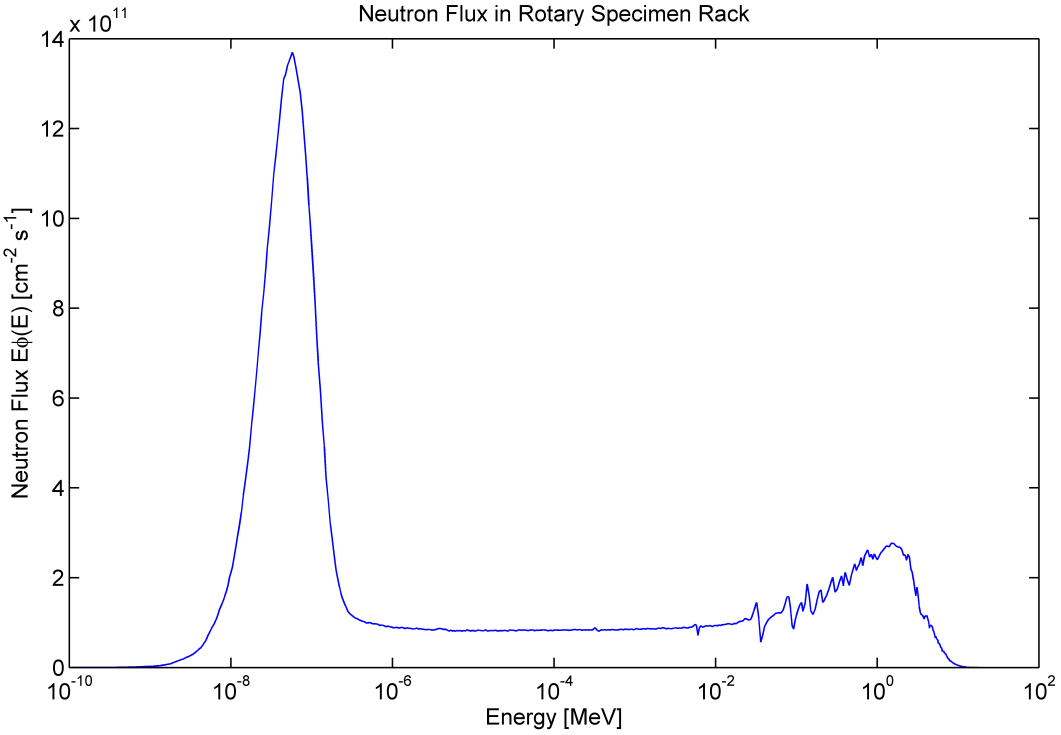

Figure 3.5: The neutron flux spectrum within the RSR at full reactor power.

Equations 3.2 and 3.3 reveal a 1 MeV equivalent flux of $(7.17 \pm 0.04) \times 10^{11}$ cm^{-2} s^{-1} at 950 kW power.

3.4 Post-irradiation Preparation

The post-irradiation samples were transferred back to Sandia National Laboratories where subsequent electronic characterization was performed. First, platinum top electrodes were deposited by RF magnetron sputtering through a shadow mask. A Lesker 18 sputtering system was used to deposit the Pt in nominally 100 nm thick layers. The sputtering system is shown in figure 3.6.

The shadow mask comprised a square grid of square holes with 2 mm center-to-center separation. In order to calibrate data from electronic measurements correctly, electrode areas had to be known to good accuracy. This is somewhat difficult since the edges of the electrodes are not perfectly sharp and the corners tend to be slightly rounded. The electrode areas were measured via an optical microscope mounted with a digital camera. Images were collected and analyzed using ImageJ image processing software.[56] The image pixels were converted to color intensity values. The highly reflective Pt metal under illumination from the microscope lamp results in lighter areas than the underlying PZT. A threshold was set to convert the color image into a binary image. If a pixel intensity was above the threshold it is given a value of 0. Below the threshold it is given a value of 1. The resulting image consists of black patches indicating the electrode areas. A particle measurement algorithm in the software was then used to identify the edges of the electrodes and measure

Figure 3.6: The Lesker 18 sputtering system used to deposit Pt top electrodes to the PZT films.[55]

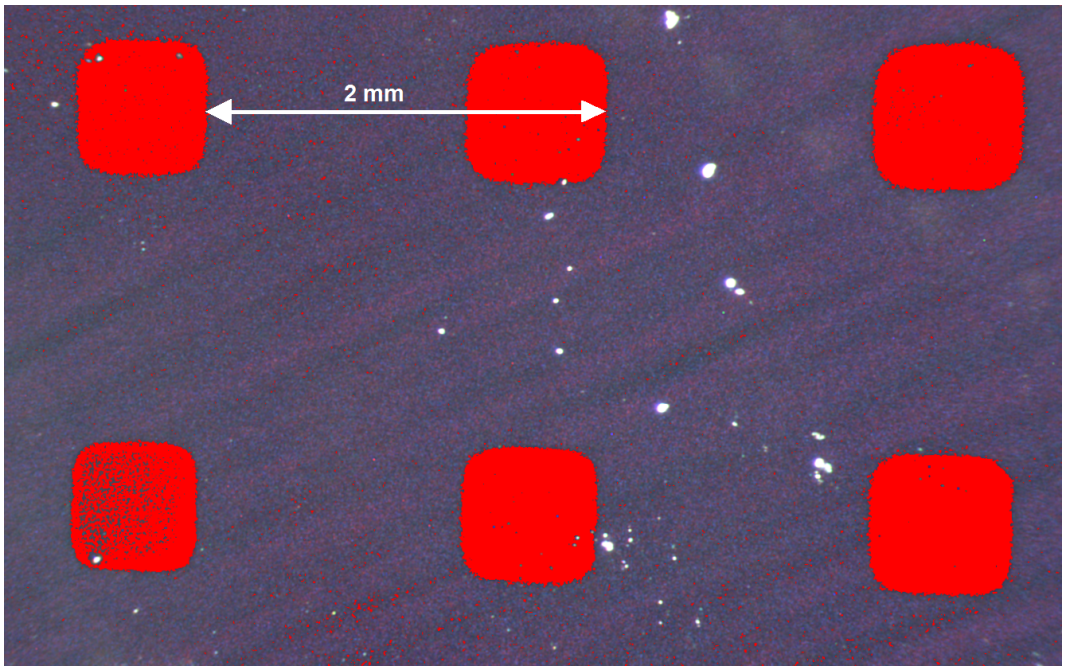

Figure 3.7: Optical micrograph of a PZT film with deposited Pt electrodes overlaid with red areas indicating the color intensity threshold.

their areas. Figure 3.7 illustrates this thresholding technique. The red areas indicate pixels above the threshold assumed to be part of the Pt electrodes. Note that there are pixels below the threshold which are still clearly within the electrode area. These still contribute to the area since an option was selected to include holes enclosed within the electrode boundary defined in the particle measurement algorithm.

Chapter 4

Characterization

4.1 Introduction

As stated before, the objective of this work is to attempt to better identify the types of defects present in neutron irradiated PZT that are responsible for altering the dielectric and domain switching properties. The hypothesis expounded by Miclea *et al.* and other authors that oxygen vacancies are the dominant defects in neutron irradiated PZT seems to result in large discrepancies between experimental and theoretical values. Careful attention must be paid to other point defects, point defect complexes and defect clusters as well as said defects' influence on domain wall mobility and domain switching.

In order to help shed some light on what defects are present and influencing ferroelectric properties, a number of characterization techniques were employed.

4.2 Scanning Electron Microscopy and X-Ray Diffraction

Secondary electron scanning electron microscope (SEM) images were taken to characterize the pre- and post-irradiation morphology for each film as well as accurately measure the film thicknesses. Micrographs of the A films, shown in figure 4.1, revealed a high concentration of surface fluorite, and an average perovskite grain diameter of 125 $\pm$ 8 nm. The surface fluorite appears as lighter, fine-grained patches. In contrast, set B had low concentrations of surface fluorite and an average perovskite grain diameter of 120 $\pm$ 13 nm as seen in figure 4.2. Cross-sectional micrographs (for an example see figure 3.2) revealed high density, columnar grain morphologies in both film sets.

Grain diameters were determined via particle area measurements taken with ImageJ according to ASTM standard E112.[57] In a similar manner to the electrode area measurements mentioned previously, the images were first converted to binary format by applying a grey level threshold. This separated the image into black and white regions representing the grains and grain boundaries. This approach was applied in a series of patches spanning multiple grains so as to as to remove fluorite rich regions from the count and to deal with large scale brightness and contrast variations across the image. The areas of the white regions (grains) were then determined using a built-in algorithm within ImageJ for measuring particle area. Grains straddling the image borders were excluded as they would otherwise bias the true size distribution. The remaining areas were converted to effective diameters assuming circular

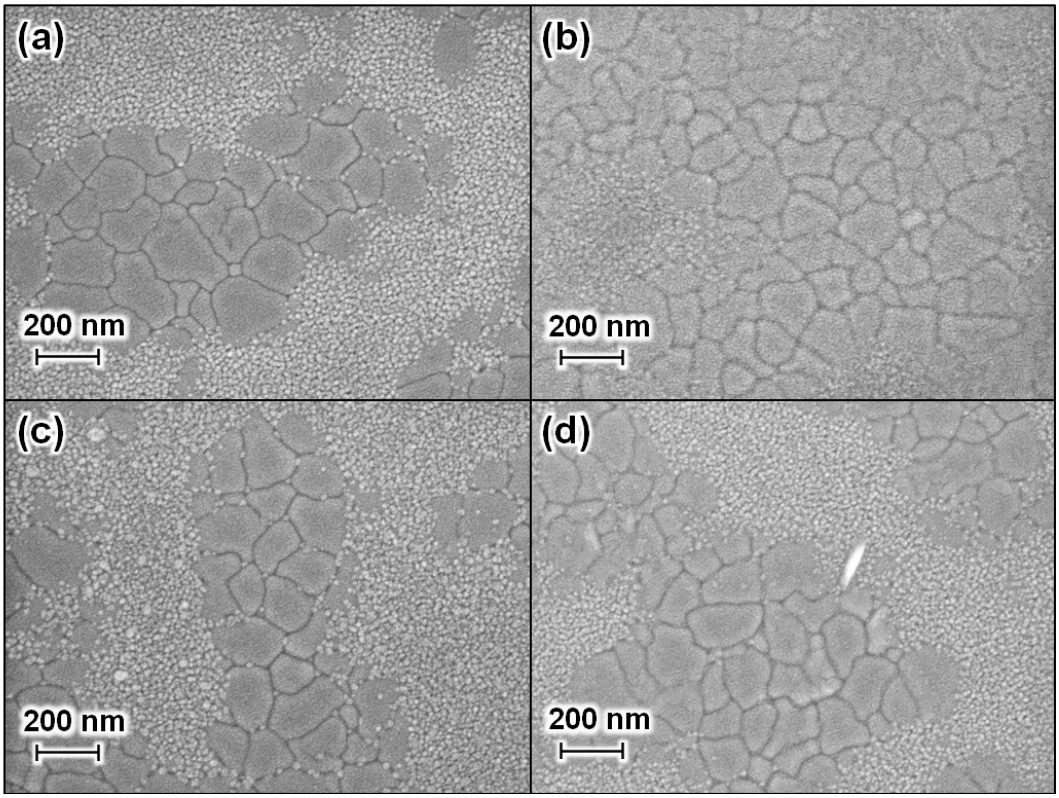

Figure 4.1: SEM plan view micrographs of PZT film set A at neutron fluence: control (a), 0.7×10^{15} cm^{-2} (b), 1.3×10^{15} cm^{-2} (c), 5.2×10^{15} cm^{-2} (d). The fine grained regions are surface fluorite.

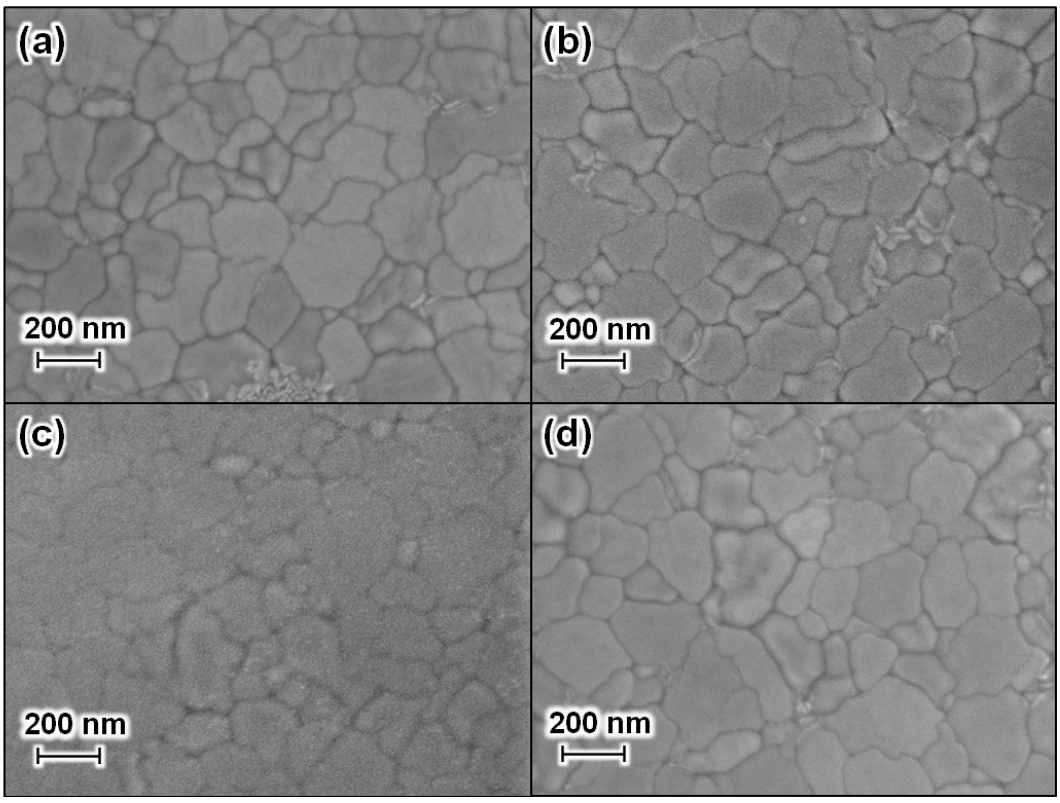

Figure 4.2: SEM plan view micrographs of PZT film set B at neutron fluence: control (a), 1.3×10^{15} cm^{-2} (b), 2.6×10^{15} cm^{-2} (c), 5.2×10^{15} cm^{-2} (d).

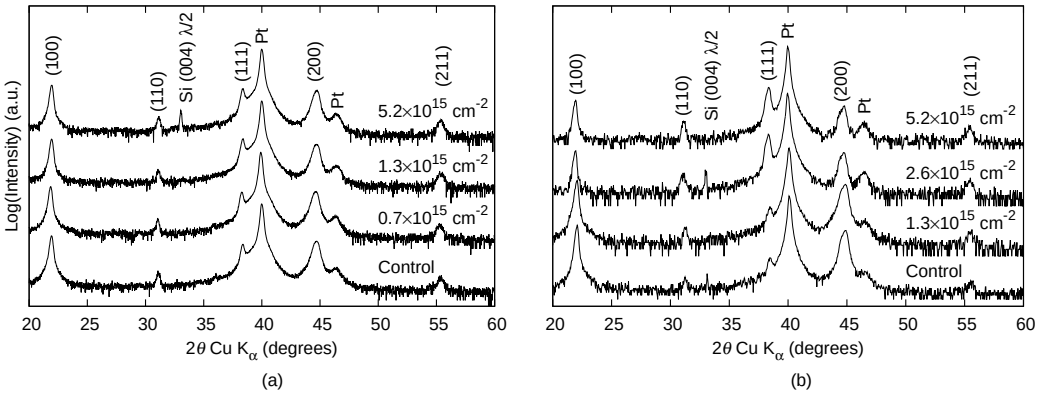

Figure 4.3: XRD spectra of control and irradiated set A (a) and set B (b) films stacked in order of fluence (control on the bottom). Unlabeled indices are for PZT.

grains using the formula $d = 2\sqrt{A/\pi}$ where d is the grain diameter and A is the measured area.

No noticeable changes in morphology were observed. This is unsurprising since the observable morphological changes seen at grain boundaries in most materials such as void and precipitate nucleation only occur at much higher doses (>dpa).

Grazing incidence Cu K_α X-Ray Diffraction (XRD) measurements were taken with a Bragg-Brentano geometry to identify the grain orientations. The spectra indicate that the films are single phase and polycrystalline with predominantly (100) and (111) oriented grains. The XRD spectra are shown in figure 4.3.

4.3 Hysteresis Loops

Polarization-electric field hysteresis curves measure the polarization response from an applied AC field. Several features of the hysteresis curves may be used to gain some insight into the ferroelectric properties. The saturation polarization, for example, gives some indication of the intrinsic polarizability of the material, as well as the total volume of polarizable material. The remanent polarization is related to the stability of the domain structure at zero applied field. A low remanent polarization in relation to the saturation polarization indicates a relatively high amount of reverse domain nucleation above the coercive field, relaxation phenomena, leakage, or a combination thereof. Assuming symmetric hysteresis curves, the coercive field measures the average intrinsic coercive field, that is, the field needed to reverse a domain in the absence of defects. Shifts in the center of the curve along the field axis indicate the presence of a constant internal bias field. Distortions resulting in pinching of the cusps can indicate space charge effects.

Polarization-electric field hysteresis curves were measured using a Radiant Precision Workstation. This device is based on the concept of the virtual ground circuit illustrated in figure 4.4. In the virtual ground circuit method, the output of a transimpedance amplifier acts in such a way to force the positive node to equal the negative, input node. In this way, the device under test in this case the ferroelectric capacitor is virtually grounded.[58] This essentially eliminates any impedance and parasitic capacitance from the test circuit. As long as grounded BNC cables are used, the only other external capacitance

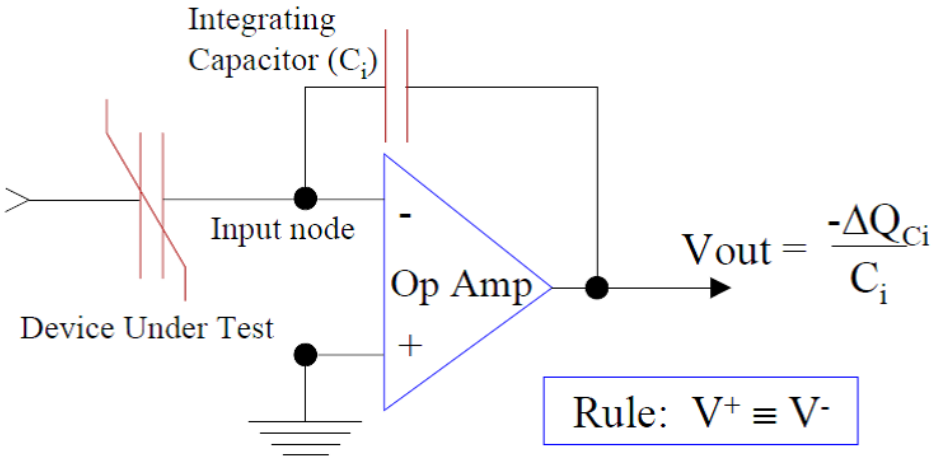

Figure 4.4: The virtual ground circuit used to measure polarization-electric field hysteresis curves and First Order Reversal Curves (FORC).[58]

comes from the particular test fixture or probe station connected to the ferroelectric capacitor. For the measurements conducted, a probe station with micropositioners and wire probe tips was used. The drive tip was placed directly on the surface of the top Pt electrodes while the return tip was placed on an exposed area of the bottom Pt film near the edge of each diced sample. The Pt was exposed by simply scoring through the perovskite layer with a razor blade. The probe tips were separated by several millimeters during each measurement. This separation ensured that the parasitic capacitance due to the probe station was negligibly small.

Nested 1 kHz PE loops were measured using a Radiant Precision Workstation to identify changes in polarization reversal characteristics.The hysteresis measurement is conducted by first applying a pre-cycle bipolar triangle

wave to negatively polarize the specimen, followed by a delay, then repeating the cycle whilst sampling the polarization. An example of a drive voltage signal is shown in figure 4.5. The peak-to-peak voltage, DC bias, delay time, and cycle period can be specified. As the figure indicates, the applied signal is not a true triangle wave, but rather, a stepped triangle wave. The steps are needed so that only a single voltage is sampled during the integration time. All hysteresis curves were measured using a 1 ms cycle period, a 1 s delay between pre-cycle and measurement cycle, and no DC bias. For the set A samples 4, 8, 12, 16 and 20 V peak-to-peak cycles were applied. The maximum voltage corresponded to an applied field amplitude of 313 kV cm^{-1}. For the set B samples, 10, 20, 30, 40, 50, 60, 70 and 80 V cycles were applied with a corresponding maximum field amplitude of 1113 kV cm^{-1}. Initial attempts were made to test the set A samples with the broader range of voltages used for set B. Above, 20 V however, the set A samples had a high probability of dielectric breakdown leading to shorting of the capacitors. Thus the lower maximum voltage and step size was adopted. In order to mitigate measurement uncertainty as much as possible, as many measurements were taken as non-defective electrodes on each sample. Between 11 and 15 electrodes were measured per sample (depending on the coverage of the shadow mask and the number of defective electrodes).

The set A samples exhibited a noted decrease in polarization with increasing fluence with representative hysteresis loops shown in figure 4.6. Average remanent polarization, P_r, and coercive field, E_c, values that were cal-

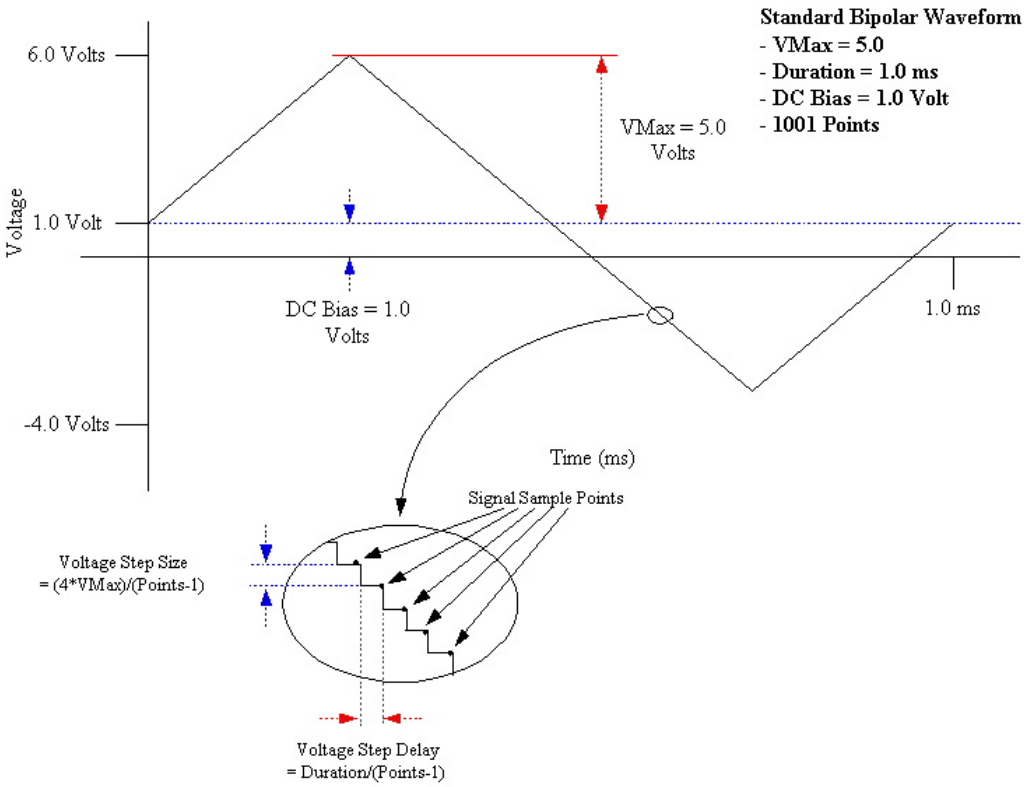

Figure 4.5: Drive voltage signal used during the polarization-electric field hysteresis curve acquisition.[59]

culated over measurements of several electrodes appear as text insets in the figure. Each reported value represents the average of the magnitudes of the positive and negative remanent polarization or coercive field. The uncertainties represent the standard error on the mean. The positive coercive field was inferred by linearly extrapolating a portion of the ascending curve to zero polarization. This was done to help eliminate the effect of the loop discontinuity; an artifact of leakage and relaxation after the pre-cycle. No statistically significant changes in the coercive field were observed. These observations are consistent with those of other authors studying neutron irradiation effects on PZT films.[34] The low amplitude loops (the inner loops) of the set A films show signs of distortion upon irradiation with the negative field cusps becoming pinched. This might suggest that space charge evolves in a preferred way. The behavior of the ferroelectric layer is nominally symmetric with regards to the direction of polarization. The asymmetry between the bottom and top electrode-perovskite interfaces, however, can bring about strain fields, dissimilar defects and variation in the density of nucleation sites. These thin film features are likely to influence the distribution of space charge.

In the set B samples, saturation polarization is stable up to the highest fluence (see figure 4.7). Remanent polarization appears to decrease with total fluence, albeit less dramatically than for set A. Based on the number of sample points and their non-monotonic behavior, however, the trend is statistically weaker and it is therefore unclear if the changes are radiation induced or due to electrode-electrode variations and macroscopic variations across the

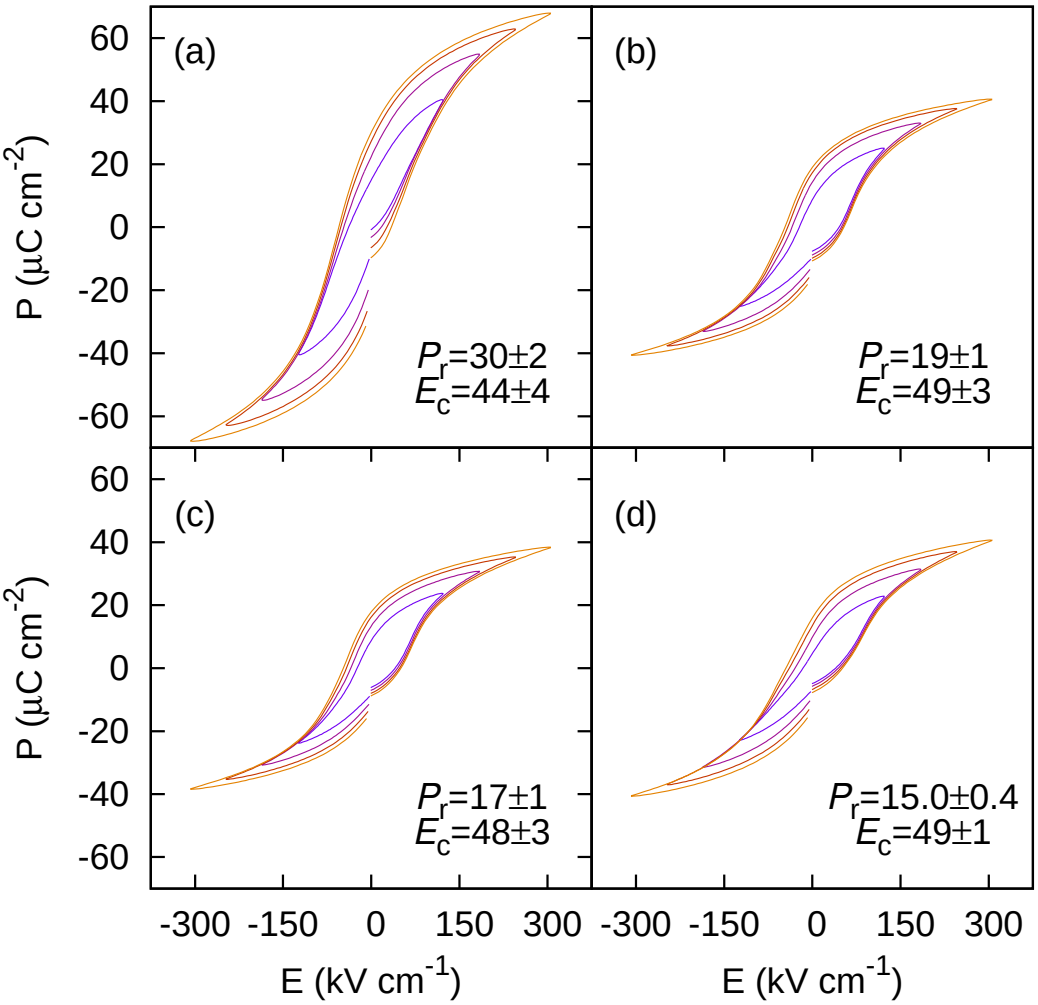

[H]

Figure 4.6: Polarization-field hysteresis loops for set A films irradiated at fluence: control (a), 0.7×10^{15} cm^{-2} (b), 1.3×10^{15} cm^{-2} (c), 5.2×10^{15} cm^{-2} (d).

wafer. In either case, the actual loss of polarization due to irradiation induced damage is comparatively small. The small polarization loss at these fluences is more comparable to the damage accumulation reported for bulk PZT.[35,36] Thus, sample quality must play an important role in damage accumulation rates. The set A films were prepared with a 5% lower excess lead amount, manifesting in a large fraction of the surface covered in surface fluorite. The slight differences in excess lead amount and processing conditions appear to be related to the initial film electrical properties.

4.4 First Order Reversal Curves

Domain wall motion and domain switching may be investigated with first order reversal curves (FORC).[60] Quantitative analysis of FORC measurements can be framed in terms of the Preisach model, which assumes that a ferroelectric material can be described as an ensemble of elementary units of hysteresis.[61]

4.4.1 Theory

The Preisach model is based on the assumption that the response of a generic hysteretic system upon the application of an external force is equivalent to the collective response of an ensemble of hysterons to the same force. A hysteron is an elementary hysteresis response. It is bistable meaning it has two stable states (one actually considers multistable hysterons in more general versions of the Preisach model). As a convention, these states are defined to

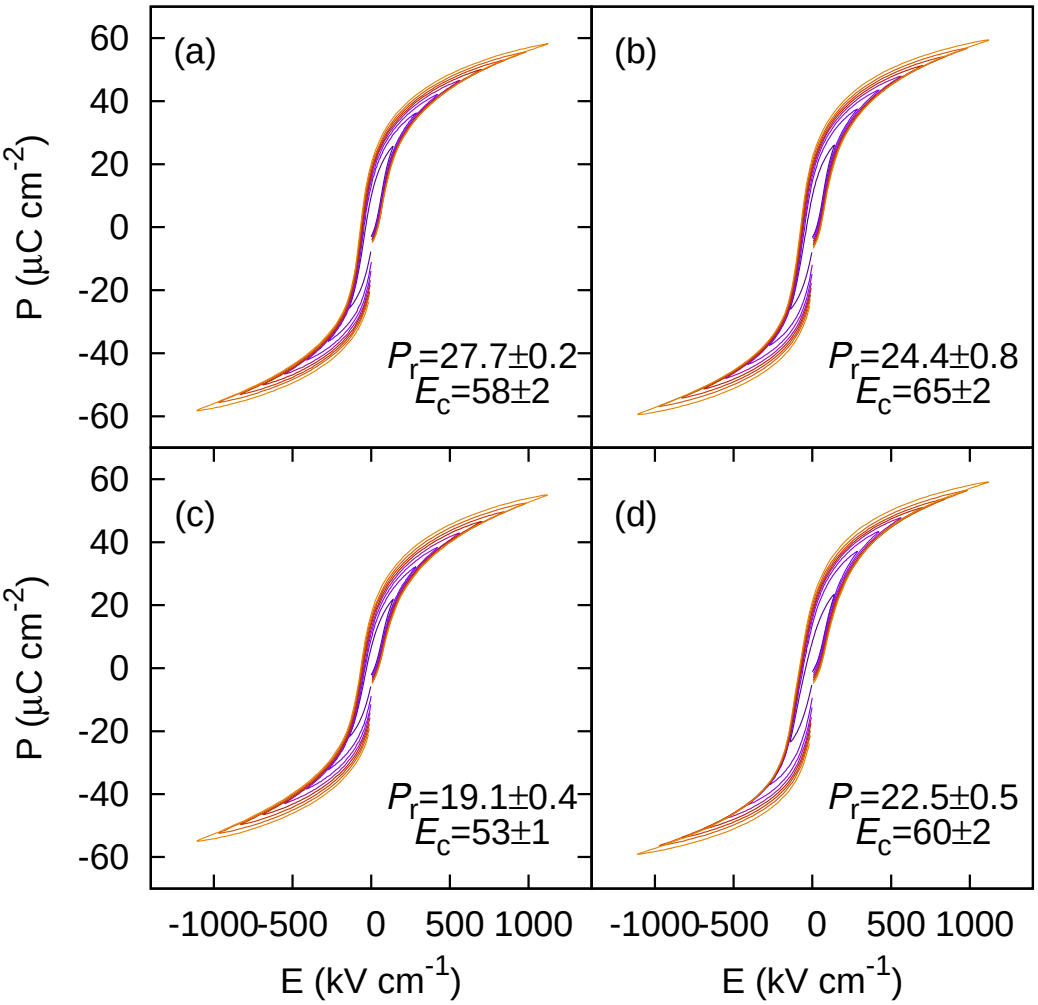

[H]

Figure 4.7: Polarization-field hysteresis loops for set B films irradiated at fluence: control (a), 1.3×10^{15} cm^{-2} (b), 2.6×10^{15} cm^{-2} (c), 5.2×10^{15} cm^{-2} (d).

have unit strength so that the unit response is either +1 or -1. A hysteron for a ferroelectric system is illustrated in figure 4.8. It amounts to a square relay response of the polarization as a function of applied electric field. It is completely characterized by two switching fields α and β. If the initial polarization state is negative, the polarization will remain negative as long as the applied field is less than the up switching field α. Above α, however, the polarization will switch to the +1 state. In order to revert the state back to -1 the applied field must fall below the down switching field, β. The fact that, in general, $\alpha > \beta$ captures the essential feature of a hysteretic system; namely, the state is history dependent.

To construct the general time varying polarization response of a ferroelectric slab, $P(t)$, under the influence of an arbitrary time varying electric field, $E(t)$, we sum the responses from an ensemble of hysterons.

$$P(t) = \sum_i \gamma(E(t); \alpha_i, \beta_i) \tag{4.1}$$

$\gamma(E(t); \alpha_i, \beta_i)$ is the hysteron response function for the i^{th} hysteron in the ensemble, characterized by switching fields α_i and β_i. In the continuum limit equation 4.1 becomes.

$$P(t) = \int d\alpha d\beta \mu(\alpha, \beta) \gamma(E(t); \alpha, \beta) \tag{4.2}$$

Note that the hysteron index has been dropped and a hysteron density function, $\mu(\alpha, \beta)$, is added. $\mu(\alpha, \beta) d\alpha d\beta$ counts the differential number of

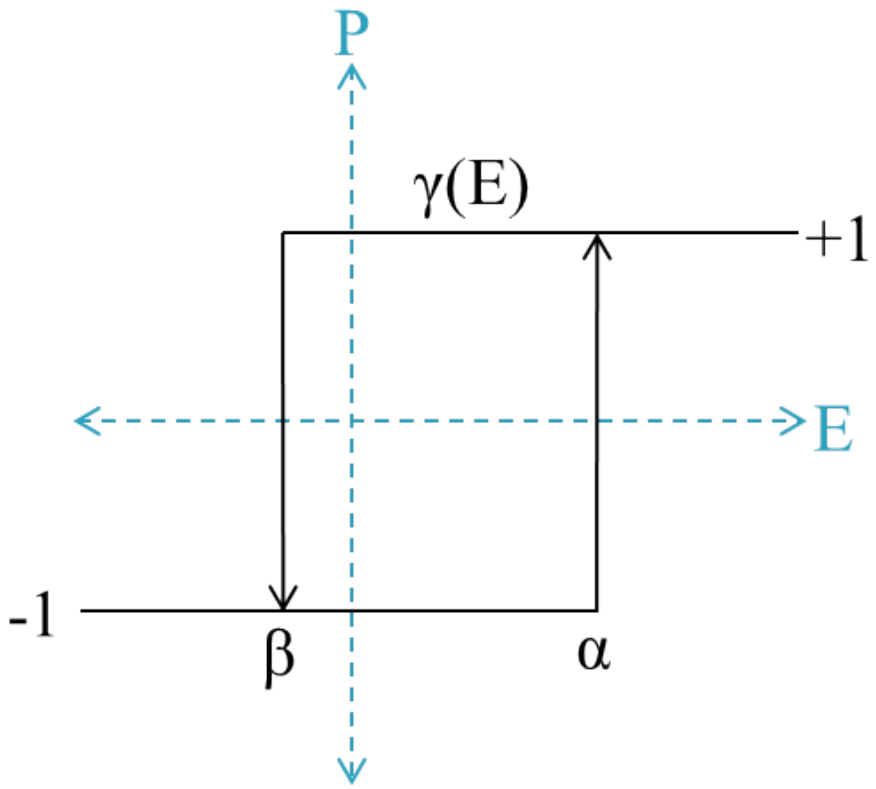

Figure 4.8: Hysteron for a ferroelectric system. The polarization-electric field response exhibits a square loop with switching fields α and β.

hysterons with switching fields within area $d\alpha d\beta$ about (α, β). This density function uniquely defines the hysteretic properties of the system.

The hysteron density function can be extracted from the response by the careful selection of the time varying electric field. First, assume that all hysterons are in the negative polarization state. This situation corresponds physically with the case where the ferroelectric is initially poled with a large negative field. Increasing the field then to a value of α gives the following polarization response.

$$P_{-\infty\to\alpha} = \int_{-\infty}^{\infty}\int_{-\infty}^{\alpha} d\alpha' d\beta' \mu(\alpha', \beta') - \int_{-\infty}^{\infty}\int_{\alpha}^{\infty} d\alpha' d\beta' \mu(\alpha', \beta') \tag{4.3}$$

Since the history is known, the integral can be broken up into positive and negative contributions. If the electric field is then reversed at $E = \alpha$ and brought down to β the polarization response is.

$$P_{\alpha\to\beta} = P_{-\infty\to\alpha} - 2\int_{\beta}^{\infty}\int_{-\infty}^{\alpha} d\alpha' d\beta' \mu(\alpha', \beta') \tag{4.4}$$

Hysterons where $\alpha < \beta$ are unphysical. Therefore, the density function is zero for those values and the second term in equation 4.4 amounts to a finite volume integral in the $\alpha\beta$ plane. We define the function

$$F(\alpha, \beta) = \frac{1}{2}[P_{-\infty\to\alpha} - P_{\alpha\to\beta}] \tag{4.5}$$

It is straightforward to show that

$$F(\alpha,\beta)-F(\alpha-d\alpha,\beta)-F(\alpha,\beta-d\beta)+F(\alpha-d\alpha,\beta-d\beta)=\int_{\beta-d\beta}^{\beta}\int_{\alpha-d\alpha}^{\alpha}d\alpha d\beta\mu(\alpha,\beta) \tag{4.6}$$

Therefore

$$\mu(\alpha,\beta)=\frac{\partial^2 F(\alpha,\beta)}{\partial\alpha\partial\beta} \tag{4.7}$$

Thus the hysteron density can be determined from the family of reversal curves described by $F(\alpha,\beta)$. This function is sometimes referred to as the Everett function. The importance of equations 4.5 and 4.7 is that they demonstrate how it is possible to completely determine the hysteresis properties of a ferroelectric based on polarization measurements alone.

It should be mentioned that the Preisach formalism is a purely phenomological model used to capture the features of generic hysteretic systems. It isn't guaranteed to emerge from the physical properties of a ferroelectric material. It turns out, however, that the Preisach model can be derived from the equations of motion describing the propagation of a domain wall across a noisy free energy landscape.[62] The derivation is lengthy and will not be presented here. Suffice to say, the hysteron density is determined by the diffusion and drift terms within a Fokker-Planck equation describing the probability distribution for a domain wall's position coordinate.

4.4.2 First Order Reversal Curve Measurements

The true Preisach model is based on the assumption that the hysteretic system has two properties; congruency and deletion.[60] Congruency implies that any two closed loops bounded by the same two field values are congruent (although possibly shifted in polarization). Deletion implies that hysterons must always switch at their switching fields (hysterons may not freeze or lag). If both congruency and deletion hold, the hysteron density is called the Preisach function. In real systems these properties are not always found to hold. However, the Preisach model loses little of its usefulness. Under more relaxed assumptions the term First Order Reversal Curves label is preferred. FORC describes the descending branches of polarization curve originating from a point where the applied field is reversed. It is closely related to the Everett function discussed in the previous section as it amounts to a family of reversal curves measured with reference to the polarization of the reversal point.

The utility of the FORC/Preisach concept is that FORC can be easily measured. Graphical representations of their associated hysteron density functions are valuable tools for visualizing reversible and irreversible contributions and the influence of defects and other properties on switching behavior. FORC has been successfully applied to studying the effects of dopants, film thickness, fatigue and porosity in PZT thin films.[63–66]

FORC measurements were taken using a Radiant Precision Workstation using the same probe station setup as was used for measuring hysteresis loops.

The films were initially pre-poled to -283 kV cm^{-1}. Then a sequence of 39 biased, monopolar, triangle voltage pulses was applied and the polarization response measured. Typical FORC data is shown in Figure 4.9. The pulse width was 10 ms, the time between pulses was 1 s during which the films were re-poled at -283 kV cm^{-1}. Subsequent pulse maxima increased in 0.5 V increments corresponding to a final measurement range of -271 to +271 kV cm^{-1} in 14.3 kV cm^{-1} increments. The FORC were calculated by subtracting the polarization on each descending branch $P_{\alpha\to\beta}$ from the polarization at the reversal points $P_{-\infty\to\alpha}$.

In order to avoid resolution bias, the data was binned into 14.3 kV cm^{-1} width bins, the coarsest resolution of the measurement. The hysteron density, $\mu(\alpha, \beta)$, is given by equation 4.7. The mixed derivative was calculated numerically using a forward differencing scheme and a step size equal to the data bin width.

As with the hysteresis loops and capacitance measurements, between 11 and 15 electrodes were measured per neutron dose level to account for electrode-electrode variance which might otherwise be erroneously attributed to radiation effects.

Representative hysteron distributions for films from sets A and B, shown in Figures 4.10 and 4.11, respectively, clearly show a band along the $\alpha = \beta$ line corresponding to reversible contributions as well as a strong peak associated with irreversible contributions in the lower right quadrant. The first notable trend is that this peak decays and broadens with increasing fluence.

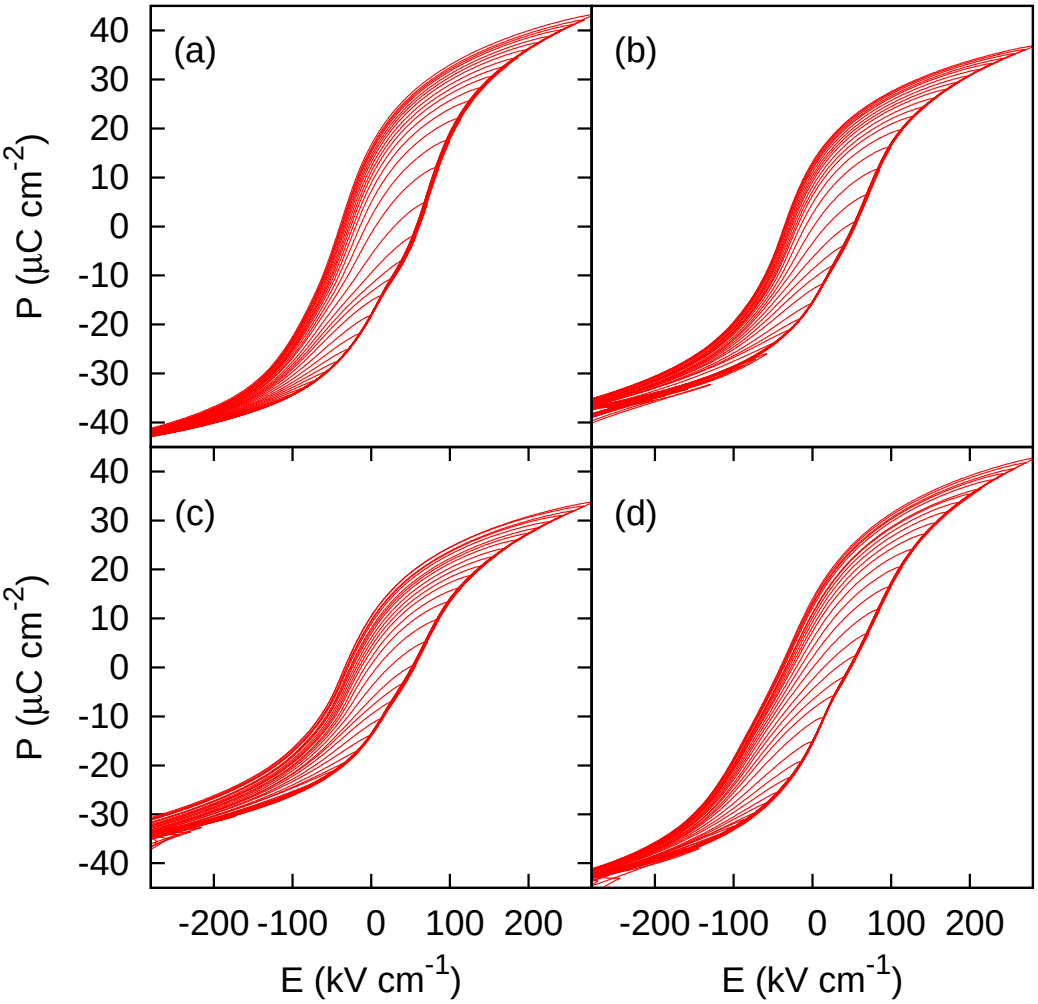

Figure 4.9: Representative FORC data for set B films irradiated at fluence: control (a), 1.3×10^{15} cm^{-2} (b), 2.6×10^{15} cm^{-2} (c), 5.2×10^{15} cm^{-2} (d).

Given that the saturation polarization does not similarly decay in set B, the total integrated volumes under the hysteron distributions are approximately equal. Thus the number of hysterons is mostly conserved for that film set and the observed changes in the hysteron density can be described as redistribution. In contrast, the drop in polarization for the set A films implies that the change in hysteron densities can either be interpreted as hysteron extinction or otherwise as a significant redistribution of hysterons to fields in excess of 313 kV cm^{-1} (the measurable field range for the set A film).

Figure 4.12 shows the integrated reversible bands for each set of films. This band represents the hysteron density under the $\alpha = \beta$ line as a function of the up-switching field α. The integration was performed over 3 bin widths ($3\sqrt{2}$ bin widths in the $\alpha = -\beta$ direction). Integrating over this range was sufficient for capturing the majority of the reversible hysterons while minimizing the irreversible hysteron overlap. At low bias, the two films exhibit different behaviors. The reversible contribution of film set A drops steadily with fluence while only small changes are seen in film set B. This suggests that for film set B, redistribution of hysterons in the irreversible sector of the plane primarily occurs by the transfer of hysterons to higher magnitude field values (i.e., large absolute values of α and β) while in film set A, hysteron extinction in the reversible sector also occurs. Importantly, the tails of the reversible curves do not vary significantly with fluence. At these tails, the bias field is large and most of the mobile domain walls are driven out of the grains. Thus the extrinsic contribution is negligible and the value reflects intrinsic contributions

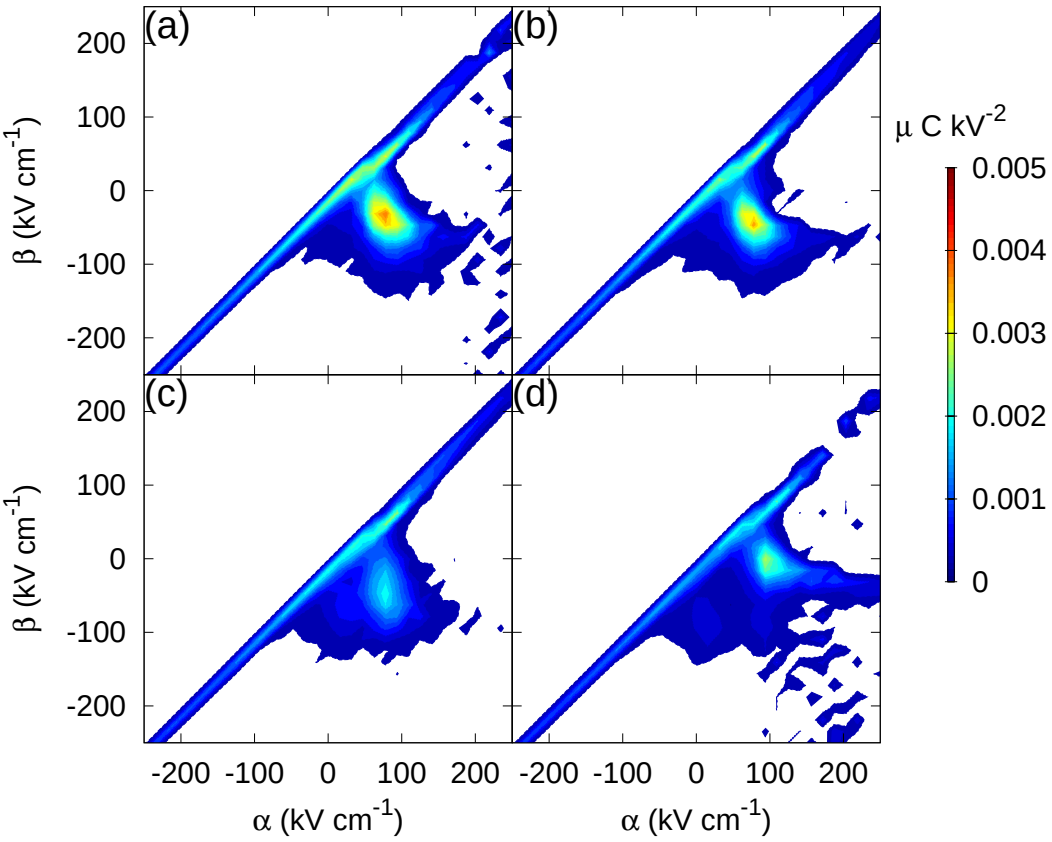

Figure 4.10: Hysteron densities for set A films irradiated at fluence: control (a), 0.7×10^{15} cm^{-2} (b), 1.3×10^{15} cm^{-2} (c), 5.2×10^{15} cm^{-2} (d).

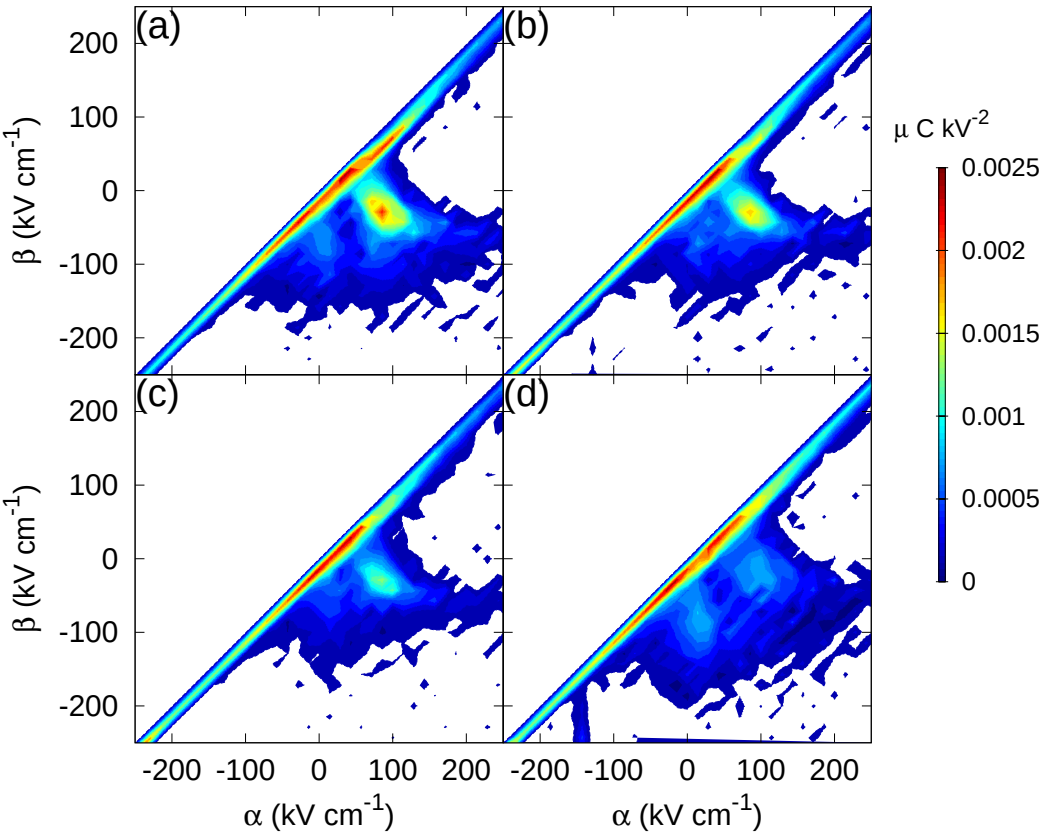

Figure 4.11: Hysteron densities for set B films irradiated at fluence: control (a), 1.3×10^{15} cm^{-2} (b), 2.6×10^{15} cm^{-2} (c), 5.2×10^{15} cm^{-2} (d).

only. This data indicates that the intrinsic permittivity values are the same for both films (as expected for PZT films of the same composition) and that the changes that occur at low bias fields are entirely extrinsic in nature (i.e., due to changes in reversible domain wall motion). The difference in peak height between set A and B films is significant. It could reflect either a difference in the amount of reversible behavior and/or artifacts from the higher leakage in set A films. As mentioned before, loss tangent measurements indicate greater conductivity (and therefore leakage) in the set A films. Domain wall density and pinning strength, however, also influence the low field reversibility. Indeed the difference in peak shape - with the set A films being more peaked - is an indication that the domain dynamics are different. More subtly, leakage and domain wall pinning are expected to be interrelated. Charged defects may act both as pinning sites for domain walls and traps for mobile charge carriers. The concentrations and energy levels associated with carrier traps influence carrier mobility (and therefore leakage). In either case, greater significance is attached to the relative changes in hysteron densities than to absolute differences in values between film sets A and B.

Another feature apparent in the FORC analysis is the presence of imprint. The majority of hysterons have an up-switching field at α=80 kV cm^{-1} and a down-switching field of β=-30 kV cm^{-1} implying that there is a negative built-in bias field with respect to the polarity of the measurement (top electrode at the high potential). At the highest fluence there is also the formation of a second peak. The peak is faintly visible in set A and notable in set B. The

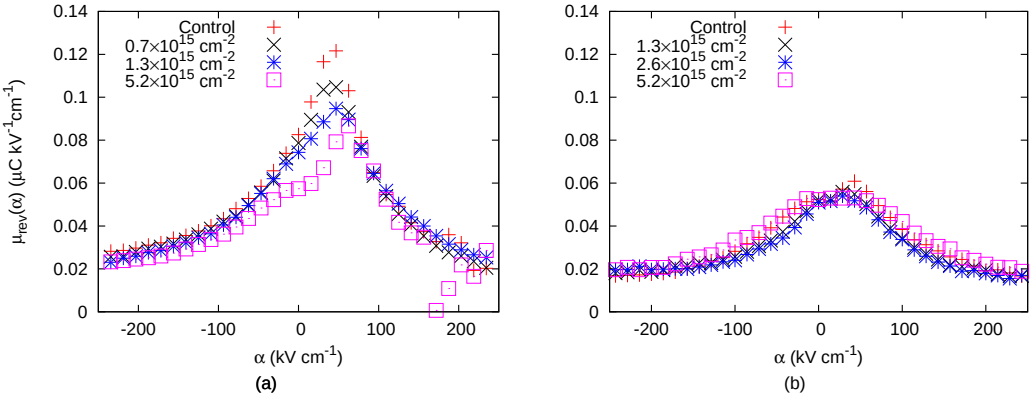

Figure 4.12: Reversible hysteron density as a function of the up-switching field, α, for film set A (a) and film set B (b).

two peaks are separated by a field of 76 kV cm^{-1}. The double peak is characteristic of localized built-in fields such as those caused by DDs. Over long time scales DDs can align with the spontaneous polarization by thermal migration whereas on the time scales that the FORC measurements are performed, DDs are essentially frozen in place. In an otherwise purely intrinsic ferroelectric, the DDs oriented with the direction of the applied field stabilize domains with spontaneous polarizations also in the direction of the applied field. In figure 4.13, the slab represents a region of ferroelectric material. DDs (blue ovals) are oriented with the initial domain structure along the directions of spontaneous polarization (of which there are two in subfigure I). In this schematic, the DDs are the only extrinsic feature. The corresponding points on the PE loop are shown at the bottom of the figure. The black arrows represent the local electric field due to the combined effects of the ferroelectric polarization, the DDs and the applied electric field, while the grey walls indicate domain

walls and the red arrows correspond to the applied electric field. As indicated, the DDs create local bias regions that parallel the initial domain structure. In the initially unpoled slab the bias regions reinforce the domain structure (I). As the external field is varied, however, the bias regions shift the local electric field, altering the coercive field relative to the applied field at different regions of the crystal. Importantly, at points II and V, where the DD-free ferroelectric would normally switch from one saturation state to the other, the DDs stabilize the multi-domain structure. Conversely, domains containing DDs anti-aligned with the applied field are less stable. Consequently, the measured PE loop is split instead of square. In terms of the hysteron representation, a perfect hysteron appears as a delta function in the $\alpha\beta$ plane as indicated by figure 4.14a. Hysteron splitting occurs in the plane parallel to the $\alpha = \beta$ direction as shown in figure 4.14b. Convolving the hysteron splitting effect with the peak in the hysteron density predicts a double peak. Additionally, DDs are expected to preferentially align anti-parallel to the direction of the imprint field in order to reduce the total energy of the electric field. Indeed, based on the location of the second peak, the localized built-in fields are predominantly oriented in the negative direction with respect to imprint.

4.5 Rayleigh Analysis

In the regime of low bias, domain wall restructuring is minimal and domain wall contributions to the dielectric permittivity are largely determined by local domain wall motion.[67] Non-linear dielectric response is a consequence

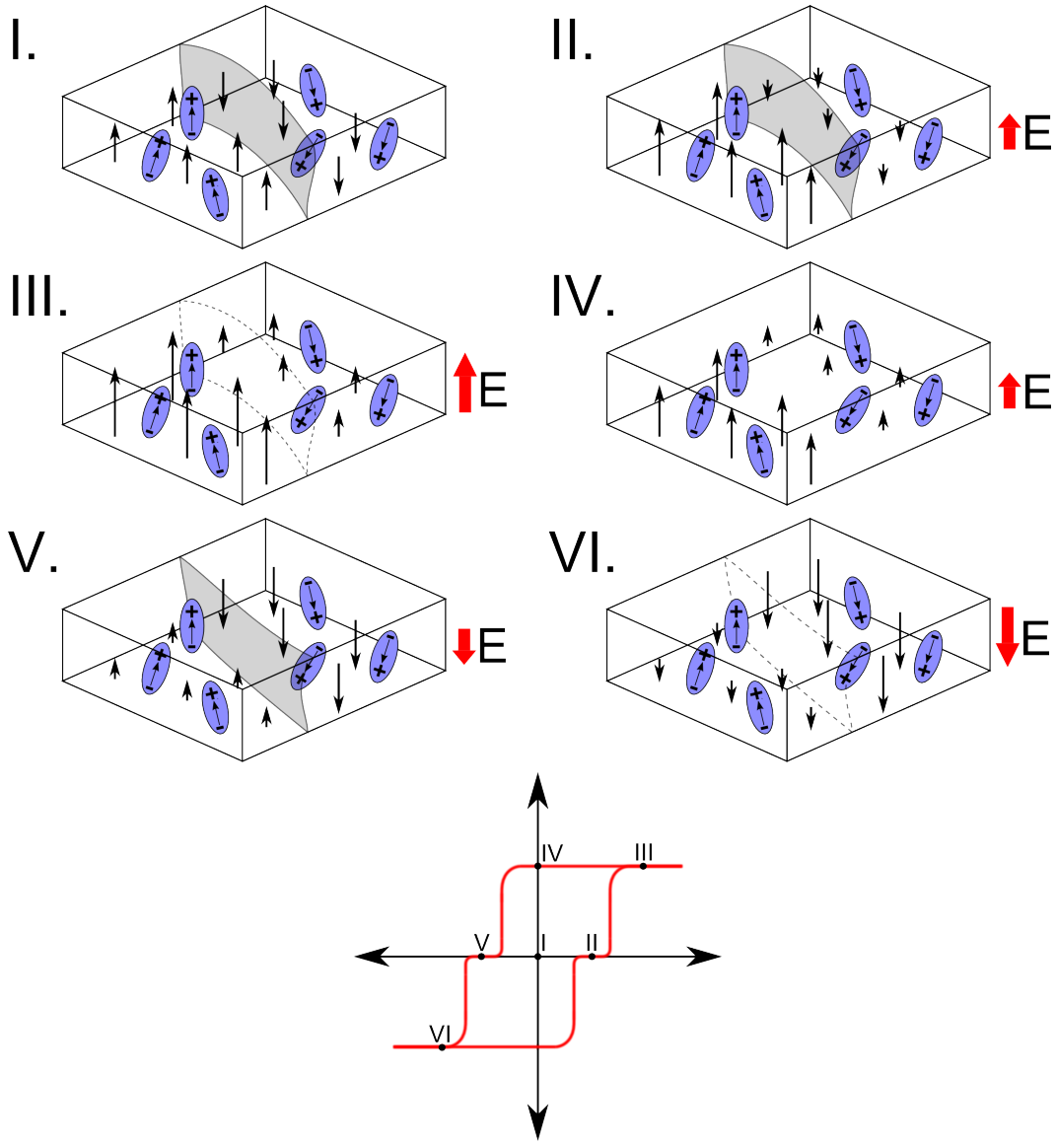

Figure 4.13: Illustration of the domain switching process in an intrinsic ferroelectric slab with static defect dipoles (DDs).

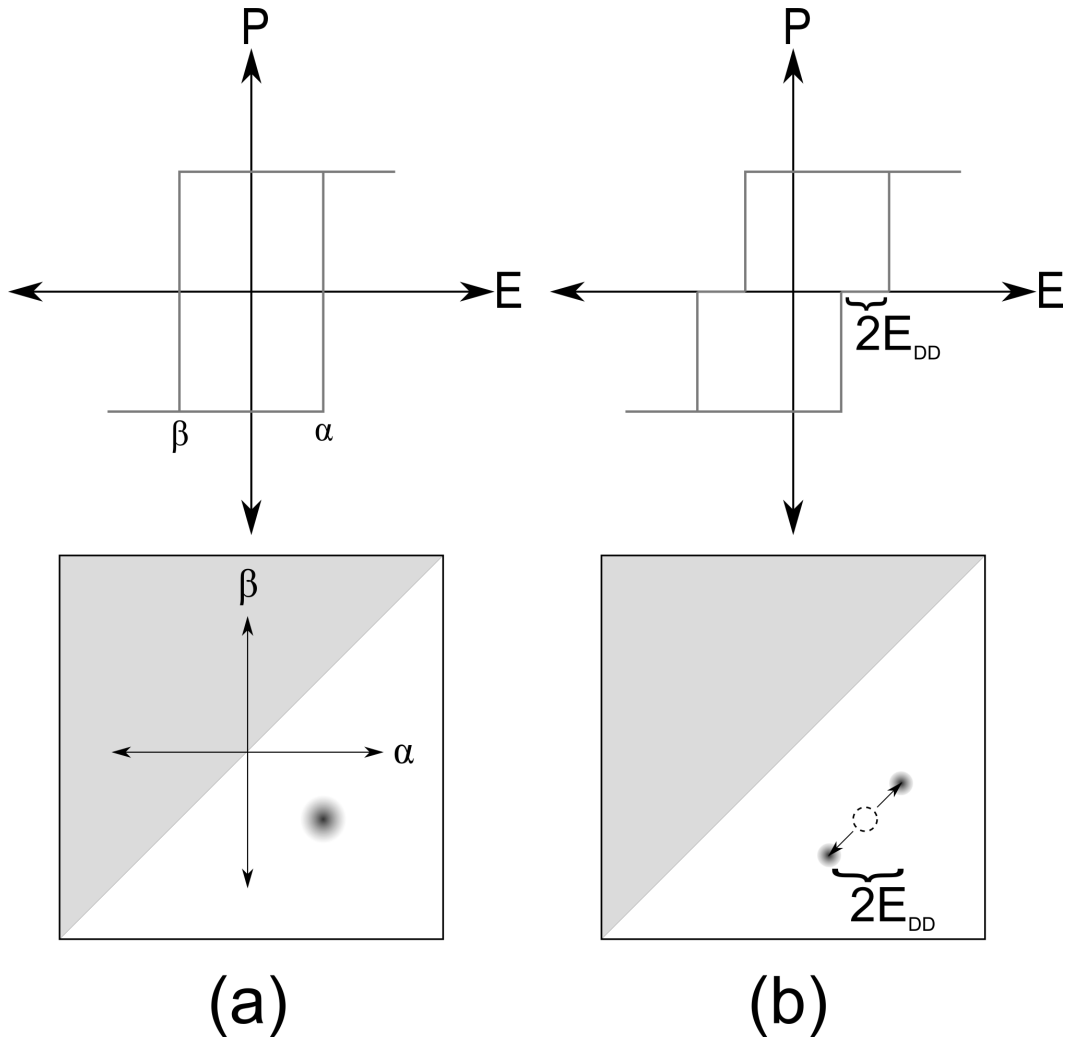

Figure 4.14: The representation of a single hysteron (a) and split hysteron (b) as PE loops (top) and as a delta functions in the $\alpha\beta$ plane (bottom).

of reversible and irreversible motion across a (presumably) random field of domain pinning sites. Under low amplitude applied AC fields, the domain walls oscillate between pinning sites in a reversible manner. At higher amplitude fields, the domain walls may be moved across pinning sites resulting in irreversible domain wall motion. Reversible and irreversible motion contributes to non-linear dielectric behavior as described by the Rayleigh relation.

$$\epsilon' = \epsilon'_{init} + \alpha' E_0 \tag{4.8}$$

ϵ' is the real component of permittivity, ϵ'_{init} is the contribution of intrinsic permittivity and reversible domain wall motion, α' is the irreversible Rayleigh parameter and E_0 is the amplitude of the applied AC field. Note that α' here is different from the α switching field appearing in FORC. Measurement of the Rayleigh parameters has been used extensively to characterize domain wall dynamics in polycrystalline ceramics, single crystals, polycrystalline thin films, and epitaxial thin film ferroelectrics.[68–78] The Rayleigh relation is only valid when the effects of domain wall-domain wall interactions and saturation are negligible.[67] This is the case for applied fields well below the coercive field (typically less than 0.5 E_c). Above this so-called *Rayleigh regime*, higher order non-linear terms begin to influence the permittivity and FORC is a more useful tool for examining domain switching.[79,80]

Domain wall mobility in the Rayleigh regime was investigated by measuring capacitance at applied AC fields from 0.2 to 16.2 kV cm^{-1} (measured

peak-to-peak) and frequencies from 1 to 100 kHz with a Hewlett Packard 4192A impedance analyzer. The Rayleigh measurements were made prior to all other electronic measurements to avoid domain restructuring which occurs at high fields.

Rayleigh measurements of the real portion of relative permittivity indicate a general decrease in permittivity with fluence (Figs. 4.15a and 4.15b). Best fit values of the Rayleigh parameters (ϵ' intercept and slope) from equation 4.8 were both found to decrease with fluence (Figs. 4.15c, 4.15d and Table 4.1). This implies that both the combined intrinsic/reversible contribution and the extrinsic contribution to the permittivity decrease after irradiation. Moreover, the set A films exhibited a stronger decrease in both Rayleigh parameters with dose, suggesting that the initial microstructure is connected to the rate of nucleation and/or growth of domain wall pinning sites. It is not possible to quantitatively decouple the intrinsic and reversible components from these results alone. However, that it is anticipated that reversible domain wall motion dominates the low field response.[81] Additional support for this can be found from the FORC analysis where the reversible hysteron density indicates that the intrinsic contribution does not change with fluence at high fields as shown in Figure 4.12. Thus the change in ϵ'_{init} reflects a decrease in the reversible domain wall motion only. The physical interpretation of a decrease in reversible motion is that local wells in the free energy landscape associated with domain wall configuration become narrower with fluence; possibly due to an increase in the density of pinning sites. Additionally - given the constant

intrinsic permittivity - the decrease in ϵ'_{init} and α point to a loss of irreversible extrinsic domain wall motion. This is connected to an overall increase in the average magnitude of barriers in the random free energy landscape.

Interestingly, the Rayleigh parameters for the unirradiated set A films were higher than for the unirradiated set B films. As mentioned before, there is some ambiguity as to the source of this difference, be it from true reversibility or leakage. However, since the same Rayleigh parameters for the set A films decreased to well below the values for the set B films at the highest fluence, it is certain that the relative change was greater for the set A films. Thus, upon irradiation, the set A films saw much greater effects from domain wall pinning sites. This evidence suggests that there are microstructural features that do not participate (or at least do not participate strongly) in domain wall pinning but that do strongly influence the rate of growth and/or nucleation of domain wall pinning sites. Such features seem to play an important role in the rate of radiation damage accumulation in PZT.

This behavior can be ascribed to an increase in domain size and/or strength of pinning defects. These two mechanisms are interrelated, however, as charged defects help stabilize the domain structure. The formation of such pinning sites also offers an explanation as to the peak broadening seen in the irreversible hysteron density. Hysteron coercivity increases with strength and density of pinning sites. In the $\alpha\beta$ plane, an increase in coercivity is manifested as the redistribution of hysterons in the direction of higher $\alpha - \beta$. Spreading in the direction parallel to the $\alpha = \beta$ reflects built-in depolarizing

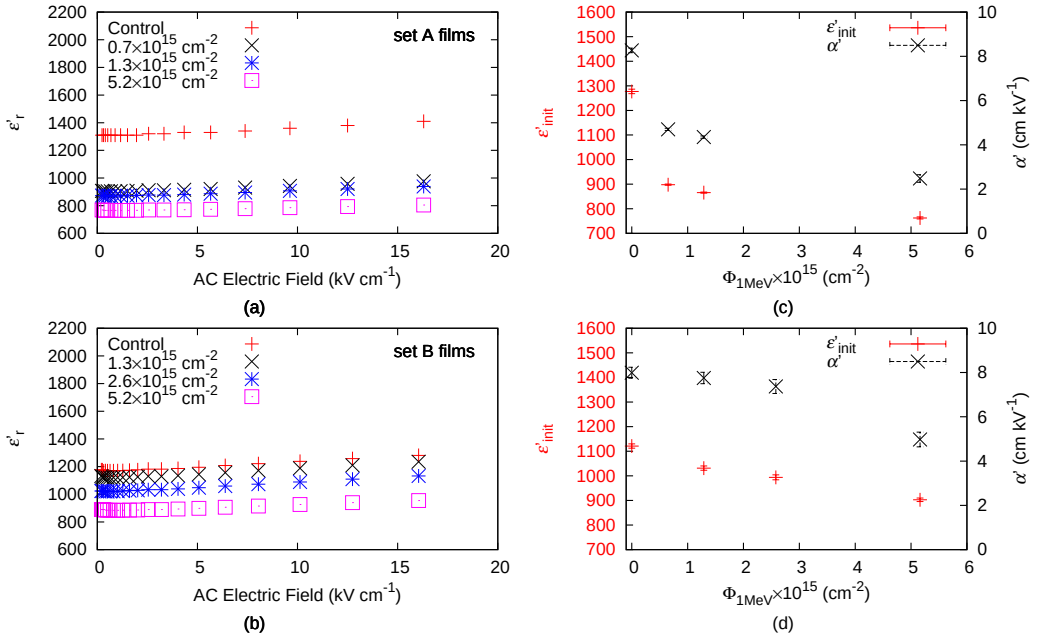

Figure 4.15: Relative permittivity at 1 kHz applied field curves for film set A (a) and film set B (b) and the extracted Rayleigh parameters as a function of fluence for film set A (c) and film set B (d).

Table 4.1: Rayleigh parameters for set A and set B films at 1 kHz.

$\Phi_{1\mathrm{MeV}}$ (cm^{-2})	ϵ'_{init}	α' (cm kV^{-1})	α'/ϵ'_{init} (cm kV^{-1})
	Set A		
control	1277±9	8.27±0.10	$(6.47\pm0.09)\times10^{-3}$
0.65×10^{15}	898±2	4.70±0.05	$(5.23\pm0.06)\times10^{-3}$
1.29×10^{15}	866±2	4.35±0.05	$(5.02\pm0.06)\times10^{-3}$
5.16×10^{15}	763±4	2.38±0.17	$(3.3\pm0.2)\times10^{-3}$
	Set B		
control	1121±1	8.0±0.2	$(7.1\pm0.2)\times10^{-3}$
1.29×10^{15}	1031±1	7.8±0.3	$(7.5\pm0.3)\times10^{-3}$
2.58×10^{15}	994±1	7.4±0.3	$(7.4\pm0.3)\times10^{-3}$
5.16×10^{15}	903±1	5.0±0.3	$(5.5\pm0.4)\times10^{-3}$

fields that alter the stable domain configuration at constant bias field. As discussed above, some of these built-in depolarizing fields are due to oriented DDs but other charged defects may also contribute to the spreading seen in the FORC data. An average increase in the coercivity of irreversible hysterons is manifested as an increase in macroscopic hysteresis. E_c is stationary under symmetrical spreading along the $\alpha = \beta$ direction. Thus the observation that the macroscopic coercive field is stationary (or nearly so) upon irradiation suggests that the majority of hysteron distribution occurs as spreading along the $\alpha = \beta$ direction.

Measured loss tangents were approximately 4.5% and 3.5% at 1kHz for film sets A and B, respectively. These results suggest that the set A films exhibit greater leakage. During AC poling, artificially high measured polarization values are a known artifact of leakage. Thus, the larger overall polarization response from the set A films may reflect greater leakage. This seems plausible given the difference in initial film quality and the lower dielectric breakdown field of the set A films.

4.6 Summary

In summary the electronic characterization measurements have revealed the following effects in irradiated PZT films

- Trends in hysteresis curve distortion and Rayleigh parameters suggest that damage accumulation is concomitant with initial film quality

- Lower quality films exhibit a loss of remanant polarization upon irradiation indicating anti-domain nucleation, enhanced relaxation, inhibition of full switching, and/or leakage

- First Order Reversal Curves (FORC) and small signal permittivity measurements showed that, upon irradiation, the noise component of the domain wall free energy landscape becomes amplified while intrinsic reversible effects were practically unperturbed. This suggests extrinsic pinning sites are the dominant defect with regard to changes in hysteresis characteristics

- The onset of hysteron peak splitting with irradiation also suggests defect dipoles (DDs) are introduced as one type of irradiation induced pinning site

More succinctly, neutron irradiation introduces defects which impede domain wall motion and stabilize the domain structure. The effectiveness of such defects appears to be linked with pre-irradiation microstructure and defect density.

Chapter 5

Modeling

5.1 Introduction

The objectives of modeling the radiation damage event are twofold: 1) to determine the displacements per atom (dpa) dose to the material and 2) to provide as a starting point for subsequent rate theory calculations the source rate of point defects. The latter can only be realized if one carefully considers all of the source and sink strengths for point defects and defect clusters within the material. This generally requires a sequence of computationally expensive numerical studies using a suite of different numerical techniques such as local density approximation density functional theory (LDADFT), molecular dynamics (MD), kinetic Monte Carlo (KMC), etc. Given accurate information about the microstructure of the material, diffusion constants, etc. these techniques will yield decent quantitative predictions. But as the particular microstructure of the material can only be so well replicated in numerical studies and higher order defect reactions quickly complicate the defect evolution, the net predictive power of such advanced modeling techniques tends to be more qualitative than quantitative. Some meaningful conclusions, however, can be gleaned without these modeling techniques by considering just the primary recoil distribution and early phases of the damage cascade.

5.2 Theory

The equation for the rate, R_D, at which atoms are displaced within a material undergoing irradiation is given by

$$R_D = \int dE \phi(E) \sigma_D(E) \tag{5.1}$$

$\phi(E)$ is the neutron flux and $\sigma_D(E)$ is the so-called displacement cross section defined as the integral over recoil energy, T, of the energy transfer cross section, $\sigma(E,T)$ and ν, the displacements per primary knock-on atom (PKA) of energy T.

$$\sigma_D(E) = \int dT \sigma(E,T) \nu(T) \tag{5.2}$$

Note that in a compound each element will have a different energy transfer cross section and ν value. Therefore the total displacement rate for a compound must be a mixture of the displacement rates for each target element.

$$R_{D,\text{total}} = \sum_i n_i R_{D,i} \tag{5.3}$$

where the index, i, runs over each element in the compound and n_i is the atom fraction of element i.

The flux spectrum is, of course, specific to the irradiation environment and the energy transfer cross sections can either be prepared from nuclear data libraries or derived assuming some appropriate potential (e.g. hard sphere

scattering for low energy neutrons). It remains to determine ν. This value depends on the process in which the PKA's energy is dissipated through both electronic and nuclear stopping. The nuclear stopping process amounts to the formation of a damage cascade(s). Thus the number of displacements created by the PKA is related to the amount of energy it loses through nuclear stopping. This quantity is called the damage energy. Although the processes involved are quite complex, some approximate expressions for ν exist. One of the best known examples is the Norgett Robinson and Torrens (NRT) standard.[82]

$$\nu(T) = \frac{0.8\xi(T)T}{2E_d} \tag{5.4}$$

where E_d is the displacement energy and ξ is a numerical approximation to the Lindhard partition function written in universal units. The Lindhard partition function describes the fraction of recoil energy consumed in the creation of displacements.

$$\xi(T) = \int_0^T dE \frac{S_n(E)}{S_n(E) + S_e(E)} \tag{5.5}$$

S_n and S_e are the stopping powers corresponding to nuclear and electronic processes, respectively.

Although the NRT standard is ubiquitous in many transport and data library codes because it can be calculated relatively easily, it has a few shortcomings. Firstly, the relative number of displacements can vary from element

to element. That variation might even depend on the PKA element and energy. Secondly, the NRT standard says nothing about the spatial configuration of displacements around a PKA trajectory. Cascade size, cascade shape, and the separation between terminal sub-cascades all have ramifications on the recombination efficiency and clustering rates. Having some knowledge of the spatial distribution is helpful in gaining insight into the defect evolution. Thirdly, there are cases where it has been shown to yield inaccurate results. The discrepancies are often due to phenomena not accounted for in the standard such as energy dissipation through focusing and channeling, replacement collisions etc.

Therefore a different strategy in calculating the displacement rate is to bypass the displacement cross section and instead calculate the primary recoil spectrum. The production rate of PKAs of element i with recoil energy T is given by

$$R_{d,i}(T) = \int dE \phi(E) \sigma_i(E, T) \tag{5.6}$$

The total displacement rate for each element is then simply

$$R_{D,j} = \sum_i \int dT R_{d,i}(T) \nu_{i \to j}(T) \tag{5.7}$$

where $\nu_{i \to j}(T)$ is the number of displaced atoms of element j due to a PKA of energy T and element i. One can then randomly draw PKAs from the primary recoil spectrum, use them to initiate damage cascade simulations and analyze the results to determine the displacement rates for each element.

5.3 Calculation of the Energy Transfer Cross Sections

In order to evaluate equation 5.6, one needs the neutron flux spectrum which was already discussed in chapter 3 and the energy transfer cross sections. The energy transfer cross sections were obtained from the Evaluated Nuclear Data Library VII (ENDF-VII)[83] neutron-nuclear data libraries and processed using the nuclear data processing code NJOY99.[84] NJOY99 takes the raw nuclear data files, available for each nuclide, and performs a variety of routines to extract the desired data in this case, group-to-group energy transfer cross sections.

The cross sections prepared were reconstructed at 300K with Doppler broadening. All sections (mt numbers) were evaluated for mf file 26. File 26 corresponds to a matrix of neutron group to residual nucleus group cross sections (i.e. the energy transfer cross section). The sand-ii 620 group structure was selected as it had a fine enough energy resolution to capture all spectral details, it's a stardard group structure in a number of nuclear data codes, and its provided as a preset group structure within NJOY99.

Group cross sections were prepared for each stable isotope of the four elements in PZT (Pb, Zr, Ti and O). A parser program written in C++ was used to convert the NJOY99 output files into a matrix format suitable for subsequent numeric integration with the neutron flux. An example of a few of the energy transfer cross sections are shown in figure 5.1. Note that the elastic cross section resembles that of hard sphere scattering except at high energies. Many of the threshold reactions are small in comparison with elastic

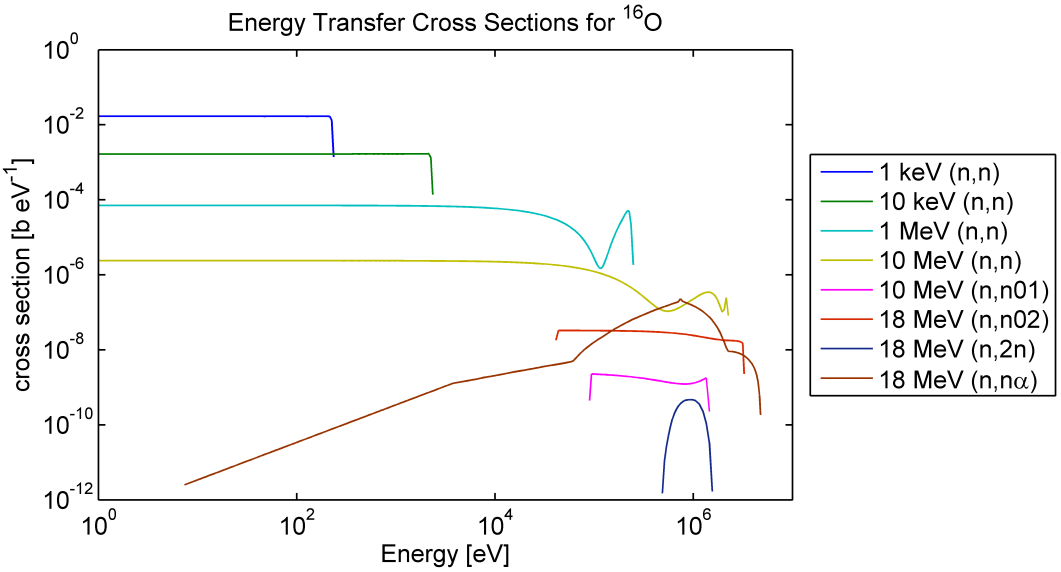

Figure 5.1: Various energy transfer cross sections for ^{16}O including elastic scattering at different neutron energies, inelastic scattering, and threshold absorption reactions.

scattering but are, however, capable of yielding PKAs with recoils in excess of 1 MeV.

5.4 Determination of the Primary Recoil Spectrum

In order to have a neutron flux with a group structure compatible with the energy transfer cross sections for numerical integration, the flux was re-tallied in MCNPX with the 620 sand-ii energy bins rather than the group structure of the Si damage function. The numerical integration was performed with the help of a Matlab script. In essence it calculated the following quantities

$$R_{d,k}(T) = \sum_{i=1}^{620} \phi(E_i)\sigma_k(E_i, T_j) \tag{5.8}$$

where the k index indicates the element and i and j are indices for the neutron and PKA energy groups, respectively.

The residuals in the primary recoil spectrum are actually more diverse than just the isotopes of the four elements in PZT. The threshold absorption reactions such as $(n, n\alpha)$, (n, p), etc. produce secondary charged particles as well as PKAs of different nuclides to those initially present in the material. Rather than attempt to account for every heavy recoiling particle in the damage simulations, all recoils from the same target were treated as identical to the target. Thus, for example, ^{206}Tl PKAs produced in the $^{206}\mathrm{Pb}(n,p)^{206}\mathrm{Tl}$ reaction were added to the primary recoil spectrum of ^{206}Pb. The reason for doing this was that 1) the amount of threshold reactions is typically much lower than scattering events so, in a Monte Carlo simulation where events are drawn from the recoil distribution, the threshold reaction products wouldn't occur frequently enough to provide statistically meaningful information 2) the masses of the products are usually not far away from the target atom's. Provided the product's recoil energy is accounted for, the small mass differences will not greatly impact the displacement production rates.The resulting primary recoil spectrum is shown in figure 5.2.

Note that most PKAs above 1eV have energies between 100 eV and 100 keV with very few reaching as high as 1 MeV. In fact the greatest numbers

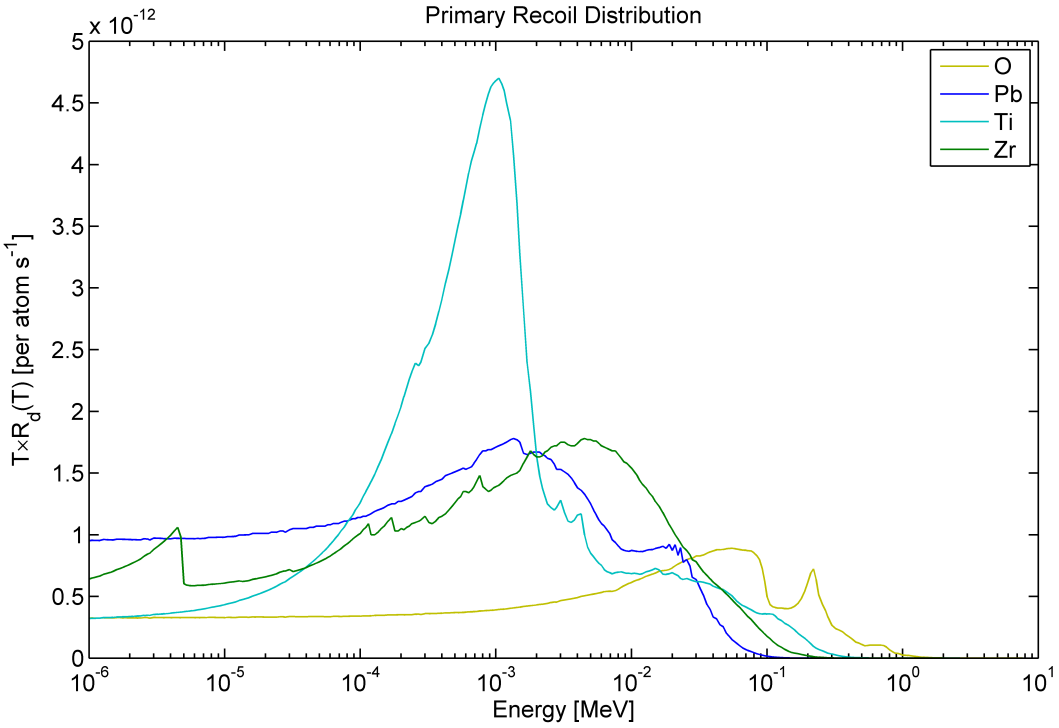

Figure 5.2: The primary recoil spectrum for the four target elements within the PZT samples.

of recoils actually occur at lower energies (meV range) than those displayed in the graph. These are due to thermal neutron scattering. However, recoils with energies lower than the threshold displacement energy on the order of tens of eV only contribute to phonon excitations. Thus, from the perspective of damage cascades, that portion of the primary recoil spectrum is ignored.

5.5 Damage Cascade Simulations

The damage cascades were simulated using the Stopping and Range of Ions in Matter (SRIM) code.[85] SRIM operates under the binary collision approximation (BCA). The BCA assumes that all interatomic collisions are binary, meaning each atom may only interact with one other at a time. The advantage of this assumption is that it reduces the computational effort considerably. Simulations of full damage cascades take only a matter of seconds permitting the tallying of many histories. Its most significant disadvantage, however, is that it is only a realistic assumption during the early stages of cascade development (up to a few ps). SRIM therefore will predict the damage cascades up to the point where the number of displacements peaks. The ensuing cascade quench involves brute force solutions to the multi-body dynamics that only molecular dynamics codes can provide.

For PKAs created through neutron interactions, SRIM relies on an input deck with starting positions, energies, directions and elements for each of the PKAs in the simulation. To generate this simulation, a C++ program was written to draw from the primary recoil spectrum in a Monte Carlo fashion.

The program used a simple rejection sampling algorithm. A random integer was generated to select from the recoil spectrum energy groups above 10 eV. Another random number was selected between zero and a maximum value (set as the maximum peak in the recoil spectrum). If it fell above the group spectrum value at the selected energy group it was rejected. Otherwise, an energy was drawn from the energy group bounds. In this fashion, a sample of initial PKA conditions was generated, which matched the primary recoil spectrum calculated earlier. The position of the PKAs were uniformly distributed in a 3500×3500×3500 $\mathring{A}$ box. 3500 $\mathring{A}$ signifies the approximate thickness of the experimental samples used in the characterization studies. Realistic loss of displacements from PKAs leaving the PZT layer is incorporated in this manner. The direction of the PKAs was spherically sampled. The assumption of isotropic PKA direction is perhaps slightly erroneous. At the position of the sample vials within the TRIGA core, fast neutrons are neither isotropic nor completely monodirectional. More fast neutrons tend to come from the direction of the fuel assembly than from the reflector. That being said, convolution of the scattering angle with the neutron direction and the fact that most neutron damage cascades are roughly isotropic in shape suggests that there is defect texting due to the reactor flux shape is not an important enough effect to worry about.

SRIM will only simulate one type of PKA at a time so separate sets of damage cascade histories for each of the four elements were created. Important parameters for the simulations are the displacement energies. These

Table 5.1: Displacements per ion as calculated with SRIM.

	Displacements per ion			
PKA	Pb	Zr	Ti	O
Pb	5.4	3.0	2.5	16.2
Zr	8.0	4.6	4.1	27.7
Ti	6.4	3.7	3.3	22.6
O	14.5	8.3	7.1	48.0

values are related to the binding forces of the atom within its crystal structure and the ballistic trajectory of the PKA past repulsive barrier atoms. Calculating the displacement energy is non-trivial. Typically *ab initio* methods are needed and careful energy and angular sampling is required. Experimental techniques involving electron irradiations have also been employed to measure displacement energy thresholds. Since both routes were outside the schedule, experimental capabilities and scope of this work, values of the displacement energies were estimated from the literature. Experimental and computational work on radiation damage in the perovskites, $SrTiO_3$ and $CaTiO_3$, reveal displacement energies of roughly 70 eV for the cations and 50 eV for the O anions.[86,87] Based on the reasonable similarities between the values between these two materials and the chemical and structural similarities between these materials and PZT, the values in the literature were deemed appropriate first order estimates. Average displacement values were obtained from the damage output files. Table 5.1 shows these values broken up by PKA element and number of displaced atoms of each type.

The integrated recoil spectrum was then summed and convolved with

Table 5.2: Displacements per atom by element.

Element	dpa s^{-1}
Pb	7.1E-11
Zr	4.0E-11
Ti	3.5E-11
O	2.3E-10
Total	3.8E-10

the displacements per ion values to yield the dpa rates. These values are included in table 5.2. According to these values, the maximum dose the samples experienced (the 2 hr irradiation) was 2.7×10^{-6} dpa. This is small compared to the dpa values normally encountered when discussing phenomena such as swelling and embrittlement of reactor core materials. Nevertheless, the electronic behavior of the PZT films is shown to drift significantly at these doses, indicating a high sensitivity of the ferroelectric properties to neutron damage compared with mechanical irradiation effects.

The spatial character of the damage cascades can be gleaned from SRIM's graphic output of the damage cascades projected into one of the planes of the simulation volume. Examples are seen in figures 5.3, 5.4, 5.5 and 5.6. Each of these figures displays the results of only a few histories - far fewer than are actually used to generate the damage tallies. These results show that Pb and Zr PKAs are more likely to generate single, large-volume cascades while Ti and O are more likely to have smaller sub-clusters along the PKA trajectory. The O PKAs have the sparsest sub-cascade structure.

The relative number of each type of displacement roughly matches the

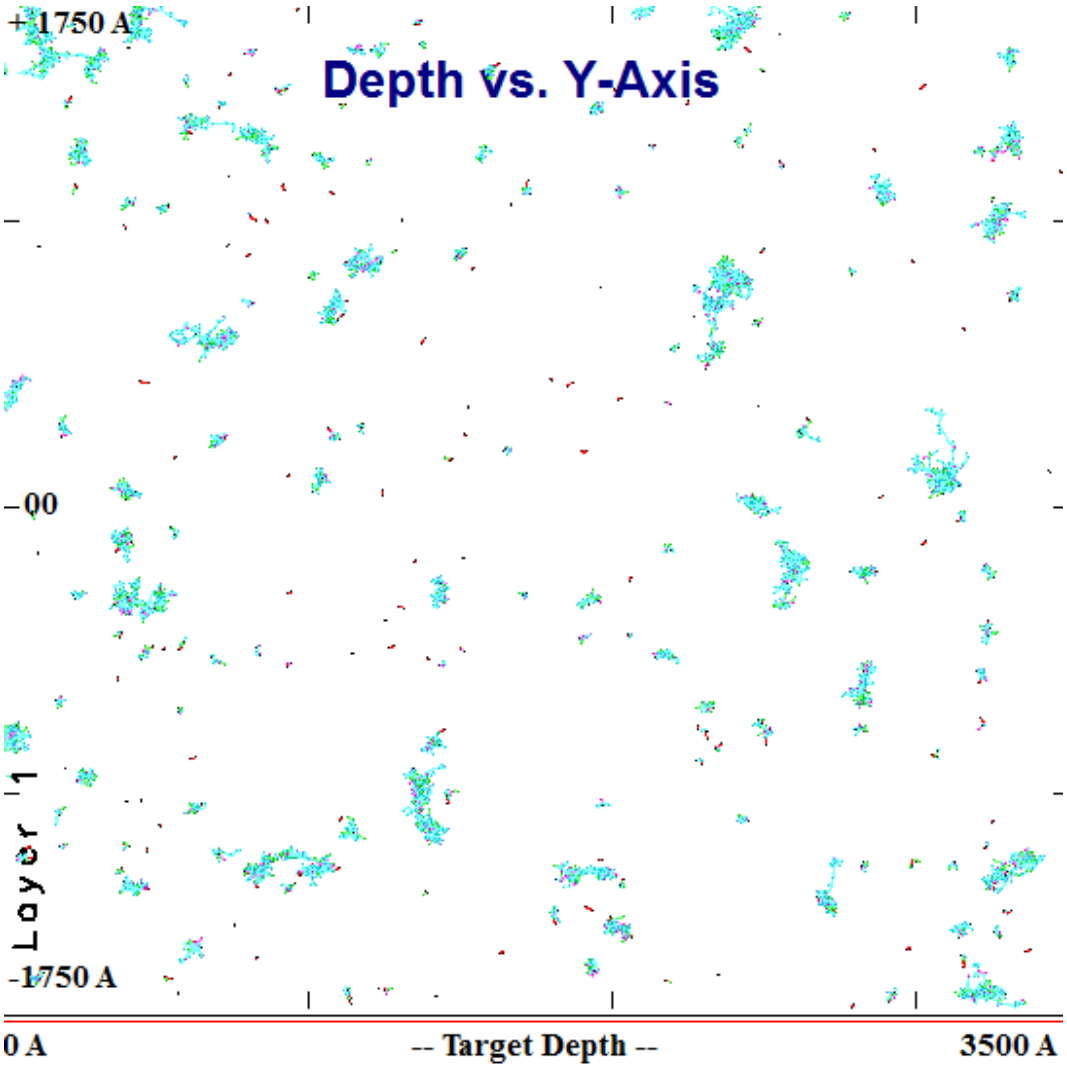

Figure 5.3: Damage cascades from Pb PKAs in a 350 nm PZT film

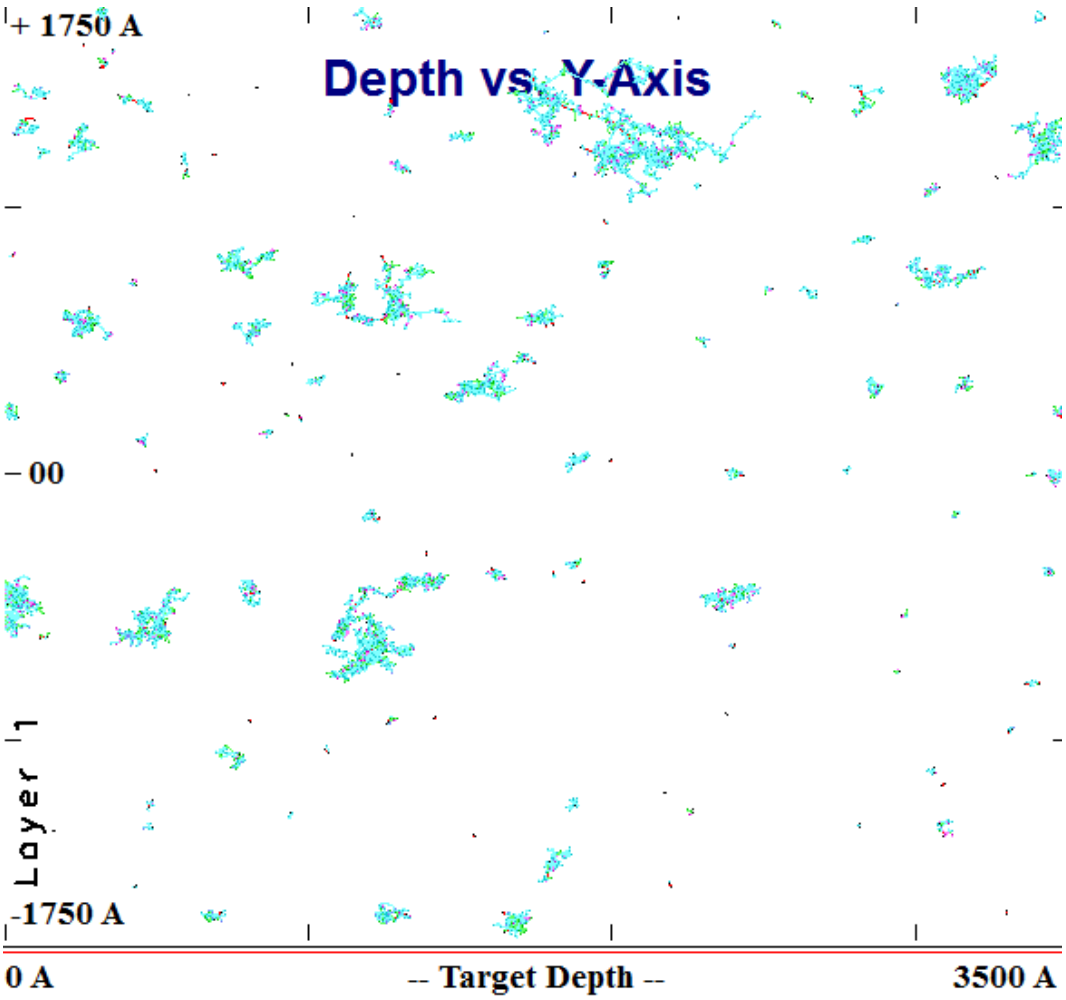

Figure 5.4: Damage cascades from Zr PKAs in a 350 nm PZT film

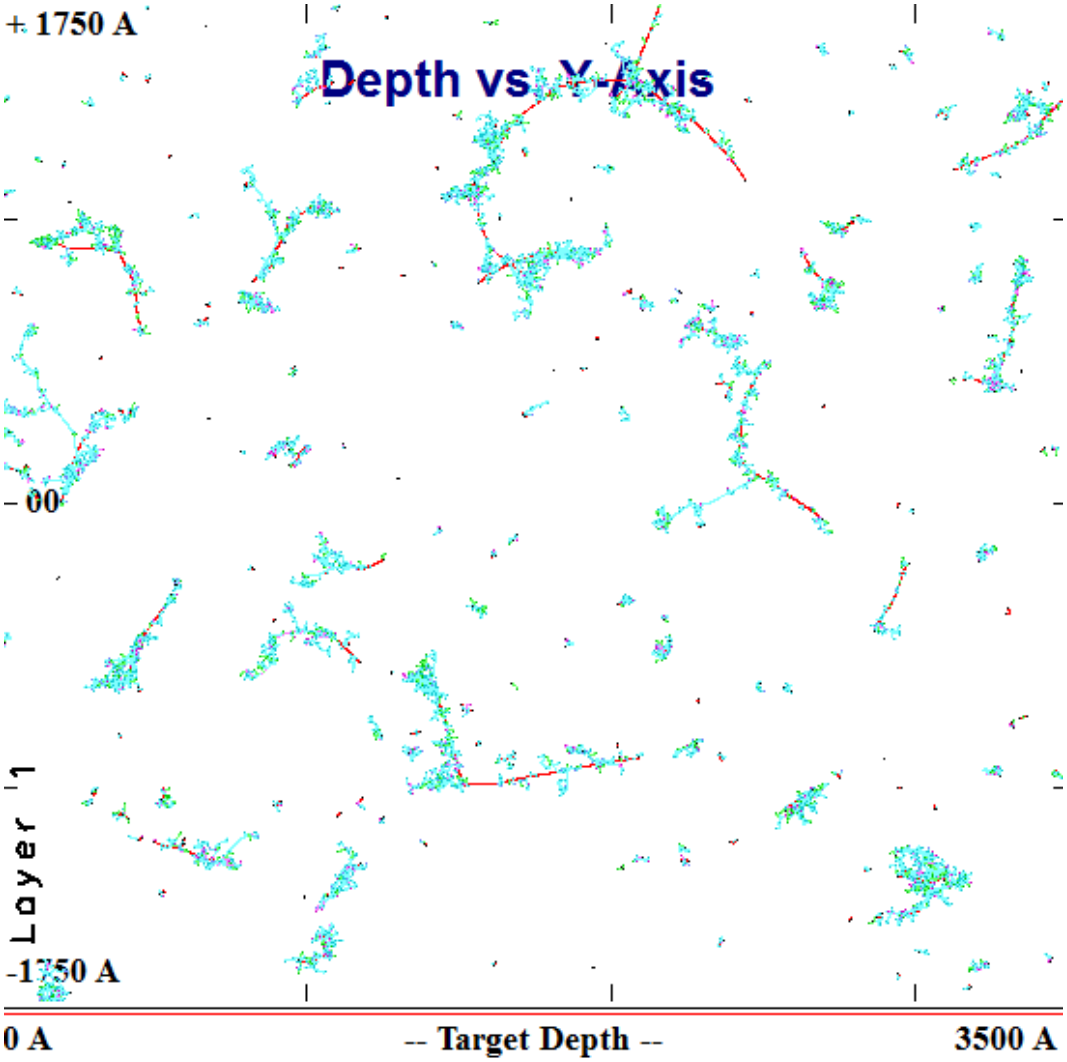

Figure 5.5: Damage cascades from Ti PKAs in a 350 nm PZT film

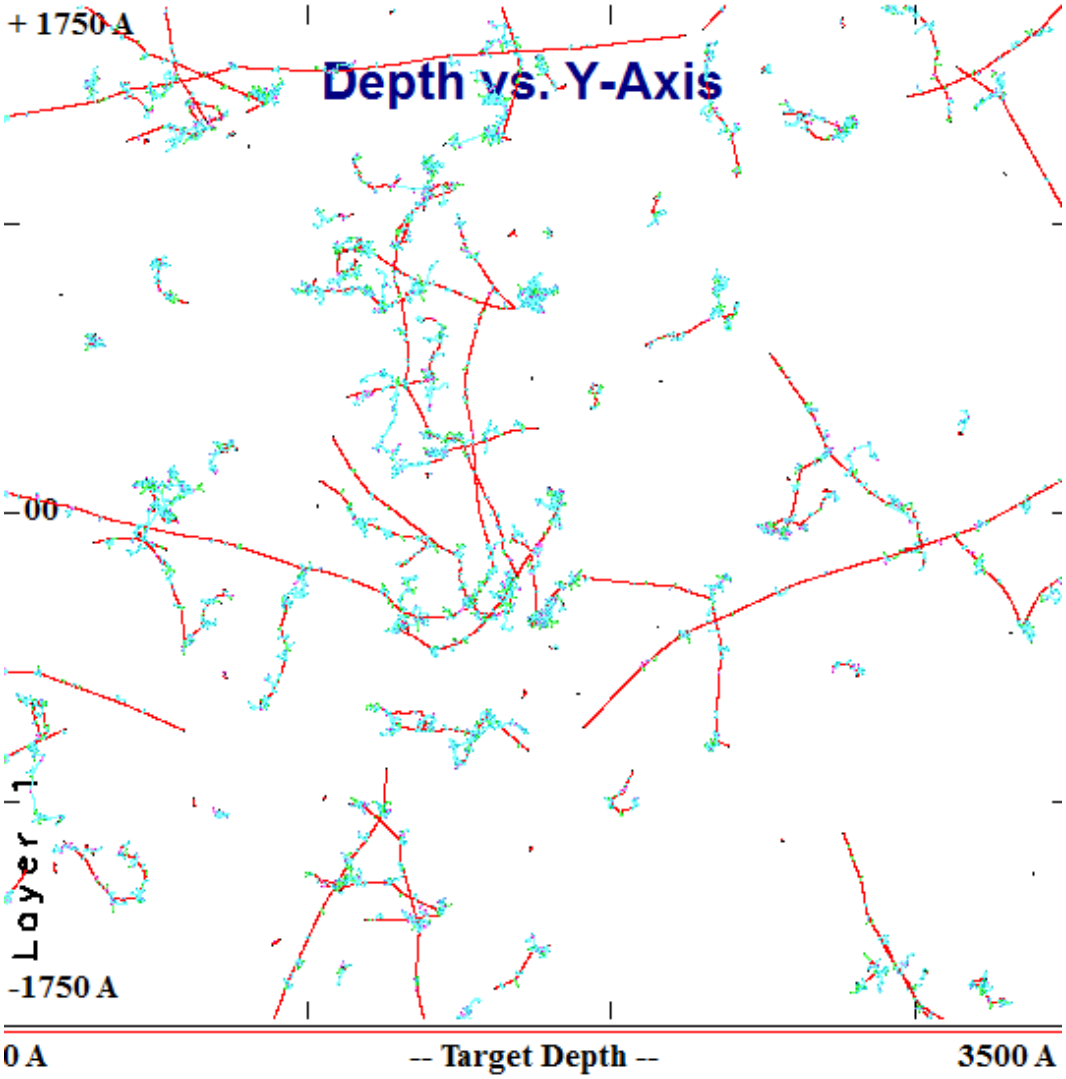

Figure 5.6: Damage cascades from O PKAs in a 350 nm PZT film

atom fractions of each element. This indicates that the damage energy is consumed in approximately equal amounts by all sub-lattices. Stark differences between the defect distributions between clusters are therefore not likely to occur. Interestingly there is a slight difference between the production rates of Pb and O displacement and the stoichiometry with Pb displacements being slightly below the expected 20% of the total dpa and O being slightly above the expected 60%. If these results reflect reality it would represent a source bias. For cooperative defect reactions involving two different point defect species, such a source bias can have ramifications for defect evolution. For example, the accumulation of any defect complex incorporating both a Pb and O vacancy would necessarily compete with O recombination and enhance the O interstitial concentration. Extensive rate theory studies will be needed to ascertain what consequences this discrepancy has on defect evolution.

As mentioned before, it is not possible to quantitatively predict the outcome of the cascade quench using the BCA. However, some order-of-magnitude inferences can be made based on facts about the cascade quench. It is known that a large number of displacements produced recombine in-cascade.[88] The survival fraction of free point defects is typically be on the order of a few percent to perhaps 10% for certain ceramics, which have higher survival fractions than metals and semiconductors.[13] Assuming such values, a calculation of the number of surviving point defects within a $100 \times 100 \times 100$ nm volume, based on the SRIM derived dpa values, is only expected to be on the order of 1 to 10 for the samples irradiated to the highest fluence (about 1 in 10^8 or 10^7 atoms).

Point defects, being mobile, tend to diffuse in the crystal until they find another point defect, impurity or sink to bind to. Thus the free point defect concentration will continue to decrease during the evolution phase. In doping studies, which proponents of the oxygen vacancy mechanism of radiation degradation cite, dopant concentrations of at least a few tenths of a percent are necessary to see measureable changes in ferroelectric properties; far more than the concentrations of point defects induced by damage cascades.[89–91] It therefore seems unlikely that the observed ferroelectric changes in the characterized films are solely due to vacancies.

High energy cascades on the other hand will generally introduce defect clusters. In fact in-cascade clustering generally dominates the survival fraction with about 20-50% of the surviving point defects residing in clusters.[92,93] The number of defects within the clusters exhibits a distribution with di-vacancies/intersitials being the most common followed by tri-vacancies/intersititals, etc.[94] The tail of the distribution depends on the cascade energy with higher energy cascades being more likely to produce large clusters of tens of defects in size. A conservative estimate of the density of clusters within the irradiated PZT samples can be calculated assuming PKAs with energies in excess of 10 keV will produce one defect cluster on average. This is a conservative estimate both because cascades as small as 1 keV could be expected to generate clusters and because large cascades can generate multiple clusters.

The integral production rate of primary recoils above 10 keV is 6.8×10^{-12}. The corresponding number of clusters per $100 \times 100 \times 100$ nm is 3.8

after 2 hrs irradiation. If we extend the cascade energy down to 1 keV, the number of clusters becomes 10.6. Thus, based on these order-of-magnitude arguments it is expected that the concentration of clusters is comparable if not greater than that of the point defects. Of the two classes of defects, the clusters would be expected to have a greater influence on domain wall motion and polarizability because they are larger more extended objects and therefore more capable of disrupting long range polarization order.

This is given as the reasoning for a hypothesis that point defect clusters can actually dominate the ferroelectric response. Further work will be needed to test it. Firstly, one must demonstrate that they exert significantly greater forces on domain walls and/or they reduce the polarizability. More quantitatively exact estimates of the defect concentrations via MD, KMC and other modeling methodologies are also desired to show that clusters are produced in concentrations at least at high as those of the various point defects. Finally, one needs to determine the link between defect clusters and defect dipoles (DDs). As mentioned in chapter 2, oxygen vacancy acceptor impurities have been widely cited as important defect complexes for the ferroelectric properties of PZT. The question posed here is, do higher order defect clusters such as those produced in damage cascades have a strong electric dipole field? Along similar lines, do defect clusters behave like DDs? Answering these questions is a substantial task. It requires first characterizing the structure of each type of cluster and then calculating the displacement of the electric field due to the cluster. It does appear that, as far as studying neutron irradiation effects

in PZT is concerned, examining the role of clusters on ferroelectric properties merits further study.

Finally, some attention must be paid to the role of pre-irradiation microstructure on the formation and interactions of defects generated in the cascades as there is strong evidence from the hysteresis and Rayleigh measurements that the fluorite rich films degrade faster. The formation of immobile defect clusters away from pre-irradiation defects would not be expected to differ much between films unless strain field or space charge effects help govern the formation of such clusters. In can be stated, however, that cascades forming nearby or overlapping with microstructural features yield a different set of immobile defects. In the thin film samples where the fraction of cascades occurring near grain boundaries and interfaces is large, it is not hard to see how of immobile defects produced near or on the fluorite-perovskite interface could be different in character to those produced, for example, within a grain. Mobile point defects and clusters on the other hand can diffuse to such microstructural features easily and are therefore very much influenced by qualities of the material. A full understanding of the role of pre-irradiation microstructure (especially the surface fluorite layer or at least what defects it is symptomatic of) on the stages of cascade formation and defect evolution will require extensive numerical modeling work.

Chapter 6

Conclusions and Future Work

6.1 Conclusions

Neutron radiation effects on the ferroelectric material lead zirconate titantate (PZT) were studied to reveal mechanisms by which PZT based devices degrade in neutron environments. Thin film PZT capacitors were prepared using wet chemical techniques. The samples differed in initial film quality with one film exhibiting superior electronic characteristics and a more perfect microstructure while the other had poor electronic characteristics and a significant concentration of non-ferroelectric surface fluorite. The films were irradiated in the core of the 1 MW TRIGA MARK II research reactor at the University of Texas at Austin to expose them to different levels of damage. Subsequent electronic characterization was performed at Sandia National Laboratories to ascertain if any dose-property trends could be seen in the samples.

Measurements of hysteresis curves revealed a difference in the amount of damage accumulation between the two films with the superior films failing to show statistically significant signs of loss in macroscopic polarization or loop distortion. In contrast, the poorer films exhibited a loss in both absolute remanent polarization as well as remanent polarization relative to the saturation

polarization indicating loss of polarizability revealing anti-domain nucleation above the coercive field, enhanced relaxation, leakage or any combination of the above. The films were nominally equivalent in composition and processing. That said, there were differences in the pre-irradiation microstructure. It is proposed that these differences are at least partially responsible for the discrepancy between damage accumulation rates.

First Order Reversal Curves (FORC) were measured to determine the hysteron distributions for the irradiated samples. Results indicated increased spreading and attenuation of the irreversible hysteron peak with increasing fluence. This is taken as evidence that radiation induced defect structures magnify the random free energy landscape of the material, inducing shifts in local switching fields. Additionally, the formation of a double peak in the irreversible portion of the hysteron density function was observed. The double peak can be explained in terms of dipolar defect structures that are effectively frozen on timescales of the measurement. Examination of the reversible hysterons showed an increase in extrinsic effects especially in the poorer quality films and little to no change in intrinsic reversible contributions.

Small signal permittivity measurements were performed to determine the change in linear (initial permittivity) and first order non-linear component (Rayleigh parameter) with dose. Both the initial permittivity and the Rayleigh parameter decreased with fluence. Taken together with the behavior of the reversible hysteron density in the FORC analysis, these results indicate an increase in the extrinsic irreversible contribution to domain wall motion.

Physically this implies that domain walls are dragged across a rougher pinning field in the irradiated PZT. Thus at least some of the radiation induced defects act as pinning sites for domain walls. As with the hysteresis measurements, the damage accumulation rate was larger for the poorer quality film further adding to the evidence that poorer pre-irradiation microstructure is more susceptible to damage. Simulations of the radiation damage cascades were performed using the binary collision approximation (BCA) code SRIM. First, energy transfer cross sections for nuclides in PZT were prepared from the ENDF-VII nuclear data libraries and the data library processing code NJOY99. Next, 620 group neutron fluxes were generated via the radiation transport code MCNPX and adjusted to reflect measured values of the thermal and epithermal flux at the position in the reactor core where the samples were located during irradiation. Then, the group fluxes were combined with the energy transfer cross sections to create SRIM input files with primary knock-on atom sources obeying the primary recoil spectrum. Results of the SRIM simulations were used to determine the displacement rates and accumulated displacements per atom (dpa) in the PZT films. Comparison, of the displacement rates and primary recoil spectrum with typical values of defect survival rates found in the literature suggest that both free point defect and defect clusters are present only in small concentrations, even up to the highest irradiation dose. Furthermore, there is no indication that the concentration of free defects should be much larger than that of the defect clusters. In fact, based on a conservative estimate, defect clusters are expected to be the

dominant defect species. It is therefore proposed that defect clusters play a much more prominent role in domain wall pinning and loss of polarizability than previously considered. Further work will be need to both investigate the dipolar nature of such defect clusters to establish the connection, if any, between radiation induced clusters and the hysteron peak splitting seen in the analysis of the FORC curves. Additionally, the interaction of point defects and defect clusters with the pre-irradiation microstructure during and immediately following the damage cascade is deemed an important area for further research.

6.2 Future Work

6.2.1 Experimental Work

The hypothesis that defect clusters play a central role in the loss of domain wall mobility and domain switching requires validation/falsification. Further experimental work could be done to help identify the types and concentrations of defects produced from in-cascade clustering. A list of techniques which have been used in other materials to characterize specific clusters (especially lower order clusters such as di-vacancies/interstitials and complexes) are shown below.

- Positron annihilation spectroscopy (PAS)
- Rutherford backscattering spectrometry
- Photoluminescence spectroscopy

- Electron paramagnetic resonance spectroscopy (EPR)
- Transmission electron microscopy (TEM)

Each of these measurements is capable of detecting spectral features associated with defects. Combined with appropriate assumptions or numerical models, particular peaks might be identified with cluster defects. The last technique, EPR, has an additional advantage in that it is sensitive to dipolar defects. Thus it is conceivable that one would be able to investigate the relationships between defect dipoles, clusters and domain wall pinning. EPR can be used to confirm or refute the evidence presented in this work that defect dipoles are introduced PZT upon irradiation.

Based on our knowledge of clustering mechanisms in the damage cascade, it is expected that most clusters will be of low order (di-,tri-,tetra- defects). It is unclear if it is possible to use microscopic techniques such as transmission electron microscopy (TEM) to detect such clusters directly. However, some of the more energetic cascades are capable of producing large clusters and/or regions with a high density of small clusters. Such, high-damage regions might show reasonable levels of contrast to facilitate characterization. Combined TEM/spectroscopic techniques might be another avenue for investigating the concentration of small clusters. The fine structure details of the plasmon peak and core-loss edges within an electron energy loss spectroscopy (EELS) spectrum are particularly sensitive to perturbations in the local electron density around atoms. A sensitivity analysis of the fine structure features

due to point defects and defect clusters should be carried out through a combination of experiment and numerical modeling to ascertain whether or not such an analysis is even feasible. Finally, in the interest of more accurately simulating damage cascades (whether through BCA or MD), accurate displacement energies should be known. These values can be predicted using *ab initio* calculations or measured directly through electron irradiation experiments.

6.2.2 Modeling

There is an almost limitless amount of work that could be done with regard to modeling the radiation damage event, damage evolution, and the relationship between defects and ferroelectric properties. At the fundamental level one is interested in determining interatomic potentials, displacement energies, and the energies of formation for various stable defects. These pieces of data can be generated through *ab initio* calculations using, for example, local density approximation density functional theory (LDADFT).

Although, it is a computationally expensive technique the most accurate damage cascade simulations are obtained through molecular dynamics (MD) simulations. Therefore, revisiting the damage cascade simulations with MD is desired. More important than accuracy, however, MD enables one to determine the total survival fractions, the free point defect fraction, clustered defect fraction, and cluster morphology following the cascade quench. Such pieces of information would replace some of the order-of-magnitude arguments made about the concentration of clusters in the irradiated material with more

rigorously obtained values. These values - along with others gathered through MD simulations such as sink strengths, emission rates and diffusion coefficients - are necessary ingredients in subsequent kinetic Monte Carlo (KMC) or rate theory calculations.

KMC and rate theory are used to study the defect evolution out to time scales where the post-irradiation microstructure can be said to be at equilibrium. At this point, results of the modeling can be corroborated with a number of experimental measurements through the use of mesoscale models. For example, phase field theory is a technique that can be used to simulate the effects of pinning fields on domain wall motion. Knowledge about the annealed defect microstructure could be used to construct accurate pinning fields and test the effect of said pinning fields on properties such as the relative permittivity or the hysteron distribution. Thus the phase field methodology is a promising route for further translating the series of damage models into predictions that might be directly compared with some of the electronic characterization measurements presented in this work.

Appendices

Appendix A

Codes for Analyzing FORC Data

A.1 RAW2VP.exe

This C++ helper program was used to parse the raw data files aquired from the reversal field sweeps.

```
/* This program is used to prepare the raw V-P data from Vision in
a simple two column format which can easily be graphed. Note that
the output format excludes information such as remenant polarization
and coercive fields and includes all ascending and descending branches
in the order that they were measured.*/
#include <iostream>
#include <fstream>
#include <string>
using namespace std;
int main()
{
int i;
int N=200; // N is the total number of execution counts
for (i=1;i<=N;i++){
string line;
for (int j=1; j<=34; j++){ // Skip the first 34 lines of header info
getline(cin,line);
}
int points;
cin >> line; // read in the label "points:"
cin >> points; // store the number of points
for (int j=1; j<=5; j++){ // skip more header lines
getline(cin,line);
}
float temp, V, P; // V=voltage, P=polarization
for (int j=1; j<=points; j++){ // read in the V and P for the number of points measured
cin >> temp; // ignore the point number and time stamp
cin >> temp;
cin >> temp; // store V and P
V=temp;
cin >> temp;
P=temp;
printf("%2.4f %1.4f \n",V,P); //print V and P to std out
getline(cin,line); // discard the remaining whitespace
}
for (int j=1; j<=12; j++){ //skip the footer lines
getline(cin,line);
}
}
```

A.2 VP2F.exe

This C++ helper program was used to convert raw voltage-polarization data into an Everette function

```
#include <iostream>
#include <fstream>
#include <string>
using namespace std;
int main(){
float V_1, V_2, V_3, P_1, P_2, P_3;
float alpha, beta, P_alpha, P_beta, F;
string line;
cin >> V_1;
cin >> P_1;
cin >> V_2;
cin >> P_2;
cin >> V_3;
cin >> P_3;
int i;
for(i=1;i<=10000000;i++){
if((V_3<V_2)&&(V_2>V_1)){
alpha=V_2;
P_alpha=P_2;
printf("%2.4f %2.4f %1.4E \n",alpha,alpha,0.0);
}
if(V_3<V_2){
beta=V_3;
P_beta=P_3;
F=(P_alpha-P_beta)/2;
printf("%2.4f %2.4f %1.4E \n",alpha,beta,F);
}
V_1=V_2;
P_1=P_2;
V_2=V_3;
P_2=P_3;
cin >> V_3;
cin >> P_3;
}
```

A.3 FORC.m

This OCTAVE file is used both to perform the forward differencing on the Everette function and also to display the hysteron density functions graphically.

```
close all
clear all
graphics_toolkit ("gnuplot")
lin=linspace(1.0,0,100).^1;
map=[lin',lin',lin'];
colormap(map);

path1='C:\Users\Joseph\Desktop\FORC\Preisach';
path2=['<CONTROL>';'<DOSE1>';'<DOSE2>';'<DOSE3>'];
path3='.txt';
```

```
for i=1:4
fullpath=strcat(path1,path2(i,:),path3);
fid=fopen(fullpath);
data=dlmread(fid);
xx=data(1:39,:)*10/.320;
yy=data(40:78,:)*10/.320;
zz=data(79:117,:)*0.7;
fclose(fid);
s=sum(sum(zz))*(5/.320)^2
j=i;
if i>2
j++;
end
j
%subplot(2,3,j)
switch i
case 1
axes();
%set(gca,'ActivePositionProperty','position');
set(gca,'Position',[0.1 0.5 0.4 0.4]);
case 2
axes('Position',[0.4 0.5 0.4 0.4]);
get(gca,'Position')
case 3
axes('Position',[0.1 0.1 0.4 0.4]);
get(gca,'Position')
case 4
axes('Position',[0.4 0.1 0.4 0.4]);
get(gca,'Position')
end
v=linspace(0,0.005,25);
[C,h1]=contourf(xx,yy,zz,v);
%set(h1,'EdgeColor','none');
set(h1,'LineWidth',0.1);
h2 = gca;
set(h2,'PlotBoxAspectRatio',[1 1 1],'FontName','Helvetica')
caxis([0 0.005]);
xlim([-250 250]);
ylim([-250 250]);

%% Option with labels on all axes
% switch i
% case 1
% xlabel({'\alpha (kV {cm}^{-1})';' ';'(a)'},'FontName','Helvetica');
% ylabel('\beta (kV {cm}^{-1})','FontName','Helvetica');
% case 2
% xlabel({'\alpha (kV {cm}^{-1})';' ';'(b)'},'FontName','Helvetica');
% case 3
% xlabel({'\alpha (kV {cm}^{-1})';' ';'(c)'},'FontName','Helvetica');
% ylabel('\beta (kV {cm}^{-1})','FontName','Helvetica');
% case 4
% xlabel({'\alpha (kV {cm}^{-1})';' ';'(d)'},'FontName','Helvetica');
% end

% Option with labels only on left and bottom sides
switch i
case 1
ylabel('\beta (kV {cm}^{-1})','FontName','Helvetica','FontSize',14);
text(-250,225,'(a)','FontName','Helvetica','FontSize',18,'Color',[0 0 0]);
set(gca,'XTickLabel','','FontSize',14);

case 2
text(-250,225,'(b)','FontName','Helvetica','FontSize',18,'Color',[0 0 0]);
set(gca,'YTickLabel','','XTickLabel','');

case 3
xlabel({'\alpha (kV {cm}^{-1})'},'FontName','Helvetica','FontSize',14);
ylabel('\beta (kV {cm}^{-1})','FontName','Helvetica','FontSize',14);
text(-250,225,'(c)','FontName','Helvetica','FontSize',18,'Color',[0 0 0]);
set(gca,'FontSize',14);

case 4
xlabel({'\alpha (kV {cm}^{-1})'},'FontName','Helvetica','FontSize',14);
text(-250,225,'(d)','FontName','Helvetica','FontSize',18,'Color',[0 0 0]);
set(gca,'YTickLabel','','FontSize',14);
end
```

```
end

% subplot(2,3,[3 6]);
axes('Position',[0.8 0.25 0.1 0.5])
set(gca,'Visible','off');
caxis([0 0.005]);
h=colorbar('FontSize',14,'FontName','Helvetica','location','west');
title(h,'\mu C {kV}^{-2}','Fontsize',14);
set(gcf,'PaperUnits','inches');
print -depsc C:\Users\Joseph\Desktop\Irradiation\epsfiles\<SAMPLE> FORC.eps;
```

Appendix B

Codes for Preparing Primary Recoil Spectrum

B.1 NJOY99 Template

The primary recoil spectrum (termed residual production by NJOY99 conventions) was prepared using the following template for the NJOY99 input deck. "MAT" is replaced with the ENDF-VII ID numbers for each of the stable isotopes of Pb, Zr, Ti and O.

```
moder
 20 -21
 reconr
 -21 -22
 'Recoil Template'
 MAT/
 .005/
 0/
 broadr
 -21 -22 -23
 MAT 1/
 .005/
 300
 0/
 unresr
 -21 -23 -24
 MAT 1 1 1
 300
 1e10
 0/
 groupr
 20 -24 0 -25/
 MAT 12 0 4 0 1 1/
 'Residual Production'/
 300/
 1e10/
 0.2 0.0253 1e5 2e6
 26/
 0/
 0/
 moder
 -25 28
 Stop
```

B.2 NJOY99 Output Parser

NJOY99's output format is not directly suitable for performing numerical integraton. Therefore the following C++ code was writen to parse the output files and store the residual production cross sections in group-to-group matrices.

```
#include <iostream>
#include <string>
#include <cmath>
using namespace std;
int main(){
string line;
string strfind ("for mf");
char mf[]={'0','0','0','\0'},mt[]={'0','0','0','\0'},reaction[10];
int count=0,flag=0,found,from=1,old_from=0,to=1,newreaction;

float a[]={0.0,0.0,0.0,0.0,0.0,0.0},temp;
char b[]={'+','+','+','+','+','+'};
int c[]={00,00,00,00,00,00};


while(cin.eof()!=1){
getline(cin,line);
found = line.find(strfind);
if(found!=std::string::npos){
        newreaction = 1;
  sscanf(line.c_str(),"%*7c %3c %*6c %3c %s",mf,mt,reaction);
if(mt[2]==')
         mt[2]=' ';
             cout << mf << "\t" << mt << "\t" << reaction << endl;

for(int i=1;i<=4;i++) getline(cin,line);

               count = 620;
               to = 0;

getline(cin,line);

       while(line.length()!=1){
sscanf(line.c_str(),"%d %d %f %c %d %f %c %d %f %c %d %f %c %d %f %c %d %f %c   %d",&from,&to,&a[0],&b[0],&c[0],&a[1],&b[1],
&c[1],&a[2],&b[2],&c[2],&a[3],&b[3],&c[3],&a[4],&b[4],&c[4],&a[5],&b[5],&c[5]);

 if((from!=old_from)||(newreaction==1)){
if(flag==1){
for(int i=0;i<(620-count);i++){
printf("%E\t",0.0);
}
}
count = 0;
printf("\n");
printf("%d\t",from);
old_from = from;


       for(int i=1;i<to;i++){
        printf("%E\t",0.0);
               count++;
       }
       }

       if(line.c_str()[5]!='n'){
for(int i=0;i<6;i++){
if(b[i]=='+'){
temp = a[i]*pow(10.0,c[i]);
printf("%E\t",temp);
```

```
}

if(b[i]=='-'){
temp = a[i]*pow(10.0,-c[i]);
printf("%E\t",temp);
}

a[i]=0.0;
b[i]='+';
c[i]=00;
}
count = count+6;
flag = 1;
                }

        getline(cin,line);
                newreaction = 0;
        }

             cout << endl << endl;
flag=0;
}
}
return 0;
}
```

B.3 Recoil Spectra.m

The following MATLAB script was used to numerically integrate the 620 group neutron flux in the rotary specimen rack (RSR) with the 620-by-620 group residual production cross sections produced by NJOY99.

```
flux = zeros(620,1);
fluxerror = flux;

fid = fopen('C:/Users/Joseph/Desktop/NJOY99/flux.txt');
A = textscan(fid,'%f %f');
flux = A{1,1};
fluxerror = A{1,2};
fclose(fid);

str = 'C:/Users/Joseph/Desktop/NJOY99/';
files = {
'o16.txt';
'pb204.txt';
'pb206.txt';
'pb207.txt';
'pb208.txt';
'ti46.txt';
'ti47.txt';
'ti48.txt';
'ti49.txt';
'ti50.txt';
'zr90.txt';
'zr91.txt';
'zr92.txt';
'zr93.txt';
'zr94.txt';
'zr95.txt';
'zr96.txt'};

for i=1:17

recoil = zeros(620,1);
```

```
myfile = strcat(str,'matrix/',char(files(i)))
fid = fopen(myfile)

fgetl(fid);
fgetl(fid);

while ~feof(fid)
    a = fgetl(fid);
    if isempty(a)
        a = fgetl(fid);
        a = fgetl(fid);
    else
        from = sscanf(a,'%d',1);
        to = sscanf(a,'%f',620);
        recoil(1:length(to)) = recoil(1:length(to))+flux(from)*to;
    end
end

fclose(fid);

myfile = strcat(str,'recoil/',char(files(i)))
fid = fopen(myfile,'w')
fprintf(fid,'%e \n',recoil);
fclose(fid);

end
```

Appendix C

MCNPX Deck of TRIGA Reactor

This is the MCNPX input deck of the TRIGA MARK II research reactor at the University of Texas at Austin modified to include a 620 group volumetric flux tally in the rotary specimen rack (RSR). The original code was written by Jon Braisted in 2007.[50]

```
---------- UT-TRIGA - Core Model - 07/12/2007 ----------
c
c    Coordinate origin on core axis at core midplane
c    - Experiment tubes, empty beam ports, empty RSR
c    - Central thimble fixed and flooded with no sample
c    - Core fully fuelled
c
c -------------------------------------------------------------
c             Beginning of Cell Card Specification
c -------------------------------------------------------------
c -----------
c Core region
c -----------
1099  1  -1.0  -202  +206
              -231  +232  -233  +234  -235  +236
              -241  +242  -243  +244  -245  +246
            +5000 +5001 +5002 +5003 +5004 +5005 +5006 +5007 +5008 +5009
            +5010 +5011 +5012 +5013 +5014 +5015 +5016 +5017 +5018 +5019
            +5020 +5021 +5022 +5023 +5024 +5025 +5026 +5027 +5028 +5029
            +5030 +5031 +5032 +5033 +5034 +5035 +5036 +5037 +5038 +5039
            +5040 +5041 +5042 +5043 +5044 +5045 +5046       +5048 +5049
            +5050 +5051 +5052 +5053 +5054 +5055 +5056 +5057 +5058 +5059
            +5060 +5061 +5062 +5063 +5064 +5065 +5066 +5067 +5068 +5069
            +5070 +5071 +5072             +5075 +5076 +5077 +5078 +5079
            +5080 +5081 +5082 +5083 +5084 +5085 +5086 +5087 +5088 +5089
            +5090 +5091 +5092 +5093 +5094 +5095 +5096 +5097 +5098 +5099
            +5100       +5102 +5103 +5104 +5105 +5106 +5107 +5108 +5109
            +5110       +5112 +5113 +5114             +5117       +5119
            +5120
            +1963 +1964 +1965  +1966                  $ Mapping experiment
            +1940                                     $ 3L
            +2000 +2001 +2002 +2003 +2004 +2005 +2006
c            +5118                                     $ PNT
c
 520   0   -201 +207 -1963  fill=101 (10) $         Flux mapping water cells
 521   0   -201 +207 -1964  fill=101 (11)
 522   0   -201 +207 -1965  fill=101 (12)
 523   0   -201 +207 -1966  fill=101 (13)
c
 600   0   -110 +120 -5000  fill=82 (100) $ A1 - CT
 601   0   -110 +120 -5001  fill=8  (101) $ B1
 602   0   -110 +120 -5002  fill=8  (102) $ B2
 603   0   -110 +120 -5003  fill=8  (103) $ B3
 604   0   -110 +120 -5004  fill=8  (104) $ B4
```

```
 605   0   -110 +120 -5005  fill=8  (105) $ B5
 606   0   -110 +120 -5006  fill=8  (106) $ B6
 607   0   -110 +120 -5007  fill=7  (107) $ C1 - CR(T)
 608   0   -110 +120 -5008  fill=8  (108) $ C2
 609   0   -110 +120 -5009  fill=8  (109) $ C3
 610   0   -110 +120 -5010  fill=8  (110) $ C4
 611   0   -110 +120 -5011  fill=8  (111) $ C5
 612   0   -110 +120 -5012  fill=8  (112) $ C6
 613   0   -110 +120 -5013  fill=9  (113) $ C7 - CR(R)
 614   0   -110 +120 -5014  fill=8  (114) $ C8
 615   0   -110 +120 -5015  fill=8  (115) $ C9
 616   0   -110 +120 -5016  fill=8  (116) $ C10
 617   0   -110 +120 -5017  fill=8  (117) $ C11
 618   0   -110 +120 -5018  fill=8  (118) $ C12
 619   0   -110 +120 -5019  fill=8  (119) $ D1
 620   0   -110 +120 -5020  fill=8  (120) $ D2
 621   0   -110 +120 -5021  fill=8  (121) $ D3
 622   0   -110 +120 -5022  fill=8  (122) $ D4
 623   0   -110 +120 -5023  fill=8  (123) $ D5
 624   0   -110 +120 -5024  fill=9  (124) $ D6 - CR(S1)
 625   0   -110 +120 -5025  fill=8  (125) $ D7
 626   0   -110 +120 -5026  fill=8  (126) $ D8
 627   0   -110 +120 -5027  fill=8  (127) $ D9
 628   0   -110 +120 -5028  fill=8  (128) $ D10
 629   0   -110 +120 -5029  fill=8  (129) $ D11
 630   0   -110 +120 -5030  fill=8  (130) $ D12
 631   0   -110 +120 -5031  fill=8  (131) $ D13
 632   0   -110 +120 -5032  fill=9  (132) $ D14 - CR(S2)
 633   0   -110 +120 -5033  fill=8  (133) $ D15
 634   0   -110 +120 -5034  fill=8  (134) $ D16
 635   0   -110 +120 -5035  fill=8  (135) $ D17
 636   0   -110 +120 -5036  fill=8  (136) $ D18
 637   0   -110 +120 -5037  fill=8  (137) $ E1
 638   0   -110 +120 -5038  fill=8  (138) $ E2
 639   0   -110 +120 -5039  fill=8  (139) $ E3
 640   0   -110 +120 -5040  fill=8  (140) $ E4
 641   0   -110 +120 -5041  fill=8  (141) $ E5
 642   0   -110 +120 -5042  fill=8  (142) $ E6
 643   0   -110 +120 -5043  fill=8  (143) $ E7
 644   0   -110 +120 -5044  fill=8  (144) $ E8
 645   0   -110 +120 -5045  fill=8  (145) $ E9
 646   0   -110 +120 -5046  fill=8  (146) $ E10
c 647   0   -110 +120 -5047  fill=8  (147) $ E11 - 3L
 648   0   -110 +120 -5048  fill=8  (148) $ E12
 649   0   -110 +120 -5049  fill=8  (149) $ E13
 650   0   -110 +120 -5050  fill=8  (150) $ E14
 651   0   -110 +120 -5051  fill=8  (151) $ E15
 652   0   -110 +120 -5052  fill=8  (152) $ E16
 653   0   -110 +120 -5053  fill=8  (153) $ E17
 654   0   -110 +120 -5054  fill=8  (154) $ E18
 655   0   -110 +120 -5055  fill=8  (155) $ E19
 656   0   -110 +120 -5056  fill=8  (156) $ E20
 657   0   -110 +120 -5057  fill=8  (157) $ E21
 658   0   -110 +120 -5058  fill=8  (158) $ E22
 659   0   -110 +120 -5059  fill=8  (159) $ E23
 660   0   -110 +120 -5060  fill=8  (160) $ E24
 661   0   -110 +120 -5061  fill=8  (161) $ F1
 662   0   -110 +120 -5062  fill=8  (162) $ F2
 663   0   -110 +120 -5063  fill=8  (163) $ F3
 664   0   -110 +120 -5064  fill=8  (164) $ F4
 665   0   -110 +120 -5065  fill=8  (165) $ F5
 666   0   -110 +120 -5066  fill=8  (166) $ F6
 667   0   -110 +120 -5067  fill=8  (167) $ F7
 668   0   -110 +120 -5068  fill=8  (168) $ F8
 669   0   -110 +120 -5069  fill=8  (169) $ F9
 670   0   -110 +120 -5070  fill=8  (170) $ F10
 671   0   -110 +120 -5071  fill=8  (171) $ F11
 672   0   -110 +120 -5072  fill=8  (172) $ F12
c 673   0   -110 +120 -5073  fill=8  (173) $ F13 - 3L
c 674   0   -110 +120 -5074  fill=8  (174) $ F14 - 3L
 675   0   -110 +120 -5075  fill=8  (175) $ F15
 676   0   -110 +120 -5076  fill=8  (176) $ F16
 677   0   -110 +120 -5077  fill=8  (177) $ F17
 678   0   -110 +120 -5078  fill=8  (178) $ F18
 679   0   -110 +120 -5079  fill=8  (179) $ F19
 680   0   -110 +120 -5080  fill=8  (180) $ F20
```

```
 681   0   -110 +120 -5081  fill=8  (181) $ F21
 682   0   -110 +120 -5082  fill=8  (182) $ F22
 683   0   -110 +120 -5083  fill=8  (183) $ F23
 684   0   -110 +120 -5084  fill=8  (184) $ F24
 685   0   -110 +120 -5085  fill=8  (185) $ F25
 686   0   -110 +120 -5086  fill=8  (186) $ F26
 687   0   -110 +120 -5087  fill=8  (187) $ F27
 688   0   -110 +120 -5088  fill=8  (188) $ F28
 689   0   -110 +120 -5089  fill=8  (189) $ F29
 690   0   -110 +120 -5090  fill=8  (190) $ F30
 691   0   -110 +120 -5091  fill=6  (191) $ G2 - Graphite
 692   0   -110 +120 -5092  fill=8  (192) $ G3
 693   0   -110 +120 -5093  fill=8  (193) $ G4
 694   0   -110 +120 -5094  fill=8  (194) $ G5
 695   0   -110 +120 -5095  fill=8  (195) $ G6
 696   0   -110 +120 -5096  fill=8  (196) $ G8
 697   0   -110 +120 -5097  fill=8  (197) $ G9
 698   0   -110 +120 -5098  fill=8  (198) $ G10
 699   0   -110 +120 -5099  fill=8  (199) $ G11
 700   0   -110 +120 -5100  fill=8  (200) $ G12
c 701   0   -110 +120 -5101  fill=6  (201) $ G14
 702   0   -110 +120 -5102  fill=8  (202) $ G15
 703   0   -110 +120 -5103  fill=6  (203) $ G16 - Graphite
 704   0   -110 +120 -5104  fill=8  (204) $ G17
 705   0   -110 +120 -5105  fill=8  (205) $ G18
 706   0   -110 +120 -5106  fill=6  (206) $ G20 - Graphite
 707   0   -110 +120 -5107  fill=8  (207) $ G21
 708   0   -110 +120 -5108  fill=8  (208) $ G22
 709   0   -110 +120 -5109  fill=8  (209) $ G23
 710   0   -110 +120 -5110  fill=6  (210) $ G24 - Graphite
c 711   0   -110 +120 -5111  fill=8  (211) $ G26
 712   0   -110 +120 -5112  fill=8  (212) $ G27
 713   0   -110 +120 -5113  fill=8  (213) $ G28
 714   0   -110 +120 -5114  fill=8  (214) $ G29
c 715   0   -110 +120 -5115  fill=8  (215) $ G30
c 716   0   -110 +120 -5116  fill=8  (216) $ G32 - Source
 717   0   -110 +120 -5117  fill=6  (217) $ G33 - Graphite
c 718   0   -110 +120 -5118  fill=8  (218) $ G34 - PNT
 719   0   -110 +120 -5119  fill=6  (219) $ G35 - Graphite
 720   0   -110 +120 -5120  fill=6  (220) $ G36 - Graphite
c
c 750   0     -110 +120 -1940  fill=96   (50)    $ Sleeve irradiator
c
c 751   0     -110 +120 -961   fill=40   (20)    $ 3L(Mat) irradiator
c
 751   0     -110 +120 -1940   fill=45   (50)    $ 3L(Cd) irradiator
c
c 752   0     -110 +120 -5118  fill=30   (218)   $ tPNT irradiator
c
c 752   0     -110 +120 -5118  fill=35   (218)   $ ePNT irradiator
c
c -----------------------
c Lower grid plate region
c -----------------------
  1  2  -2.7   -206  +207
               -211  +212  -213  +214  -215  +216
               -221  +222  -223  +224  -225  +226
             +5000 +5001 +5002 +5003 +5004 +5005 +5006 +5007 +5008 +5009
             +5010 +5011 +5012 +5013 +5014 +5015 +5016 +5017 +5018 +5019
             +5020 +5021 +5022 +5023 +5024 +5025 +5026 +5027 +5028 +5029
             +5030 +5031 +5032 +5033 +5034 +5035 +5036 +5037 +5038 +5039
             +5040 +5041 +5042 +5043 +5044 +5045 +5046       +5048 +5049
             +5050 +5051 +5052 +5053 +5054 +5055 +5056 +5057 +5058 +5059
             +5060 +5061 +5062 +5063 +5064 +5065 +5066 +5067 +5068 +5069
             +5070 +5071 +5072             +5075 +5076 +5077 +5078 +5079
             +5080 +5081 +5082 +5083 +5084 +5085 +5086 +5087 +5088 +5089
             +5090 +5091 +5092 +5093 +5094 +5095 +5096 +5097 +5098 +5099
             +5100       +5102 +5103 +5104 +5105 +5106 +5107 +5108 +5109
             +5110       +5112 +5113 +5114             +5117       +5119
             +5120
             +1963 +1964 +1965  +1966                  $ Mapping experiment
             +1940                                     $ 3L
c             +5118                                      $ PNT
c             +5111 +5115
c             +5039 +5040 +5063 +5064 +5065 +5093 +5094  $ Elements in 6L
c             +961                                       $ 3L
```

```
c
c -----------------------
c Upper grid plate region
c -----------------------
  2  2  -2.7   -203  -201  +202
             +5000 +5001 +5002 +5003 +5004 +5005 +5006 +5007 +5008 +5009
             +5010 +5011 +5012 +5013 +5014 +5015 +5016 +5017 +5018 +5019
             +5020 +5021 +5022 +5023 +5024 +5025 +5026 +5027 +5028 +5029
             +5030 +5031 +5032 +5033 +5034 +5035 +5036 +5037 +5038 +5039
             +5040 +5041 +5042 +5043 +5044 +5045 +5046       +5048 +5049
             +5050 +5051 +5052 +5053 +5054 +5055 +5056 +5057 +5058 +5059
             +5060 +5061 +5062 +5063 +5064 +5065 +5066 +5067 +5068 +5069
             +5070 +5071 +5072             +5075 +5076 +5077 +5078 +5079
             +5080 +5081 +5082 +5083 +5084 +5085 +5086 +5087 +5088 +5089
             +5090 +5091 +5092 +5093 +5094 +5095 +5096 +5097 +5098 +5099
             +5100       +5102 +5103 +5104 +5105 +5106 +5107 +5108 +5109
             +5110       +5112 +5113 +5114             +5117       +5119
             +5120
             +1963 +1964 +1965  +1966                  $ Mapping experiment
             +1940                                     $ 3L
c             +5118                                      $ PNT
c             +5111 +5115
c             +5039 +5040 +5063 +5064 +5065 +5093 +5094  $ Elements in 6L
c             +961                                       $ 3L
c
c ----------------------
c Reactor core structure
c ----------------------
c Inner core shroud
c -----------------
 10  2  -2.7   -300  +302  -303  +202            $ Alignment ring
 11  2  -2.7   -300  -202  +352                  $ Alignment ring
              (+231: -232: +241: -242:
               +233: -234: +243: -244:
               +235: -236: +245: -246)
 12  2  -2.7   +305  -306  +307                  $ Shroud load ring
              (-311  +312  -321  +322
               -313  +314  -323  +324
               -315  +316  -325  +326)
 13  2  -2.7   -301  -352  +304                  $ Alignment ring
              (+331: -332: +341: -342:
               +333: -334: +343: -344:
               +335: -336: +345: -346)
 14  2  -2.7   +231  -331  -233  +236            $ Reflector plate
               -352  +306
 15  2  -2.7   -232  +332  +234  -235            $ Reflector plate
               -352  +306
 16  2  -2.7   +241  -341  -343  -345            $ Reflector, bp3
               -352  +306  +363
 17  2  -2.7   -242  +342  +344  +346            $ Reflector plate
               -352  +306
 18  2  -2.7   +233  -333  -331  -343            $ Reflector plate
               -352  +306
 19  2  -2.7   -234  +334  +332  +344            $ Reflector plate
               -352  +306
 20  2  -2.7   +235  -335  +332  -345            $ Reflector plate
               -352  +306
 21  2  -2.7   -236  +336  -331  +346            $ Reflector plate
               -352  +306
 22  2  -2.7   +243  -343  -241  -233            $ Reflector plate
               -352  +306
 23  2  -2.7   -244  +344  +242  +234            $ Reflector plate
               -352  +306
 24  2  -2.7   +245  -345  -241  -235            $ Reflector plate
               -352  +306
 25  2  -2.7   -246  +346  +242  +236            $ Reflector plate
               -352  +306
 26  2  -2.7   +241  -363  +364  -360            $ Reflector BP3
 27  2  -2.7   -361  +362  -100                  $ Reflector BP1&5
c
c --------------------------------
c Reflector outer shroud structure
c --------------------------------
 30  2  -2.7   -355  +361                        $ Reflector cylin
               -350  +351  -352  +353
 31  2  -2.7   +355  +363                        $ Reflector cylin
```

```
              -350  +351  -352  +353
 32  2  -2.7   -370  +371  -372  +373           $ Cylinder, top
 33  2  -2.7   -374  -375  +376                 $ Cylinder, bot
              (+331: -332: +341: -342:
               +333: -334: +343: -344:
               +335: -336: +345: -346)
 34  2  -2.7   -370  +374  -375  +377           $ Reflector edge ring
 35  2  -2.7   -352  -371  +380  +381           $ Reflector RSR unit
 36  2  -2.7   -380  +300  +381  -382           $ Reflector RSR unit
 37  2  -2.7   -352  +301  -300  +381           $ Reflector RSR unit
 38  1  -1.0   +370  -351  -377  +120           $ Edge ring error
c
c ----------------------------
c Reflector graphite moderator
c ----------------------------
 40  4  -2.25    -400  +401  -402  +403         $ Reflector graphite
 41  4  -2.25    -400  -403  +375  -404  +361
               (+411: -412: +421: -422:
                +413: -414: +423: -424:
                +415: -416: +425: -426)
               #(-361  +405)                   $ Graphite, bp1&5
 42  4  -2.25   (-400  -403  +375  +404  +363
               (+411: -412: +421: -422:
                +413: -414: +423: -424:
                +415: -416: +425: -426))
               #(-406 +408) #(-407 +409)       $ Graphite, bp3
 43  8 -1.15e-3 (+371 -351 -373 +403)     #40   $ Graphite void?????
 44  8 -1.15e-3 (-351  -403  +375  -404  +361
               (+331: -332: +341: -342:
                +333: -334: +343: -344:
                +335: -336: +345: -346)) #41   $ graphite void
 45  8 -1.15e-3 (-351  -403  +375  +404  +363
               (+331: -332: +341: -342:
                +333: -334: +343: -344:
                +335: -336: +345: -346)) #42   $ graphite void
 46  8 -1.15e-3  -304  +403  -301
               (+331: -332: +341: -342:
                +333: -334: +343: -344:
                +335: -336: +345: -346)        $ graphite void
 47  8 -1.15e-3  +301  -371  +403  -381         $ graphite void
c
c ------------------
c Pool coolant water
c ------------------
 50  1  -1.0   -203  +201  -110                 $ Above upper grid plate
            +5000 +5001 +5002 +5003 +5004 +5005 +5006 +5007 +5008 +5009
            +5010 +5011 +5012 +5013 +5014 +5015 +5016 +5017 +5018 +5019
            +5020 +5021 +5022 +5023 +5024 +5025 +5026 +5027 +5028 +5029
            +5030 +5031 +5032 +5033 +5034 +5035 +5036 +5037 +5038 +5039
            +5040 +5041 +5042 +5043 +5044 +5045 +5046       +5048 +5049
            +5050 +5051 +5052 +5053 +5054 +5055 +5056 +5057 +5058 +5059
            +5060 +5061 +5062 +5063 +5064 +5065 +5066 +5067 +5068 +5069
            +5070 +5071 +5072             +5075 +5076 +5077 +5078 +5079
            +5080 +5081 +5082 +5083 +5084 +5085 +5086 +5087 +5088 +5089
            +5090 +5091 +5092 +5093 +5094 +5095 +5096 +5097 +5098 +5099
            +5100       +5102 +5103 +5104 +5105 +5106 +5107 +5108 +5109
            +5110       +5112 +5113 +5114             +5117       +5119
            +5120
            +1940                                      $ 3L
c            +5118                                       $ PNT
c            +5111 +5115
c            +5039 +5040 +5063 +5064 +5065 +5093 +5094  $ Elements in 6L
c            +961                                       $ 3L
c
 51  1  -1.0   +203  -302  +202  -110           $ Upper gridplate
 52  1  -1.0   +302  -300  +303  -110           $ Upper gridplate
 53  1  -1.0   -305  -306  +307                 $ Lower gridplate
            +5000 +5001 +5002 +5003 +5004 +5005 +5006 +5007 +5008 +5009
            +5010 +5011 +5012 +5013 +5014 +5015 +5016 +5017 +5018 +5019
            +5020 +5021 +5022 +5023 +5024 +5025 +5026 +5027 +5028 +5029
            +5030 +5031 +5032 +5033 +5034 +5035 +5036 +5037 +5038 +5039
            +5040 +5041 +5042 +5043 +5044 +5045 +5046       +5048 +5049
            +5050 +5051 +5052 +5053 +5054 +5055 +5056 +5057 +5058 +5059
            +5060 +5061 +5062 +5063 +5064 +5065 +5066 +5067 +5068 +5069
            +5070 +5071 +5072             +5075 +5076 +5077 +5078 +5079
            +5080 +5081 +5082 +5083 +5084 +5085 +5086 +5087 +5088 +5089
```

```
            +5090 +5091 +5092 +5093 +5094 +5095 +5096 +5097 +5098 +5099
            +5100       +5102 +5103 +5104 +5105 +5106 +5107 +5108 +5109
            +5110       +5112 +5113 +5114             +5117       +5119
            +5120
            +1940                                      $ 3L
c            +5118                                       $ PNT
c            +5111 +5115
c            +5039 +5040 +5063 +5064 +5065 +5093 +5094  $ Elements in 6L
c            +961                                       $ 3L
c
 54  1  -1.0   -307  +120                      $ Lower gridplate
              (-311  +312  -321  +322
               -313  +314  -323  +324
               -315  +316  -325  +326)
            +5000 +5001 +5002 +5003 +5004 +5005 +5006 +5007 +5008 +5009
            +5010 +5011 +5012 +5013 +5014 +5015 +5016 +5017 +5018 +5019
            +5020 +5021 +5022 +5023 +5024 +5025 +5026 +5027 +5028 +5029
            +5030 +5031 +5032 +5033 +5034 +5035 +5036 +5037 +5038 +5039
            +5040 +5041 +5042 +5043 +5044 +5045 +5046       +5048 +5049
            +5050 +5051 +5052 +5053 +5054 +5055 +5056 +5057 +5058 +5059
            +5060 +5061 +5062 +5063 +5064 +5065 +5066 +5067 +5068 +5069
            +5070 +5071 +5072             +5075 +5076 +5077 +5078 +5079
            +5080 +5081 +5082 +5083 +5084 +5085 +5086 +5087 +5088 +5089
            +5090 +5091 +5092 +5093 +5094 +5095 +5096 +5097 +5098 +5099
            +5100       +5102 +5103 +5104 +5105 +5106 +5107 +5108 +5109
            +5110       +5112 +5113 +5114             +5117       +5119
            +5120
            +1940                                      $ 3L
c            +5118                                       $ PNT
c            +5111 +5115
c            +5039 +5040 +5063 +5064 +5065 +5093 +5094  $ Elements in 6L
c            +961                                       $ 3L
c
 55  1  -1.0   -207  +306                      $ Lower gridplate
              (-231  +232  -241  +242
               -233  +234  -243  +244
               -235  +236  -245  +246)
            +5000 +5001 +5002 +5003 +5004 +5005 +5006 +5007 +5008 +5009
            +5010 +5011 +5012 +5013 +5014 +5015 +5016 +5017 +5018 +5019
            +5020 +5021 +5022 +5023 +5024 +5025 +5026 +5027 +5028 +5029
            +5030 +5031 +5032 +5033 +5034 +5035 +5036 +5037 +5038 +5039
            +5040 +5041 +5042 +5043 +5044 +5045 +5046       +5048 +5049
            +5050 +5051 +5052 +5053 +5054 +5055 +5056 +5057 +5058 +5059
            +5060 +5061 +5062 +5063 +5064 +5065 +5066 +5067 +5068 +5069
            +5070 +5071 +5072             +5075 +5076 +5077 +5078 +5079
            +5080 +5081 +5082 +5083 +5084 +5085 +5086 +5087 +5088 +5089
            +5090 +5091 +5092 +5093 +5094 +5095 +5096 +5097 +5098 +5099
            +5100       +5102 +5103 +5104 +5105 +5106 +5107 +5108 +5109
            +5110       +5112 +5113 +5114             +5117       +5119
            +5120
            +1940                                      $ 3L
c            +5118                                       $ PNT
c            +5111 +5115
c            +5039 +5040 +5063 +5064 +5065 +5093 +5094  $ Elements in 6L
c            +961                                       $ 3L
c
 56  1  -1.0   -206  +207                      $ Lower gridplate
              (+211: -212: +221: -222:
               +213: -214: +223: -224:
               +215: -216: +225: -226)
              (-231  +232  -241  +242
               -233  +234  -243  +244
               -235  +236  -245  +246)
 57  1  -1.0   -351  +371  +372  -110          $ Upper reflector
 58  1  -1.0   -374  -376  +120                $ Lower reflector
              (+311: -312: +321: -322:
               +313: -314: +323: -324:
               +315: -316: +325: -326)
 59  1  -1.0   +306  -376                      $ Lower reflector
              (+331: -332: +341: -342:
               +333: -334: +343: -344:
               +335: -336: +345: -346)
              (-311  +312  -321  +322
               -313  +314  -323  +324
               -315  +316  -325  +326)
c
```

```
c ------------------
c Pool coolant water
c ------------------
 950  8 -1.15e-3 -150 +160 -165
      *TRCL (-60.00    00.00   00.00   00  90  90   90  00  90) $NP
 951  8 -1.15e-3 -150 +160 -165
      *TRCL ( 57.96   -15.53   00.00   00  90  90   90  00  90) $NPP
 952  8 -1.15e-3 -150 +160 -165
      *TRCL ( 42.43    42.43   00.00   00  90  90   90  00  90) $FC
 60  1  -1.0   +350  -355  +361
              (-100  -110  +120) #950 #951       $ Beam ports 1&5
 61  1  -1.0   +350  +355  +363
              (-100  -110  +120) #950 #952
             #(-406 +408) #(-407 +409)           $ Beam ports 2&4
 62  1  -1.0   -363  +364  +360  -100            $ Reflector BP3
 63  1  -1.0   -350  +351  +352  -110            $ Reflector cylinder
 64  1  -1.0   -350  +351  -353  +120            $ Reflector cylinder
 65  1  -1.0   -370  +374  -377  +120            $ Reflector edgering
 66  1  -1.0   +300  -371  +303  -110            $ RSR removal
 67  2  -2.7   +370  -351  -375  +377            $ edge ring error
 68  2  -2.7   -351  +370  -372  +373            $ edge ring error
c ---------------------
c BP2, BP4 structure
c ---------------------
 71  2  -2.7    (-406  +430) +350  +355  -100    $ Reflector BP2
 72  2  -2.7    (-407  +440) +350  +355  -100    $ Reflector BP4
c
c -------------
c BP3 structure
c -------------
 73  2  -2.7     +461  -462  -464                $ Reflector BP3
 74  2  -2.7     -463  +464  +461  -100          $ Reflector BP3
 75  1  -1.0     +241  -364  -461                $ Reflector BP3
 76  1  -1.0     +463  -364  +461  -100          $ Reflector BP3
c
c --------------------
c BP1, BP3, BP5 cavity
c --------------------
 77  8 -1.15e-3  +450  -362  -451                  $ Reflector BP1
 78  8 -1.15e-3  +462  -464  -453                  $ Reflector BP3
 79  8 -1.15e-3  -450  -362  +455
c
c ------------------------------
c BP1, BP2, BP3, BP4, BP5 cavity
c ------------------------------
 81  8 -1.15e-3  +451  -362  -100       #95  VOL=1   $ Reflector BP1
 82  8 -1.15e-3 (-430  +408) +350  -100 #96  VOL=1   $ Reflector BP2
 83  8 -1.15e-3  +453  -464  -100       #97  VOL=1   $ Reflector BP3
 84  8 -1.15e-3 (-440  +409) +350  -100 #98  VOL=1   $ Reflector BP4
 85  8 -1.15e-3  -455  -362  -100       #99  VOL=1   $ Reflector BP5
c
 95  8 -1.15e-3  -171
 96  8 -1.15e-3  -172
 97  8 -1.15e-3  -173
 98  8 -1.15e-3  -174
 99  8 -1.15e-3  -175
c
c ------------------------------
c Rotary specimen rack (RSR) unit
c ------------------------------
 90  8 -1.15e-3  +300  -303  +352  -371          $ RSR unit
 91  8 -1.15e-3  +300  +304  -352  -380          $ RSR unit
 92  8 -1.15e-3  +300  -304  -380  +382          $ RSR unit
       vol=1
c
c ----------------------------------
c Fill universe for reactor core grid
c ----------------------------------
c Graphite reflector elements, U=6
c --------------------------------
 100  1 -1.0     #101  #102  #103
                 #104  #105  #106        u=6
 101  2 -2.7     -623  -609  +206        u=6      $ lower fitting
 102  2 -2.7     -605  -620  +621        u=6      $ end closure
 103  4 -2.25    -605  -621  +622        u=6      $ graphite
 104  2 -2.7     -605  -622  +623        u=6      $ end closure
```

```
 105  2 -2.7     +620  -609  -201        u=6      $ upper fitting
 106  2 -2.7     +605  -607  -620  +623  u=6      $ element clad
c
c --------------------------
c Transient control rod, U=7
c --------------------------
 110  1 -1.0     #111  #112  #113  #114
                 #115  #116  #117        u=7
 111  2 -2.7     -500  -510  +511        u=7      $ end plug
 112  2 -2.7     -500  -511  +512        u=7      $ spacer plug
 113  6 -2.52    -500  -512  +513        u=7      $ absorber
 114  2 -2.7     -500  -513  +514        u=7      $ spacer plug
 115  8 -1.15e-3 -500  -514  +515        u=7      $ air follower
 116  3 -7.8     -500  -515  +516        u=7      $ end plug
 117  3 -7.8     +500  -502  -510  +516  u=7      $ element clad
c
c --------------------------------
c Standard triga fuel element, U=8
c --------------------------------
c Temperature in fuel rod assumed 600 K at full power
 120  1 -1.0     #121  #122  #123
                 #124  #125  #126
                 #127  #128  #129        u=8      $ element clad
 121  3 -7.8     -615  -603  +206        u=8      $ lower fitting
 122  3 -7.8     -600  -610  +611        u=8      $ end closure
 123  4 -2.25    -600  -611  +612        u=8      $ graphite
 124  5 -6.05    -600  -612  +613  +650  u=8    TMP1=5.1702E-8  $ fuel at 600K
 125  7 -6.49    -650  -612  +613        u=8      $ Zr rod
 126  4 -2.25    -600  -613  +614        u=8      $ graphite
 127  3 -7.8     -600  -614  +615        u=8      $ end closure
 128  3 -7.8     +610  -603  -201        u=8      $ upper fitting
 129  3 -7.8     +600  -602  -610  +615  u=8      $ element clad
c
c ---------------------------------------------------
c Fuel follower control rods (reg, shim1, shim2), U=9
c ---------------------------------------------------
c Temperature assumed 300 C at full power
 130  1  -1.0     #131  #132  #133  #134  #135
                 #136  #137  #138  #139  #140
                 #141  #142  #143         u=9
 131  3  -7.8     -505  -520  +521         u=9      $ end plug
 132  8  -1.15e-3 -505  -521  +522         u=9      $ top space
 133  2  -2.7     -505  -522  +523         u=9      $ spacer plug
 134  8  -1.15e-3 -505  -523  +524         u=9      $ void gap
 135  6  -2.52    -505  -524  +525         u=9      $ absorber
 136  2  -2.7     -505  -525  +526         u=9      $ spacer plug
 137  8  -1.15e-3 -505  -526  +527         u=9      $ void gap
 138  5  -6.05    -505  -527  +528  +550   u=9  TMP1=5.1702E-8 $ fuel follower
 139  7  -6.49    -550  -527  +528         u=9      $ Zr rod
 140  2  -2.7     -505  -528  +529         u=9      $ spacer plug
 141  8  -1.15e-3 -505  -529  +530         u=9      $ bot space
 142  3  -7.8     -505  -530  +531         u=9      $ end plug
 143  3  -7.8     +505  -507  -520  +531   u=9      $ element clad
c
c --------------------------------------
c Modifications and experiment components
c --------------------------------------
c Pneumatic transfer system (PTS) without Cd, U=30 - JDB - 4/13/2007
c ------------------------------------------------
 300   1  -1.0     #301 #302 #303
                  #304 #305 #306
                  #307 #308              U=30    $ Water surrounding PTS
 301   2  -2.7     -910 +911 +933         U=30    $ Al transport tube
 302   8  -1.15e-3 -911 +912 +933         U=30    $ Air gap
 303   2  -2.7     -912 +913 +915         U=30    $ Al sample tube
 304   8  -1.15e-3 -913      +915 #308    U=30    $ Sample location
 305   2  -2.7     -910 +934 -933         U=30    $ Al transport tube bottom
 306   2  -2.7     -912 +931 -915         U=30    $ Al sample tube bottom
 307   8  -1.15e-3 +933 -931 -912         U=30    $ Air gap beneath sample tube
 308   8  -1.15e-3 -908 +909 -907         U=30    $ Sample location for tally
c
c -----------------------------------------------
c Pneumatic transfer system (PTS) with Cd, U=35 - JDB - 4/13/2007
c -----------------------------------------------
 350   1  -1.0     #351 #352 #353
                  #354 #355 #356
```

```
                  #357 #358 #359 #360    U=35    $ Water surrounding PTS
 351   2  -2.7     -910 +911 +933         U=35    $ Al transport tube
 352   8  -1.15e-3 -911 +914 +933         U=35    $ Air gap
 353  10  -8.65    -914 +912 +931         U=35    $ Cd liner
 354   2  -2.7     -912 +913 +915         U=35    $ Al sample tube
 355   8  -1.15e-3 -913      +915 #360    U=35    $ Sample location
 356   2  -2.7     -910 +934 -933         U=35    $ Al transport tube bottom
 357   2  -2.7     -912 +931 -915         U=35    $ Al sample tube bottom
 358  10  -8.65    -914 -931 +932         U=35    $ Cd liner beneath sample
 359   8  -1.15e-3 +933 -932 -914         U=35    $ Air gap beneath sample tube
 360   8  -1.15e-3 -908 +909 -907         U=35    $ Sample location for tally
c
c ----------------------------------
c 3-element irradiator with Cd, U=40
c ----------------------------------
 400   1  -1.0    #401  #402  #403  #404
                  #405  #406  #407  #408
                  #409  #410              u=40     $ Water
 401   2  -2.7    -920  +921  -958  +959  u=40     $ Al outer
 402   8 -1.15e-3 -921  +924  -958  +959  u=40     $ Air gap
 403  10 -11.4    -924  +922  -958  +959  u=40     $ Pb liner
 404   2  -2.7    -922  +923  -958  +959  u=40     $ Al liner
 405   8 -1.15e-3 -923         -963  +965  u=40     $ Air in sample location
 406   8 -1.15e-3 -923         -958  +963  u=40     $ Air above sample location
 407   2  -2.7    -962         -957  +958  u=40     $ Upper end cap
 408   2  -2.7    -920         -959  +960  u=40     $ Lower end cap
 409   2  -2.7    -923         -965  +966  u=40
 410  11 -11.4    -923         -966  +959  u=40
c
c ----------------------------------
c 3-element irradiator with Cd, U=45
c ----------------------------------
c 450  1  -1.0   #451  #452  #453  #454           $ #461 #462 #463 #465
c                #455  #456  #457  #458
c                #459  #460              U=45     $ Water
c 451  1  -1.0   -920  +921  -958  +959  U=45     $ Al outer
c 452  1  -1.0   -922  +923  -958  +959  U=45     $ Al liner
c 453  1  -1.0   +922  -924  -958  +959  U=45     $ Cd liner
c 454  1  -1.0   -921  +924  -958  +959  U=45     $ Air gap
c 455  1  -1.0   -923         -963  +965  U=45     $ Air in sample location
c 456  1  -1.0   -923         -958  +963  u=45     $ Air above sample location
c 457  1  -1.0   -962         -957  +958  u=45     $ Upper end cap
c 458  1  -1.0   -920         -959  +960  u=45     $ Lower end cap
c 459  1  -1.0   -923         -965  +966  u=45
c 460  1  -1.0   -923         -966  +959  u=45
c
 450  1  -1.0    #451  #452  #453  #454           $ #461 #462 #463 #465
                 #455  #456  #457  #458
                 #459  #460              U=45     $ Water
 451  2  -2.7    -920  +921  -958  +959  U=45     $ Al outer
 452  2  -2.7    -922  +923  -958  +959  U=45     $ Al liner
 453 10  -11.34   +922  -924  -958  +959  U=45     $ Cd liner
 454  8 -1.15e-3 -921  +924  -958  +959  U=45     $ Air gap
 455  8 -1.15e-3 -923         -963  +965  U=45     $ Air in sample location
           vol=1
 456  8 -1.15e-3 -923         -958  +963  u=45     $ Air above sample location
 457  2  -2.7    -962         -957  +958  u=45     $ Upper end cap
 458  2  -2.7    -920         -959  +960  u=45     $ Lower end cap
 459  2  -2.7    -923         -965  +966  u=45
 460 11  -8.65   -923         -966  +959  u=45     $ Changed to Pb
c
c 461  2  -2.7       +1956  -957 -1941 +1942 U=45     $ Al outer
c 462 11 -11.4       +1955  -958 -1942 +1943 U=45     $ Pb in sleeve
c 463  2  -2.7       +1956  -957 -1943 +1944 u=45     $ Al inner
c 464  2  -2.7        +958  -957 -1942 +1943 u=45     $ Al donut top (lid)
c 465  2  -2.7       +1956 -1955 -1942 +1943 u=45     $ Al donut bottom
c
c ------------------------------------
c 3-element irradiator (unlined), U=50
c ------------------------------------
 490  8 -1.15e-3 #491  #492  #493  #494  U=50     $
 491  2  -2.7    -922  +923  -950  +955  U=50     $ T3 can cylinder
 492  2  -2.7    +922  -924  -950  +955  U=50     $ T3 can liner
 493  2  -2.7    -923  +950  -951         U=50     $ T3 can upper
 494  2  -2.7    -923  -955  +956         U=50     $ T3 can lower
c
```

```
c ----------------------------------------
c Water cells for mapping experiment, u=101
c ----------------------------------------
 515   1    -1.0  #516                 u=101
 516   1    -1.0  -754 +782 -750       u=101
c
c ----------------------------------------
c Large irradiator with cadmium sleeve, u=96
c ----------------------------------------
 811   1  -1.0       #812  #813  #814  #815
                     #816  #817  #818  #819
                     #820  #821               u=96    $ Water outside of 7L
 812   2  -2.7      -1941 +1942 -1951 +1955   u=96    $ Al clad outer, sleeve
 813   8  -1.15e-3  -1942 +1947 -1951 +1955   u=96    $ Air, sleeve
 821  10  -8.65     -1947 +1943 -1951 +1955   u=96    $ Cadmium, sleeve
 814   2  -2.7      -1943 +1944 -1951 +1955   u=96    $ Al clad inner, sleeve
 815   2  -2.7      -1945 +1946 -1951 +1955   u=96    $ Al clad, can
 816   8  -1.15e-3  -1946       -1951 +1955   u=96    $ Air inside can
 817   2  -2.7      -1950 +1951 -1941 +1944   u=96    $ Al lid, sleeve, upper
 818   2  -2.7      -1955 +1956 -1941 +1944   u=96    $ Al lid, sleeve, lower
 819   2  -2.7      -1950 +1951 -1945         u=96    $ Al lid, can, upper
 820   2  -2.7      -1955 +1956 -1945         u=96    $ Al lid, can, lower
c
c ---------------
c 1-inch detector
c ---------------
 1740  1  -1.0     #1741  #1742             U=81     $ element clad
 1741  8  -1.15e-3 -638 -639 +640 #1742     U=81
 1742  8  -1.15e-3 -638 -641 +642           U=81     $ flux tally for 1" dia FC
c
c ----------------------
c Central thimble (CT), u=82 - JDB
c ----------------------
 1750  1  -1.0  #1751 #1752           u=82
 1751  2  -2.7  -442  +443  +207      u=82
 1752  1  -1.0  -446  +447  -445      u=82
c
c
c ---------------------------
c Photon Radial Profile Holes
c ---------------------------
 1800  1  -1.0  -2000
 1801  1  -1.0  -2001
 1802  1  -1.0  -2002
 1803  1  -1.0  -2003
 1804  1  -1.0  -2004
 1805  1  -1.0  -2005
 1806  1  -1.0  -2006
c
c -------------
c Outside world
c -------------
 2999  0           +100: +110: -120
c
c ------------------------------------------------------------
c                  End of Cell Card Specification
c ------------------------------------------------------------

c ------------------------------------------------------------
c            Beginning of Surface Card Specification
c ------------------------------------------------------------
c Hexagonal cell lattice surfaces
c --------------------------------
 101     PX      +2.17678              $ Fuel lattice hex-prism
 102     PX      -2.17678              $ Fuel lattice hex-prism
 103     P   +1   1.73205  0  +4.35356  $ Fuel lattice hex-prism
 104     P   +1   1.73205  0  -4.35356  $ Fuel lattice hex-prism
 105     P   -1   1.73205  0  +4.35356  $ Fuel lattice hex-prism
 106     P   -1   1.73205  0  -4.35356  $ Fuel lattice hex-prism
 107     CZ      +2.51353              $ Maximum lattice diagonal radius
c
 108     py       5.65531
 109     py      -5.65531
c
c ------------------------
c Axial and radial domain
```

```
c ------------------------
 100     CZ     +75
 110     PZ     +75                  $ Upper bound
 120     PZ     -75                  $ Lower bound
 150     CZ     +5.08                $ Detector Cylinder
 160     PZ     +10                  $ Detector Lower
 165     PZ     +30                  $ Detector Upper
c
 171     s      60.000 -36.000  -6.985  2.5     $ BP1
 172     s      60.000  36.000  -6.985  2.5     $ BP2
 173     s       0.000  70.000  -6.985  2.5     $ BP3
 174     s     -60.000  36.000  -6.985  2.5     $ BP4
 175     s     -60.000 -36.000  -6.985  2.5     $ BP5
c
c --------------------------------
c Reactor core grid plate surfaces
c --------------------------------
 200     CZ       1.91135             $ Grid plate element holes
 201     PZ     +32.3850              $ Upper grid plate region
 202     PZ     +30.7975              $ Upper grid plate region
 203     CZ      27.6225              $ Upper grid plate diameter - effective core diameter
 205     CZ       1.5875              $ Grid plate coolant holes
 206     PZ     -33.17875             $ Lower grid plate region
 207     PZ     -36.35375             $ Lower grid plate region
 211     PX     +26.1216              $ Lower grid plate edge
 212     PX     -26.1216              $ Lower grid plate edge
 213     P   +1   0.57735  0  +29.0240 $ Lower grid plate edge
 214     P   +1   0.57735  0  -29.0240 $ Lower grid plate edge
 215     P   -1   0.57735  0  +29.0240 $ Lower grid plate edge
 216     P   -1   0.57735  0  -29.0240 $ Lower grid plate edge
 221     PY     +25.1360              $ Lower grid plate edge
 222     PY     -25.1360              $ Lower grid plate edge
 223     P   +1   1.73205  0  +52.2432 $ Lower grid plate edge
 224     P   +1   1.73205  0  -52.2432 $ Lower grid plate edge
 225     P   -1   1.73205  0  +52.2432 $ Lower grid plate edge
 226     P   -1   1.73205  0  -52.2432 $ Lower grid plate edge
 231     PX     +26.6700              $ Core shroud inside surface
 232     PX     -26.6700              $ Core shroud inside surface
 233     P   +1   0.57735  0  +29.2100 $ Core shroud inside surface
 234     P   +1   0.57735  0  -29.2100 $ Core shroud inside surface
 235     P   -1   0.57735  0  +29.2100 $ Core shroud inside surface
 236     P   -1   0.57735  0  -29.2100 $ Core shroud inside surface
 241     PY     +25.4000              $ Core shroud inside surface
 242     PY     -25.4000              $ Core shroud inside surface
 243     P   +1   1.73205  0  +54.9275 $ Core shroud inside surface
 244     P   +1   1.73205  0  -54.9275 $ Core shroud inside surface
 245     P   -1   1.73205  0  +54.9275 $ Core shroud inside surface
 246     P   -1   1.73205  0  -54.9275 $ Core shroud inside surface
c
c ------------------------
c Core structure surfaces
c ------------------------
c Reflector inner shroud
c ----------------------
 300     CZ      30.083125            $ Grid plate alignment ring
 301     CZ      29.765625            $ Grid plate alignment ring
 302     CZ      27.9400              $ Grid plate alignment ring
 303     PZ     +33.9725              $ Grid plate alignment ring
 304     PZ     +26.3525              $ Grid plate alignment ring
c
c ----------------
c Shroud load ring
c ----------------
 305     CZ      27.9400              $ Reflector shroud load ring   $ 24.7650
 306     PZ     -37.30625             $ Reflector shroud load ring
 307     PZ     -39.52875             $ Reflector shroud load ring
c
 311     PX     +29.2100              $ Reflector shroud support
 312     PX     -29.2100              $ Reflector shroud support
 313     P   +1   0.57735  0  +32.385  $ Reflector shroud support
 314     P   +1   0.57735  0  -32.385  $ Reflector shroud support
 315     P   -1   0.57735  0  +32.385  $ Reflector shroud support
 316     P   -1   0.57735  0  -32.385  $ Reflector shroud support
 321     PY     +27.9400              $ Reflector shroud support
 322     PY  -27.9400                 $ Reflector shroud support
 323     P   +1   1.73205  0  +59.3725 $ Reflector shroud support
```

```
 324     P   +1   1.73205  0  -59.3725 $ Reflector shroud support
 325     P   -1   1.73205  0  +59.3725 $ Reflector shroud support
 326     P   -1   1.73205  0  -59.3725 $ Reflector shroud support
c
 331     PX     +27.3050               $ Core shroud plate exterior
 332     PX     -27.3050               $ Core shroud plate exterior
 333     P   +1   0.57735  0  +29.8450 $ Core shroud plate exterior
 334     P   +1   0.57735  0  -29.8450 $ Core shroud plate exterior
 335     P   -1   0.57735  0  +29.8450 $ Core shroud plate exterior
 336     P   -1   0.57735  0  -29.8450 $ Core shroud plate exterior
 341     PY     +26.0350               $ Core shroud plate exterior
 342     PY     -26.0350               $ Core shroud plate exterior
 343     P   +1   1.73205  0  +56.5150 $ Core shroud plate exterior
 344     P   +1   1.73205  0  -56.5150 $ Core shroud plate exterior
 345     P   -1   1.73205  0  +56.5150 $ Core shroud plate exterior
 346     P   -1   1.73205  0  -56.5150 $ Core shroud plate exterior
c
c ----------------------
c Reflector outer shroud
c ----------------------
 350     CZ     +54.76875    $ Reflector outer shroud
 351     CZ     +53.49875    $ Reflector outer shroud
 352     PZ     +28.8925     $ Outer shroud upper edge
 353     PZ     -32.0675     $ Outer shroud lower edge
 355     PY       0.0        $ Core shroud section plane
c
c --------------------
c Reflector beam ports
c --------------------
 360     PY     +55.5625                 $ Radial penetrating beam port
 361     C/X    -35.2552  -6.985   7.62   $ Tangential thru beam port
 362     C/X    -35.2552  -6.985   6.9088 $ Tangential thru beam port
 363     C/Y      0.0     -6.985  10.160  $ Radial penetrating beam port
 364     C/Y      0.0     -6.985   9.525  $ Radial penetrating beam port
c
 370     CZ      53.3400     $ Reflector top shroud
 371     CZ      37.4650     $ Reflector top shroud
 372     PZ     +29.5275     $ Reflector top shroud
 373     PZ     +28.2575     $ Reflector top shroud
 374     CZ      52.0700     $ Reflector inner shroud base
 375     PZ     -27.9400     $ Reflector inner shroud base
 376     PZ     -29.5275     $ Reflector inner shroud base
 377     PZ     -36.8300     $ Reflector shroud edge ring
c
c ---------------------
c RSR experiment system
c ---------------------
 380     CZ     +37.1475     $ RSR cavity outer ring
 381     PZ      +6.9850     $ RSR cavity base
 382     PZ      +7.3025     $ RSR cavity base
c
c --------------------------
c Graphite reflector surfaces
c --------------------------
 400     CZ      53.0225     $ Graphite reflector outer radius
 401     CZ      37.7825     $ Graphite reflector inner radius
 402     PZ      27.6225     $ Graphite reflector upper section
 403     PZ       6.3500     $ Graphite reflector section plane
 404     PY     -20.32       $ Graphite reflector section plane
 405     PY     -35.2552     $ Beam port penetration
c        C/Y      0.0     -6.985  10.160         $ Radial penetrating beam port, bp3
c        C/X    -35.2552  -6.985   7.62          $ Tangential thru beam port,  bp1&5
 406  2  CY      7.62        $ Tangential beam port, bp2
 407  4  CY      7.62        $ Radial beam port, bp4
 408  2  PY      0.0         $ Tangential beam port, bp2
 409  4  PY      0.0         $ Radial beam port, bp4
 411     PX    +27.78125               $ Graphite inner surface
 412     PX    -27.78125               $ Graphite inner surface
 413     P   +1  0.57735  0  +31.00875  $ Graphite inner surface +1
 414     P   +1  0.57735  0  -31.00875  $ Graphite inner surface +1
 415     P   -1  0.57735  0  +31.00875  $ Graphite inner surface +1
 416     P   -1  0.57735  0  -31.00875  $ Graphite inner surface +1
 421     PY    +26.431875               $ Graphite inner surface
 422     PY    -26.431875               $ Graphite inner surface
 423     P   +1  1.73205  0  +57.30875  $ Graphite inner surface +1
 424     P   +1  1.73205  0  -57.30875  $ Graphite inner surface +1
```

```
 425     P   -1  1.73205  0  +57.30875  $ Graphite inner surface +1
 426     P   -1  1.73205  0  -57.30875  $ Graphite inner surface +1
c
 430  2  CY      6.9088      $ Tangential beam port, bp2
 440  4  CY      6.9088      $ Radial beam port, bp4
 450     PX      0.0         $ BP1&5 origin
c
c ---------------
c Central thimble - JLP
c ---------------
 442     CZ      1.50        $ Central thimble guide rod OD
 443     CZ      1.415       $ Central thimble guid rod ID
 444     CZ      1.25        $ Central thimble sample holder OD
 445     CZ      1.185       $ Central thimble sample holder ID
 446     PZ      2.5         $ Central thimble upper sample hodler
 447     PZ     -2.5         $ Central thibmle lower sample holder
c    beam port tally surfaces bp1&5 and bp3
 451     PX     +10.16       $ BP1
 453     PY     +40.90       $ BP3
 455     PX     -10.16       $ BP5
c    pool structure pipe, bp3
 461     PY     +25.600               $ Radial penetrating beam port, bp3
 462     PY     +26.235               $ Radial penetrating beam port, bp3
 463     C/Y      0.0  -6.985  7.62    $ Radial penetrating beam port, bp3
 464     C/Y      0.0  -6.985  6.9088  $ Radial penetrating beam port, bp3
c
c ------------------------
c Control element surfaces
c ------------------------
 500     CZ       1.5113     $ Control element - absorber surface, radius
 502     CZ       1.5875     $ Control element - clad outer surface
 505     CZ       1.6637     $ Control element - absorber surface, radius
 507     CZ       1.7145     $ Control element - clad outer surface
c
 510  7   PZ     +24.765      $ Control element - element plug, end
 511  7   PZ     +24.13       $ Control element - magneform plug, upper
 512  7   PZ     +19.05       $ Control element - absorber surface,length/2
 513  7   PZ     -19.05       $ Control element - absorber surface,length/2
 514  7   PZ     -21.59       $ Control element - magneform plug, lower
 515  7   PZ     -70.8025     $ Control element - air follower section
 516  7   PZ     -72.7075     $ Control element - element plug, end
c
 517      pz     +75
 518      pz     -75
 519      cz     1.5875
 532      cz     1.7145
c
 520  7   PZ     +34.925      $ Control element - element plug, end
 521  7   PZ     +31.115      $ Control element - void gap
 522  7   PZ     +20.6375     $ Control element - magneform plug, upper
 523  7   PZ     +19.3675     $ Control element - void gap
 524  7   PZ     +19.05       $ Control element - absorber surface,length/2
 525  7   PZ     -19.05       $ Control element - absorber surface,length/2
 526  7   PZ     -20.32       $ Control element - magneform plug, lower
 527  7   PZ     -20.955      $ Control element - void gap
 528  7   PZ     -59.055      $ Control element - fuel follower section
 529  7   PZ     -61.595      $ Control element - void gap
 530  7   PZ     -74.93       $ Control element - magneform plug, bottom
 531  7   PZ     -74.99       $ Control element - element plug, end
c
 550     CZ       0.28575    $ Zirconium rod
c
c ------------------------------------
c Fuel and moderator element surfaces
c ------------------------------------
 600     CZ       1.816      $ Fuel element - fuel region surface, radius
 602     CZ       1.867      $ Fuel element - clad outer surface
 603     CZ       1.5306     $ Fuel - adapter effective radius, lower
 604     CZ       1.9426     $ Fuel - adapter effective radius, upper
 605     CZ       1.816      $ Graphite element - element surface, radius
 606     CZ       1.867      $ Graphite element - clad outer surface
 607     CZ       1.867      $ Graphite element - clad outer surface
 608     CZ       1.9426     $ Graphite - adapter effective radius, upper
 609     CZ       1.5306     $ Graphite - adapter effective radius, lower
c
 610     PZ     +28.5877     $ Fuel element - element end region, upper
```

```
 611     PZ     +27.7368     $ Fuel element - graphite end region, upper
 612     PZ     +19.05       $ Fuel element - fuel surface, length/2
 613     PZ     -19.05       $ Fuel element - fuel surface, length/2
 614     PZ     -27.7368     $ Fuel element - graphite end region, lower
 615     PZ     -28.5877     $ Fuel element - element end region, lower
c
 620     PZ     +28.5877     $ Graphite element - element end, upper
 621     PZ     +27.7368     $ Graphite element - graphite end, upper
 622     PZ     -27.7368     $ Graphite element - graphite end, lower
 623     PZ     -28.5877     $ Graphite element - element end, lower
c
 635     PZ      15.24               $ Flux Tally
 636     PZ     -15.24               $ Flux Tally
 637     CZ      0.4                 $ Flux Tally hole for the KSU detector
 638     CZ      1.27
 639     PZ      7.7851
 640     PZ     -7.7851
 641     PZ      6.35
 642     PZ     -6.35
c
 650     CZ       0.28575           $ Zirconium rod
c
 660     CZ       1.5306            $ Element adapter effective radius
 661     CZ       1.867             $ Element clad outer surface
 662     PZ     +32.3850            $ Upper grid plate, top
 663     PZ     +28.5877            $ Element end region, upper
 664     PZ     -28.5877            $ Element end region, lower
 665     PZ     -33.17875           $ Lower grid plate, top
 666     cz       1.91135           $ Upper grid plate holes
c
c -------------------------------
c Boundaries for large irradiator
c -------------------------------
 701     PX     +8.70712
 703     PX    +10.8839
 708     PX    +19.59102
 710     PX     21.7678
 712     PX     19.59102
 717     PX     10.8839
 702      P     -1   1.73205   0  -26.12136
 704      P     -1   1.73205   0  -21.7678
 705      P      1   1.73205   0    4.35356
 706      P     -1   1.73205   0  -26.12136
 707      P      1   1.73205   0    8.70712
 709      P      1   1.73205   0    4.35356
 711      P     -1   1.73205   0  -43.5356
 713      P     -1   1.73205   0  -47.88916
 714      P      1   1.73205   0  -13.06068
 715      P     -1   1.73205   0  -43.5356
 716      P      1   1.73205   0  -17.41424
 718      P      1   1.73205   0  -13.06068
c
c --------------------------
c Reactor core modifications
c --------------------------
c Center tube irradiations
c ------------------------
 900     CZ       1.905               $ Center tube outer radius
 901     CZ       1.69418             $ Center tube inner radius
 905     CZ       1.5                 $ Sample radius
 907     PZ      +0.5                 $ Sample length
 908     CZ       0.5                 $ Sample radius (PTS)
 909     PZ      -0.5                 $ Sample length
c
c -------------------
c PNT tube dimensions
c -------------------
 910     CZ      +1.74625             $ Al transport tube outer radius
 911     CZ      +1.53543             $ Al transport tube inner radius
 912     CZ      +1.11125             $ Al sample tube outer radius
 913     CZ      +0.86995             $ Al sample tube inner radius
 914     CZ      +1.16205             $ Cd two layer liner
 915     PZ       -2.07645            $ PTS sample stop
 916     PZ     -18.89125             $ Cd absorber end
 917     PZ     -21.1264591           $ Cd absorber disk, upper edge
 918     PZ     -21.17725             $ Cd absorber disk, lower edge
```

```
 919     PZ     -30.32125              $ PTS bottom section
 931     PZ      -2.94775              $ Al sample tube bottom
 932     PZ      -2.99855              $ Bottom of Cd liner
 933     PZ      -3.37193              $ Top of Al transport tube
 934     PZ      -3.58275              $ Bottom of Al transport tube
c
c ---------------------------------
c 3-element irradiator with Cd or Pb
c ---------------------------------
c Reference to lower grid plate -33.17875
 920     c/z      0 0 +2.38125              $ Al can outer radius
 921     c/z      0 0 +2.23393              $ Al can inner radius
 922     c/z      0 0 +2.06375              $ Al sleeve outer radius
 923     c/z      0 0 +1.93929              $ Al sleeve inner radius
 924     c/z     0 0 +2.16535              $ Cd liner outer radius
c 930     c/z     0 -0 +0.47625              $ Al structure rod
c 940     PZ     -30.xxxx               $ Al bearing section
 950     PZ      +2.54                 $ Al upper end cap
 951     PZ      +2.5908               $ Al upper end cap
 955     PZ      -2.54                 $ Al lower end cap
 956     PZ      -2.5908               $ Al lower end cap
c
 957     pz     +99.82125              $ Al upper end cap, top
 958     pz     +96.82125              $ Al upper end cap, bottom
 963     pz     +30.7975               $ Bottom of upper grid plate
 959     pz     -26.19375              $ Al lower end cap, top
 960     pz     -31.27385              $ Al lower end cap, bottom
 962     c/z     -15.23746 -8.79856 +3.00000
c
 961    c/z     -15.23746 -8.79856 +3.0099
c
 965     pz     -25.55875              $ Top of Al in Al sleeve
 966     pz     -26.09215              $ Top of Cd liner in sleeve
 967     pz     -26.19375              $ Top of lower end cap
c
c ---------------------------------------------
c Large irradiator surfaces with cadmium sleeve
c ---------------------------------------------
c 1940     c/z     15.23746  -11.31062  5.27939   $ Center of irradiator
c 1940     c/z     +10.8839  +8.79856  2.4        $ Center of 3L irradiator
 1940     c/z     -15.24 -8.80 +2.4               $ Center of 3L irradiator
c
  1941     cz      5.08
  1942     cz      4.7625
  1943     cz      3.81
  1944     cz      3.4925
  1945     cz      3.175
  1946     cz      2.8575
  1947     cz      2.0000
 c
 1950      pz      +32.3850              $ Al upper end cap
 1951      pz      +32.22625             $ Al upper end cap
 1955      pz      -33.02                $ Al lower end cap
 1956      pz      -33.17875             $ Al lower end cap
c
c --------------------------------------
c Surfaces for flux mapping with Ni wire - JDB
c --------------------------------------
 1963    c/z    2.17678  -1.2573   +0.16   $ A
 1964    c/z   15.23746  -1.2573   +0.16   $ K
 1965    c/z   19.59102  -1.2573   +0.16   $ L
 1966    c/z   23.94458  -1.2573   +0.16   $ M
c
 750  cz     0.15875
 751  cz     0.16
 754  pz    32.385
 782  pz    -36.35375
c
c ---------------------------
c Photon Radial Profile Holes
c ---------------------------
 2000  s    +0.0  +2.51353      +0.0  0.3175
 2001  s    +0.0  +5.020706     +0.0  0.3175
 2002  s    +0.0  +10.05412     +0.0  0.3175
 2003  s    +0.0  +12.56765     +0.0  0.3175
 2004  s    +0.0  +17.59470     +0.0  0.3175
```

```
 2005  s    +0.0  +20.10823     +0.0  0.3175
 2006  s    +0.0  +25.0         +0.0  0.3175
c
c
c ----------------------
c Upper grid plate holes
c ----------------------
 5000  c/z  +0.00000  +0.00000  +1.91135  $ Upper grid plate hole, A1
 5001  c/z  +4.35356  +0.00000  +1.91135  $ Upper grid plate hole, B1
 5002  c/z  +2.17678  -3.76936  +1.91135  $ Upper grid plate hole, B2
 5003  c/z  -2.17678  -3.76936  +1.91135  $ Upper grid plate hole, B3
 5004  c/z  -4.35356  +0.00000  +1.91135  $ Upper grid plate hole, B4
 5005  c/z  -2.17678  +3.76936  +1.91135  $ Upper grid plate hole, B5
 5006  c/z  +2.17678  +3.76936  +1.91135  $ Upper grid plate hole, B6
 5007  c/z  +8.70712  +0.00000  +1.91135  $ Upper grid plate hole, C1
 5008  c/z  +6.53034  -3.76936  +1.91135  $ Upper grid plate hole, C2
 5009  c/z  +4.35356  -7.54126  +1.91135  $ Upper grid plate hole, C3
 5010  c/z  -0.00000  -7.54126  +1.91135  $ Upper grid plate hole, C4
 5011  c/z  -4.35356  -7.54126  +1.91135  $ Upper grid plate hole, C5
 5012  c/z  -6.53034  -3.76936  +1.91135  $ Upper grid plate hole, C6
 5013  c/z  -8.70712  +0.00000  +1.91135  $ Upper grid plate hole, C7
 5014  c/z  -6.53034  +3.76936  +1.91135  $ Upper grid plate hole, C8
 5015  c/z  -4.35356  +7.54126  +1.91135  $ Upper grid plate hole, C9
 5016  c/z  -0.00000  +7.54126  +1.91135  $ Upper grid plate hole, C10
 5017  c/z  +4.35356  +7.54126  +1.91135  $ Upper grid plate hole, C11
 5018  c/z  +6.53034  +3.76936  +1.91135  $ Upper grid plate hole, C12
 5019  c/z +13.06068  +0.00000  +1.91135  $ Upper grid plate hole, D1
 5020  c/z +10.88390  -3.76936  +1.91135  $ Upper grid plate hole, D2
 5021  c/z  +8.70712  -7.54126  +1.91135  $ Upper grid plate hole, D3
 5022  c/z  +6.53034 -11.31062  +1.91135  $ Upper grid plate hole, D4
 5023  c/z  +2.17678 -11.31062  +1.91135  $ Upper grid plate hole, D5
 5024  c/z  -2.17678 -11.31062  +1.91135  $ Upper grid plate hole, D6
 5025  c/z  -6.53034 -11.31062  +1.91135  $ Upper grid plate hole, D7
 5026  c/z  -8.70712  -7.54126  +1.91135  $ Upper grid plate hole, D8
 5027  c/z -10.88390  -3.76936  +1.91135  $ Upper grid plate hole, D9
 5028  c/z -13.06068  +0.00000  +1.91135  $ Upper grid plate hole, D10
 5029  c/z -10.88390  +3.76936  +1.91135  $ Upper grid plate hole, D11
 5030  c/z  -8.70712  +7.54126  +1.91135  $ Upper grid plate hole, D12
 5031  c/z  -6.53034 +11.31062  +1.91135  $ Upper grid plate hole, D13
 5032  c/z  -2.17678 +11.31062  +1.91135  $ Upper grid plate hole, D14
 5033  c/z  +2.17678 +11.31062  +1.91135  $ Upper grid plate hole, D15
 5034  c/z  +6.53034 +11.31062  +1.91135  $ Upper grid plate hole, D16
 5035  c/z  +8.70712  +7.54126  +1.91135  $ Upper grid plate hole, D17
 5036  c/z +10.88390  +3.76936  +1.91135  $ Upper grid plate hole, D18
 5037  c/z +17.41424  +0.00000  +1.91135  $ Upper grid plate hole, E1
 5038  c/z +15.23746  -3.76936  +1.91135  $ Upper grid plate hole, E2
 5039  c/z +13.06068  -7.54126  +1.91135  $ Upper grid plate hole, E3
 5040  c/z +10.88390 -11.31062  +1.91135  $ Upper grid plate hole, E4
 5041  c/z  +8.70712 -15.08252  +1.91135  $ Upper grid plate hole, E5
 5042  c/z  +4.35356 -15.08252  +1.91135  $ Upper grid plate hole, E6
 5043  c/z  -0.00000 -15.08252  +1.91135  $ Upper grid plate hole, E7
 5044  c/z  -4.35356 -15.08252  +1.91135  $ Upper grid plate hole, E8
 5045  c/z  -8.70712 -15.08252  +1.91135  $ Upper grid plate hole, E9
 5046  c/z -10.88390 -11.31062  +1.91135  $ Upper grid plate hole, E10
 5047  c/z -13.06068  -7.54126  +1.91135  $ Upper grid plate hole, E11
 5048  c/z -15.23746  -3.76936  +1.91135  $ Upper grid plate hole, E12
 5049  c/z -17.41424  +0.00000  +1.91135  $ Upper grid plate hole, E13
 5050  c/z -15.23746  +3.76936  +1.91135  $ Upper grid plate hole, E14
 5051  c/z -13.06068  +7.54126  +1.91135  $ Upper grid plate hole, E15
 5052  c/z -10.88390 +11.31062  +1.91135  $ Upper grid plate hole, E16
 5053  c/z  -8.70712 +15.08252  +1.91135  $ Upper grid plate hole, E17
 5054  c/z  -4.35356 +15.08252  +1.91135  $ Upper grid plate hole, E18
 5055  c/z  -0.00000 +15.08252  +1.91135  $ Upper grid plate hole, E19
 5056  c/z  +4.35356 +15.08252  +1.91135  $ Upper grid plate hole, E20
 5057  c/z  +8.70712 +15.08252  +1.91135  $ Upper grid plate hole, E21
 5058  c/z +10.88390 +11.31062  +1.91135  $ Upper grid plate hole, E22
 5059  c/z +13.06068  +7.54126  +1.91135  $ Upper grid plate hole, E23
 5060  c/z +15.23746  +3.76936  +1.91135  $ Upper grid plate hole, E24
 5061  c/z +21.76780  +0.00000  +1.91135  $ Upper grid plate hole, F1
 5062  c/z +19.59102  -3.76936  +1.91135  $ Upper grid plate hole, F2
 5063  c/z +17.41424  -7.54126  +1.91135  $ Upper grid plate hole, F3
 5064  c/z +15.23746 -11.31062  +1.91135  $ Upper grid plate hole, F4
 5065  c/z +13.06068 -15.08252  +1.91135  $ Upper grid plate hole, F5
 5066  c/z +10.88390 -18.85188  +1.91135  $ Upper grid plate hole, F6
 5067  c/z  +6.53034 -18.85188  +1.91135  $ Upper grid plate hole, F7
 5068  c/z  +2.17678 -18.85188  +1.91135  $ Upper grid plate hole, F8
```

```
 5069  c/z  -2.17678 -18.85188  +1.91135  $ Upper grid plate hole, F9
 5070  c/z  -6.53034 -18.85188  +1.91135  $ Upper grid plate hole, F10
 5071  c/z -10.88390 -18.85188  +1.91135  $ Upper grid plate hole, F11
 5072  c/z -13.06068 -15.08252  +1.91135  $ Upper grid plate hole, F12
 5073  c/z -15.23746 -11.31062  +1.91135  $ Upper grid plate hole, F13
 5074  c/z -17.41424  -7.54126  +1.91135  $ Upper grid plate hole, F14
 5075  c/z -19.59102  -3.76936  +1.91135  $ Upper grid plate hole, F15
 5076  c/z -21.76780  +0.00000  +1.91135  $ Upper grid plate hole, F16
 5077  c/z -19.59102  +3.76936  +1.91135  $ Upper grid plate hole, F17
 5078  c/z -17.41424  +7.54126  +1.91135  $ Upper grid plate hole, F18
 5079  c/z -15.23746 +11.31062  +1.91135  $ Upper grid plate hole, F19
 5080  c/z -13.06068 +15.08252  +1.91135  $ Upper grid plate hole, F20
 5081  c/z -10.88390 +18.85188  +1.91135  $ Upper grid plate hole, F21
 5082  c/z  -6.53034 +18.85188  +1.91135  $ Upper grid plate hole, F22
 5083  c/z  -2.17678 +18.85188  +1.91135  $ Upper grid plate hole, F23
 5084  c/z  +2.17678 +18.85188  +1.91135  $ Upper grid plate hole, F24
 5085  c/z  +6.53034 +18.85188  +1.91135  $ Upper grid plate hole, F25
 5086  c/z +10.88390 +18.85188  +1.91135  $ Upper grid plate hole, F26
 5087  c/z +13.06068 +15.08252  +1.91135  $ Upper grid plate hole, F27
 5088  c/z +15.23746 +11.31062  +1.91135  $ Upper grid plate hole, F28
 5089  c/z +17.41424  +7.54126  +1.91135  $ Upper grid plate hole, F29
 5090  c/z +19.59102  +3.76936  +1.91135  $ Upper grid plate hole, F30
 5091  c/z +23.94458  -3.76936  +1.91135  $ Upper grid plate hole, G2
 5092  c/z +21.76780  -7.54126  +1.91135  $ Upper grid plate hole, G3
 5093  c/z +19.59102 -11.31062  +1.91135  $ Upper grid plate hole, G4
 5094  c/z +17.41424 -15.08252  +1.91135  $ Upper grid plate hole, G5
 5095  c/z +15.23746 -18.85188  +1.91135  $ Upper grid plate hole, G6
 5096  c/z  +8.70712 -22.62124  +1.91135  $ Upper grid plate hole, G8
 5097  c/z  +4.35356 -22.62124  +1.91135  $ Upper grid plate hole, G9
 5098  c/z  -0.00000 -22.62124  +1.91135  $ Upper grid plate hole, G10
 5099  c/z  -4.35356 -22.62124  +1.91135  $ Upper grid plate hole, G11
 5100  c/z  -8.70712 -22.62124  +1.91135  $ Upper grid plate hole, G12
 5101  c/z -15.23746 -18.85188  +1.91135  $ Upper grid plate hole, G14
 5102  c/z -17.41424 -15.08252  +1.91135  $ Upper grid plate hole, G15
 5103  c/z -19.59102 -11.31062  +1.91135  $ Upper grid plate hole, G16
 5104  c/z -21.76780  -7.54126  +1.91135  $ Upper grid plate hole, G17
 5105  c/z -23.94458  -3.76936  +1.91135  $ Upper grid plate hole, G18
 5106  c/z -23.94458  +3.76936  +1.91135  $ Upper grid plate hole, G20
 5107  c/z -21.76780  +7.54126  +1.91135  $ Upper grid plate hole, G21
 5108  c/z -19.59102 +11.31062  +1.91135  $ Upper grid plate hole, G22
 5109  c/z -17.41424 +15.08252  +1.91135  $ Upper grid plate hole, G23
 5110  c/z -15.23746 +18.85188  +1.91135  $ Upper grid plate hole, G24
 5111  c/z  -8.70712 +22.62124  +1.91135  $ Upper grid plate hole, G26
 5112  c/z  -4.35356 +22.62124  +1.91135  $ Upper grid plate hole, G27
 5113  c/z  +4.35356 +22.62124  +1.91135  $ Upper grid plate hole, G29
 5114  c/z  -0.00000 +22.62124  +1.91135  $ Upper grid plate hole, G28
 5115  c/z  +8.70712 +22.62124  +1.91135  $ Upper grid plate hole, G30
 5116  c/z +15.23746 +18.85188  +1.91135  $ Upper grid plate hole, G32
 5117  c/z +17.41424 +15.08252  +1.91135  $ Upper grid plate hole, G33
 5118  c/z +19.59102 +11.31062  +1.91135  $ Upper grid plate hole, G34
 5119  c/z +21.76780  +7.54126  +1.91135  $ Upper grid plate hole, G35
 5120  c/z +23.94458  +3.76936  +1.91135  $ Upper grid plate hole, G36
c
c ----------------------
c Cut planes for tallies
c ----------------------
 6000  pz   +32
 6001  pz   +31
 6002  pz   +30
 6003  pz   +29
 6004  pz   +28
 6005  pz   +27
 6006  pz   +26
 6007  pz   +25
 6008  pz   +24
 6009  pz   +23
 6010  pz   +22
 6011  pz   +21
 6012  pz   +20
 6013  pz   +19
 6014  pz   +18
 6015  pz   +17
 6016  pz   +16
 6017  pz   +15
 6018  pz   +14
 6019  pz   +13
```

```
 6020  pz   +12
 6021  pz   +11
 6022  pz   +10
 6023  pz    +9
 6024  pz    +8
 6025  pz    +7
 6026  pz    +6
 6027  pz    +5
 6028  pz    +4
 6029  pz    +3
 6030  pz    +2
 6031  pz    +1
 6032  pz    +0
 6033  pz    -1
 6034  pz    -2
 6035  pz    -3
 6036  pz    -4
 6037  pz    -5
 6038  pz    -6
 6039  pz    -7
 6040  pz    -8
 6041  pz    -9
 6042  pz   -10
 6043  pz   -11
 6044  pz   -12
 6045  pz   -13
 6046  pz   -14
 6047  pz   -15
 6048  pz   -16
 6049  pz   -17
 6050  pz   -18
 6051  pz   -19
 6052  pz   -20
 6053  pz   -21
 6054  pz   -22
 6055  pz   -23
 6056  pz   -24
 6057  pz   -25
 6058  pz   -26
 6059  pz   -27
 6060  pz   -28
 6061  pz   -29
 6062  pz   -30
 6063  pz   -31
 6064  pz   -32
 6065  pz   -33
 6066  pz   -34
 6067  pz   -35
 6068  pz   -36
c
 7000  pz   +30.861
 7001  pz   +27.305
 7002  pz   +25.781
 7003  pz   +22.225
 7004  pz   +20.701
 7005  pz   +17.145
 7006  pz   +15.621
 7007  pz   +12.065
 7008  pz   +10.541
 7009  pz    +6.985
 7010  pz    +5.461
 7011  pz    +1.905
 7012  pz    +0.381
 7013  pz    -3.175
 7014  pz    -4.699
 7015  pz    -8.255
 7016  pz    -9.779
 7017  pz   -13.335
 7018  pz   -14.859
 7019  pz   -18.415
 7020  pz   -19.939
 7021  pz   -23.495
 7022  pz   -25.019
 7023  pz   -28.575
 7024  pz   -30.099
 7025  pz   -33.655
```

```
 7026  pz   -35.179
c
 8000  pz     +30.7975              $ Bottom of upper grid plate region
 8001  pz     +27.7368              $ Top of graphite region
 8002  pz     +19.05                $ Top of fuel region
 8003  pz     -19.05                $ Bottom of fuel region
 8004  pz     -27.7368              $ Bottom of graphite region
 8005  pz     -33.17875             $ Top of lower grid plate region
c
c ---------------------------------------------------------------
c              End of Surface Card Specification
c ---------------------------------------------------------------

c ---------------------------------------------------------------
c           Beginning of Material Card Specification
c ---------------------------------------------------------------
c -------------------------
c Beam tube transformations
c -------------------------
c tr1: Through port, small, BP1
c tr2: Tangential port, small, BP2
c tr3: Radial port, large, BP3
c tr4: Radial port, small, BP4
c tr5: Through port, large, BP5
c
 *tr1  0.0      -35.255  -6.985   00  90  90    90  00  90
 *tr2  +35.255  -06.222  -6.985   30 120  90    60  30  90
 *tr3  0.0      +25.600  -6.985   00  90  90    90  00  90
 *tr4  -22.871  +13.216  -6.985   60  30  90   150  60  90
 *tr5  0.0      -35.255  -6.985   00  90  90    90  00  90
c
c the '*' just makes the transformation in degrees
c
c ---------------------------
c Control rod transformations
c ---------------------------
c Shutdown condition - 000 units
c Low power critical - 525 units
c Design high power - 700 units
c Full out condition - 960 units
c
 tr6  0  0  00.00     1 0 0  0 1 0
 tr7  0  0  15.00     1 0 0  0 1 0               $ Formerly 19.05, 8.33, 12.37
 tr8  0  0  27.78     1 0 0  0 1 0
 tr9  0  0  38.10     1 0 0  0 1 0
c
c ----------------------------------
c Mapping experiment transformations
c ----------------------------------
 tr10    +2.17678  -1.2573  0.0
 tr11   +15.23746  -1.2573  0.0
 tr12   +19.59102  -1.2573  0.0
 tr13   +23.94458  -1.2573  0.0
c
c ------------------------------------
c Irradiation facility transformations
c ------------------------------------
 tr20   -15.23746 -8.79856  0.0       $ Center of 3L irradiator
c tr50  +15.23746 -11.31062 0.0       $ Center of 6L irradiator
c tr50  +10.8839  +8.79856  0.0       $ Center of 3L irradiator
 tr50   -15.24    -8.80     0.0       $ Center of 3L irradiator
c
c -------------------------------
c Grid plate hole transformations
c -------------------------------
 tr100   -0.00000  +0.00000  0.0    $  A1
 tr101   +4.35356  +0.00000  0.0    $  B1
 tr102   +2.17678  -3.76936  0.0    $  B2
 tr103   -2.17678  -3.76936  0.0    $  B3
 tr104   -4.35356  +0.00000  0.0    $  B4
 tr105   -2.17678  +3.76936  0.0    $  B5
 tr106   +2.17678  +3.76936  0.0    $  B6
 tr107   +8.70712  +0.00000  0.0    $  C1
 tr108   +6.53034  -3.76936  0.0    $  C2
 tr109   +4.35356  -7.54126  0.0    $  C3
 tr110   -0.00000  -7.54126  0.0    $  C4
```

```
tr111   -4.35356  -7.54126  0.0    $  C5
tr112   -6.53034  -3.76936  0.0    $  C6
tr113   -8.70712  +0.00000  0.0    $  C7
tr114   -6.53034  +3.76936  0.0    $  C8
tr115   -4.35356  +7.54126  0.0    $  C9
tr116   -0.00000  +7.54126  0.0    $  C10
tr117   +4.35356  +7.54126  0.0    $  C11
tr118   +6.53034  +3.76936  0.0    $  C12
tr119  +13.06068  +0.00000  0.0    $  D1
tr120  +10.88390  -3.76936  0.0    $  D2
tr121   +8.70712  -7.54126  0.0    $  D3
tr122   +6.53034 -11.31062  0.0    $  D4
tr123   +2.17678 -11.31062  0.0    $  D5
tr124   -2.17678 -11.31062  0.0    $  D6
tr125   -6.53034 -11.31062  0.0    $  D7
tr126   -8.70712  -7.54126  0.0    $  D8
tr127  -10.88390  -3.76936  0.0    $  D9
tr128  -13.06068  +0.00000  0.0    $  D10
tr129  -10.88390  +3.76936  0.0    $  D11
tr130   -8.70712  +7.54126  0.0    $  D12
tr131   -6.53034 +11.31062  0.0    $  D13
tr132   -2.17678 +11.31062  0.0    $  D14
tr133   +2.17678 +11.31062  0.0    $  D15
tr134   +6.53034 +11.31062  0.0    $  D16
tr135   +8.70712  +7.54126  0.0    $  D17
tr136  +10.88390  +3.76936  0.0    $  D18
tr137  +17.41424  +0.00000  0.0    $  E1
tr138  +15.23746  -3.76936  0.0    $  E2
tr139  +13.06068  -7.54126  0.0    $  E3
tr140  +10.88390 -11.31062  0.0    $  E4
tr141   +8.70712 -15.08252  0.0    $  E5
tr142   +4.35356 -15.08252  0.0    $  E6
tr143   -0.00000 -15.08252  0.0    $  E7
tr144   -4.35356 -15.08252  0.0    $  E8
tr145   -8.70712 -15.08252  0.0    $  E9
tr146  -10.88390 -11.31062  0.0    $  E10
tr147  -13.06068  -7.54126  0.0    $  E11
tr148  -15.23746  -3.76936  0.0    $  E12
tr149  -17.41424  +0.00000  0.0    $  E13
tr150  -15.23746  +3.76936  0.0    $  E14
tr151  -13.06068  +7.54126  0.0    $  E15
tr152  -10.88390 +11.31062  0.0    $  E16
tr153   -8.70712 +15.08252  0.0    $  E17
tr154   -4.35356 +15.08252  0.0    $  E18
tr155   -0.00000 +15.08252  0.0    $  E19
tr156   +4.35356 +15.08252  0.0    $  E20
tr157   +8.70712 +15.08252  0.0    $  E21
tr158  +10.88390 +11.31062  0.0    $  E22
tr159  +13.06068  +7.54126  0.0    $  E23
tr160  +15.23746  +3.76936  0.0    $  E24
tr161  +21.76780  +0.00000  0.0    $  F1
tr162  +19.59102  -3.76936  0.0    $  F2
tr163  +17.41424  -7.54126  0.0    $  F3
tr164  +15.23746 -11.31062  0.0    $  F4
tr165  +13.06068 -15.08252  0.0    $  F5
tr166  +10.88390 -18.85188  0.0    $  F6
tr167   +6.53034 -18.85188  0.0    $  F7
tr168   +2.17678 -18.85188  0.0    $  F8
tr169   -2.17678 -18.85188  0.0    $  F9
tr170   -6.53034 -18.85188  0.0    $  F10
tr171  -10.88390 -18.85188  0.0    $  F11
tr172  -13.06068 -15.08252  0.0    $  F12
tr173  -15.23746 -11.31062  0.0    $  F13
tr174  -17.41424  -7.54126  0.0    $  F14
tr175  -19.59102  -3.76936  0.0    $  F15
tr176  -21.76780  +0.00000  0.0    $  F16
tr177  -19.59102  +3.76936  0.0    $  F17
tr178  -17.41424  +7.54126  0.0    $  F18
tr179  -15.23746 +11.31062  0.0    $  F19
tr180  -13.06068 +15.08252  0.0    $  F20
tr181  -10.88390 +18.85188  0.0    $  F21
tr182   -6.53034 +18.85188  0.0    $  F22
tr183   -2.17678 +18.85188  0.0    $  F23
tr184   +2.17678 +18.85188  0.0    $  F24
tr185   +6.53034 +18.85188  0.0    $  F25
tr186  +10.88390 +18.85188  0.0    $  F26
```

```
 tr187  +13.06068 +15.08252  0.0    $  F27
 tr188  +15.23746 +11.31062  0.0    $  F28
 tr189  +17.41424  +7.54126  0.0    $  F29
 tr190  +19.59102  +3.76936  0.0    $  F30
 tr191  +23.94458  -3.76936  0.0    $  G2
 tr192  +21.76780  -7.54126  0.0    $  G3
 tr193  +19.59102 -11.31062  0.0    $  G4
 tr194  +17.41424 -15.08252  0.0    $  G5
 tr195  +15.23746 -18.85188  0.0    $  G6
 tr196   +8.70712 -22.62124  0.0    $  G8
 tr197   +4.35356 -22.62124  0.0    $  G9
 tr198   -0.00000 -22.62124  0.0    $  G10
 tr199   -4.35356 -22.62124  0.0    $  G11
 tr200   -8.70712 -22.62124  0.0    $  G12
 tr201  -15.23746 -18.85188  0.0    $  G14
 tr202  -17.41424 -15.08252  0.0    $  G15
 tr203  -19.59102 -11.31062  0.0    $  G16
 tr204  -21.76780  -7.54126  0.0    $  G17
 tr205  -23.94458  -3.76936  0.0    $  G18
 tr206  -23.94458  +3.76936  0.0    $  G20
 tr207  -21.76780  +7.54126  0.0    $  G21
 tr208  -19.59102 +11.31062  0.0    $  G22
 tr209  -17.41424 +15.08252  0.0    $  G23
 tr210  -15.23746 +18.85188  0.0    $  G24
 tr211   -8.70712 +22.62124  0.0    $  G26
 tr212   -4.35356 +22.62124  0.0    $  G27
 tr213   +4.35356 +22.62124  0.0    $  G29
 tr214   -0.00000 +22.62124  0.0    $  G28
 tr215   +8.70712 +22.62124  0.0    $  G30
 tr216  +15.23746 +18.85188  0.0    $  G32
 tr217  +17.41424 +15.08252  0.0    $  G33
 tr218  +19.59102 +11.31062  0.0    $  G34
 tr219  +21.76780  +7.54126  0.0    $  G35
 tr220  +23.94458  +3.76936  0.0    $  G36
c
c ---------------------------
c Reactor component materials
c ---------------------------
c m1 - water
c m2 - aluminum (structural) type 6061
c m3 - stainless steel (structural) type 304
c m4 - graphite (carbon)
c m5 - fresh U-ZrH fuel
c m6 - B4C (boron carbide)
c m7 - zirconium (rod)
c m8 - air
c m10 - cadmium (neutron absorber liner)
c m11 - lead (neutron absorber liner)
c m54 - ar cme
 m1   1001         0.66667
      8016         0.33333
mt1  lwtr.60t                   $294K cme
c mpn1  0 0
 m2  13027        -0.9685
     26000.50c    -0.0070
     29000.50c    -0.0025
     14000.60c    -0.0060
     12000.66c    -0.0110
     24000.50c    -0.0035
     25055        -0.0015
c mpn2 0 0 0 0 0 0 0 0
 m3  26000.50c    -0.6785
      6000        -0.0080
     14000.60c    -0.0100
     24000.50c    -0.1800
     28000.50c    -0.0980
     25055        -0.0180
     15031        -0.0045
     16000.66c    -0.0030
c mpn3  0 0 0 0 0 0 0 0 0
 m4    6000         1.0
mt4  grph.60t                     $ 294K cme
c mpn4  0
 m5  40090.71c        -0.462589265
     40091.71c        -0.100879525
     40092.71c        -0.154196422
```

```
     40094.71c        -0.156264362
     40096.71c        -0.025174926
      1001.71c        -0.0158955
     92238.71c        -0.068170
     92235.71c        -0.016830
c mpn5 0 0 82208 82208
mt5  zr/h.62t               $600K cme
     h/zr.62t               $600K cme
 m6    5010        0.1584
       5011        0.6416
       6000        0.2
c mpn6  0 0 0
 m7   40090       51.45
      40091       11.22
      40092       17.15
      40094       17.38
      40096       2.8
c mpn7  0
 m8    8016       -0.23
       7014       -0.77
c mpn8  0 0
 m10  48000.42c    1.0
c mpn10 0
 m11  82000.42c   -1.0
c mpn11 0
 m12  28058        1              $  nickel     (n,p)  a/o  68.0
 m13  28064        1              $  nickel     (n,g)  a/o   0.9
 m14  79197        1              $  gold       (n,g)  a/o 100.0
 m15  29063        1              $  copper     (n,g)  a/o  69.1
 m16  26058        1              $  iron       (n,g)  a/o   0.2
 m17  26054        1              $  iron       (n,p)  a/o   5.8
 m18  42098        1              $  molybdenum (n,g)  a/o  24.1
 m19  27059        1              $  cobalt     (n,g)  a/o 100.0
 m20  13027        1              $  aluminum   (n,g)  a/o 100.0
c
c -------
c Tallies
c -------
c
c f14:n    (1752<u=82)
c fc14     Flux tally for CT
c e14      0.50e-6 1.00e-2 1.50e+1  T
c
c f24:n    (1752<u=82)
c fc24     Flux tally for CT spectrum
c e24     1.000E-11 5.000E-09 1.000E-08 1.500E-08 2.000E-08 2.500E-08
c          3.000E-08 3.500E-08 4.200E-08 5.000E-08 5.800E-08 6.700E-08
c          8.000E-08 1.000E-07 1.520E-07 2.510E-07 4.140E-07 6.830E-07
c          1.125E-06 1.855E-06 3.059E-06 5.040E-06 8.315E-06 1.371E-05
c          2.260E-05 3.727E-05 6.144E-05 1.013E-04 1.670E-04 2.754E-04
c          4.540E-04 7.485E-04 1.234E-03 2.035E-03 2.404E-03 2.840E-03
c          3.355E-03 5.531E-03 9.119E-03 1.503E-02 1.989E-02 2.554E-02
c          4.087E-02 6.738E-02 1.111E-01 1.832E-01 3.020E-01 3.887E-01
c          4.979E-01 6.392E-01 8.208E-01 1.108 1.353 1.737
c          2.231 2.865 3.678 4.965 6.065 10.0
c          14.91 16.90 20.00 25.00 T
c
c  f74:n    455                                                    $(455<u=45) this is old input
c fc74     Flux tally for 3L(Pb) profile
c fs74     6002 6007 6012 6017 6022 6027 6032 6037 6042 6047 6052 6057
c fq74     s f
c
c f84:n    (455<u=45)                                                     $3L tally
c fc84     Flux tally for 3L(Pb) spectrum
c fs84     6002 6007 6012 6017 6022 6027 6032 6037 6042 6047 6052 6057
c e84      1.000E-11 5.000E-09 1.000E-08 1.500E-08 2.000E-08 2.500E-08
c          3.000E-08 3.500E-08 4.200E-08 5.000E-08 5.800E-08 6.700E-08
c          8.000E-08 1.000E-07 1.520E-07 2.510E-07 4.140E-07 6.830E-07
c          1.125E-06 1.855E-06 3.059E-06 5.040E-06 8.315E-06 1.371E-05
c          2.260E-05 3.727E-05 6.144E-05 1.013E-04 1.670E-04 2.754E-04
c          4.540E-04 7.485E-04 1.234E-03 2.035E-03 2.404E-03 2.840E-03
c          3.355E-03 5.531E-03 9.119E-03 1.503E-02 1.989E-02 2.554E-02
c         4.087E-02 6.738E-02 1.111E-01 1.832E-01 3.020E-01 3.887E-01
c         4.979E-01 6.392E-01 8.208E-01 1.108 1.353 1.737
c          2.231 2.865 3.678 4.965 6.065 10.0
c          14.91 16.90 20.00 25.00 T
```

```
c
c f15:n  -15.24 -8.8 0 0                                                    $Point detector at middle of 3L
c fc15   Point detector at middle of 3L
c  e15      1.000E-11 5.000E-09 1.000E-08 1.500E-08 2.000E-08 2.500E-08
c           3.000E-08 3.500E-08 4.200E-08 5.000E-08 5.800E-08 6.700E-08
c           8.000E-08 1.000E-07 1.520E-07 2.510E-07 4.140E-07 6.830E-07
c           1.125E-06 1.855E-06 3.059E-06 5.040E-06 8.315E-06 1.371E-05
c           2.260E-05 3.727E-05 6.144E-05 1.013E-04 1.670E-04 2.754E-04
c           4.540E-04 7.485E-04 1.234E-03 2.035E-03 2.404E-03 2.840E-03
c           3.355E-03 5.531E-03 9.119E-03 1.503E-02 1.989E-02 2.554E-02
c           4.087E-02 6.738E-02 1.111E-01 1.832E-01 3.020E-01 3.887E-01
c           4.979E-01 6.392E-01 8.208E-01 1.108 1.353 1.737
c           2.231 2.865 3.678 4.965 6.065 10.0
c           14.91 16.90 20.00 25.00 T
c
c f25:n  -15.24 -8.8 0 2.4                                                  $Ring detector at middle of 3L
c fc25   Ring detector at middle of 3L
c  e25      1.000E-11 5.000E-09 1.000E-08 1.500E-08 2.000E-08 2.500E-08
c           3.000E-08 3.500E-08 4.200E-08 5.000E-08 5.800E-08 6.700E-08
c           8.000E-08 1.000E-07 1.520E-07 2.510E-07 4.140E-07 6.830E-07
c           1.125E-06 1.855E-06 3.059E-06 5.040E-06 8.315E-06 1.371E-05
c           2.260E-05 3.727E-05 6.144E-05 1.013E-04 1.670E-04 2.754E-04
c           4.540E-04 7.485E-04 1.234E-03 2.035E-03 2.404E-03 2.840E-03
c           3.355E-03 5.531E-03 9.119E-03 1.503E-02 1.989E-02 2.554E-02
c           4.087E-02 6.738E-02 1.111E-01 1.832E-01 3.020E-01 3.887E-01
c           4.979E-01 6.392E-01 8.208E-01 1.108 1.353 1.737
c           2.231 2.865 3.678 4.965 6.065 10.0
c           14.91 16.90 20.00 25.00 T
c
c f35:n  -15.24 -8.8 -26.19375 0
c fc35   Point Detector at bottom of 3L
c
c f45:n  -15.24 -8.8 -19 0
c fc45   Point detector at bottom of fuel in 3L
c
c f55:n  -15.24 -8.8 +19 0
c fc55   Point detector at top of fuel in 3L
c
c f65:n  -15.24 -8.8 +30.7975 0
c fc65  Point detector at top of 3L
c f114:n   92
c fc114    Flux tally for RSR
c fs114    6022
c e114     0.50e-6 1.00e-2 1.50e+1  T
c
 f124:n   92
 fc124    Flux tally for RSR spectrum
c fs124             6022           $ 2nd segment is approx. sample location
c SAND-ii 620 group energy bins
e124 1.000E-10 1.050E-10 1.100E-10 1.150E-10 1.200E-10 1.275E-10
     1.350E-10 1.425E-10 1.500E-10 1.600E-10 1.700E-10 1.800E-10
     1.900E-10 2.000E-10 2.100E-10 2.200E-10 2.300E-10 2.400E-10
     2.550E-10 2.700E-10 2.800E-10 3.000E-10 3.200E-10 3.400E-10
     3.600E-10 3.800E-10 4.000E-10 4.250E-10 4.500E-10 4.750E-10
     5.000E-10 5.250E-10 5.500E-10 5.750E-10 6.000E-10 6.300E-10
     6.600E-10 6.900E-10 7.200E-10 7.600E-10 8.000E-10 8.400E-10
     8.800E-10 9.200E-10 9.600E-10 1.000E-09 1.050E-09 1.100E-09
     1.150E-09 1.200E-09 1.275E-09 1.350E-09 1.425E-09 1.500E-09
     1.600E-09 1.700E-09 1.800E-09 1.900E-09 2.000E-09 2.100E-09
     2.200E-09 2.300E-09 2.400E-09 2.550E-09 2.700E-09 2.800E-09
     3.000E-09 3.200E-09 3.400E-09 3.600E-09 3.800E-09 4.000E-09
     4.250E-09 4.500E-09 4.750E-09 5.000E-09 5.250E-09 5.500E-09
     5.750E-09 6.000E-09 6.300E-09 6.600E-09 6.900E-09 7.200E-09
     7.600E-09 8.000E-09 8.400E-09 8.800E-09 9.200E-09 9.600E-09
     1.000E-08 1.050E-08 1.100E-08 1.150E-08 1.200E-08 1.275E-08
     1.350E-08 1.425E-08 1.500E-08 1.600E-08 1.700E-08 1.800E-08
     1.900E-08 2.000E-08 2.100E-08 2.200E-08 2.300E-08 2.400E-08
     2.550E-08 2.700E-08 2.800E-08 3.000E-08 3.200E-08 3.400E-08
     3.600E-08 3.800E-08 4.000E-08 4.250E-08 4.500E-08 4.750E-08
     5.000E-08 5.250E-08 5.500E-08 5.750E-08 6.000E-08 6.300E-08
     6.600E-08 6.900E-08 7.200E-08 7.600E-08 8.000E-08 8.400E-08
     8.800E-08 9.200E-08 9.600E-08 1.000E-07 1.050E-07 1.100E-07
     1.150E-07 1.200E-07 1.275E-07 1.350E-07 1.425E-07 1.500E-07
     1.600E-07 1.700E-07 1.800E-07 1.900E-07 2.000E-07 2.100E-07
     2.200E-07 2.300E-07 2.400E-07 2.550E-07 2.700E-07 2.800E-07
     3.000E-07 3.200E-07 3.400E-07 3.600E-07 3.800E-07 4.000E-07
```

4.250E-07 4.500E-07 4.750E-07 5.000E-07 5.250E-07 5.500E-07
5.750E-07 6.000E-07 6.300E-07 6.600E-07 6.900E-07 7.200E-07
7.600E-07 8.000E-07 8.400E-07 8.800E-07 9.200E-07 9.600E-07
1.000E-06 1.050E-06 1.100E-06 1.150E-06 1.200E-06 1.275E-06
1.350E-06 1.425E-06 1.500E-06 1.600E-06 1.700E-06 1.800E-06
1.900E-06 2.000E-06 2.100E-06 2.200E-06 2.300E-06 2.400E-06
2.550E-06 2.700E-06 2.800E-06 3.000E-06 3.200E-06 3.400E-06
3.600E-06 3.800E-06 4.000E-06 4.250E-06 4.500E-06 4.750E-06
5.000E-06 5.250E-06 5.500E-06 5.750E-06 6.000E-06 6.300E-06
6.600E-06 6.900E-06 7.200E-06 7.600E-06 8.000E-06 8.400E-06
8.800E-06 9.200E-06 9.600E-06 1.000E-05 1.050E-05 1.100E-05
1.150E-05 1.200E-05 1.275E-05 1.350E-05 1.425E-05 1.500E-05
1.600E-05 1.700E-05 1.800E-05 1.900E-05 2.000E-05 2.100E-05
2.200E-05 2.300E-05 2.400E-05 2.550E-05 2.700E-05 2.800E-05
3.000E-05 3.200E-05 3.400E-05 3.600E-05 3.800E-05 4.000E-05
4.250E-05 4.500E-05 4.750E-05 5.000E-05 5.250E-05 5.500E-05
5.750E-05 6.000E-05 6.300E-05 6.600E-05 6.900E-05 7.200E-05
7.600E-05 8.000E-05 8.400E-05 8.800E-05 9.200E-05 9.600E-05
1.000E-04 1.050E-04 1.100E-04 1.150E-04 1.200E-04 1.275E-04
1.350E-04 1.425E-04 1.500E-04 1.600E-04 1.700E-04 1.800E-04
1.900E-04 2.000E-04 2.100E-04 2.200E-04 2.300E-04 2.400E-04
2.550E-04 2.700E-04 2.800E-04 3.000E-04 3.200E-04 3.400E-04
3.600E-04 3.800E-04 4.000E-04 4.250E-04 4.500E-04 4.750E-04
5.000E-04 5.250E-04 5.500E-04 5.750E-04 6.000E-04 6.300E-04
6.600E-04 6.900E-04 7.200E-04 7.600E-04 8.000E-04 8.400E-04
8.800E-04 9.200E-04 9.600E-04 1.000E-03 1.050E-03 1.100E-03
1.150E-03 1.200E-03 1.275E-03 1.350E-03 1.425E-03 1.500E-03
1.600E-03 1.700E-03 1.800E-03 1.900E-03 2.000E-03 2.100E-03
2.200E-03 2.300E-03 2.400E-03 2.550E-03 2.700E-03 2.800E-03
3.000E-03 3.200E-03 3.400E-03 3.600E-03 3.800E-03 4.000E-03
4.250E-03 4.500E-03 4.750E-03 5.000E-03 5.250E-03 5.500E-03
5.750E-03 6.000E-03 6.300E-03 6.600E-03 6.900E-03 7.200E-03
7.600E-03 8.000E-03 8.400E-03 8.800E-03 9.200E-03 9.600E-03
1.000E-02 1.050E-02 1.100E-02 1.150E-02 1.200E-02 1.275E-02
1.350E-02 1.425E-02 1.500E-02 1.600E-02 1.700E-02 1.800E-02
1.900E-02 2.000E-02 2.100E-02 2.200E-02 2.300E-02 2.400E-02
2.550E-02 2.700E-02 2.800E-02 3.000E-02 3.200E-02 3.400E-02
3.600E-02 3.800E-02 4.000E-02 4.250E-02 4.500E-02 4.750E-02
5.000E-02 5.250E-02 5.500E-02 5.750E-02 6.000E-02 6.300E-02
6.600E-02 6.900E-02 7.200E-02 7.600E-02 8.000E-02 8.400E-02
8.800E-02 9.200E-02 9.600E-02 1.000E-01 1.050E-01 1.100E-01
1.150E-01 1.200E-01 1.275E-01 1.350E-01 1.425E-01 1.500E-01
1.600E-01 1.700E-01 1.800E-01 1.900E-01 2.000E-01 2.100E-01
2.200E-01 2.300E-01 2.400E-01 2.550E-01 2.700E-01 2.800E-01
3.000E-01 3.200E-01 3.400E-01 3.600E-01 3.800E-01 4.000E-01
4.250E-01 4.500E-01 4.750E-01 5.000E-01 5.250E-01 5.500E-01
5.750E-01 6.000E-01 6.300E-01 6.600E-01 6.900E-01 7.200E-01
7.600E-01 8.000E-01 8.400E-01 8.800E-01 9.200E-01 9.600E-01
1.000E+00 1.100E+00 1.200E+00 1.300E+00 1.400E+00 1.500E+00
1.600E+00 1.700E+00 1.800E+00 1.900E+00 2.000E+00 2.100E+00
2.200E+00 2.300E+00 2.400E+00 2.500E+00 2.600E+00 2.700E+00
2.800E+00 2.900E+00 3.000E+00 3.100E+00 3.200E+00 3.300E+00
3.400E+00 3.500E+00 3.600E+00 3.700E+00 3.800E+00 3.900E+00
4.000E+00 4.100E+00 4.200E+00 4.300E+00 4.400E+00 4.500E+00
4.600E+00 4.700E+00 4.800E+00 4.900E+00 5.000E+00 5.100E+00
5.200E+00 5.300E+00 5.400E+00 5.500E+00 5.600E+00 5.700E+00
5.800E+00 5.900E+00 6.000E+00 6.100E+00 6.200E+00 6.300E+00
6.400E+00 6.500E+00 6.600E+00 6.700E+00 6.800E+00 6.900E+00
7.000E+00 7.100E+00 7.200E+00 7.300E+00 7.400E+00 7.500E+00
7.600E+00 7.700E+00 7.800E+00 7.900E+00 8.000E+00 8.100E+00
8.200E+00 8.300E+00 8.400E+00 8.500E+00 8.600E+00 8.700E+00
8.800E+00 8.900E+00 9.000E+00 9.100E+00 9.200E+00 9.300E+00
9.400E+00 9.500E+00 9.600E+00 9.700E+00 9.800E+00 9.900E+00
1.000E+01 1.010E+01 1.020E+01 1.030E+01 1.040E+01 1.050E+01
1.060E+01 1.070E+01 1.080E+01 1.090E+01 1.100E+01 1.110E+01
1.120E+01 1.130E+01 1.140E+01 1.150E+01 1.160E+01 1.170E+01
1.180E+01 1.190E+01 1.200E+01 1.210E+01 1.220E+01 1.230E+01
1.240E+01 1.250E+01 1.260E+01 1.270E+01 1.280E+01 1.290E+01
1.300E+01 1.310E+01 1.320E+01 1.330E+01 1.340E+01 1.350E+01
1.360E+01 1.370E+01 1.380E+01 1.390E+01 1.400E+01 1.410E+01
1.420E+01 1.430E+01 1.440E+01 1.450E+01 1.460E+01 1.470E+01
1.480E+01 1.490E+01 1.500E+01 1.510E+01 1.520E+01 1.530E+01
1.540E+01 1.550E+01 1.560E+01 1.570E+01 1.580E+01 1.590E+01
1.600E+01 1.610E+01 1.620E+01 1.630E+01 1.640E+01 1.650E+01
1.660E+01 1.670E+01 1.680E+01 1.690E+01 1.700E+01 1.710E+01
1.720E+01 1.730E+01 1.740E+01 1.750E+01 1.760E+01 1.770E+01

```
     1.780E+07 1.790E+07 1.800E+07 T
c e124    1.000E-11 5.000E-09 1.000E-08 1.500E-08 2.000E-08 2.500E-08
c          3.000E-08 3.500E-08 4.200E-08 5.000E-08 5.800E-08 6.700E-08
c          8.000E-08 1.000E-07 1.520E-07 2.510E-07 4.140E-07 6.830E-07
c          1.125E-06 1.855E-06 3.059E-06 5.040E-06 8.315E-06 1.371E-05
c          2.260E-05 3.727E-05 6.144E-05 1.013E-04 1.670E-04 2.754E-04
c          4.540E-04 7.485E-04 1.234E-03 2.035E-03 2.404E-03 2.840E-03
c          3.355E-03 5.531E-03 9.119E-03 1.503E-02 1.989E-02 2.554E-02
c          4.087E-02 6.738E-02 1.111E-01 1.832E-01 3.020E-01 3.887E-01
c          4.979E-01 6.392E-01 8.208E-01 1.108 1.353 1.737
c          2.231 2.865 3.678 4.965 6.065 10.0
c          14.91 16.90 20.00 25.00 T
c
c f184:n    (124<u=8)                                                    $TRIGA Fuel
c fc184     Flux tally for TRIGA Fuel spectrum
c e184      1.000E-11 5.000E-09 1.000E-08 1.500E-08 2.000E-08 2.500E-08
c          3.000E-08 3.500E-08 4.200E-08 5.000E-08 5.800E-08 6.700E-08
c          8.000E-08 1.000E-07 1.520E-07 2.510E-07 4.140E-07 6.830E-07
c          1.125E-06 1.855E-06 3.059E-06 5.040E-06 8.315E-06 1.371E-05
c          2.260E-05 3.727E-05 6.144E-05 1.013E-04 1.670E-04 2.754E-04
c          4.540E-04 7.485E-04 1.234E-03 2.035E-03 2.404E-03 2.840E-03
c          3.355E-03 5.531E-03 9.119E-03 1.503E-02 1.989E-02 2.554E-02
c          4.087E-02 6.738E-02 1.111E-01 1.832E-01 3.020E-01 3.887E-01
c          4.979E-01 6.392E-01 8.208E-01 1.108 1.353 1.737
c          2.231 2.865 3.678 4.965 6.065 10.0
c          14.91 16.90 20.00 25.00 T
c f134:n   (516<u=101)
c fc134    Flux tally for mapping experiment profile
c fs134    7001 7003 7005 7007 7009 7011 7013 7015 7017 7019 7021 7023 7025
c fq134    s f
c
c f204:n   (124<u=8) T
c fc204    Total fission power tally for fuel elements
c fm204    -3.84962E+02 5 -6
c fq204    f s
c
c f214:n   (138<u=9) T
c fc214    Total fission power tally for fuel followers
c fm214    -3.21529E+02 5 -6
c fq214    f s
c
c f224:n   (124<u=8)   T
c fc224    Total flux for fuel elements
c fq224    f s
c
c f234:n   (138<u=9) T
c fc234    Total flux for fuel followers
c fq234    f s
c
c f244:n   (124<u=8) (138<u=9)  T
c fc244    Total flux for fuel
c fq244    f s
c
c f314:n   (1752<u=82)
c fc314    Reaction rate tally for CT
c fm314    (1  14  102)
c
c f394:n   (455<u=45)
c fc394    Reaction rate tally for 3L(Cd) profile
c fs394    6002 6007 6012 6017 6022 6027 6032 6037 6042 6047 6052 6057
c fm394    (1  12  103)
c          (1  13  102)
c          (1  14  102)
c          (1  15  102)
c          (1  16  102)
c          (1  17  103)
c          (1  18  102)
c          (1  19  102)
c          (1  20  102)
c fq394    s f
c
c f414:n   92
c fc414    Reaction rate tally for RSR
c fs414    6022
c fm414    (1  12  103)
c          (1  14  102)
```

```
c          (1  19  102)
c fq414    s f
c
c f434:n   (516<u=101)
c fc434    Reaction rate tally for mapping experiment
c fm434    (1   12  103)
c fs434    7001 7003 7005 7007 7009 7011 7013 7015 7017 7019 7021 7023 7025
c fq434    s f
c
c f504:n   95  96 97 98 99
c fc504    BP Neutron Flux Tally by Three Energy Groups
c e504     0.50e-6 1.00e-2 1.50e+1  T
c
c f624:p   (455<u=45)
c fc624    Photon tally for 3L(Cd) profile
c fs624    6002 6007 6012 6017 6022 6027 6032 6037 6042 6047 6052 6057
c fq624    s f
c
c f644:n   (455<u=45)
c fc644    Flux tally for 3L(Cd) profile
c fs644    6002 6007 6012 6017 6022 6027 6032 6037 6042 6047 6052 6057
c e644     0.50e-6 1.00e-2 1.50e+1  T
c
c f654:n   (455<u=45)
c fc654    3L Neutron Tally for Calculation of Neutron Dose (Kerma)
c de654    2.50E-08 1.00E-07 1.00E-06 1.00E-05 1.00E-04 1.00E-03
c          1.00E-02 1.00E-01 5.00E-01 1 2 2.5 5 7 10 14 20
c df654    3.67E-06 3.67E-06 4.46E-06 4.54E-06 4.18E-06 3.76E-06
c          3.56E-06 2.17E-05 9.26E-05 1.32E-04 1.43E-04 1.25E-04
c          1.56E-04 1.47E-04 1.47E-04 2.08E-04 2.27E-04
c fs654    6002 6007 6012 6017 6022 6027 6032 6037 6042 6047 6052 6057
c fq654    s f
c
c f664:p   (455<u=45)
c fc664    3L Photon Tally for Calculation of Photon Dose (Kerma)
c de664    1.00E-02 3.00E-02 5.00E-02 7.00E-02 1.00E-01 1.50E-01
c          2.00E-01 2.50E-01 3.00E-01 0.35 0.4 0.45 0.5 0.55 0.6
c          0.65 0.7 0.8 1.0 1.4 1.8 2.2 2.6 2.8 3.25 3.75 4.25 4.75
c          5.0 5.25 5.75 6.25 6.75 7.5 9.0 11.0 13.0 15.0
c df664    3.96E-06 5.82E-07 2.90E-07 2.58E-07 2.83E-07 3.79E-07
c          5.01E-07 6.31E-07 7.59E-07 8.78E-07 9.85E-07 1.08E-06
c          1.17E-06 1.27E-06 1.36E-06 1.44E-06 1.52E-06 1.68E-06
c          1.98E-06 2.51E-06 2.99E-06 3.42E-06 3.82E-06 4.01E-06
c          4.41E-06 4.83E-06 5.23E-06 5.60E-06 5.80E-06 6.01E-06
c          6.37E-06 6.74E-06 7.11E-06 7.66E-06 8.77E-06 1.03E-05
c          1.18E-05 1.33E-05
c fs664    6002 6007 6012 6017 6022 6027 6032 6037 6042 6047 6052 6057
c fq664    s f
c
c f674:n   (455<u=45)
c fc674    3L Neutron Tally for Calculation of Hardness Factor
c de674    1.03E-10 1.08E-10 1.13E-10 1.18E-10 1.24E-10 1.31E-10 1.39E-10
c          1.46E-10 1.55E-10 1.65E-10 1.75E-10 1.85E-10 1.95E-10 2.05E-10
c          2.15E-10 2.25E-10 2.35E-10 2.48E-10 2.63E-10 2.75E-10 2.90E-10
c          3.10E-10 3.30E-10 3.50E-10 3.70E-10 3.90E-10 4.13E-10 4.38E-10
c          4.63E-10 4.88E-10 5.13E-10 5.38E-10 5.63E-10 5.88E-10 6.15E-10
c          6.45E-10 6.75E-10 7.05E-10 7.40E-10 7.80E-10 8.20E-10 8.60E-10
c          9.00E-10 9.40E-10 9.80E-10 1.03E-09 1.08E-09 1.13E-09 1.18E-09
c          1.24E-09 1.31E-09 1.39E-09 1.46E-09 1.55E-09 1.65E-09 1.75E-09
c          1.85E-09 1.95E-09 2.05E-09 2.15E-09 2.25E-09 2.35E-09 2.48E-09
c          2.63E-09 2.75E-09 2.90E-09 3.10E-09 3.30E-09 3.50E-09 3.70E-09
c          3.90E-09 4.13E-09 4.38E-09 4.63E-09 4.88E-09 5.13E-09 5.38E-09
c          5.63E-09 5.88E-09 6.15E-09 6.45E-09 6.75E-09 7.05E-09 7.40E-09
c          7.80E-09 8.20E-09 8.60E-09 9.00E-09 9.40E-09 9.80E-09 1.03E-08
c          1.08E-08 1.13E-08 1.18E-08 1.24E-08 1.31E-08 1.39E-08 1.46E-08
c          1.55E-08 1.65E-08 1.75E-08 1.85E-08 1.95E-08 2.05E-08 2.15E-08
c          2.25E-08 2.35E-08 2.48E-08 2.63E-08 2.75E-08 2.90E-08 3.10E-08
c          3.30E-08 3.50E-08 3.70E-08 3.90E-08 4.13E-08 4.38E-08 4.63E-08
c          4.88E-08 5.13E-08 5.38E-08 5.63E-08 5.88E-08 6.15E-08 6.45E-08
c          6.75E-08 7.05E-08 7.40E-08 7.80E-08 8.20E-08 8.60E-08 9.00E-08
c          9.40E-08 9.80E-08 1.03E-07 1.08E-07 1.13E-07 1.18E-07 1.24E-07
c          1.31E-07 1.39E-07 1.46E-07 1.55E-07 1.65E-07 1.75E-07 1.85E-07
c          1.95E-07 2.05E-07 2.15E-07 2.25E-07 2.35E-07 2.48E-07 2.63E-07
c          2.75E-07 2.90E-07 3.10E-07 3.30E-07 3.50E-07 3.70E-07 3.90E-07
c          4.13E-07 4.38E-07 4.63E-07 4.88E-07 5.13E-07 5.38E-07 5.63E-07
c          5.88E-07 6.15E-07 6.45E-07 6.75E-07 7.05E-07 7.40E-07 7.80E-07
```

```
c          8.20E-07 8.60E-07 9.00E-07 9.40E-07 9.80E-07 1.03E-06 1.08E-06
c          1.13E-06 1.18E-06 1.24E-06 1.31E-06 1.39E-06 1.46E-06 1.55E-06
c          1.65E-06 1.75E-06 1.85E-06 1.95E-06 2.05E-06 2.15E-06 2.25E-06
c          2.35E-06 2.48E-06 2.63E-06 2.75E-06 2.90E-06 3.10E-06 3.30E-06
c          3.50E-06 3.70E-06 3.90E-06 4.13E-06 4.38E-06 4.63E-06 4.88E-06
c          5.13E-06 5.38E-06 5.63E-06 5.88E-06 6.15E-06 6.45E-06 6.75E-06
c          7.05E-06 7.40E-06 7.80E-06 8.20E-06 8.60E-06 9.00E-06 9.40E-06
c          9.80E-06 1.03E-05 1.08E-05 1.13E-05 1.18E-05 1.24E-05 1.31E-05
c          1.39E-05 1.46E-05 1.55E-05 1.65E-05 1.75E-05 1.85E-05 1.95E-05
c          2.05E-05 2.15E-05 2.25E-05 2.35E-05 2.48E-05 2.63E-05 2.75E-05
c          2.90E-05 3.10E-05 3.30E-05 3.50E-05 3.70E-05 3.90E-05 4.13E-05
c          4.38E-05 4.63E-05 4.88E-05 5.13E-05 5.38E-05 5.63E-05 5.88E-05
c          6.15E-05 6.45E-05 6.75E-05 7.05E-05 7.40E-05 7.80E-05 8.20E-05
c          8.60E-05 9.00E-05 9.40E-05 9.80E-05 1.03E-04 1.08E-04 1.13E-04
c          1.18E-04 1.24E-04 1.31E-04 1.39E-04 1.46E-04 1.55E-04 1.65E-04
c          1.75E-04 1.85E-04 1.95E-04 2.05E-04 2.15E-04 2.25E-04 2.35E-04
c          2.48E-04 2.63E-04 2.75E-04 2.90E-04 3.10E-04 3.30E-04 3.50E-04
c          3.70E-04 3.90E-04 4.13E-04 4.38E-04 4.63E-04 4.88E-04 5.13E-04
c          5.38E-04 5.63E-04 5.88E-04 6.15E-04 6.45E-04 6.75E-04 7.05E-04
c          7.40E-04 7.80E-04 8.20E-04 8.60E-04 9.00E-04 9.40E-04 9.80E-04
c          1.03E-03 1.08E-03 1.13E-03 1.18E-03 1.24E-03 1.31E-03 1.39E-03
c          1.46E-03 1.55E-03 1.65E-03 1.75E-03 1.85E-03 1.95E-03 2.05E-03
c          2.15E-03 2.25E-03 2.35E-03 2.48E-03 2.63E-03 2.75E-03 2.90E-03
c          3.10E-03 3.30E-03 3.50E-03 3.70E-03 3.90E-03 4.13E-03 4.38E-03
c          4.63E-03 4.88E-03 5.13E-03 5.37E-03 5.63E-03 5.88E-03 6.15E-03
c          6.45E-03 6.75E-03 7.05E-03 7.40E-03 7.80E-03 8.20E-03 8.60E-03
c          9.00E-03 9.40E-03 9.80E-03 1.03E-02 1.08E-02 1.13E-02 1.18E-02
c          1.24E-02 1.31E-02 1.39E-02 1.46E-02 1.55E-02 1.65E-02 1.75E-02
c          1.85E-02 1.95E-02 2.05E-02 2.15E-02 2.25E-02 2.35E-02 2.48E-02
c          2.63E-02 2.75E-02 2.90E-02 3.10E-02 3.30E-02 3.50E-02 3.70E-02
c          3.90E-02 4.13E-02 4.38E-02 4.63E-02 4.88E-02 5.13E-02 5.38E-02
c          5.63E-02 5.88E-02 6.15E-02 6.45E-02 6.75E-02 7.05E-02 7.40E-02
c          7.80E-02 8.20E-02 8.60E-02 9.00E-02 9.40E-02 9.80E-02 0.1025
c          0.1075   0.1125   0.1175   0.12375  0.13125  0.13875  0.14625
c          0.155    0.165    0.175    0.185    0.195    0.205    0.215
c          0.225    0.235    0.2475   0.2625   0.275    0.29     0.31
c          0.33     0.35     0.37     0.39     0.4125   0.4375   0.4625
c          0.4875   0.5125   0.5375   0.5625   0.5875   0.615    0.645
c          0.675    0.705    0.74     0.78     0.82     0.86     0.9
c          0.94     0.98     1.05     1.15     1.25     1.35     1.45
c          1.55     1.65     1.75     1.85     1.95     2.05     2.15
c          2.25     2.35     2.45     2.55     2.65     2.75     2.85
c          2.95     3.05     3.15     3.25     3.35     3.45     3.55
c          3.65     3.75     3.85     3.95     4.05     4.15     4.25
c          4.35     4.45     4.55     4.65     4.75     4.85     4.95
c          5.05     5.15     5.25     5.35     5.45     5.55     5.65
c          5.75     5.85     5.95     6.05     6.15     6.25     6.35
c          6.45     6.55     6.65     6.75     6.85     6.95     7.05
c          7.15     7.25     7.35     7.45     7.55     7.65     7.75
c          7.85     7.95     8.05     8.15     8.25     8.35     8.45
c          8.55     8.65     8.75     8.85     8.95     9.05     9.15
c          9.25     9.35     9.45     9.55     9.65     9.75     9.85
c          9.95     10.05    10.15    10.25    10.35    10.45    10.55
c          10.65    10.75    10.85    10.95    11.05    11.15    11.25
c          11.35    11.45    11.55    11.65    11.75    11.85    11.95
c          12.05    12.15    12.25    12.35    12.45    12.55    12.65
c          12.75    12.85    12.95    13.05    13.15    13.25    13.35
c          13.45    13.55    13.65    13.75    13.85    13.95    14.05
c          14.15    14.25    14.35    14.45    14.55    14.65    14.75
c          14.85    14.95    15.05    15.15    15.25    15.35    15.45
c          15.55    15.65    15.75    15.85    15.95    16.05    16.15
c          16.25    16.35    16.45    16.55    16.65    16.75    16.85
c          16.95    17.05    17.15    17.25    17.35    17.45    17.55
c          17.65    17.75    17.85    17.95    18.05    18.15    18.25
c          18.35    18.45    18.55    18.65    18.75    18.85    18.95
c          19.05    19.15    19.25    19.35    19.45    19.55    19.65
c          19.75    19.85    19.95
c  df674   1.5471   1.5117   1.4764   1.445    1.4081   1.3668   1.3294
c          1.2948   1.2575   1.2189   1.1834   1.1511   1.1225   1.0945
c          1.0678   1.0447   1.0217   0.99545  0.96654  0.94426  0.91947
c          0.88938  0.86182  0.83681  0.81396  0.79319  0.77183  0.7487
c          0.72869  0.70929  0.69201  0.67559  0.66034  0.64626  0.63144
c          0.61669  0.60274  0.58979  0.57569  0.56079  0.54754  0.53445
c          0.52212  0.51126  0.50044  0.48942  0.47822  0.46705  0.45713
c          0.44546  0.43241  0.42057  0.40964  0.39784  0.38565  0.37444
c          0.36422  0.35519  0.34632  0.33791  0.3306   0.32333  0.31504
```

```
c          0.30591  0.29887  0.29105  0.28154  0.27283  0.26492  0.2577
c          0.25113  0.24438  0.23706  0.23072  0.22458  0.21911  0.21391
c          0.20908  0.20461  0.19992  0.19525  0.19082  0.18672  0.18225
c          0.17753  0.17332  0.16917  0.16525  0.1618   0.15837  0.15485
c          0.15125  0.14773  0.14461  0.14084  0.13677  0.13295  0.1295
c          0.12577  0.12187  0.11834  0.11522  0.11215  0.10936  0.10684
c          0.10435  0.10215  9.95E-02 9.66E-02 9.43E-02 9.19E-02 8.89E-02
c          8.61E-02 8.36E-02 8.13E-02 7.92E-02 7.70E-02 7.47E-02 7.27E-02
c          7.08E-02 6.90E-02 6.74E-02 6.59E-02 6.45E-02 6.31E-02 6.16E-02
c          6.03E-02 5.90E-02 5.77E-02 5.62E-02 5.48E-02 5.35E-02 5.23E-02
c          5.12E-02 5.02E-02 4.91E-02 4.80E-02 4.69E-02 4.59E-02 4.47E-02
c          4.35E-02 4.23E-02 4.12E-02 4.00E-02 3.88E-02 3.76E-02 3.65E-02
c          3.56E-02 3.47E-02 3.39E-02 3.31E-02 3.24E-02 3.16E-02 3.07E-02
c          3.00E-02 2.92E-02 2.82E-02 2.74E-02 2.65E-02 2.57E-02 2.51E-02
c          2.44E-02 2.37E-02 2.31E-02 2.25E-02 2.19E-02 2.14E-02 2.09E-02
c          2.05E-02 2.00E-02 1.96E-02 1.91E-02 1.87E-02 1.83E-02 1.78E-02
c          1.74E-02 1.70E-02 1.66E-02 1.62E-02 1.59E-02 1.55E-02 1.52E-02
c          1.48E-02 1.45E-02 1.41E-02 1.37E-02 1.33E-02 1.29E-02 1.26E-02
c          1.22E-02 1.18E-02 1.15E-02 1.12E-02 1.10E-02 1.07E-02 1.05E-02
c          1.03E-02 9.99E-03 9.71E-03 9.50E-03 9.24E-03 8.92E-03 8.64E-03
c          8.36E-03 8.12E-03 7.90E-03 7.68E-03 7.48E-03 7.27E-03 7.07E-03
c          6.89E-03 6.74E-03 6.59E-03 6.44E-03 6.30E-03 6.16E-03 6.03E-03
c          5.89E-03 5.76E-03 5.61E-03 5.48E-03 5.36E-03 5.24E-03 5.12E-03
c          5.00E-03 4.89E-03 4.79E-03 4.69E-03 4.59E-03 4.47E-03 4.35E-03
c          4.24E-03 4.13E-03 4.01E-03 3.88E-03 3.76E-03 3.65E-03 3.55E-03
c          3.46E-03 3.38E-03 3.31E-03 3.24E-03 3.16E-03 3.06E-03 3.00E-03
c          2.92E-03 2.82E-03 2.73E-03 2.65E-03 2.57E-03 2.50E-03 2.44E-03
c          2.37E-03 2.31E-03 2.25E-03 2.19E-03 2.14E-03 2.10E-03 2.05E-03
c          2.00E-03 1.96E-03 1.91E-03 1.87E-03 1.82E-03 1.78E-03 1.73E-03
c          1.69E-03 1.65E-03 1.62E-03 1.58E-03 1.55E-03 1.52E-03 1.48E-03
c          1.45E-03 1.41E-03 1.37E-03 1.33E-03 1.29E-03 1.25E-03 1.22E-03
c          1.32E-03 2.30E-03 3.42E-03 5.14E-03 7.47E-03 9.81E-03 1.21E-02
c          1.50E-02 1.72E-02 1.88E-02 2.07E-02 2.41E-02 2.85E-02 3.25E-02
c          3.45E-02 3.63E-02 3.92E-02 4.34E-02 4.75E-02 5.17E-02 5.54E-02
c          5.88E-02 6.22E-02 6.56E-02 6.89E-02 7.21E-02 7.53E-02 7.87E-02
c          8.35E-02 8.90E-02 9.40E-02 9.84E-02 0.1028   0.10719  0.11159
c          0.1168   0.12285  0.1289   0.13495  0.14249  0.15156  0.16064
c          0.16972  0.17996  0.19106  0.20215  0.21324  0.22433  0.2355
c          0.24679  0.25808  0.26937  0.28343  0.3002   0.31377  0.32985
c          0.35143  0.37279  0.39399  0.41513  0.43618  0.45989  0.48723
c          0.52114  0.60851  0.58219  0.60668  0.63186  0.65704  0.6847
c          0.71492  0.74514  0.77536  0.80966  0.84755  0.88541  0.92327
c          0.96113  0.99898  1.036    1.0762   1.121    1.1658   1.2108
c          1.2701   1.3422   1.4141   1.4853   1.5655   1.6551   1.7385
c          1.8209   1.9007   1.9792   2.0501   2.1161   2.1808   2.2613
c          2.3631   2.4527   2.5568   2.6896   2.8231   2.9491   2.9958
c          3.6977   3.2342   3.0268   2.8203   2.4702   1.847    1.4987
c          47.95    11.453   7.992    6.9729   7.1782   6.8319   6.5956
c          6.3106   6.1853   6.0401   5.8443   5.6119   5.4173   5.1978
c          4.876    4.4319   3.9828   3.3528   2.5526   1.8707   1.3509
c          4.3232   19.048   64.493   114.1    111.28   91.836   78.667
c          69.75    64.073   58.46    54.959   52.558   51.326   50.237
c          49.28    50.095   49.722   52.107   51.897   52.654   53.508
c          55.405   57.416   77.958   124.55   58.334   52.618   55.29
c          56.767   59.302   64.575   87.944   136.8    78.336   87.781
c          111.49   111.79   75.692   62.673   88.994   88.76    98.979
c          105.98   163.02   78.342   129.21   129.4    95.218   106.92
c          105.49   102.82   118.92   131.19   115.67   106.91   135.04
c          98.845   120.2    131.5    118.02   113.87   119.06   111.27
c          69.524   115.13   108.84   134.34   131.64   108.71   164.41
c          134.86   140.92   138.38   158.64   185.61   160.67   145.5
c          149.16   170.31   145.7    120.15   116.98   145.6    152.07
c          180.05   164.7    137.1    153      127.71   175.38   150.09
c          139.27   119.27   150.92   162.25   146.89   141.77   161.1
c          139.16   169.27   168.43   167.05   162.91   170.31   174.8
c          175.34   186.4    165      154.43   158.42   162.02   166.61
c          165.83   163.86   146.75   160.22   177.57   174.58   153.88
c          150.69   166.21   169.82   164.41   156.1    161.96   164.06
c          164.49   166.21   168.63   163.36   164.67   154.76   154.6
c          155.51   159      162.91   160.05   158.75   155.61   159.52
c          166.03   165.38   168.62   165.79   166.62   165.46   165.66
c          168.17   167.95   167.71   167.47   167.22   167.27   167.6
c          167.94   168.28   168.62   168.66   168.39   168.11   167.83
c          167.53   167.16   166.73   166.29   165.86   165.4    165.54
c          166.34   167.14   167.94   168.73   169.21   169.37   169.52
c          169.66   169.79   169.93   170.09   170.25   170.4    170.56
```

```
c          170.72   170.86   171.32   173.63   176.3    177.74   177.89
c          178.03   178.18   178.32   178.27   178.01   177.76   177.5
c          177.24   177.49   178.28   179.08   179.88   180.67   181.24
c          181.58   181.91   182.24   182.59   182.94   183.28   183.62
c          183.97   184.31   184.45   184.37   184.28   184.2    184.11
c          184      183.88   183.75   183.63   183.51   183.38   183.25
c          183.12   183      182.87
c fs674    6002 6007 6012 6017 6022 6027 6032 6037 6042 6047 6052 6057
c fq674    s f
c
c *f694:n  (455<u=45)
c fc694    3L Neutron Tally for Calculation of Average Neutron Energy
c fs694    6002 6007 6012 6017 6022 6027 6032 6037 6042 6047 6052 6057
c fq694    s f
c
c *f704:p  (455<u=45)
c fc704    3L Photon Tally for Calculation of Average Photon Energy
c fs704    6002 6007 6012 6017 6022 6027 6032 6037 6042 6047 6052 6057
c fq704    s f
c
c f714:p   (1752<u=82)
c fc714    CT Photon Tally
c
c f724:p   (1752<u=82)
c fc724    CT Photon Tally for Calculation of Photon Dose (Kerma)
c de724    1.00E-02 3.00E-02 5.00E-02 7.00E-02 1.00E-01 1.50E-01
c          2.00E-01 2.50E-01 3.00E-01 0.35 0.4 0.45 0.5 0.55 0.6
c          0.65 0.7 0.8 1.0 1.4 1.8 2.2 2.6 2.8 3.25 3.75 4.25 4.75
c          5.0 5.25 5.75 6.25 6.75 7.5 9.0 11.0 13.0 15.0
c df724    3.96E-06 5.82E-07 2.90E-07 2.58E-07 2.83E-07 3.79E-07
c          5.01E-07 6.31E-07 7.59E-07 8.78E-07 9.85E-07 1.08E-06
c          1.17E-06 1.27E-06 1.36E-06 1.44E-06 1.52E-06 1.68E-06
c          1.98E-06 2.51E-06 2.99E-06 3.42E-06 3.82E-06 4.01E-06
c          4.41E-06 4.83E-06 5.23E-06 5.60E-06 5.80E-06 6.01E-06
c          6.37E-06 6.74E-06 7.11E-06 7.66E-06 8.77E-06 1.03E-05
c          1.18E-05 1.33E-05
c
c *f734:p  (1752<u=82)
c fc734    CT Photon Tally for Calculation of Average Photon Energy
c
c f804:p   1800 1801 1802 1803 1804 1805 1806
c fc804    Photon Tally for Radial Profile
c
c f824:n   (124<u=8)
c fc824    Neutron flux tally for peaking factors in fuel pins
c fs824    6015 6017 6019 6021 6023 6025 6027 6029 6031 6033 6035 6037
c          6039 6041 6043 6045 6047 6049 T
c fq824    s f
c
c f17:n    (124<u=8)
c fc17     Fission energy deposition averaged over a cell [MeV/g]
c fs17     6015 6017 6019 6021 6023 6025 6027 6029 6031 6033 6035 6037
c          6039 6041 6043 6045 6047 6049 T
c fq17     s f
c
c ------------------------
c Criticality calculation
c ------------------------
c 100000 n/cycle, 1.000 as initial guess, skip 30, total of 50 keff cycles,
c automatic plotting of three combined keff tally
c
 kcode   1000000 1.000 30 130 4500 0 6500 1
 mplot freq 10 kcode 16 scales 2
 ksrc     -4.5  21.8  13   0    21.8  13   4.5  21.8  13  -11    18    13
          -6.5  18.0  13  -2    18.0  13   2.0  18    13    6.5  18    13
          11    18    13 -17.5  14.3  13 -13    14.3  13   -9    14.3  13
          -4.5  14.3  13   0    14.3  13   4.5  14.3  13    9    14.3  13
          13    14.3  13 -19.5  10.5  13 -15.5  10.5  13  -11    10.5  13
          -6.5  10.5  13   2    10.5  13   6.5  10.5  13   11    10.5  13
          15.5  10.5  13  19.5  10.5  13 -22     6.8  13  -17.5   6.8  13
         -13     6.8  13  -9     6.8  13  -4.5   6.8  13    0     6.8  13
           4.5   6.8  13   9     6.8  13  13     6.8  13   17.5   6.8  13
         -19.5   2.8  13 -15.5   2.8  13 -11     2.8  13   -6.5   2.8  13
          -2     2.8  13   2     2.8  13   6.5   2.8  13   11     2.8  13
          15.5   2.8  13  19.5   2.8  13 -22    -0.8  13  -17.5  -0.8  13
         -13    -0.8  13  -4.5  -0.8  13   4.5  -0.8  13   13    -0.8  13
```

```
          17.5  -0.8  13  22    -0.8  13 -24    -4.6  13  -19.5  -4.6  13
         -15.5  -4.6  13 -11    -4.6  13  -6.5  -4.6  13   -2    -4.6  13
           2    -4.6  13   6.5  -4.6  13  11    -4.6  13   15.5  -4.6  13
          19.5  -4.6  13 -22    -8.3  13  -9    -8.3  13   -4.5  -8.3  13
           0    -8.3  13   4.5  -8.3  13   9    -8.3  13   13    -8.3  13
          17.5  -8.3  13  22    -8.3  13 -11   -12    13   -6.5 -12    13
           2   -12    13   6.5 -12    13  11   -12    13   15.5 -12    13
          19.5 -12    13 -17.5 -15.9  13 -13   -15.9  13   -9   -15.9  13
          -4.5 -15.9  13   0   -15.9  13   4.5 -15.9  13    9   -15.9  13
          13   -15.9  13  17.5 -15.9  13 -15.5 -19.7  13  -11   -19.7  13
          -6.5 -19.7  13  -2   -19.7  13   2   -19.7  13    6.5 -19.7  13
          11   -19.7  13  -4.5 -23.5  13   0   -23.5  13    4.5 -23.5  13
c
c KCODE nsrck rkk ikz kct msrk knrm mrkp kc8
c  nsrck - number of source histories per cycle (def=1000)
c  rkk   - initial guess for keff (def=1.0)
c  ikz   - number of cycles to be skipped before beginning tally accumulation
c  kct   - number of cycles to be done (def=ikz+100)
c  msrk  - number of source points for which to allocate storage (def=4500)
c  knrm  - controls normalization of tallies
c            knrm=0, normalization by weight (def)
c            knrm=1, normalization by number of histories
c  mrkp  - maximum number of cycle values on MCTAL or RUNTPE (def=6500)
c  kc8   - controls the number of cycles over which summary and tally info
c          are averaged
c            kc8=0, averaged over all cycles
c            kc8=1, averaged over all active cycles (def)
c
c PIKMT    1001  0   5010  0   5011  0   6000  0   7014  0   8016  0
c         12000  0  13027  0  14000  0  15031  0  16000  0  24000  0
c         25055  0  26000  0  26054  0  26058  0  27059  0  28000  0
c         28058  0  28064  0  29000  0  29063  0  30000  0  40090  0
c         40091  0  40092  0  40094  0  40096  0  42098  0  48000 -1
c         79197  0  82000  0  92235  0  92238  0
 thtme 0     $ time in shakes (1e-8 sec) at which thermal temperatures...
 mode n
 phys:n 20 0 0 -1 100
c mode p
c phys:p  100 1 0 0 1 -102    $ -102, Analog sampling, models only, multigroup + line emission
 imp:n   1 311r 0
c imp:p   1 311r 0
 print
c
c BURN
c  TIME=T1,T2,T3...  - duration of burn step i (days)
c  PFRAC=F1,F2,F3... - power fraction of each time step
c  POWER=P           - power level (MW)
c  MAT=M1,M2,M3...   - list of material numbers to include in the burn
c  OMIT=J1,N1,I11,I12... J2,N2,I21,I22...
c  AFMIN=A           - atom frac. min. below which the atom frac. is set to zero
c  BOPT=B1,B2,B3...  - B1 - Q value multiplier
c                      B2 - burn table output frequency, ordering, content flag
c
c tmesh
c  cmesh1:n
c  cora1 0 44i 45
c  corb1 -45 59i 45
c  corc1 1 358i 360
c endmd
```

Bibliography

[1] A. H. Johnston. Radiation damage of electronic and optoelectronic devices in space. In *The 4th International Workshop on Radiation Effects on Semiconductor Devices for Space Applications*, 2000.

[2] E. J. Daly. *AIP Conf. Proc.*, 186:483, 1989.

[3] A. Holmes-Siedle and L. Adams. *Handbook of Radiation Effects*. Oxford University Press, New York, 1993.

[4] J. A. Simpson. *Ann. Rev. Nucl. Part. Sci.*, 33:323, 1983.

[5] K.-H. Kampert and M. Unger. *arXiv:1201.0018v2 [astro-ph.HE]*, 2012.

[6] J. N. Goswami, R. E. McGuire, R. C. Reddy, D. Lai, and R. Jha. *J. Geophys. Res.*, 93:7195, 1988.

[7] J. W. Wilson, F. A. Cucinotta, J. L. Shinn, L. C. Simonsen, R. R. Dubey, W. R. Jordan, T. D. Jones, C. K. Chang, and M. Y. Kim. *Radiat. Meas.*, 30:361, 1999.

[8] L. Remec. Study of neutron flux and dpa attenuation in the reactor pressure-vessel wall, ornl/nrc/ltr-99/5, 1999.

[9] U. Jendirch and N. Tricot. Neutron fluence at the reactor pressure vessel wall - a comparison of french and german procedures and strategies in pwrs, 2002.

[10] H. L. Brode. A review of nuclear explosion phenomena pertinent to protective construction, 1964.

[11] A. G. Holmes-Siedle. Radiation effects in the joint european torus experiment - guidlines for preliminary design, final report r857/2.

[12] G. Lindström. *Nucl. Instrum. Meth. A*, 512:30, 2003.

[13] G. J. Dienes. *Ann. Rev. Nucl. Sci.*, 2:187, 1953.

[14] S. Wood, N. J. Doyle, J. A. Spitznagel, W. J. Choyke, R. M. More, J. N. McGruer, and R. B. Irwin. *IEEE Trans. Nucl. Sci.*, 28:4107, 1981.

[15] `http://www.physikinstrumente.com/en/products/primages.php?sortnr=400600.00`, April 2013.

[16] T. R. Welberry, D. J. Goossens, R. L. Withers, and K. Z. Baba-Kishi. *Metall. Mater. Trans. A*, 41:1110, 2010.

[17] S. C. Lee, G. Teowee, R. D. Schrimpf, D. P. Birnie, D. R. Uhlmann, and K. F. Galloway. *IEEE Trans. Nucl. Sci.*, 39:2036, 1992.

[18] D. A. Hall. *J. Mater. Sci.*, 36:4575, 2001.

[19] W. L. Warren, G. E. Pike, K. Vanheusden, D. Dimos, B. A. Tuttle, and J. Robertson. *J. Appl. Phys.*, 79:9250, 1996.

[20] R. A. Eichel. *J. Am. Ceram. Soc.*, 91:691, 2008.

[21] O. S. Ovchinnikov, S. Jesse, P. Bintacchit, S. Trolier-McKinstry, and S. V. Kalinin. *Phys. Rev. Lett.*, 103:157203, 2009.

[22] X. L. Zhang, Z. X. Chen, L. E. Cross, and W. A. Schulze. *J. Mater. Sci.*, 18:968, 1983.

[23] N. Izyumskaya, Y.-I. Alivov, S.-J. Cho, H. Morkoç, H. Lee, and Y.-S. Kang. Processing, structure, properties and applications of pzt thin films, 2007.

[24] S. I. Cho, J. K. Lee, W. H. Yoon, J. O. Lee, S. S. Jung, and W. C. Seo. *Mod. Phys. Lett. B.*, 22:833, 2008.

[25] M. Budimir, A. Mohimi, C. Selcuk, and T.-H.Gan. High temperature nde ultrasound transducers for condition monitoring of superheated steam pipes in nuclear power plants. In *Nuclear Energy for New Europe*, 2011.

[26] F. P. J. Augereau, J.-Y. Ferrandis, J.-F. Villard, D. Fourmentel, M. Dierckx, and J. Wagemans. Effect of intense neutrons dose radiation on piezoceramics. In *Acoustics '08*, 2008.

[27] J. F. Scott, C. A. Araujo, H. B. Meadows, L. D. McMillan, and A. Shawabkeh. *J. Appl. Phys.*, 66:1, 1989.

[28] J. F. Scott and C. A. Araujo. *Science*, 246:1400, 1989.

[29] G. Rebeiz and J. Muldavin. *IEEE Microwave Mag.*, 2:59, 2001.

[30] S. Bing, C. Liguo, R. Weibin, X. Min, and R. Changhai. The research on a novel pzt actuated precise tilt positioning system. In *Industrial Electronics and Applications, 2009. ICIEA 2009. 4th IEEE Conference*, page 1748, 2009.

[31] S. Takechi, T. Onishi, S. Minami, T. Miyachi, M. Fujii, N. Hasebe, K.-I. Nogami, H. Ohashi, S. Sasaki, H. Shibata, T. Iwai, E. Grün, R. Srama, and N. Okada. *Rev. Scie. Instrum.*, 79:043303, 2008.

[32] T. Miyachi, N. Hasebe, H. Ito, T. Masumara, H. Yoshioka, N. Yamashita, O. Okudaira, T. Marukami, Y. Uchihori, M. Sato, and T. Tou. Study of low-q pzt as a radiation detector. In *Nuclear Science Symposium Conference Record, 2002 IEEE*, volume 1, page 9, 2002.

[33] R. Bittner, K. Humer, H. K. Weber, K. Kudzins, A. Sterberg, D. A. Lesnyh, D. V. Kulikov, and Y. V. Trushin. *Integr. Ferroelectr.*, 72:47, 2005.

[34] R. A. Moore, J. M. Benedetto, J. M. McGarrity, and F. B. McLean. *IEEE Trans. Nucl. Sci.*, 38:1078, 1991.

[35] C. Miclea, C. Tanasoiu, C. F. Miclea, I. Spanulescu, and M. Cioangher. *J. Phys. IV*, 128:115, 2005.

[36] M. I. Toacsan, A. Ioachim, L. Nedelcu, and H. V. Alexandru. *Prog. Solid State Ch.*, 35:531, 2007.

[37] D. V. Kulikov, Y. V. Trushin, R. Buttner, K. Humer, H. W. Weber, A. R. Stenberg, D. A. Lesnyh, and A. A. Schmidt. In *4th Int. Workshop NDTCS*.

[38] J. A. Gallego-Juarez. *J. Phys. E*, 22:804, 1989.

[39] B. Jaffe, W. R. Cook, and H. Jaffe Jr. *Piezoelectric Ceramics*. Academic Press, New York, 1971.

[40] S. M. Selbach, T. Tybell, M.-A. Einarsrud, and T. Grande. *Appl. Phys. Lett.*, 98:091912, 2011.

[41] C. H. Park and D. J. Chadi. *Phys. Rev. B*, 57:13961, 1998.

[42] D. V. Kulikov and Y. V. Trushin. *Ferroelectrics*, 304:5, 2004.

[43] J. M. Benedetto, R. A. Moore, F. B. McLean, and P. S. Brody. *IEEE Trans. Nucl. Sci.*, 37:1713, 1990.

[44] J. Gao, L. Zheng, B. Huang, Z. Song, L. Yang, Y. Fan, D. Zhu, and C. Lin. *Semicond. Sci. Technol.*, 14:836, 1999.

[45] I. Baturin, N. Menou, V. Shur, C. Muller, and D. Kuznetsov. *Mater. Sci. Eng. B-Adv.*, 120:141, 2005.

[46] C. T. Shelton, P. G. Kotula, G. L. Brennecka, P. G. Lam, K. E. Meyer, J. P. Maria, B. J. Gibbons, and J. F. Ihlefeld. *Adv. Funct. Mater.*, 22:2295, 2012.

[47] G. L. Brennecka, J. F. Ihlefeld, J. P. Maria, B. A. Tuttle, and P. G. Clem. *J. Am. Ceram. Soc.*, 93:3935, 2010.

[48] R. A. Assink and R. W. Schwartz. *Chem. Mater.*, 5:511, 1993.

[49] `http://www.nanokote.com.au/n/metal-finishes`, April 2013.

[50] J. Braisted. Ph.D. thesis, The University of Texas at Austin, 2008.

[51] D. M. Zangirolami, A. V. Ferreira, and A. H. Oliveira. *Braz. J. Phys.*, 39:260, 2009.

[52] ASTM E 722 94. Standard practice for characterizing neutron energy fluence spectra in terms of an equivalent monoenergetic neutron fluence for radiation-hardness testing of electronics, 1994.

[53] `mcnpx.lanl.gov/docs/MCNPX_2.6.0_Manual.pdf`, April 2013.

[54] ASTM E 262 08. Standard test method for determining thermal neutron reaction rates and thermal neutron fluence rates by radioactivation techniques, 2008.

[55] `http://www.lesker.com/newweb/Vacuum_systems/deposition_systems_pvd_lab18.cfm`, April 2013.

[56] `http://rsbweb.nih.gov/ij/docs/index.html`, April 2013.

[57] ASTM E 112 12. Standard test methods for determining average grain size, 2012.

[58] J. T. Evans. Characterizing ferroelectric materials, 2011. Tutorial talk.

[59] http://www.ferrodevices.com/1/297/files/VII.Tasks-D.Measurement-1.HysteresisTasks-i.Hysteresis.pdf#search="hysteresismeasurement", April 2013.

[60] I. D. Mayergoyz. *Mathematical Models of Hysteresis and Their Applications.* Elsevier, Amsterdam, 2003.

[61] F. Preisach. *Z. Phys.*, 94:277, 1935.

[62] D. Bertotti, I. D. Mayergoyz, V. Basso, and A. Magni. *Phys. Rev. E*, 60:1428, 1999.

[63] W. Zhu, I. Fujii, and S. Trolier-McKinstry. *J. Appl. Phys.*, 109:064105, 2011.

[64] I. Fujii, E. Hong, and S. Trolier-McKinstry. *IEEE Trans. Ultrason. Ferroelectr. Freq. Control*, 57:1717, 2010.

[65] A. Stancu, D. Ricinschi, L. Mitoseriu, P. Postolache, and M. Okuyama. *Appl. Phys. Lett.*, 83:3767, 2003.

[66] L. Stoleriu, A. Stancu, L. Mitoseriu, D. Piazza, and C. Galassi. *Phys. Rev. B*, 74:174107, 2006.

[67] D. Damjanovic. *The Science of Hysteresis.* Elsevier, Amsterdam, 2005.

[68] D. Damjanovic and M. Demartin. *J. Phys. D Appl. Phys.*, 29:2057, 1996.

[69] R. E. Eitel, T. R. Shrout, and C. A. Randall. *J. Appl. Phys.*, 99:124110, 2006.

[70] Q. M. Zhang, W. Y. Pan, S. J. Jang, and L. E. Cross. *J. Appl. Phys.*, 64:6445, 1988.

[71] A. Pramanick, D. Damjanovic, J. E. Daniels, J. C. Nino, and J. L. Jones. *J. Am. Ceram. Soc.*, 94:293, 2011.

[72] A. Bernal and N. Bassiri-Gharb. *Appl. Phys. Lett.*, 95:042902, 2009.

[73] M. Davis, D. Damjanovic, and N. Setter. *J. Appl. Phys.*, 95:5679, 2004.

[74] M. Davis, D. Damjanovic, and N. Setter. *J. Appl. Phys.*, 100:084103, 2006.

[75] N. B. Gharb and S. Trolier-McKinstry. *J. Appl. Phys.*, 97:064106, 2005.

[76] D. V. Taylor and D. Damjanovic. *J. Appl. Phys.*, 82:1973, 1997.

[77] D. V. Taylor and D. Damjanovic. *Appl. Phys. Lett.*, 73:2045, 1998.

[78] J. F. Ihlefeld, C. M. Folkman, S. H. Baek, G. L. Brennecka, M. C. George, J. F. Carroll, and C. B. Eom. *Appl. Phys. Lett.*, 97:262904, 2010.

[79] A. Stancu, C. Pike, L. Stoleriu, P. Postolache, and D. Cimpoesu. *J. Appl. Phys.*, 93:6620, 2003.

[80] A. Stancu, D. Ricinschi, L. Mitoseriu, D. Piazza, and C. Galassi. *Phys. Rev. B*, 74:174107, 2006.

[81] Y. Bastani, T. Schmitz-Kempen, A. Roelofs, and N. Bassiri-Gharb. *J. Appl. Phys.*, 109:014115, 2011.

[82] M. H. Norgett, M. T. Robinson, and I. M. Torrens. *Nucl. Engr. Design*, 33:50, 1975.

[83] `http://www.nndc.bnl.gov/exfor/endf00.jsp`, April 2013.

[84] `http://t2.lanl.gov/nis/codes/njoy99/`, April 2013.

[85] `http://www.srim.org/`, April 2013.

[86] Y. Guo, G. Xie, M. Tang, Y. Xiao, S. Yan, and Y. Zhou. *Radiat. Eff. Defect S.*, 2013. DOI: 10.1080/10420150.2013.792818.

[87] K. L. Smith and N. J. Zaluzec. *J. Nucl. Mat.*, 336:261, 2005.

[88] G. S. Was. *Fundamentals of Radiation Materials Science.* Springer, Heidelberg, 2007.

[89] Y.-H. Son, K.-T. Kim, and C.-I. Kim. *J. Vac. Sci. Technol. A*, 22:1743, 2004.

[90] Y. J. Yu, H. L.W. Chan, F. P.Wang, and L. P. Zhao. *Microelectron. Eng.*, 66:726, 2003.

[91] T. Haccart, D. Remiens, , and E. Cattan. *Thin Solid Films*, 423:235, 2003.

[92] L. Van Brutzel, J.-M. Delaye, D. Ghaleb, and M. Rarivomanantsoa. *Phil. Mag.*, 83:4083, 2010.

[93] D. J. Bacon, F. Gao, and Y. N. Osetsky. *J. Nucl. Mat.*, 276:1, 2000.

[94] ed. R.E. Stoller. *Comprehensive Nuclear Materials: Primary Radiation Damage Formation.* Elsevier, 2012.

Vita

Joseph Turner Graham was born in Manitou Springs, Colorado in 1987. He studied at McGill University in Montreal, Quebec from 2006 until 2009 when he graduated with a B.S. in physics. Later that year he enrolled as a graduate student at the University of Texas at Austin with the Nuclear and Radiation Engineering program within the Mechanical Engineering department. Graduating in 2011 with his M.S.E he elected to continue his education at the doctoral level.

Joseph holds a Nuclear Regulatory Commission Fellowship Grant and was a former fellow with the National Institute for Nano Engineering, a program through which he was able to conduct his doctoral research at Sandia National Laboratories. Joseph is also a recipient of the 2012 Department of Energy's Fuel Cycle Student Innovator Award.

Joseph has accepted an offer to work as a post-doctorate researcher at the University of Tennessee at Knoxville where he will be conducting ion beam irradiation experiments to study radiation effects in ceramics with nuclear applications.

Permanent address: joe.t.graham@gmail.com

This dissertation was typeset with LaTeX[†] by the author.

[†]LaTeX is a document preparation system developed by Leslie Lamport as a special version of Donald Knuth's TeX Program.